

AFRL-AFOSR-UK-TR-2013-0011



**Plasma detachment mechanisms in propulsive
magnetic nozzles**

**Eduardo Ahedo
Mario Merino**

**Universidad Politecnica de Madrid
Plasmas and Space Propulsion Team
Calle Ramiro de Maeztu 7
Madrid, Spain 28040**

EOARD Grant 12-2043

Report Date: March 2013

Final Report from 7 March 2012 to 6 March 2013

Distribution Statement A: Approved for public release distribution is unlimited.

**Air Force Research Laboratory
Air Force Office of Scientific Research
European Office of Aerospace Research and Development
Unit 4515 Box 14, APO AE 09421**

REPORT DOCUMENTATION PAGE

Form Approved OMB No. 0704-0188

Public reporting burden for this collection of information is estimated to average 1 hour per response, including the time for reviewing instructions, searching existing data sources, gathering and maintaining the data needed, and completing and reviewing the collection of information. Send comments regarding this burden estimate or any other aspect of this collection of information, including suggestions for reducing the burden, to Department of Defense, Washington Headquarters Services, Directorate for Information Operations and Reports (0704-0188), 1215 Jefferson Davis Highway, Suite 1204, Arlington, VA 22202-4302. Respondents should be aware that notwithstanding any other provision of law, no person shall be subject to any penalty for failing to comply with a collection of information if it does not display a currently valid OMB control number.

PLEASE DO NOT RETURN YOUR FORM TO THE ABOVE ADDRESS.

1. REPORT DATE (DD-MM-YYYY) 7 March 2013	2. REPORT TYPE Final Report	3. DATES COVERED (From - To) 7 March 2012 - 6 March 2013
--	---------------------------------------	--

4. TITLE AND SUBTITLE Plasma detachment mechanisms in propulsive magnetic nozzles	5a. CONTRACT NUMBER FA8655-12-1-2043
	5b. GRANT NUMBER Grant 12-2043
	5c. PROGRAM ELEMENT NUMBER 61102F

6. AUTHOR(S) Eduardo Ahedo Mario Merino	5d. PROJECT NUMBER
	5d. TASK NUMBER
	5e. WORK UNIT NUMBER

7. PERFORMING ORGANIZATION NAME(S) AND ADDRESS(ES) Universidad Politecnica de Madrid Plasmas and Space Propulsion Team Calle Ramiro de Maeztu 7 Madrid, Spain 28040	8. PERFORMING ORGANIZATION REPORT NUMBER N/A
--	--

9. SPONSORING/MONITORING AGENCY NAME(S) AND ADDRESS(ES) EOARD Unit 4515 BOX 14 APO AE 09421	10. SPONSOR/MONITOR'S ACRONYM(S) AFRL/AFOSR/UK/EOARDD
	11. SPONSOR/MONITOR'S REPORT NUMBER(S) AFRL-AFOSR-UK-TR-2013-0011

12. DISTRIBUTION/AVAILABILITY STATEMENT
Distribution A: Approved for public release; distribution is unlimited.

13. SUPPLEMENTARY NOTES

14. ABSTRACT
A 2D fluid model of the helicon source has been derived and matched to a similar model of the magnetic nozzle. Attention has been given to the 2D neutral depletion and the plasma confinement from rear and lateral walls of the source. Source performances are given in terms of the propellant utilization and production efficiency. Ranges of design and operational parameters for optimal performances are identified. Analytic solutions compare well with numerical solutions within appropriate parametric ranges. The matching of the source model with a divergent MN model has allowed the first complete characterization of the plasma discharge in a helicon plasma thruster. Additionally, it has allowed to solve a previous inconsistency in relating the plasma temperature with the absorbed power, which turns out to involve the plasma expansion in the MN. The different contributions to the thrust and the energy balance have been analyzed. Encouraging values of the thrust efficiency are obtained. Further work should try to couple this plasma flow model with a 2D model of the plasma-wave interaction, in order to ascertain the validity of the assumptions made in the flow model here or how they should be modified. For instance, a non-Maxwellian distribution function of electrons could modify the results. Also, a downstream plasma detachment model would allow us to avoid the downstream plate included here.

15. SUBJECT TERMS
EOARD, Electric Propulsion, Electromagnetic Fields, Electromagnetics

16. SECURITY CLASSIFICATION OF:			17. LIMITATION OF ABSTRACT SAR	18. NUMBER OF PAGES 126	19a. NAME OF RESPONSIBLE PERSON Kevin Bollino, Lt Col, USAF
a. REPORT UNCLAS	b. ABSTRACT UNCLAS	c. THIS PAGE UNCLAS			19b. TELEPHONE NUMBER (Include area code) +44 (0)1895 616007

FINAL REPORT

Plasma detachment mechanisms in propulsive magnetic nozzles

Eduardo Ahedo
Mario Merino

*Plasmas and Space Propulsion Team,
Universidad Politécnica de Madrid, Spain*

Award FA8655-12-1-2043

Period of performance: 03/07/12 - 03/06/13
Date of report: March 7, 2013

PAGE INTENTIONALLY LEFT BLANK

ABSTRACT

The acceleration and detachment stages of a collisionless plasma jet in a divergent wall-less magnetic nozzle are studied through an axisymmetric model. The jet is emitted sonically by a cylindrical chamber simulating a helicon source. A novel integration algorithm which advances along the characteristic lines of the supersonic plasma allows reaching the region beyond the turning point of the nozzle, where large rarefaction and detachment take place. In the ideal zero Larmor radius limit of electrons, the demagnetization of massive ions is identified as the key mechanism enabling inwards detachment of the quasineutral plasma jet from the magnetic lines. Moreover, a parallel study has been devoted to show that incipient electron Larmor radius effects lead to outwards detachment of electron streamtubes, which is detrimental for inwards detachment of mass-carrying ions. Essential to this plasma detachment mechanism is the non-fulfillment of local current ambipolarity in the two-dimensional expansion of a globally-current-free plasma. The opposite requirements of ions and electrons on the magnetic field strength imply that optimal strength and shape of the magnetic nozzle have to exist, in order to maximize the contribution of the magnetic nozzle to thrust efficiency. Further research should address the very-far region, where both quasineutrality and electron-magnetization fail, and an electron collisionless-cooling mechanism seems to be primordial. Complementary to the above detachment studies the magnetic nozzle model has been extended in three ways. First, the formation and curvature of axisymmetric current-free double-layers in the nozzle and their influence on performances have been analyzed. Second, the nozzle model has been matched to a plasma source model in order to study the propulsive performances of a helicon plasma thruster. And third, an alternative hybrid code of the magnetic nozzle, capable of addressing additional plasma effects has been started to build.

PAGE INTENTIONALLY LEFT BLANK

SUMMARY OF RESULTS

The research carried out under the present grant continues the one started in grant FA8655-10-1-3085 'Magnetic nozzles for plasma thrusters: acceleration, thrust, and detachment mechanisms'. The achievements of the first grant covered (1) the study of plasma acceleration and thrust increment mechanisms in a magnetic nozzle (MN) and (2) a critical review of existing detachment theories. The MN transforms the internal energy of the plasma into axially-directed kinetic energy, thus producing a highly supersonic plasma beam. While the expansion of plasma in a MN vaguely resembles that in a solid, de Laval nozzle, the central role of long-range forces in MNs sets them apart from their solid counterparts. First, a MN has the key advantage of operating in a contactless manner, thereby avoiding severe plasma losses and wall durability problems. Second, the expansion is far from quasi-one-dimensional, and depends strongly on the form or species in which the internal plasma energy is stored, which can be different in each particular device (helicon thruster, AFMPD, VASIMR, ...). Lastly, there are significant differences in the processes of thrust production and plasma detachment. A summary of our research achievements on MNs up to May 2012 was presented in **Ref. 9**.

The mission of any propulsive nozzle is to increment the delivered thrust. In a solid nozzle, the physical mechanism of thrust is the pressure exerted on the nozzle divergent walls. In a wall-less MN, as we showed theoretically and has been confirmed experimentally later, thrust is of magnetic character. The magnetized plasma develops diamagnetic azimuthal currents on electrons that oppose those running in the thruster coils, thus creating two repelling magnetic forces: one yields positive thrust on the thruster, while the second one accelerates the plasma.

There is ample consensus that the main uncertainty about the applicability of MNs in space propulsion is the ability of the plasma to detach from the closed magnetic lines: once accelerated, it is imperative that the plasma beam releases itself from the magnetic field downstream and continues to expand freely into vacuum. If this is not the case, the returning plasma would cancel the produced thrust and impinge on the delicate spacecraft surfaces. Two important aspects to take into account when dealing with the detachment of a plasma jet are: first, ions carry almost totally the plasma mass; and second a small backflow is unavoidable in any plasma plume expanding into vacuum. Therefore, the detachment problem must determine (1) which mechanism allows ion streamtubes to detach inwards from the magnetic lines and avoid flowing back; (2) which fraction of the beam mass is backflowing; and (3) which is the contribution of a MN to thrust efficiency.

Prevailing detachment theories developed specifically for plasma thrusters with MN have focused on electron detachment, on the assumption that quasineutrality and current ambipolarity make ion and electron streamtubes coincide in current-free plasmas. In a first scenario, electron-inertia (Hooper's theory) or resistivity would produce diffusive detachment of electron streamtubes. In a second scenario, the plasma-induced magnetic field would stretch the MN downstream. Within the previous grant we had shown that these three mechanisms do not lead to inwards electron detachment in a propulsive MN: electron diffusion detaches electron tubes outwards from the magnetic lines, and the magnetic field induced by diamagnetic plasma currents opposes the applied magnetic field, thus increasing the divergence of the resulting MN.

The first goal of the present research, presented in **Ref. 1**, has been to go further in depth with the study of the effects of electron inertia. It has been shown that, up to dominant order on all components of the electron velocity, electron momentum equations still reduce to three conservation laws. It is confirmed that electron inertia leads to outward electron separation from the magnetic streamtubes. The progressive plasma filling of the adjacent vacuum region is consistent with electron-inertia being part of finite electron Larmor radius effects, which increase downstream and eventually demagnetize the plasma. It is also confirmed and carefully explained that current ambipolarity in a 2D expansion is not fulfilled and ion separation can be

either outwards or inwards of magnetic streamtubes, depending on their magnetization. Electron separation penalizes slightly the plume efficiency and is larger for plasma beams injected with large pressure gradients. The nonzero electron-inertia model of Hooper, based on cold plasmas and current ambipolarity, which predicts inwards electron separation, is shown to be physically inconsistent. Finally, the study points out the likely competition of the gyroviscous force with electron-inertia effects, making a fully consistent study of finite Larmor radius effects very complex.

The second and main goal of this research has been to demonstrate that inwards detachment of mass-carrying ions caused by ion demagnetization is the key mechanism for the detachment of a plasma jet in a propulsive MN, and it takes place even if the asymptotic limit of collisionless, fully-magnetized electrons. Different aspects and progresses of this work have been presented in **Refs. 4, 6, 8, and 10**. In fact, vacuum-chamber measurements on the MN near-region of different thrusters are confirming ion detachment as a real and robust phenomenon. However, measuring plasma expansion and detachment far downstream is more challenging due to chamber size constraints. Theoretically, ion detachment was already identified in our previous grant's research to be a relevant 2D beam feature, but again, the study covered only the MN near region, limited downstream by the MN turning point. Now, a new intrinsic integration algorithm implemented in our 2D DIMAGNO code has allowed us to overcome the MN turning point limitation and to look into the MN far region, both downstream and laterally. The magnetic strength decreases proportional to the area expansion in a divergent MN. For practical magnetic strengths and heavy propellants, ions are weakly magnetized in most or the whole MN, and their axial and radial expansion is governed by the ambipolar electric field mainly. This field deflects ion tubes radially but not enough to follow the electron/magnetic tubes, which means that current ambipolarity cannot be fulfilled everywhere (for a quasineutral, globally current-free plasma). As previously advanced, incipient electron demagnetization is detrimental for inwards beam detachment, and magnetic strength must thus be tuned in order to optimize both beam channeling and acceleration, in the near region, and detachment, in the far region. Finally, it is shown that only a marginal fraction of the beam flows back and the divergence angle of the 95%-mass tube measures the effectiveness of detachment, allowing comparisons with plumes of other plasma thrusters.

The rest of goals of this research have been focused on extending the MN code DIMAGNO in three ways. The first one, covered in **Ref. 2**, has been to address the expansion in a MN of a plasma with two disparate electron populations and the formation and two-dimensional shape of a current-free double-layer in the divergent MN. This subject is very controversial in the field of helicon thruster performances because of the claims of Charles and Boswell on thrust due to double layers. Our study was centered in the regime when the electric potential steepening can still be treated within the quasineutral approximation. The properties of this quasi-double-layer were investigated in terms of the relative fraction of the high-energy electron population, its radial distribution when injected into the nozzle, and the geometry and intensity of the applied magnetic field. The two-dimensional double layer presents a curved shape, which is dependent on the natural curvature of the equipotential lines in a magnetically expanded plasma and the particular radial distribution of high-energy electrons at injection. The double layer curvature increases the higher the nozzle divergence is, the lower the magnetic strength is, and the more peripherally hot electrons are injected. In the application of the theory to the operation of a helicon plasma thruster in space, it is shown that the curvature of the double layer does not increment the thrust, it does not modify appreciably the downstream divergence of the plasma beam, but it increases the magnetic-to-pressure thrust ratio.

The next achievement has been to match the MN model to a model of a helicon plasma source. **References 3, 7, and 9** present a model of the two-dimensional fluid-dynamics and the first analysis of propulsive performances of a helicon plasma thruster. In particular, an axisymmetric macroscopic model of the magnetized plasma flow inside the helicon thruster chamber is derived, assuming that the power absorbed from the helicon antenna emission is known.

Ionization, confinement, subsonic flows, and production efficiency inside the source are discussed in terms of design and operation parameters. Analytical solutions and simple scaling laws for ideal plasma conditions are obtained. The chamber model is then matched with DIMAGNO in order to characterize the whole plasma flow and assess thruster performances. Thermal, electric, and magnetic contributions to thrust are evaluated. The energy balance provides the power conversion between ions and electrons in chamber and nozzle, and the power distribution among beam power, ionization losses, and wall losses. Thruster efficiency is assessed and main causes of inefficiency are identified. The thermodynamic behavior of the collisionless electron population in the nozzle is acknowledged to be poorly known and crucial for a complete plasma expansion and good thrust efficiency.

The last activity carried out has been the development of an alternative MN hybrid code, HPMN, where ions and neutrals are treated as super-particles and electrons as a magnetized fluid. The main motivation of this code is to offer more flexibility than DIMAGNO to treat some non-ideal effects, such as resistivity, ionization, warm and multi-charged ions, plasma-ambient interaction, wall-effects or electron heat diffusion. Additionally, it will provide a mutual validation of DIMAGNO and HPMN. Work is in progress and first promising results were presented in **Ref. 5**.

To conclude, this research has provided crucial advances in the understanding of plasma detachment. Ion demagnetization and subsequent quasineutral separation of ion and electron streamtubes are shown to be the central elements of the detachment mechanism in a collisionless plasma with fully-magnetized electrons. The next stage of the research must address the relaxation of some of the model idealizations and limitations. First, a large downstream plasma rarefaction means that quasineutrality fails eventually. Space-charge effects should be taken into account. These are expected to set an upper-bound to the electric field and thus facilitate ion detachment. Second, for finite electron magnetization, resistivity, electron-inertia, and the plasma-induced magnetic field were shown to deteriorate electron confinement, leading to outward electron detachment, which adversely increases the effective MN divergence. The desire of full electron magnetization on one hand (to minimize the influence of these three phenomena and ensure proper channeling and acceleration of the plasma beam), and low ion magnetization on the other (to foster downstream detachment and achieve low beam divergence), set two conflicting requirements to the magnetic strength of the MN. Once the MN physics are understood, the next step is to apply DIMAGNO to optimize both the MN strength and shape, in order to maximize the thrust efficiency of the MN. Third, separation of ion and electron tubes generates longitudinal electric currents in the otherwise current-free jet. It should be settled whether their closure takes place upstream (inside the source) or downstream, by a combination of residual resistivity, geometric expansion, or entrainment of the weak background plasma. Fourth, the transition from a magnetized to an unmagnetized electron model needs to be addressed consistently. And fifth, the assumption of electron isothermality in the model, while not central for the detachment process, leads to a nonphysical, infinite (logarithmically-slow) drop of the electric potential downstream. Limited laboratory and in-space evidence (with unmagnetized collisionless plumes) suggests the electric potential to vanish as potential law of plasma density. Unfortunately, no established theory exists for the expansion of a collisionless electron population. Theoretical approaches, based on the kinetic theory, suggest the existence of a collisionless-cooling mechanism of electrons based on adiabatic invariants and effective potential barriers.

PAGE INTENTIONALLY LEFT BLANK

LIST OF ACHIEVEMENTS AND REFERENCES

Archival papers

1. 'Two-dimensional plasma expansion in a magnetic nozzle: separation due to electron inertia', E. Ahedo and M. Merino, Physics of Plasmas 19, 083501 (2012)
2. 'Two-dimensional quasi-double-layers in two-electron-temperature current-free plasmas', M. Merino and E. Ahedo, Physics of Plasmas 20, 023502 (2013)
3. 'Helicon thruster plasma modeling: two-dimensional fluid dynamics and propulsive performances', E. Ahedo and J. Navarro, in revision process by Physics of Plasmas (2013)
4. 'Theory of Plasma Detachment in a Propulsive Magnetic Nozzle', M. Merino and E. Ahedo, submitted to Physical Review Letters, February 2013

Conference papers

5. 'Fluid and Hybrid-PIC Code Comparison of the Plasma Plume in a Magnetic Nozzle', J. Navarro, M. Merino and E. Ahedo, AIAA 2012-3840, 48th Joint Propulsion Conference, Atlanta, GE, July 2012
6. 'Magnetic Nozzle Far-Field Simulation', M. Merino and E. Ahedo, AIAA 2012-3843, 48th Joint Propulsion Conference, Atlanta, GE, July 2012
7. 'A fluid-dynamic performance model of a helicon thruster', J. Navarro, M. Merino, and E. Ahedo, AIAA 2012-3955, 48th Joint Propulsion Conference, Atlanta, GE, July 2012

Other conference presentations

8. 'Advanced simulation of magnetic nozzles for plasma thrusters', M. Merino, E. Ahedo, Propulsion 2012, Bordeaux, France, May 2012 (oral)
9. 'Plasma Structure Inside and Outside a Helicon Thruster', J. Navarro, M. Merino and E. Ahedo, 39th ICOPS, Edinburgh, UK, July 2012 (poster)
10. 'Advanced Plasma Propulsion with Magnetic Nozzles: Plasma detachment', 63rd IAC, Naples, Italy, October 2012 (poster)

PhD thesis under progress. The work carried out under this grant will be part of the PhD Theses

11. 'Magnetic nozzles for advanced plasma propulsion', by Mario Merino, to be defended in July 2013
12. 'Simulation of helicon thruster plasmas', by Jaume Navarro, to be finished in 2014

References 1 to 10 are annexed to this report

PAGE INTENTIONALLY LEFT BLANK

ANNEXES

PAGE INTENTIONALLY LEFT BLANK

Two-dimensional plasma expansion in a magnetic nozzle: Separation due to electron inertia

Eduardo Ahedo^{a)} and Mario Merino

Universidad Politécnica de Madrid, 28040 Madrid, Spain

(Received 12 April 2012; accepted 13 July 2012; published online 6 August 2012)

A previous axisymmetric model of the supersonic expansion of a collisionless, hot plasma in a divergent magnetic nozzle is extended here in order to include electron-inertia effects. Up to dominant order on all components of the electron velocity, electron momentum equations still reduce to three conservation laws. Electron inertia leads to outward electron separation from the magnetic streamtubes. The progressive plasma filling of the adjacent vacuum region is consistent with electron-inertia being part of finite electron Larmor radius effects, which increase downstream and eventually demagnetize the plasma. Current ambipolarity is not fulfilled and ion separation can be either outwards or inwards of magnetic streamtubes, depending on their magnetization. Electron separation penalizes slightly the plume efficiency and is larger for plasma beams injected with large pressure gradients. An alternative nonzero electron-inertia model [E. Hooper, *J. Propul. Power* **9**, 757 (1993)] based on cold plasmas and current ambipolarity, which predicts inwards electron separation, is discussed critically. A possible competition of the gyroviscous force with electron-inertia effects is commented briefly. © 2012 American Institute of Physics. [<http://dx.doi.org/10.1063/1.4739791>]

I. INTRODUCTION

Divergent magnetic nozzles, created by longitudinal magnetic fields, are being envisaged as the acceleration stage of several advanced plasma thrusters.^{1–5} In the highly competitive and demanding area of space propulsion, the optimization of plasma thruster characteristics (performances, weight, lifetime, etc.) is crucial. Thus, the eventual implementation of magnetic nozzles requires, among other aspects, a reliable and detailed understanding of the processes governing plasma expansion and thrust transmission. With this aim we developed in Ref. 1 a two-dimensional (2D) model of the expansion of a current-free, fully ionized, near-collisionless, hot plasma (as the one we expect to be delivered by the thruster chamber) in a magnetic nozzle (with no solid walls). We showed there that a *propulsive magnetic nozzle*, capable of increasing the thrust, requires a “hot” plasma, so that plasma internal energy is transformed into ion axial directed energy, and that the nozzle thrust transmission mechanism is the magnetic force of the azimuthal plasma current onto the thruster magnetic circuit.

As usual in analyses of magnetized plasma flows, our 2D model disregarded electron inertia effects, arguing that they were marginal. This was very beneficial for solving the model, since dropping convective terms makes electron momentum equations fully algebraic. In the zero electron-inertia limit, fully magnetized electrons are channeled perfectly by the magnetic field. On the contrary, for the expected magnetic intensities and propellants in envisaged thrusters, ions are only weakly magnetized (except perhaps for very light propellants). As a consequence, it was found

that even fulfilling quasineutrality, ion streamtubes separate inwards from electron streamtubes, generating longitudinal electric currents and breaking current ambipolarity (CA).

The central motivation for discussing electron-inertia here is to analyze electron separation from the magnetic field as a step in understanding the downstream detachment of the plasma from the magnetic nozzle. In a low-beta plasma, the separation of strongly magnetized electrons from magnetic streamtubes can be achieved via resistivity or electron-inertia.⁶ At least one of these mechanisms yields a *dominant term* in the equation determining the electron separation velocity. In a hot, fully ionized plasma, resistivity is weak and electron-inertia is likely to dominate electron separation. Furthermore, electron-inertia effects will be shown to be finite electron Larmor radius (FELR) effects⁷—here, finite meaning small but non-zero. Since the nozzle magnetic field decreases downstream, FELR effects increase and drive the process of plasma demagnetization, when the magnetically channeled plasma beam expands into the adjacent vacuum region. A linear perturbation analysis of the zero-inertia model⁶ advanced that the electron fluid separates outwards from the magnetic lines. This will be confirmed by the model presented here, which accounts for nonlinear electron inertia.

Hooper,¹⁰ working with a nonzero-inertia model, found inwards plasma separation. Since his model has been the basis for other works,^{11–14} yielding inwards plasma separation too, a discussion of Hooper’s model is very pertinent here. Hooper’s model is similar to ours except for two important features, which are at the core of the disagreement with our conclusions: his model imposes current ambipolarity everywhere and is limited to the expansion of a cold plasma. In addition, Hooper applied his model only to a uniform, non-rotating beam at the nozzle throat. Schmit and Fisch¹³ applied it to plasma beams with independent, nonzero

^{a)}Electronic addresses: eduardo.ahedo@upm.es. URL: web.fmetsia.upm.es/ep2 and mario.merino@upm.es. URL: web.fmetsia.upm.es/ep2.

azimuthal ion and electron flows. Little and Choueiri¹⁴ have attempted to include the effects of plasma pressure in Hooper's model.

Electron-inertia is just one part of FELR effects. Full FELR effects include also the divergence of the gyroviscous (or stress) tensor,⁷⁻⁹ known as gyroviscous force, which is ignored in all the above models. Consistent term ordering in plasma fluid models for the case of finite Larmor radius—discussed mainly in the plasma fusion field and focused on ions, but valid for electrons too—states that the gyroviscous force is of the order of the convective electron derivative in the so-called drift ordering.⁷ Here, the possible competition of gyroviscous with electron-inertia effects will be only pointed out.

The rest of the paper is organized as follows. Section II recovers the model formulation for ions of Ref. 1. Section III derives and discusses the nonzero inertia model for the electron fluid. Section IV analyzes the plasma response in terms of main parameters. Section V discusses separately on current ambipolarity models and gyroviscous effects. Section VI compiles conclusions. A preliminary version of this work was presented as a conference paper.¹⁵

II. MODEL: NOZZLE AND ION EQUATIONS

The general assumptions and notation of the present model are identical to those in Ref. 1; only the elements that facilitate the autonomous reading of the present paper are repeated here. A current-free, fully ionized, collisionless plasma beam of radius R expands from the throat of a divergent magnetic nozzle created by a set of external coils and internal plasma currents. In the cylindrical frame of reference $\{\mathbf{1}_z, \mathbf{1}_r, \mathbf{1}_\theta\}$, with coordinates (z, r) for the axisymmetric magnitudes, the total magnetic field is $\mathbf{B} = B(\mathbf{1}_z \cos \alpha + \mathbf{1}_r \sin \alpha)$. The convention $0 < \alpha < \pi/2$ is adopted for the local magnetic angle, and the magnetic reference $\mathbf{1}_\parallel = \mathbf{B}/B$ and $\mathbf{1}_\perp = \mathbf{1}_\theta \times \mathbf{1}_\parallel$ is used too. There exists a magnetic streamfunction, ψ , satisfying $\nabla\psi = rB\mathbf{1}_\perp$. For the simulations presented here, we will consider the applied magnetic field generated by a solenoid of radius $R_S = 3.5R$ and extending from $z = -2.5R$ to $z = 2.5R$, Fig. 1(a), and we will restrict the analysis to a low-density plasma so that the induced magnetic field is negligible (its inclusion can be carried out iteratively¹⁶). Thus, the throat is located at $z = 0$ and $\alpha(0, r) = 0$. Along the paper, subscript 0 will refer to values of magnitudes at $(z, r) = (0, 0)$.

A two-fluid model is used for the quasineutral plasma, with $n \equiv n_i = n_e$ being the plasma density. The general form of fluid equations for each plasma species ($j = i, e$) is

$$\nabla \cdot n_j \mathbf{u}_j = 0, \quad (1)$$

$$m_j n_j \mathbf{u}_j \cdot \nabla \mathbf{u}_j = -\nabla \cdot \mathbf{P}_j - q_j n_j \nabla \phi + q_j n_j \mathbf{u}_j \times \mathbf{B}, \quad (2)$$

where \mathbf{u}_j is the species fluid velocity, \mathbf{P}_j is the pressure tensor, and the rest of symbols is conventional. For vector magnitudes, such as velocities \mathbf{u}_j ($j = i, e$) and current densities \mathbf{j}_j , their longitudinal (i.e., meridian) projections are denoted with a tilde: $\tilde{\mathbf{u}}_j = \mathbf{u}_j - u_{\theta j} \mathbf{1}_\theta$, etc.

The set of equations for ions can be expressed as

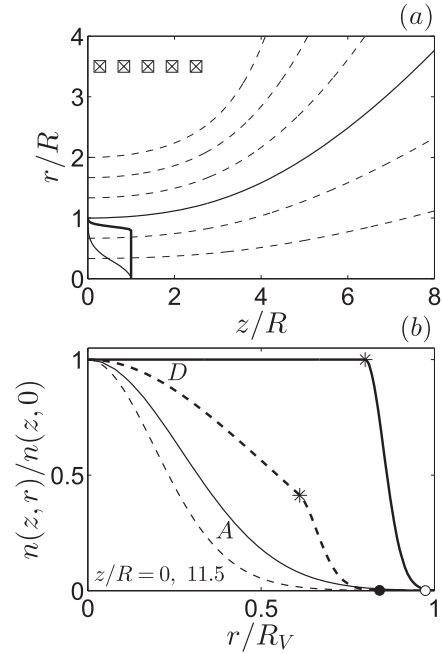


FIG. 1. (a) Magnetic field lines created by the solenoid (squares), and sketches of the two beam density profiles at the throat. The solid line corresponds to the nozzle edge $r = R_B(z)$ in the zero electron-inertia limit. (b) Density profiles at the throat and at section $z/R = 11.5$ for simulations A and D. Asterisks represent the border between the central and peripheral regions of simulation D. Circles represent the location of the magnetic nozzle edge $r = R_B(z)$ at $z/R = 11.5$ for simulations A (white) and D (black).

$$u_{ri} \frac{\partial \ln n}{\partial r} + u_{zi} \frac{\partial \ln n}{\partial z} + \frac{\partial u_{ri}}{\partial r} + \frac{\partial u_{zi}}{\partial z} = -\frac{u_{ri}}{r}, \quad (3)$$

$$u_{ri} \frac{\partial u_{ri}}{\partial r} + u_{zi} \frac{\partial u_{ri}}{\partial z} = -\frac{e}{m_i} \frac{\partial \phi}{\partial r} + u_{\theta i} \Omega_i \cos \alpha + \frac{u_{\theta i}^2}{r}, \quad (4)$$

$$u_{ri} \frac{\partial u_{zi}}{\partial r} + u_{zi} \frac{\partial u_{zi}}{\partial z} = -\frac{e}{m_i} \frac{\partial \phi}{\partial z} - u_{\theta i} \Omega_i \sin \alpha, \quad (5)$$

$$rm_i u_{\theta i} + e\psi = D_i(\psi_i), \quad (6)$$

where ϕ is the ambipolar electric potential, $\Omega_i = eB/m_i$ is the ion gyrofrequency, the ion pressure tensor has been neglected, ψ_i is the ion streamfunction, satisfying

$$\nabla \psi_j = -rn \tilde{\mathbf{u}}_j \times \mathbf{1}_\theta \quad (7)$$

(with $j = i$), and $D_i(\psi_i)$ is the total azimuthal momentum for ions in each streamline, which is determined from conditions at the throat.

In order to complete this set of equations, a relation between ϕ and n is needed, which will be provided by the electron model. Initial conditions (at $z = 0, r \leq R$) for the above equations are the same as in previous works,

$$u_{ri} = 0, \quad u_{\theta i} = 0, \quad u_{zi} = c_s M_0, \quad (8)$$

with $M_0 \geq 1$, and $n(0, r)$ is provided; Fig. 1(b) shows the density profiles used in the simulations below. Notice that ions enter the diverging nozzle without rotation (or swirling). Ion swirling is known to occur in some devices¹⁷ and has been proposed by Schmit and Fisch for increasing inwards plasma separation in the frame of Hooper's model.

III. MODEL: ELECTRON EQUATIONS

As in Ref. 1, let us consider a simple isotropic, isothermal model for the pressure tensor, i.e.,

$$\nabla \cdot \mathbf{P}_e \equiv T_e \nabla n_e. \quad (9)$$

Then because of axisymmetry and no resistivity, the azimuthal momentum equation reduces to

$$\frac{u_{re}}{r} \frac{\partial(ru_{\theta e})}{\partial r} + u_{ze} \frac{\partial u_{\theta e}}{\partial z} = \frac{eB}{m_e} u_{\perp e}. \quad (10)$$

It is evident that this equation determines $u_{\perp e}$, and yields $u_{\perp e} = 0$ in the limit $m_e/m_i \rightarrow 0$. Making use of the magnetic streamfunction, a first integral of Eq. (10) is

$$rm_e u_{\theta e} - e\psi = D_e(\psi_e), \quad (11)$$

where ψ_e is the electron streamfunction, satisfying Eq. (7) for $j=e$, and $D_e(\psi_e)$ is determined from throat conditions too. A second conservation law along electron streamtubes applies to the Bernoulli function,

$$T_e \ln n - e\phi + m_e(\tilde{u}_e^2 + u_{\theta e}^2)/2 = H_e(\psi_e), \quad (12)$$

with $H_e(\psi_e)$ also determined from throat conditions. The third scalar electron momentum equation is the projection along $\mathbf{1}_{\perp e} = \mathbf{1}_\theta \times \tilde{\mathbf{u}}_e/\tilde{u}_e$: substituting Eqs. (11) and (12) into Eq. (16) of Ref. 1 yields

$$u_{\theta e} D'_e = rH'_e + \frac{m_e}{n} \left(\kappa_e \tilde{u}_e - \frac{\partial \tilde{u}_e}{\partial \mathbf{1}_{\perp e}} \right), \quad (13)$$

where primes denote derivatives and κ_e is the meridian curvature of the electron streamtubes. Equations (11)–(13) are exact for the thermodynamic model of Eq. (9).

The electron massless model of Ref. 1 corresponds to the limit $m_e \rightarrow 0$ of Eqs. (11)–(13), which take well-known forms: Eq. (11) states that electron streamtubes are magnetic streamtubes and therefore yields $u_{\perp e} = 0$; Eq. (12) becomes the Boltzmann relation along electron streamtubes, with $-H_e/e$ the so-called “thermalized potential;” and Eq. (13) states, first, that $u_{\theta e}$ is the sum of $\mathbf{E} \times \mathbf{B}$ and $\nabla p \times \mathbf{B}$ drifts [Eq. (25) of Ref. 1], and, second, that the macroscopic azimuthal frequency is constant within streamtubes, that is,

$$\frac{u_{\theta e}}{r} \equiv w_{\theta e}(\psi_e) = -\frac{H'_e}{D'_e}, \quad (14)$$

a property known as isorotation.¹⁸ In addition, for a current-free plasma, we infer that $u_{\parallel e} \sim \tilde{u}_e \sim \tilde{u}_i \sim c_s$, whereas the value of $u_{\theta e}$ is closely dependent on the shape of $n(0, r)$. A typical range would be $O(c_s) \leq u_{\theta e} \leq O(c_e)$ with $c_e = \sqrt{T_e/m_e}$.

In a collisionless plasma, electron-inertia effects constitute the only contribution making $u_{\perp e}$ different from zero. Hence, an electron model retaining the dominant contribution of every component of \mathbf{u}_e must keep the whole equation (11) or the equivalent Eq. (10). On the contrary, the terms with $m_e \tilde{u}_e$ in Eqs. (12) and (13) yield only a contribution of

$O(m_e/m_i)$ in $u_{\parallel e}$ and $u_{\theta e}$, and therefore can be dropped. Summarizing, the proposed nonzero-inertia electron model consists of Eqs. (11), (14), and

$$T_e \ln n - e\phi = H_e(\psi_e) - m_e r^2 w_{\theta e}^2(\psi_e)/2. \quad (15)$$

This model retains fully azimuthal inertia and neglects longitudinal one. Mathematically, the withdrawal of the inertia term in Eq. (13) keeps electron momentum equations algebraic, a very positive feature to be exploited next.

Equation (15) provides the relation between n and ϕ required by Eqs. (3)–(6). However, it also involves the electron streamfunction $\psi_e(z, r)$. Since now $u_{\perp e} \neq 0$, electron streamtubes separate from magnetic streamtubes and their shape must be determined from Eq. (11). Substituting Eq. (14) into it yields

$$r^2 m_e w_{\theta e}(\psi_e) - e\psi(z, r) = D_e(\psi_e), \quad (16)$$

which is an implicit equation for $\psi_e(z, r)$. Therefore, Eqs. (15) and (16) complete the set of equations (3)–(6). Substituting the derivatives of ϕ , Eqs. (3)–(5) constitute a set of three hyperbolic equations for $M_0 > 1$ that are integrated with the method of characteristics of Ref. 1.

The magnetic and electron streamtubes that depart from $(z, r) = (0, R)$ define, respectively, the magnetic nozzle edge, $r = R_B(z)$, and the plasma beam edge, $r = R_V(z)$; their shapes are obtained from solving $\psi(0, R) = \psi(z, R_B)$ and $\psi_e(0, R) = \psi_e(z, R_V)$. Since $R_V \equiv R_B$ for $m_e/m_i \rightarrow 0$, the difference between the magnetic and beam edges measures the electron separation caused by azimuthal electron inertia. The beam edge delimits an ideal plasma/vacuum boundary. In order to minimize the effect of an artificial pressure jump there, we will consider initial density profiles decaying to near-zero at the edge; specifically, we will take $n(0, R) = 10^{-3} n_0$.

Equation (16) establishes a principal feature of our electron model: electron streamtubes and their separation from magnetic streamtubes depend exclusively on the magnetic topology and electron conservation laws, and are independent of the ion dynamics and the plasma density map. From Eqs. (7) and (16), the slope of the electron streamtubes is

$$\frac{u_{re}}{u_{ze}} = -\frac{\partial \psi_e / \partial z}{\partial \psi_e / \partial r} = \frac{eB \sin \alpha}{eB \cos \alpha - 2m_e w_{\theta e}}. \quad (17)$$

This yields a second central feature: electron separation from magnetic streamtubes depends exclusively on the sign of $w_{\theta e}(\psi_e)$, which is determined by the beam conditions at the throat. Assuming a steady-state plasma beam inside the cylindrical source upstream of the divergent nozzle, Tonks^{19,20} showed that the azimuthal electron current is always diamagnetic, which means $w_{\theta e} > 0$ (for our convention on α). Therefore, under that general equilibrium condition, one has

$$u_{re}/u_{ze} > \tan \alpha \quad (18)$$

and the electron streamtubes separate *outwards* from the magnetic streamtubes.

Furthermore, in the strong magnetization limit, the upstream plasma equilibrium corresponds to a θ -pinch,²¹

where the expanding plasma pressure gradient is balanced by the confining magnetic force generated by the azimuthal plasma current, while the confining electric force is negligible. In fact, the θ -pinch limit of Tonks is adopted here as the radial electron equilibrium at the throat

$$0 = -T_e \frac{\partial \ln n}{\partial r} - eu_{\theta e} B + \frac{m_e u_{\theta e}^2}{r}. \quad (19)$$

The last, ‘‘centrifugal’’ term is small (and partially artificial, as we will comment later) but it is kept for the mathematical consistency of our fluid model. For $n(0, r)$ given, Eq. (19) determines the distribution of angular velocities,

$$w_{\theta e}(\psi_e(0, r)) \simeq - \left[\frac{T_e}{eBr} \frac{\partial \ln n}{\partial r} \right]_{z=0}.$$

According to Eq. (17), the magnitude of the electron/magnetic separation is proportional to $w_{\theta e}/\Omega_e$, with $\Omega_e = eB/m_e$ the local electron gyrofrequency. Near the throat and for $\partial \ln n / \partial r \sim 1/R$, one has $w_{\theta e}/\Omega_e \sim (\ell_{e0}/R)^2$, which shows that electron-inertia effects are indeed FELR effects. Since $w_{\theta e}$ is conserved in the electron streamtubes, electron-inertia effects grow downstream as $w_{\theta e}/\Omega_e \propto B^{-1} \propto R_B^2$, as predicted in Ref. 6.

To complete the electron model, the electron initial longitudinal velocity must be defined. Here, we will impose current ambipolarity locally at the throat,

$$\tilde{u}_e(0, r) = \tilde{u}_i(0, r). \quad (20)$$

IV. DISCUSSION OF RESULTS

A. Plasma expansion features

The current parametric investigation is limited to the shape of the initial density profile, $n(0, r)$, and two dimensionless parameters, m_e/m_i and $\hat{\Omega}_{i0} = \Omega_{i0}R/c_s$. As an alternative to one of them, the FELR parameter $\hat{\ell}_{e0} = \ell_{e0}/R = \sqrt{m_e/m_i} \hat{\Omega}_{i0}^{-1}$ can be used. The rest of parameters of the model was discussed in previous works and they have no major relevance on the discussion here. Table I summarizes the five simulations illustrated in the figures to come. Initial density profiles are depicted in Fig. 1(b): simulations O to C correspond to a plasma beam with $w_{e0}(0, r) = \text{const}$, yielding a near-Gaussian density profile,

TABLE I. Parameters of the different simulations presented in the figures. Simulation O corresponds to the zero electron inertia limit. Simulations A and B differ in the magnetic intensity. Simulations A and C differ in the propellant. Simulations A and D differ in the initial density profiles, which are defined within the main text. All simulations take $M_0 = 1.05$ to ensure Eqs. (3)–(5) are hyperbolic.

Simulations	$\hat{\ell}_{e0}$	Ions	$\hat{\Omega}_{i0}$	n profile
O	0	...	0.409	Gaussian-like
A	5×10^{-3}	Xe ⁺	0.409	Gaussian-like
B	5×10^{-2}	Xe ⁺	0.0409	Gaussian-like
C	5×10^{-3}	H ⁺	4.67	Gaussian-like
D	5×10^{-3}	Xe ⁺	0.409	Uniform-like

$$n(0, r) = n_0 \exp \left[\frac{-2ew_{\theta e}\psi + m_e w_{\theta e}^2 r^2}{2T_e} \right]; \quad (21)$$

and simulation D corresponds to an initially near-uniform beam, treated in Subsection IV B.

Figure 2 illustrates electron and ion separation for simulations A and B, which operate with the same gas (i.e., same m_e/m_i) and different magnetic intensity B_0 . As discussed before, electron separation is outwards and it increases as the magnetic field decreases. The ambipolar electric force caused by quasineutrality tends to keep the ion streamtubes close to the electron ones. However, the incomplete ion magnetization makes them separate inwards from the electron streamtubes, except at the plasma/vacuum edge $r = R_V(z)$. Here lies a key difference with Hooper’s class of models, which tie *a priori* ion and electron streamtubes. Let $\alpha_{jB} = \text{angle}(\mathbf{B}, \tilde{\mathbf{u}}_j)$ ($j = i, e$), be the separation angles of ion and electron streamtubes with respect to the magnetic field. Figure 3 plots examples of the possible behaviors: $\alpha_{eB} = 0$ and $\alpha_{iB} < 0$, for $m_e/m_i = 0$; $\alpha_{eB} > 0$ and α_{iB} taking both signs; and $\alpha_{eB} > 0$ and $\alpha_{iB} > 0$. Simulations A and C operate with different gases but share the same magnetic intensity. This means the electron separation is the same in both cases, but ion streamtubes are (slightly) more divergent for light hydrogen ions than for heavy xenon ions.

Interestingly, in the zero-inertia limit ion separation is always inwards, i.e., $\alpha_{iB} < 0$. This implies that $u_{\theta i}$ is positive (for a plasma source yielding a negligible ion swirl current), so that the ion azimuthal current is paramagnetic and contributes negatively to the thrust.¹ For $m_e/m_i \neq 0$, the ion azimuthal current can take both signs within the plasma beam and its contribution to thrust is less negative. Anyway, this

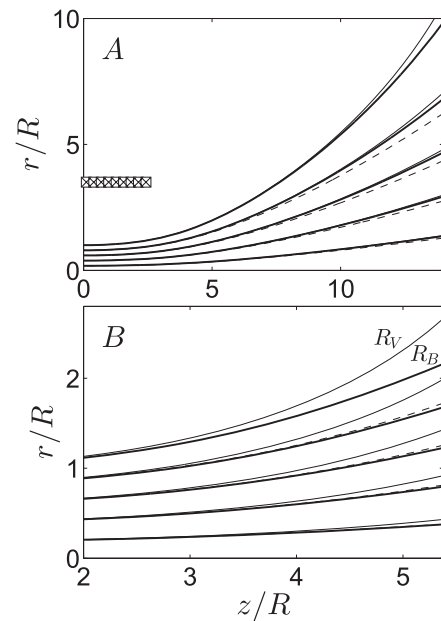


FIG. 2. Streamtubes of magnetic field (solid, thick), electrons (solid, thin), and ions (dashed) for simulations A and B. Each group of 3 lines starts from the same location at $z = 0$, thus showing the downstream electron and ion separation from the magnetic field. R_V and R_B represent the beam and nozzle edges, respectively. The electron separation of simulation A is the same as that of C. Notice the different axes scales.

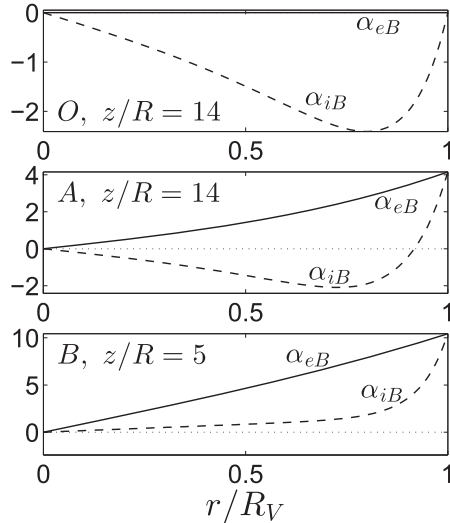


FIG. 3. Examples of local separation angles (in degrees) of electron (solid) and ion (dashed) streamtubes from the magnetic streamtubes in different simulations and at different locations (as indicated on each plot). Electron separation is always outwards; ion separation can be outwards or inwards.

contribution is marginal in all practical cases. Inwards ion separation has been observed in several recent experiments.^{22–25} Outwards ion separation, which requires outwards electron separation, has been observed too.²⁵

The outwards separation of electron streamtubes implies that a stronger radial electric field is needed to pull ions towards the more divergent beam edge and satisfy quasineutrality there. The correlation of electron separation and radial fall of the electric potential is evident in the profiles of simulations A and B in Fig. 4. The difference between simulations A and C is due to the different ion mass: lower electric fields are necessary to push lighter ions radially.

Figure 5 plots the local plume efficiency, $\eta_{plume}(z)$. This was defined in Eq. (49) of Ref. 1 as the ratio P_{zi}/P_z of the axial flows of axial versus total ion energy at sections $z = \text{const}$. We observe that electron inertia penalizes η_{plume} since the beam divergence increases, but the penalty is small since the large radial rarefaction leaves a very small beam density at the edge vicinity.

The electron inertia effects analyzed here do not modify the limits of validity of our plasma model, which were set already in Ref. 1. The model fails downstream because of (a) electron demagnetization, measured by ℓ_e/R , or (b) loss of

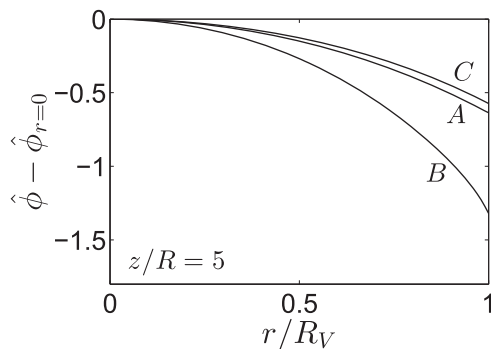


FIG. 4. Radial profile of electric potential at $z/R=5$ for simulations A, B, and C; $\phi = e\phi/T_e$.

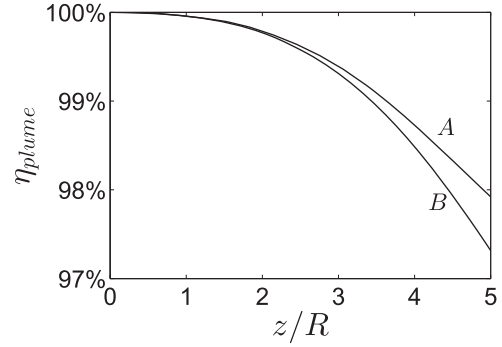


FIG. 5. Plume efficiency variation along z for simulations A and B. Plume efficiency for simulation C (not shown here) is practically identical to simulation A.

electron confinement, measured by \tilde{u}_e/c_e . Figure 6(a) illustrates the increase of ℓ_e/R caused by the decrease of magnetic intensity in a divergent topology. Figure 6(b) plots \tilde{u}_e^2/c_e^2 ; the increase of this parameter downstream (and mainly near the plasma edge) is caused by electron flux conservation under the large plasma rarefaction.¹ Since the relative contribution of electron longitudinal inertia to $u_{\theta e}$ in Eq. (13) is $O(\tilde{u}_e^2/c_e^2)$ roughly [see Section III], there is no additional restriction to the validity of the present nonzero-inertia model. To confirm this last trend, Fig. 6(c) plots constant-level lines of the ratio of the second versus the first term on

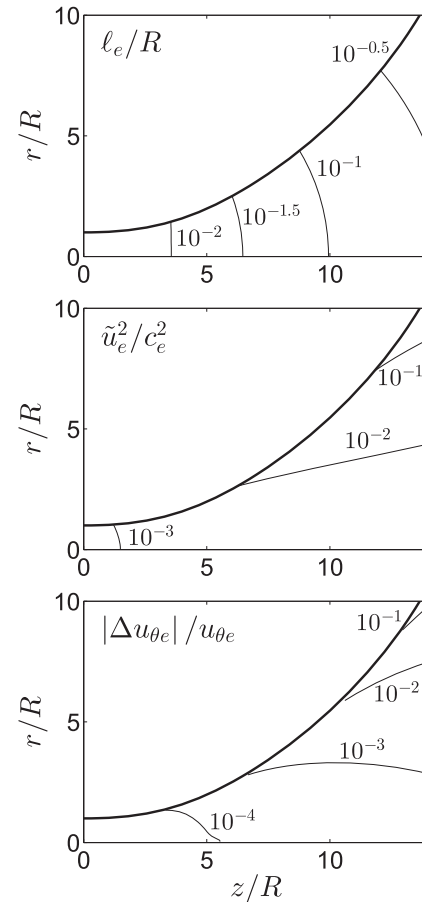


FIG. 6. 2D maps for simulation C of: (a) electron gyroradius parameter, (b) longitudinal electron velocity parameter, and (c) relative contribution of electron longitudinal inertia to $u_{\theta e}$ in Eq. (13).

the right-hand-side of Eq. (13). Additionally, since these two terms have different signs, we conclude that longitudinal inertia decreases $u_{\theta e}$ (and thus breaks isorotation). Finally, we note that, for simulation A, which uses xenon instead of hydrogen, the curves of Figs. 6(b) and 6(c) correspond to values two orders of magnitude lower, while Fig. 6(a) coincides.

B. Near-uniform beam at the throat

A uniform density profile of the injected plasma beam [i.e., $n(0, r) = \text{const} = n_0$] is often used in 2D studies of magnetic nozzles.^{10,26} That profile presents a strong discontinuity at the plasma-vacuum edge that must be discussed. In Ref. 1, we demonstrated that, in the limit $\ell_e/R \rightarrow 0$, the discontinuity is in fact a layer of $O(\ell_e)$ -thickness, where a large azimuthal electron current develops so that the resulting magnetic force balances the plasma pressure jump. Furthermore, since the azimuthal electron current is zero within the uniform beam, the electron current at the edge becomes then the *main* contribution to thrust from the magnetic nozzle.

Electron-inertia effects imply that $\ell_{e0}/R \neq 0$ and make it impossible to maintain the above two-scale analysis. In order to tackle the uniform-profile case within a one-scale analysis, here we consider a profile of $n(0, r)$, which is uniform until a certain radius R_1 close to R , and then decays exponentially to almost zero. Figure 1(b) plots the particular profile simulated here, with $R_1 = 0.8R$. There is a double interest in simulating a near-uniform profile. The first one is to validate the results of the two-scale analysis of Ref. 1 and to extend them beyond the asymptotic limit $\ell_e/R \rightarrow 0$. The second one is that a near-uniform profile highlights particular features of the expansion and separation of the plasma beam, thus casting additional light on the subject.

Figures 1(b) and 7 plot the profiles of density and azimuthal electron current, respectively, at $z/R = 0$ and 11.5 for the case of a near-uniform density profile at the throat; the Gaussian-profile case is included for comparison. For the near-uniform case, the plasma beam in the nozzle can be divided into central and peripheral regions, separated by the magnetic streamtube departing from $r = R_1$, that is

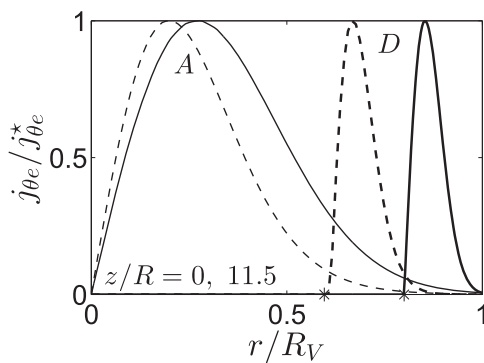


FIG. 7. Azimuthal electron currents (normalized with maximum value of each curve) for simulations A (thin) and D (thick). The dimensionless peak values are 5.46 at $z = 0$ (solid) and 0.34 at $z/R = 11.5$ (dashed) in simulation A, and 26.6 at $z = 0$ and 0.71 at $z/R = 11.5$ in simulation D. Asterisks correspond to the same points of Fig. 1(b).

$\psi(z, r) = \psi(0, R_1)$, marked with asterisks in the figures. The set of Eqs. (14) and (19) states that $u_{\theta e} = 0$ in the whole central region, which is illustrated in Fig. 7. Therefore, in the central region there is no electron separation and no magnetic force: the electron pressure gradient observed in Fig. 1(b) is balanced only by the electric force. On the contrary, the plasma behavior in the peripheral region is qualitatively identical to the one found before for the Gaussian density profile, as Figs. 1(b) and 7 illustrate too. An interesting feature is that the separation of the electron streamtubes is larger the more uniform the initial profile is (i.e., as R_1/R is closer to one), because the larger pressure gradient [$\sim T_e n_0 / (R - R_1)$] requires a larger $u_{\theta e}$, which in turn yields a larger $u_{\perp e}$. The circles in Fig. 1(b) correspond to $r = R_B$ for $z/R = 11.5$, thus showing the magnitude of the separation of the electron streamtube.

V. DISCUSSION OF MODEL ASSUMPTIONS

A. On current ambipolarity models

The local CA condition is

$$\tilde{\mathbf{u}}_i - \tilde{\mathbf{u}}_e = 0. \quad (22)$$

Since our model satisfies

$$\nabla \cdot en(\tilde{\mathbf{u}}_i - \tilde{\mathbf{u}}_e) = 0, \quad (23)$$

imposing CA at the throat section, condition (20), is enough to assure that the plasma beam is current-free in the whole nozzle, that is

$$\int_0^{R_V(z)} dr r n (u_{zi} - u_{ze}) = 0, \quad \forall z. \quad (24)$$

The imposition of CA is natural in quasi-1D models, where it is equivalent to the current-free condition, but in our 2D *diverging* nozzle model, local CA is not fulfilled in any volume, *independently* of both boundary conditions and electron-inertia effects. As discussed in Ref. 1, the non-fulfilment of CA is an *immediate* consequence of the separation between electron and ion streamtubes, which is possible thanks to the partial magnetization of ions and the ambipolar electric field preserving quasineutrality. Furthermore, Figs. 7(c) and 8(c) of Ref. 1 illustrated that imposing CA either at the throat or at a downstream section, CA is not fulfilled in the rest of nozzle sections.

Although electron-inertia effects have little to do with CA fulfilment, they have been a central piece in the formulation of Hooper's model.¹⁰ We are now able to show that this model is mathematically inconsistent and yields nonphysical solutions. Notice first, that our 2D model involves 8 independent scalar equations for 8 scalar variables: \mathbf{u}_i , \mathbf{u}_e , n , and ϕ . Clearly, none of the particle and momentum equations is dispensable; also, although the equations are coupled among them, it is possible to identify which plasma variable is determined preferentially by each equation.

Hooper applies Eq. (22) instead of Eq. (23). This substitution adds one extra equation to the problem, making it incompatible, as we show next. The set of equations (4)–(6)

plus Eq. (10) substituting $u_{\perp e}$ with $u_{\perp i}$ is complete for the four variables \tilde{u}_i , and $u_{\theta e}$ in a cold plasma. Notice that the modified Eq. (10)—or Eq. (11)—determines $u_{\theta e}$. Apart from these four equations, Eq. (3) would yield n . Still there are the two electron longitudinal momentum equations, (14) and (15), to be satisfied but only one variable, ϕ , remains undetermined. The incompatibility of this CA model lies in that Eq. (14) also determines $u_{\theta e}$ —stating it to be the well known $(en\mathbf{E} + \nabla p_e) \times \mathbf{B}$ drift. Clearly, the over-determined character of the model would be avoided by just removing the CA condition and letting Eq. (10) to determine $u_{\perp e} (\neq u_{\perp i})$, as we do.

We can venture the reasons why Hooper, in an otherwise well-reasoned and clearly presented paper, did not detect the model inconsistency. The first reason is that, although he was well aware that CA is just an approximation in a 2D model (he devotes a whole section to discuss CA) he supposed the approximation to be a good one. The second reason is that an omission on the manipulation of the equations rendered his CA model mathematically compatible. To explain it, let us first write Eqs. (14) and (15) in the compact form

$$0 = \nabla \left[T_e \ln n - e\phi + \frac{1}{2} m_e u_{\theta e}^2 \right] - \frac{u_{\theta e}}{r} \frac{dD_e}{d\psi_e} \nabla \psi_e. \quad (25)$$

Hooper's error was to treat the function $D_e(\psi_e)$ ($-e\Psi_0$ in his notation) as a constant, when, both in the general case and in his application to a uniform beam with $u_{\theta e}(0, r) = 0$, it is not. That mistake leads to the omission of the last term of Eq. (25): this term (divided by m_e) is missed in Eq. (11) of Hooper,¹⁰ in Eq. (2.8) of Schmit and Fisch,¹³ and in Eqs. (8) and (9) of Little and Choueiri.¹⁴ The maimed version of equation (25) yields only one scalar equation: $H_e(\psi_e) = \text{const}$, and misses completely the indispensable Eq. (14). The "vacancy" left by Eq. (14) was supplanted by imposing CA, leading to a model mathematically compatible but ill-derived and nonphysical.

The nonphysical aspects of Hooper's model can be discussed in terms of the electric potential. First, his cold plasma satisfies a limit form of Eq. (15): $e\phi - m_e u_{\theta e}^2/2 = 0$, Eq. (12) of Ref. 10. This implies that ϕ is minimum at the axis and grows radially, indeed pushing electrons radially outwards, fully opposed to a typical plasma expansion. Second, the nature of the electric field in the cold plasma model, responsible of keeping quasineutrality and 2D current ambipolarity, is very uncertain. Schmit and Fisch speculate on the presence of "local microscopic ambipolar electric fields," while "no macroscopic self-field can arise in the system." But our hot-plasma (quasineutral) model shows, first, that the ambipolar electric field is proportional to T_e , and second, the pressure contribution can never be dropped, even downstream, since it always dominates over the ambipolar electric force. This is true also for an adiabatic electron pressure law, instead of an isothermal one, and for a plasma beam injected at high supersonic velocities, i.e., M_0 large, a case approaching Hooper's one, and commented in Ref. 6.

Consequently, the cold-plasma case is not a regular limit of the hot-plasma model. Furthermore, as the plasma

becomes more supersonic, the perpendicular electric field and plasma rarefaction become larger. This weakens plasma quasineutrality and supports the idea that the electric field in the cold-plasma limit is of non-neutral character, generated by the space-charge being built between weakly magnetized ions trying to move axially and electrons trying to follow the divergent magnetic lines. The idea of electrostatic separation as a detachment mechanism of the far-downstream plasma was raised in Ref. 6.

Little and Choueiri¹⁴ have extended Hooper's model to a hot plasma, adding the pressure contribution to their equations for the longitudinal velocity of the electron-ion pair. Apart from using an approximate continuity equation to determine n , the main objection here is that, as Hooper, they integrate the resulting equations along the well-tied electron-ion streamlines, and they maintain the mathematical omission in Eq. (25). Instead, our ion equations (3)–(5) take $\phi(n)$ from the electron model and are integrated along the classical three families of characteristics lines of an expanding hot gas: ion streamlines and the pair of Mach lines.¹

Our conclusion is that the failure of CA and thus the presence of longitudinal currents are inherent to the 2D divergent expansion of a plasma beam with partially magnetized ions. Furthermore, we believe it to be fundamental for downstream plasma detachment.⁶ CA would be fulfilled in the ion strong-magnetization limit, defined as $\Omega_i R/c_s \rightarrow \infty$, when ion streamtubes coincide with electron and magnetic streamtubes. But the ion strong-magnetization limit is not appropriate for magnetic intensities and propellants used in plasma thrusters.¹ Besides, even if that limit is applicable at the throat region, it eventually fails downstream.

The presence of longitudinal currents raises the issue of the current closure, which was already commented in Ref. 1 and continues open. A reliable answer requires both to extend the 2D nozzle model far downstream and to match it upstream with a plasma source model. One presumes that for the plasma beam injecting into a weak environmental plasma, a far downstream current closure across the magnetic field can be postulated. Also, if the plasma beam impinges on a conducting plate, this will host the current closure path. However, if the beam impinges on an absorbing or recombining insulating surface—like in Fig. (8c) of Ref. 1—the current closure is expected to happen upstream, in the more-collisional plasma source.

B. On full FELR effects

The electron-inertia hot-plasma model discussed hereto assumes the simplest form of the pressure tensor of Eq. (9): \mathbf{P}_e is diagonal, isotropic, and isothermal. Non-isothermality is easy to take into account and leads mainly to a qualitative change on the far plasma response. Pressure anisotropy, with different parallel and perpendicular temperatures, is of interest for certain plasma thrusters, in particular the electrodeless electron cyclotron resonance thruster.^{11,27} Non-isothermality and anisotropy are dominant (i.e., zero-Larmor-radius) effects on the electron response and require an independent study.

On the contrary, the non-diagonal part of the pressure tensor, Π_e , known as the stress or gyroviscous tensor^{7–9}

defines the gyroviscous force, $G = \nabla \cdot \Pi_e$, which is a finite Larmor-radius effect. In the present case, where electron-inertia effects are limited to the azimuthal momentum equation, Eq. (10), only the component G_θ could be relevant. Although recognizing its importance, the evaluation of the gyroviscous force is a challenge which merits a dedicated work. The first difficulty is that there is no consensus on the expression of the gyroviscous force, although Ramos⁹ has derived recently a general (and extremely involved) expression of it, which, in different limits, recovers cases of other authors. In particular, for a near-Maxwellian electron velocity distribution function with temperature T_e , the gyroviscous force would reduce to Braginski's expression,⁸ which is Eq. (28) of Ref. 9.

Focusing now on that expression, the second challenge is that the gyroviscous force includes several terms, which can be grouped on two types. On the one hand, there are linear terms on first-order derivatives of \mathbf{u}_e and p_e , which would provide a *partial diamagnetic cancellation* of electron inertia.⁷ For instance, they would cancel the small "centrifugal force" in Eq. (19) and would oppose (but may not cancel) the convective radial derivative of Eq. (10). On the other hand, there is the true viscous contribution, consisting of terms with second order derivatives of \mathbf{u}_e and products of first-order derivatives of \mathbf{u}_e and p_e . These terms break the hyperbolicity of the ion equations, making our current integration approach inapplicable.

Since the gyroviscous force is proportional to $T_e/eB_0 \equiv (\ell_{e0}/R)^2$, given B_0 it vanishes, together with the pressure, only in the cold plasma case. For the case of interest of a hot-plasma in a diverging nozzle, the suitable expression of the gyroviscous force and the relative ordering of its different terms has to be assessed. This will indicate whether there is a parametric range where the gyroviscous force can dominate FELR effects.

VI. CONCLUSIONS

Electron-inertia constitutes a mechanism capable of detaching highly magnetized electrons from nozzle magnetic streamtubes. Electron-inertia effects are part of finite electron-Larmor radius effects. Therefore, they increase downstream, as the magnetic strength decreases, and constitute a sign of plasma demagnetization.

Here, dominant electron-inertia effects have been studied within an isothermal fluid model. The electron momentum equations reduce to three algebraic laws, stating conservation of the Bernoulli function and the azimuthal momentum, and isorotation along electron streamtubes. As a consequence, the shape of the electron streamtubes and thus their separation from magnetic streamtubes becomes independent of the ion dynamics. This electron model yields, under rather general equilibrium conditions on the injected plasma beam, that electrons separate outwards of the magnetic lines, the plasma beam thus progressively filling the vacuum region adjacent to the nozzle, which is coherent with FELR effects leading to plasma demagnetization.

While electron separation depends mainly on the electron Larmor radius, ion separation depends on both the ion

Larmor radius (based on the directed velocity) and the ambipolar perpendicular electric field (affected by electron separation). Both inwards and outwards ion separation from the magnetic lines can take place, as it has been observed experimentally. As long as the FELR parameter is small, it penalizes only slightly the plume efficiency. When, farther downstream, the FELR parameter becomes of order one, the plasma demagnetizes, but this nozzle region is out of the limits of the present model.

A study of near-uniform beams at the throat has confirmed a previous two-scale study for the zero electron gyro-radius limit and makes more evident the role of the azimuthal electron current on the force balance and the plasma separation, which is larger in plasma beams injected with large pressure gradients.

A dissection of Hooper's model, which yields inwards electron separation, has been undertaken in order to understand the cause of our mutual disagreement. It has been demonstrated that: (1) forcing current ambipolarity everywhere leads to an incompatible model, where $u_{\theta e}$ is determined simultaneously from two independent equations; (2) a term was erroneously omitted in the manipulation of the equations, with important consequences on the resulting model; and (3) the electric potential presents a nonphysical profile and its ambipolar character—justifying a quasineutral model—is uncertain in his cold plasma.

It is concluded that the failure of current ambipolarity is natural in the diverging expansion of a meso-magnetized plasma and possibly fundamental for its downstream detachment, but we acknowledge that the upstream and downstream current closures remain an issue to be studied. For the future, a dedicated analysis of the gyroviscous force—very scarcely studied in the plasma propulsion context—seems convenient. This force could compete with electron inertia and completes FELR effects on a hot, collisionless plasma. However, the gyroviscous force could ruin the hyperbolicity of our equations, invalidating our efficient and successful integration scheme for the plasma/nozzle problem.

ACKNOWLEDGMENTS

This work has been sponsored by the Air Force Office of Scientific Research, Air Force Material Command, USAF, under Grant No. FA8655-12-1-2043. The U.S. Government is authorized to reproduce and distribute reprints for Governmental purpose notwithstanding any copyright notation hereon. Additional support for this research was provided by the Gobierno de España (Project AYA-2010-61699).

¹E. Ahedo and M. Merino, "Two-dimensional supersonic plasma acceleration in a magnetic nozzle," *Phys. Plasmas* **17**, 073501 (2010).

²E. Ahedo, "Plasmas for space propulsion," *Plasma Phys. Controlled Fusion* **53**, 124037 (2011).

³G. Krülle, M. Auweter-Kurtz, and A. Sasoh, "Technology and application aspects of applied field magnetoplasmadynamic propulsion," *J. Propul. Power* **14**, 754–763 (1998).

⁴C. Diaz, "The VASIMR rocket," *Sci. Am.* **283**(5), 90–97 (2000).

⁵R. Winglee, T. Ziemba, L. Giersch, J. Prager, J. Carscadden, and B. R. Roberson, "Simulation and laboratory validation of magnetic nozzle effects for the high power helicon thruster," *Phys. Plasmas* **14**, 063501 (2007).

- ⁶E. Ahedo and M. Merino, "On plasma detachment in propulsive magnetic nozzles," *Phys. Plasmas* **18**, 053504 (2011).
- ⁷R. D. Hazeltine and F. L. Waelbroeck, *The Framework of Plasma Physics* (Perseus Books, 2004).
- ⁸S. I. Braginskii, in *Reviews of Plasma Physics, Volume 1*, edited by M. A. Leontovich (Consultants Bureau, New York, 1965) p. 205.
- ⁹J. J. Ramos, "General expression of the gyroviscous force," *Phys. Plasmas* **12**, 112301 (2005).
- ¹⁰E. B. Hooper, "Plasma detachment from a magnetic nozzle," *J. Propul. Power* **9**(5), 757–763 (1993).
- ¹¹J. C. Sercel, "Simple model of plasma acceleration in a magnetic nozzle," in *AIAA, DGLR, and JSASS, 21st International Electric Propulsion Conference*, AIAA Paper No. 90-2597, 1990.
- ¹²D. A. Kaufman, D. G. Goodwin, and J. C. Sercel, "Plasma separation from magnetic field lines in a magnetic nozzle," in *31st AIAA Aerospace Sciences Meeting and Exhibit*, AIAA Paper No. 93-0817, 1993.
- ¹³P. F. Schmit and N. J. Fisch, "Magnetic detachment and plume control in escaping magnetized plasma," *J. Plasma Phys.* **75**(03), 359–371 (2009).
- ¹⁴J. M. Little and E. Y. Choueiri, "The influence of induced currents on magnetic nozzle acceleration and plasma detachment," in *Proceedings of 46th Joint Propulsion Conference, Nashville, TN* (American Institute of Aeronautics and Astronautics, Washington DC, 2010), AIAA Paper No. 2010-6615.
- ¹⁵E. Ahedo and M. Merino, "On electron inertia and current ambipolarity in magnetic nozzle models," in *32nd International Electric Propulsion Conference, Wiesbaden, Germany* (Electric Rocket Propulsion Society, Fairview Park, OH, 2011), IEPC Paper No. 2011-050.
- ¹⁶M. Merino and E. Ahedo, "Plasma detachment mechanisms in a magnetic nozzle," in *Proceedings of 47th Joint Propulsion Conference, San Diego, CA* (American Institute of Aeronautics and Astronautics, Washington DC, 2011), AIAA Paper No. 2011-5999.
- ¹⁷D. B. Fradkin, A. W. Blackstock, D. J. Roehling, T. F. Stratton, M. Williams, and K. W. Liewer, "Experiments using a 25-kw hollow cathode lithium vapor mpd arcjet," *AIAA J.* **8**, 886–894 (1970).
- ¹⁸S. Chandrasekhar, "Axisymmetric magnetic fields and fluid motions," *Astrophys. J.* **124**, 232–243 (1956).
- ¹⁹L. Tonks, "Theory of magnetic effects in the plasma of an arc," *Phys. Rev.* **56**, 360–373 (1939).
- ²⁰E. Ahedo, "Parametric analysis of a magnetized cylindrical plasma," *Phys. Plasmas* **16**, 113503 (2009).
- ²¹J. Freidberg, *Plasma Physics and Fusion Energy* (Cambridge University Press, Cambridge, 2007).
- ²²W. Cox, C. Charles, R. W. Boswell, and R. Hawkins, "Spatial retarding field energy analyzer measurements downstream of a helicon double layer plasma," *Appl. Phys. Lett.* **93**, 071505 (2008).
- ²³K. Terasaka, S. Yoshimura, K. Ogiwara, M. Aramaki, and M. Y. Tanaka, "Experimental studies on ion acceleration and stream line detachment in a diverging magnetic field," *Phys. Plasmas* **17**, 072106 (2010).
- ²⁴K. Takahashi, Y. Itoh, and T. Fujiwara, "Operation of a permanent-magnets-expanding plasma source connected to a large-volume diffusion chamber," *J. Phys. D: Appl. Phys.* **44**, 015204 (2011).
- ²⁵J. P. Squire, C. S. Olsen, F. R. C. Díaz, L. D. Cassady, B. W. Longmier, M. G. Ballenger, M. D. Carter, T. W. Glover, and G. E. McCaskill, "VASIMR[®] vx-200 operation at 200 kw and plume measurements: Future plans and an iss ep test platform," in *32nd International Electric Propulsion Conference, Wiesbaden, Germany* (Electric Rocket Propulsion Society, Fairview Park, OH, 2011), IEPC Paper No. 2011-154.
- ²⁶A. V. Arefiev and B. N. Breizman, "Magnetohydrodynamic scenario of plasma detachment in a magnetic nozzle," *Phys. Plasmas* **12**, 043504 (2005).
- ²⁷W. M. Manheimer and R. F. Fernsler, "Plasma acceleration by area expansion," *IEEE Trans. Plasma Sci.* **29**, 75–84 (2001).

PAGE INTENTIONALLY LEFT BLANK

Two-dimensional quasi-double-layers in two-electron-temperature, current-free plasmas

Mario Merino^{a)} and Eduardo Ahedo^{b)}

ETS Ingenieros Aeronáuticos, Madrid Technical University, Madrid 28040, Spain

(Received 29 October 2012; accepted 16 January 2013; published online 5 February 2013)

The expansion of a plasma with two disparate electron populations into vacuum and channeled by a divergent magnetic nozzle is analyzed with an axisymmetric model. The purpose is to study the formation and two-dimensional shape of a current-free double-layer in the case when the electric potential steepening can still be treated within the quasineutral approximation. The properties of this quasi-double-layer are investigated in terms of the relative fraction of the high-energy electron population, its radial distribution when injected into the nozzle, and the geometry and intensity of the applied magnetic field. The two-dimensional double layer presents a curved shape, which is dependent on the natural curvature of the equipotential lines in a magnetically expanded plasma and the particular radial distribution of high-energy electrons at injection. The double layer curvature increases the higher the nozzle divergence is, the lower the magnetic strength is, and the more peripherally hot electrons are injected. A central application of the study is the operation of a helicon plasma thruster in space. To this respect, it is shown that the curvature of the double layer does not increment the thrust, it does not modify appreciably the downstream divergence of the plasma beam, but it increases the magnetic-to-pressure thrust ratio. The present study does not attempt to cover current-free double layers involving plasmas with multiple populations of positive ions. © 2013 American Institute of Physics. [<http://dx.doi.org/10.1063/1.4789900>]

I. INTRODUCTION

Expansion of a current-free (CF) plasma into vacuum, whether geometrically or magnetically channeled, is inherently associated with the existence of an electric field created by the plasma, which accelerates ions and confines electrons along the expansion direction (except for the small electron drift current that keeps the plasma beam globally current-free). Under certain circumstances, a significant part of the total potential drop takes place in a thin non-neutral plasma region, known as current-free double-layer (CFDL). A recent review by Singh¹ has highlighted the upsurge of research on CFDLs due to their applications to plasma acceleration, astrophysical plasmas, and helicon plasma devices (HPDs).

Several of Singh's conclusions serve as the starting framework for the present study. First, he establishes the existence of, at least, two different categories of CFDLs: the one that can develop in two-electron-temperature (2ET) plasmas and the one observed in the laboratory experiments with HPDs; furthermore, it is concluded that "the physical process taking place in the formation of 2ET-CFDLs appears to be quite different from that in the formation of HPD-CFDLs." Second, the theoretical understanding of the 2ET-CFDL is considered quite established, and this DL is regarded as a "robust phenomenon," which has been identified in laboratory experiments and in large-scale models and numerical simulations of space and astrophysical plasmas. Third, in spite of these advancements, the review expresses the neces-

sity of studying further the multi-dimensional structures of 2ET-CFDLs. And fourth, in contrast with 2ET-CFDLs, it is acknowledged that a sound theoretical development of HPD-CFDLs is still lacking. Finally, the reference list, covering theoretical, numerical, and experimental studies, presented in Singh's review is quite exhaustive; therefore, here only those works more connected to ours will be cited.

The understanding of the 2ET-CFDL is based, on the one hand, on the commendable experiments by Hairapetian and Stenzel^{2,3} with 2ET plasmas expanding in a vacuum chamber with a near-uniform magnetic field and, on the other hand, on the one-dimensional(1D) models of Bezzeries *et al.*,⁴ Perkins and Sun,⁵ Barakat and Schunk,⁶ and Ahedo and Martínez-Sánchez.⁷ The 2ET-CFDL is likely the simplest type of CFDL, since it may involve just a collisionless plasma constituted by three distinguished species: positive ions and two electronegative populations of disparate thermal energies. Commonly, these last ones are Maxwellian (or "cold") and suprathermal (or "hot") electrons. The two-dimensional (2D) structure of the 2ET-CFDL was observed experimentally by Hairapetian and Stenzel, and curved 2ET-CFDLs have been detected in astrophysical plasmas too.^{1,8} The central aim of the present work is to develop a 2D macroscopic model of the 2ET-CFDL and its surrounding plasma in order to understand the role of plasma conditions on its formation, location, and curvature.

The laboratory HPD-CFDL has been studied extensively by several groups—Refs. 9–17 being representative of such activity, — and there is evidence of the emission of suprathermal electrons in HPDs,^{11,13,18–20} possibly generated by electron-wave Landau resonance.²¹ In spite of such amount

^{a)}Electronic mail: mario.merino@upm.es. URL: web.fmetsia.upm.es/ep2.

^{b)}Electronic mail: eduardo.ahedo@upm.es.

of research and the presence of a 2ET plasma, there is an incomplete understanding of the HPD-CFDL and there are reasons to defend a separate category for them. Singh states that the HPD-CFDL is “device specific,”¹ in the sense that experimental results are diverse and a systematic characterization of the HPD-CFDL is still pending. The experimental evidence shows that the plasma in a HPD-CFDL is more complex than the one considered in the 2ET-CFDL case: in a typical HPD-CFDL experiment, the device emits a partially ionized, 2ET plasma into a background plasma, this one confined by a diffusion chamber (or the vacuum chamber). As a consequence, downstream ionization and other collisional processes can be important and a secondary, low-energy population of ions can form outside of the source (see, e.g., Fig. 1 in Ref. 15). Thus, the HPD-CFDL would involve typically a partially collisional plasma with at least five distinguished, counterstreaming species (taking into account the neutrals), as it is assumed, e.g., in the theory of Liebermann *et al.*²² That theory resembles the classical one for the current-carrying Langmuir DL,²³ laying a central role on DL formation to the presence of trapped and freely accelerated ions, while forward and backward flows of suprathermal electrons would adjust to meet the current-free condition. This 5-species HPD-CFDL is not discussed in this paper.

Interestingly, part of the experiments on HPD-CFDLs is meant to study the use of helicon plasma devices as space thrusters. However, there are two crucial conditions of a helicon plasma thruster operating *in space* that differ from those of the aforementioned HPD-CFDL *laboratory* experiments. First, for a space thruster to be competitive, the emitted plasma must be near-fully ionized and hot, which means quasi-collisionless.²⁴ And second, there is no interaction of the emitted plasma with the very tenuous plasma of the space environment in the distances of interest. Therefore, for a HPD operating in space and emitting a plasma with suprathermal electrons, a 2ET-CFDL, instead of a HPD-CFDL, could form.

In the typical configuration of a helicon thruster, the plasma, after leaving the chamber, is guided and expanded supersonically by a divergent magnetic nozzle.^{25–28} To this respect, it is important again that collisions are negligible, since otherwise they would screen the magnetic channeling and annihilate its benefit in thrust efficiency.^{29,30} This justifies that our 2D model of a 2ET-CFDL is built upon two previous ones. The first one describes the quasi-1D expansion of a 2ET plasma in a convergent-divergent geometry.^{7,31} This 1D model characterizes, in terms of the temperature and density ratios of the electron populations, the parametric regime where a CFDL is formed as a discontinuity surface of the quasineutral solution. The second model analyzes the 2D expansion of a single electron temperature (1ET) plasma—i.e., a simple plasma—in a divergent, axisymmetric magnetic nozzle.²⁹ This model shows that crucial 2D phenomena are missed by 1D nozzle models, such as the strong radial rarefaction of the beam, the separation of ion and magnetic streamtubes, the plume efficiency, and the magnetic character of thrust in the nozzle (based on the axial magnetic force of azimuthal plasma currents). The 2D model achieves a neat formulation by considering that the plasma expansion is

collisionless and electrons are fully magnetized. The inclusion of a 2ET plasma model into the 2D nozzle model allows us to analyze the formation and 2D shape of a 2ET-CFDL. The influence of the intensity and geometry of the applied magnetic field, and of the hot-to-cold electron radial distribution at injection are investigated.

A controversial subject related to helicon plasma thrusters has been whether the CFDL can have a propulsive role, since Charles and Boswell⁹ claimed that the CFDL was an innovative thrust mechanism. On the one hand, 1D models show that the 2ET-CFDL does not increment thrust and modifies very slightly the thruster efficiency.^{31,32} On the other hand, the 2D model of a 1ET plasma shows that the downstream divergence of the plasma beam (one of the features reducing the thruster efficiency), is dependent on the magnetic nozzle divergence and strength. In the present work, we assess how the curved 2D shape of the 2ET-CFDL can change the average divergence of the plasma beam and whether this can affect the thruster efficiency.

The rest of the paper is organized as follows. Section II reviews the main conclusions on 2ET-CFDLs emanating from previous studies. This review is pertinent for the discussion of the 2D-2ET model to follow, and also as a comment to subjects raised in Singh’s paper. Section III formulates the 2D-2ET plasma/nozzle model. Section IV presents main results and discusses the influence of different parameters. Section V discusses propulsive performances. Finally, concluding remarks are gathered in Sec. VI.

II. ON PROFILE STEEPENING AND DOUBLE-LAYER FORMATION

The first point we want to highlight is that an *ambipolar* steepening, at some intermediate location, of the profiles of plasma density n and electric potential ϕ , occurs naturally in a simple 1ET current-free plasma expanding into vacuum; see for instance, Fig. 1 of Ref. 1. The typical amplitude of the potential steepening is the plasma temperature, and its typical thickness (in a weakly collisional plasma) is the geometrical length R of the plasma region. In an unmagnetized cylindrical plasma expanding into vacuum, that length can be the tube radius. In a plasma channeled by a diverging magnetic nozzle, the steepening length is the curvature radius R_n of the magnetic field. Plasma profiles expectedly become more steepened as R or R_n decrease. In a multi-species plasma, with populations of different mean energies, profile slopes can depend on the locally dominant species, and additional steepening can occur.

Depending on the properties of the expanding plasma, the potential drop can concentrate locally to give rise to a DL. The most relevant literature is unanimous in that a DL is a thin, *non-neutral* layer between two adjacent *quasineutral* regions.^{32–34} This statement makes full sense only within a two-scale analysis based on the asymptotic zero-Debye-length limit, i.e., $\lambda_D/R \rightarrow 0$. In real devices and in single-scale models, where λ_D/R can be small but not zero, the above statement must be interpreted in the following way: a DL in a plasma of temperature T_e is a region where the

electric field, E , is of order $\sim T_e/(e\lambda_D)$, in contrast to a typical value of $\sim T_e/(eR)$ outside the DL. For instance, a plasma with $n \sim 10^{17} \text{ m}^{-3}$ and $T_e \sim 5 \text{ eV}$ has $\lambda_D \sim 50 \text{ }\mu\text{m}$. Thus, for $R = 5 \text{ cm}$, we have $\lambda_D/R \sim 10^{-3}$, and typical DL and ambipolar electric fields would be clearly distinct: $\sim 10^3 \text{ V/cm}$ and $\sim 1 \text{ V/cm}$, respectively.

In practice, the unequivocal presence of a DL is more difficult to ascertain when λ_D/R is moderately small or the maximum electric field in the plasma is in the intermediate range $T_e/R \ll eE \ll T_e/\lambda_D$. The term *weak DL* is sometimes used for these cases. It turns out⁷ that a 2ET-CFDL is always weak because the electric space-charge ρ_e is always small, i.e., $\rho_e/(en) \ll (1)$. The electric field of the 2ET-CFDL is $\sim T_h/(eL_{DL})$ with $L_{DL} = \sqrt{\epsilon_0 T_h/(e\rho_e)}$ and T_h the temperature of hot electrons. This weak character would explain the difficulty to distinguish, in practice, between a “true,” non-neutral CFDL and just an enhanced ambipolar steepening, termed “quasineutral steepened layer” (QSL) by Ahedo and Martínez-Sánchez.⁷ Here, we have opted for the more identifiable name of “quasi-double-layer” (QDL).

At any rate, two-scale models, like the one to be used here, are unambiguous on whether the 2ET plasma presents a QDL or a (true) DL. Bezzzerides *et al.*,⁴ for a time-dependent expansion, and Barakat and Schunk⁶ and Ahedo and Martínez-Sánchez,⁷ for a steady-state one, have demonstrated that augmenting the suprathermal electron relative density or temperature increases progressively the steepening of the QDL, until the quasineutral spatial profile becomes multivalued and a discontinuity (i.e., the DL) has to be postulated. For the standing case, Ahedo and Martínez-Sánchez determine, in the hot electron density-temperature parametric plane, the boundary line between QDL and DL regimes. Ahedo³¹ also shows that the shift of dominance from cold to hot electrons across a QDL involves a large change in the sound speed of the plasma. This makes the variation of the plasma Mach number non-monotonic, and the potential steepening is maximum around the location where the supersonic Mach number presents a local minimum. For this “anomalous thermodynamics,”⁴ Ahedo demonstrated that the transition from a QDL to a DL takes place when this minimum becomes subsonic: the quasineutral plasma cannot manage the crossing of a new sonic point and a discontinuity develops.

III. FORMULATION OF THE 2D, 2ET PLASMA MODEL

The model described in this section extends the 2D, 1ET plasma model of Ref. 29 to include different electron species. As such, only the indispensable and distinctive aspects of the extended model will be summarized below. The notation followed here is based on our previous works.^{29,31}

A collisionless, low- β , cylindrical plasma of radius R is injected sonic/supersonically at the throat of a divergent, axisymmetric magnetic field \mathbf{B} . The plasma is constituted of low-energy (“cold,” c) and high-energy (“hot,” h) electrons, and singly charged ions (i), with negligible temperature compared to “cold” electrons. The quasineutrality condition $n_i = n_h + n_c \equiv n$ is satisfied. Motion is described using the

cylindrical frame of reference $\{\mathbf{1}_z, \mathbf{1}_r, \mathbf{1}_\theta\}$ complemented with magnetic unit-vectors $\mathbf{1}_\parallel = \mathbf{B}/B$ and $\mathbf{1}_\perp = \mathbf{1}_\theta \times \mathbf{1}_\parallel$. We work in the zero Larmor radius limit of electrons,³⁵ $\ell_j = \sqrt{T_j m_e}/(eB) \ll R$ (for $j = c, h$); as a consequence, electron and magnetic streamtubes coincide ($u_{\perp j} \equiv 0$ for $j = c, h$). Ions, however, are only partially magnetized and, since ion temperature is neglected, the relevant ion Larmor radius ℓ_i is the one based on the ion longitudinal velocity, $\tilde{u}_i = \mathbf{u}_i - u_{\theta i} \mathbf{1}_\theta$, i.e., $\ell_i = \tilde{u}_i m_i / (eB)$.

The steady-state fluid equations for ions are²⁹

$$\frac{\partial u_{zi}}{\partial z} + \frac{\partial u_{ri}}{\partial r} + u_{zi} \frac{\partial \ln n}{\partial z} + u_{ri} \frac{\partial \ln n}{\partial r} = -\frac{u_{ri}}{r}, \quad (1)$$

$$m_i \left(u_{zi} \frac{\partial u_{zi}}{\partial z} + u_{ri} \frac{\partial u_{zi}}{\partial r} \right) + e \frac{\partial \phi}{\partial z} = -eu_{\theta i} B_r, \quad (2)$$

$$m_i \left(u_{zi} \frac{\partial u_{ri}}{\partial z} + u_{ri} \frac{\partial u_{ri}}{\partial r} \right) + e \frac{\partial \phi}{\partial r} = eu_{\theta i} B_z + \frac{m_i u_{\theta i}^2}{r}, \quad (3)$$

$$m_i r u_{\theta i} + e\psi = D_i(\psi_i), \quad (4)$$

where ϕ is the ambipolar potential, ψ and ψ_i are the magnetic and ion streamfunctions and $D_i(\psi_i)$ a known function of flow conditions at the throat. Besides the conservation of the canonical azimuthal momentum, Eq. (4), energy H_i is conserved on each ion streamtube,

$$m_i(\tilde{u}_i^2 + u_{\theta i}^2)/2 + e\phi = H_i(\psi_i). \quad (5)$$

To close these ion equations, the electron model must provide a relation between n and ϕ . As in Refs. 7 and 29, an isothermal fluid model is assumed for each electron species. Then, the required ϕ - n relation is simply the Boltzmann relation along each magnetic streamtube,

$$T_j \ln n_j - e\phi = H_j(\psi), \quad j = c, h, \quad (6)$$

where functions H_j are known from flow conditions at the throat. The differentiation of Eq. (6) yields:

$$dn = \left(\frac{n_c}{T_c} + \frac{n_h}{T_h} \right) ed\phi + \left(\frac{n_c}{T_c} \frac{dH_c}{d\psi} + \frac{n_h}{T_h} \frac{dH_h}{d\psi} \right) d\psi, \quad (7)$$

where the terms in the last parenthesis are related to the magnetic force of electron azimuthal current densities,

$$j_{\theta j} \equiv -en_j u_{\theta j} = rn_j \frac{dH_j}{d\psi}, \quad j = c, h. \quad (8)$$

For a supersonic ion flow, the substitution of Eq. (7) in Eqs. (2) and (3) results in a set of three hyperbolic equations, which can be solved with a forward-marching method of characteristics (MoC).^{29,36} The plasma sound speed c_s of the ion flow is given by the relation⁴

$$\frac{n}{m_i c_s^2} = \frac{n_c}{T_c} + \frac{n_h}{T_h}, \quad (9)$$

and the effective Mach number is $M = \tilde{u}_i/c_s$. At this point, it is convenient to define the hot-to-cold temperature ratio, $\tau = T_h/T_c$, and the *local* hot-electron density ratio,

$$\alpha(z, r) = n_h(z, r)/n(z, r). \quad (10)$$

There are three families of characteristic lines in the longitudinal plane, namely: the ion streamlines (i.e., the longitudinal section of ion streamtubes) and the upward- and downward-marching Mach lines, which form angles $\pm \sin^{-1}(1/M)$ with respect to the former.

The MoC, implemented in our DIMAGNO code, allows for a favorable integration scheme in terms of accuracy and computational cost. However, our approach does not allow the simulation through true DLs, associated to an additional sonic surface downstream of the throat where hyperbolicity (and quasineutrality) fails.³¹ As a consequence, our analysis of enhanced steepening in 2ET plasmas is limited to the QDL regime where the minimum ion Mach number, M , in the divergent nozzle is still supersonic. This restriction is not critical for present purposes since, despite the formal differences related to the zero Debye-length limit, QDL and DL structures represent the same physical phenomenon with a different degree of intensity. Nonetheless, one observation is necessary. While a DL is a sharp discontinuity in the quasi-neutral scale and its location is perfectly defined, the location of the QDL is partially arbitrary. In the present 2D model, the location of the QDL is defined as the surface formed by the minima of M along each magnetic line, which is almost coincident with the surface of maxima of E .

Notice that, as expressed by Eq. (6), the 1D model dependency of electron dynamics on ϕ is still essentially valid for the 2D model, but limited to each magnetic line separately. Clearly, in the 2D model, $\phi = \phi(z, r)$ results from the hyperbolic plasma response, and also $M = M(\phi, \psi, \psi_i)$. Since the potential and the Mach number depend on the whole plasma flow, the formation of the QDL in the magnetic nozzle is a fully 2D effect.

Plasma conditions at the throat (i.e., at $z=0$ and $0 \leq r \leq R$) are

$$\begin{aligned} \tilde{\mathbf{u}}_c = \tilde{\mathbf{u}}_h = \tilde{\mathbf{u}}_i = M_0 c_s(0, r) \mathbf{1}_z, \quad \phi = 0, \\ n = n_0 \exp(-ar^2/R^2), \quad \alpha(0, r) \text{ known}, \end{aligned} \quad (11)$$

where subindex 0 denotes values at the origin ($z = r = 0$), and $\alpha(0, r)$ refers to the radial distribution of hot electrons, Eq. (10). We shall take $M_0 = 1.01$ to comply with hyperbolicity of the ion equations, and $a = 3 \ln 10$ [so that $n(0, R)/n_0 = 10^{-3}$]. For sake of illustration, we will use the divergent magnetic nozzle created by a single loop of radius R_L placed at $z = 0$. The rest of the parameters of the model are: (1) the constant hot-to-cold electron temperature ratio $\tau = T_h/T_c$; (2) the nozzle divergence rate, measured by R/R_L or more precisely by $R/R_n(0, R)$; and (3) the magnetic strength at the throat, measured by the dimensionless gyro-frequency at the throat, $\hat{\Omega}_{i0} = eB_0R/\sqrt{m_i T_c}$.

Several observations on Eq. (11) are due. First, note that the assumption of current-free flow is not essential for our model. As such, we expect it to be applicable to plasmas with a net current smaller than the electron thermal current, so that most cold electrons are effectively confined. Second, $\phi(0, r) = 0$ means that each electron species is in a θ -pinch equilibrium at the throat, with the radial pressure gradient

balanced by the magnetic force due to azimuthal currents, which are essential for the electromagnetic thrust.²⁹ And third, it must be acknowledged that, since a theory on the hot-electron velocity distribution function has not yet been established, any modeling of that distribution is highly speculative. In the present case, this affects the thermodynamic models for cold and hot electrons as well as the relative hot-electron radial distribution $\alpha(0, r)$. Our choice for two superimposed Maxwellian, isothermal populations is based (in the absence of a better criterion) on simplicity and on the fact that Bezzeres *et al.*⁴ and others^{37,38} showed explicitly that the enhancement of the steepening and the DL formation do not depend particularly on the thermodynamic equation of state but on the disparities of energies between cold and hot electrons. With respect to the distribution of $\alpha(0, r)$, the simplest choice corresponds to identical radial profiles of hot and cold electron densities at the throat, i.e. $\alpha(0, r) = \text{const}$, which besides has the advantage of allowing direct comparison with the 1D 2ET-CFDL model. On the contrary, the general case of different radial profiles for cold and hot electrons at the throat, $\alpha(0, r) \neq \text{const}$, is genuinely 2D. Experimentalists have detected (or inferred) the two extreme cases: hot electrons forming preferentially either near the edge^{11,39,40} or around the center^{3,18} of the plasma beam. Both possibilities are explored here.

IV. LOCATION AND CURVATURE OF THE 2D QDL

The discussion of QDLs herein is illustrated with several simulation cases, which are described in Table I: Simulation T0 illustrates the expansion of a 1ET plasma, with $\alpha(0, r) = 0$; T4 and T8 take $\alpha(0, r) = 0.04$ and 0.08 , respectively. In particular, simulation T4, with 4% of hot electron relative density at the throat and nearly unmagnetized ions, constitutes the reference simulation against which the rest of 2ET plasma cases are compared. In simulation S, the strength of the magnetic field is 1000 times larger than in T4, thus ions are highly magnetized at the throat, with $\ell_i/R = 0.02$ there. In simulation D, the nozzle divergence rate is

TABLE I. Summary of the different parameters used for each simulation. Simulation T0 describes a simple 1ET plasma (i.e., single temperature electrons). Simulation T4 is our reference 2ET plasma. All other simulations deviate from it in the value of one of the parameters (highlighted in bold-face): simulation T8 has a higher fraction of hot electrons, simulation S has stronger magnetic field, and simulation D has a more divergent nozzle (roughly half the curvature radius). Simulations T4, T8, S, and D all have $\alpha(0, r) = \text{const}$. In simulations P and C, the function changes according to $g^\pm(r) \propto [2 \pm \cos(\pi r/R)]$, while keeping an average value of 0.04, as in T4; simulations P and C concentrate hot electrons in the periphery and the beam axis respectively. All simulations have $\tau = 18$ and $M = 1.01$.

Simulation	$\alpha(0, r)$	$\hat{\Omega}_{i0}$	R_L/R
T0 (simple 1ET plasma)	0	0.05	3.5
T4	4%	0.05	3.5
T8	8%	0.05	3.5
S (strength)	4%	50	3.5
D (divergence)	4%	0.05	2.5
P (periphery)	$g^-(r)$	0.05	3.5
C (center)	$g^+(r)$	0.05	3.5

roughly twice that of T4. Finally, in simulations P and C, hot electrons concentrate at the periphery and the center of the beam, respectively, while having the same integral fraction at $z = 0$ as simulation T4, i.e.,

$$\bar{\alpha}_0 = \int_0^R r n_h dr / \int_0^R r n dr = 0.04. \quad (12)$$

(Notice that $\bar{\alpha}_0$ should not be confused with α_0 in Refs. 7 and 31, where subindex 0 referred to the stagnation conditions of the flow far upstream of the nozzle throat, a region not treated here).

According to the 1D model, the hot-to-cold temperature ratio τ defines the intensity of the steepening and the critical value of $\bar{\alpha}_0$ for DL formation.⁷ In the present simulations, it has been fixed at $\tau = 18$. For this value of τ , the 1D model predicts that the parametric transition from solutions with a QDL to those with a DL takes place at $\bar{\alpha}_0 \simeq 10\%$.

A. Influence of the hot-electron fraction

Figure 1 shows plasma properties for simulations T0, T4, and T8. Color maps represent the electric field strength; equipotential surfaces and electric field lines are also shown. The 2ET plasmas of T4 and T8 exhibit the formation of a steady-state QDL (displayed as a thick dashed line). The plots above the 2D maps of Fig. 1 present the evolution of the electric potential ϕ , electric field $\mathbf{E} = -\nabla\phi$, and ion Mach number M along the axis (i.e., for $r = 0$).

In agreement with the experiments of Hairapetian-Stenzel³ and the 1D model, as $\alpha(0, r)$ increases: (1) the

position of the QDL surface shifts towards the throat, (2) the local maximum of the electric field increases, and (3) the local minimum of the supersonic Mach number becomes closer to 1. The novel 2D feature is the curvature of the QDL, which agrees qualitatively with the convex U-shaped steepenings detected experimentally.^{11,16} In fact, the QDL convexity mimics that of the nearby equipotential surfaces, i.e., the QDL surface is almost an equipotential one. This property is only satisfied when $\alpha(0, r)$, $\phi(0, r)$, and $H_i(0, r)$ are constant at the throat and $u_{0i} \ll \tilde{u}_i$. In this case, $\phi = \text{const}$ surfaces are constant surfaces for $\alpha(z, r)$ and $M(z, r)$ too, and consequently, the QDL matches them as well. Notice that the curvature of the QDL is similar in simulations T4 and T8.

In addition, the shape of the initial plasma density profile given by Eq. (11) is propagated along equipotential surfaces, so that plasma density is the magnitude changing most along the QDL surface [indeed decreasing three orders of magnitude from the center to the edge for the initial conditions used here, Eq. (11)]. Figure 2 presents the evolution of plasma density in the magnetic nozzle and shows that a decrease in density takes place across the QDL in simulations T4 and T8. The strong difference between $\phi = \text{const}$ and $n = \text{const}$ surfaces in these simulations is also found experimentally (cf. Figs. 8(a) and 9 of Ref. 10). The pressure gradient in the $\mathbf{1}_\perp$ direction, linked to the density profile, is balanced by the magnetic force on the azimuthal electron current and the electric force, Eq. (8).

Figure 3 displays the local angle \widehat{EB} formed between \mathbf{E} and \mathbf{B} . The ambipolar electric field, self-adjusted by the plasma, guarantees quasineutrality in the whole plasma domain, by taking the correct magnitude and direction to steer

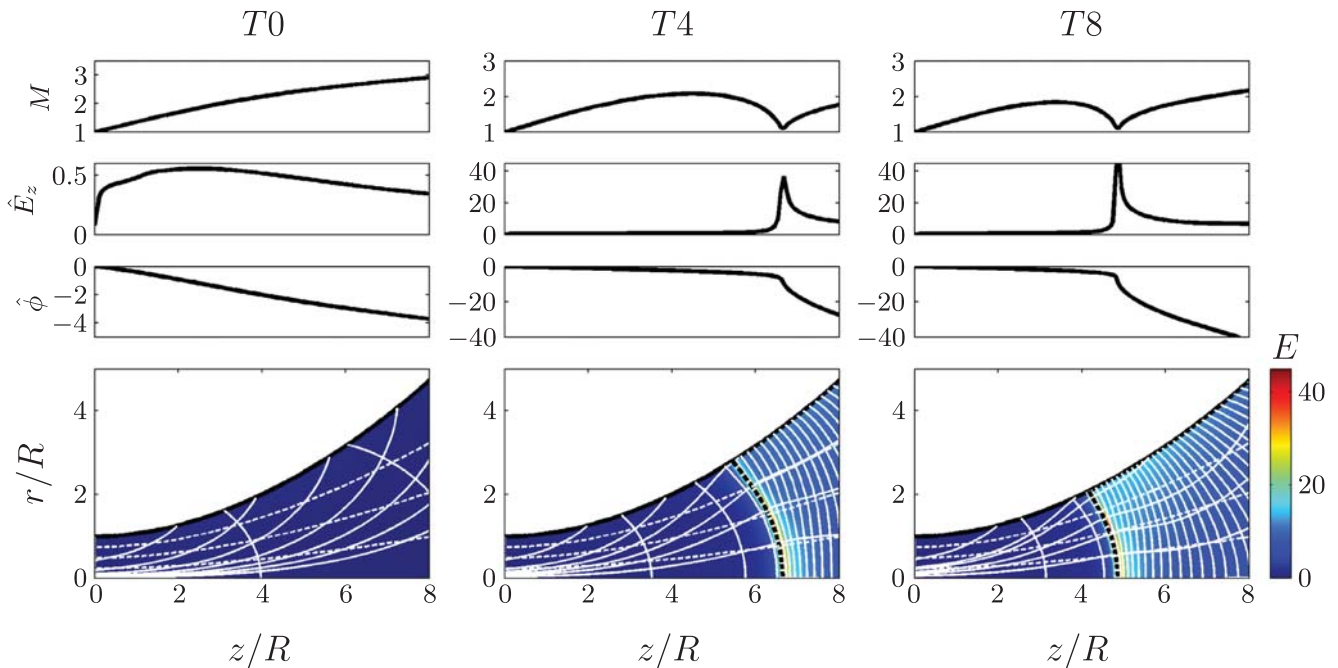


FIG. 1. Map of the intensity of the non-dimensional electric field $\widehat{E} = eER/T_c$ for simulations T0, T4, and T8. Contours show isopotentials of $\widehat{\phi} = e\phi/T_c$, and \mathbf{E} streamlines (orthogonal to the former). The separation between each two successive $\widehat{\phi}$ -lines is $\Delta\widehat{\phi} = 2$. Thin dashed lines show the direction of the magnetic field. Thick dashed lines represent the QDL location in simulations T4 and T8. The evolution of $\widehat{\phi}$, \widehat{E} , and M along the axis ($r = 0$) is depicted in the panels on top for each simulation.

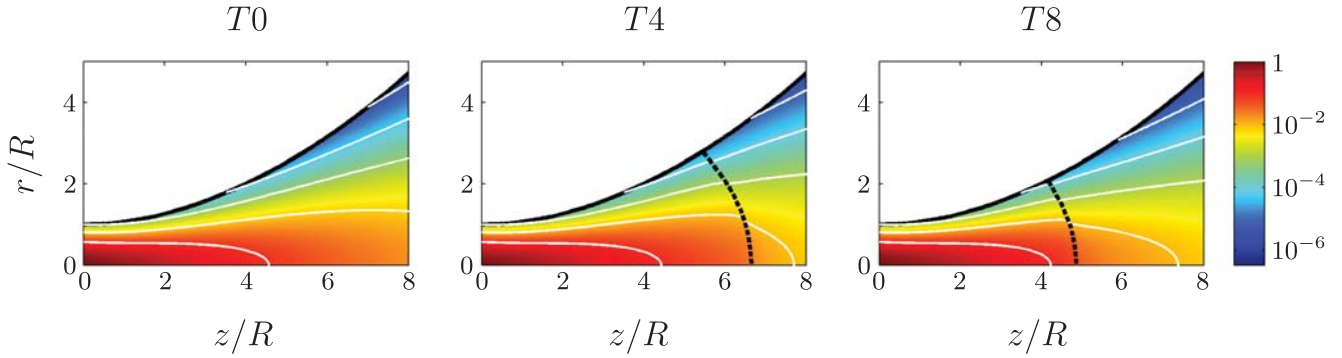


FIG. 2. Maps of n/n_0 in simulations T0, T4, and T8. Thick dashed lines represent the QDL location. Density decreases one order of magnitude between each two consecutive lines.

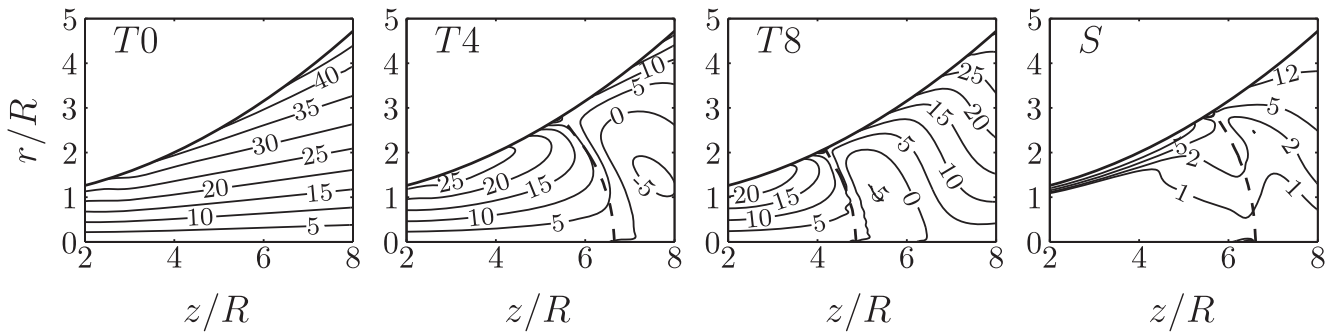


FIG. 3. Detail of the local \widehat{EB} angle in the nozzle (in deg) for different simulations. Dashed lines represent the QDL location.

the ion trajectories as required. In the 1ET plasma of simulation T0, equipotential surfaces are curved as a consequence of nozzle divergence and the need of a perpendicular electric field to radially expand the ions. This perpendicular field—and \widehat{EB} —increases from the axis towards the beam edge, where the highest ion deflection is demanded. Cases T4 and T8 of Fig. 3 show that the formation of a QDL implies a strong change of the electric field direction around and downstream of the QDL. The electric field becomes almost parallel with the magnetic field at and after the QDL, but still imparts a large radial acceleration to ions as a consequence of the curvature of the layer. The small negative values of \widehat{EB} that can occur downstream of the QDL suggest that ions can leave the layer with an excess of outwards velocity that the ambipolar electric field needs to accommodate downstream.

B. Influence of magnetic strength and divergence

For nearly unmagnetized ions, as in simulations T0 or T4, the perpendicular electric field satisfies $E_{\perp} \simeq m_i \tilde{u}_i^2 / (e R_i)$, with R_i the meridian curvature radius of the ion streamtube. For higher magnetization cases, i.e., $\widehat{\Omega}_{i0} \gg 1$, E_{\perp} is lower since part of this ion deflection task is taken by the magnetic force on ions, $j_{0i} B$. Therefore, assuming $R_i \simeq R_n \geq O(R)$ as general estimates, we have $E_{\perp} \leq O(M_0^2 T_e / (e R))$. The effect of increasing B is illustrated here with simulation S (Fig. 4). The enhanced magnetic field of simulation S decreases the required E_{\perp} for ion expansion, while E_{\parallel} remains basically unaffected (cf. simulation T4 in Fig. 1). Consequently, the \widehat{EB} angle is notably decreased with respect to T4 (as can be observed in Fig. 3) and the equipotential surfaces become almost perpendicular to \mathbf{B} . Since the QDL closely matches the local

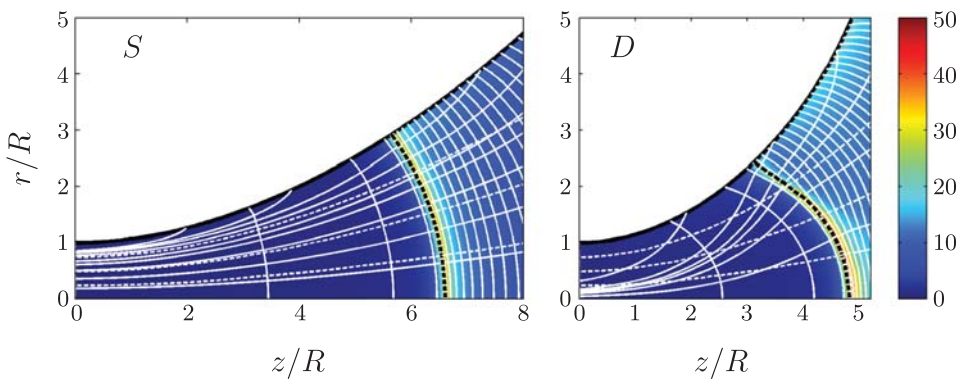


FIG. 4. Electric field and QDL position (thick line) of simulations S and D (for small and large nozzle divergence). The horizontal and vertical scales of both figures are the same, in ratio 1:1. The description of lines is as in Fig. 1.

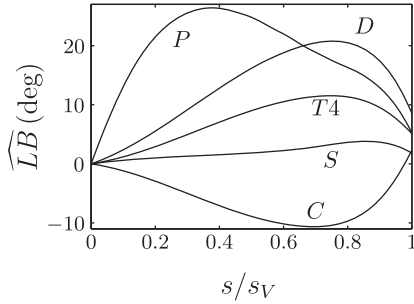


FIG. 5. Angle \widehat{LB} (in deg) formed by the QDL surface normal and the magnetic field, in simulations T4, S, D, P, and C. s/s_V is the normalized arc length along the meridional projection of the QDL, running from the axis to the plasma border V .

equipotential surfaces when $\alpha(0, r) = \text{const}$, the curvature of the resulting QDL is lower in simulation S. This is in agreement with the observed tendency in the experiments of Hairapetian *et al.*³ for increasing values of B . This effect is more apparent in Fig. 5, where the angle \widehat{LB} between the QDL surface normal and the local magnetic field of the different simulations has been plotted. From these results, it is easy to infer that the partial ion magnetization case will be contained within the no-magnetization limit (which is practically T4) and the full-magnetization one (where $\widehat{LB} \simeq 0$ as $E_\perp \rightarrow 0$ and $\nabla\phi \parallel \mathbf{B}$). [This will not be necessarily true for the more intricate cases with $\alpha(0, r) \neq \text{const}$ described in Sec. IV C.]

The divergence rate of the magnetic field can have similar effects on the curvature of the QDL. By roughly halving the value of R_n in simulation D (more diverging nozzle), a larger E_\perp is generated in the plasma beam, which results in more curved equipotentials and hence a more curved QDL, as can be appreciated in Fig. 4, and also in a larger \widehat{LB} angle (Fig. 5).

In conclusion, the strength and curvature of the magnetic field can alter the convexity of the QDL, as the necessary E_\perp for the ion expansion changes, but it must be emphasized that they have no direct influence on the formation of the QDL itself nor the magnitude of the potential jump across it, which depend only on the distribution of hot and cold electrons.

To this respect, Singh¹ suggests that when B is increased the “full development of the ion cyclotron motion” can have a relevant role in the curvature of the plasma column and, in particular, in the sign of E_\perp (changing from $E_\perp > 0$ to $E_\perp < 0$

as ions gyrate outwards). This phenomenon is not found in our model, where the supersonic ions, advancing in a diverging magnetic field, do not establish any distinguishable cyclotron motion in the range of magnetizations studied, and in any case, their tendency is to separate inwards from the magnetic tubes due to inertia.²⁹ Moreover, since the ion Larmor radius is $\ell_i \propto 1/B$, any effect proportional to ℓ_i should diminish when increasing B .

Also, it has been claimed that an “abruptly divergent” magnetic field is relevant for DL formation,¹ even in the case of a simple 1ET plasma.⁴¹ In the frame of our model, an “abrupt” nozzle would correspond to a magnetic curvature radius R_n satisfying $\lambda_D \ll R_n \ll R$, which would lead to $T_e/(e\lambda_D) \gg E_\perp \gg T_e/(eR)$. Two observations are pertinent here. First, as commented in Sec. II, in the absence of other mechanisms, there is no DL formation in 1ET plasmas,^{5,32} just a natural steepening of characteristic length R_n . Second, abrupt divergence seems highly undesirable for the main purpose of a magnetic nozzle, that is, to efficiently channel and expand the plasma beam emitted by the plasma source, with minimal plume divergence.

C. Influence of the hot electron injection zone

In a real device, the radial profiles of low- and high-energy electrons at the source exit (or the nozzle throat) are likely not the same, and will depend on the particularities of the plasma source. The effects and main tendencies to be expected when $\alpha(0, r) \neq \text{const}$ are explored here with simulations P and C. In both of them and to facilitate comparison, the radially averaged value of $\alpha(0, r)$ is chosen to coincide with simulation T4 ($\bar{\alpha}_0 = 4\%$) but a sinusoidal radial dependence has been added. Specifically, we take

$$\alpha(0, r) \propto [2 \pm \cos(\pi r/R)], \quad (13)$$

with + sign for C and lower – sign for P. Thus, the sequence of simulations $P \rightarrow T4 \rightarrow C$ corresponds to progressively displacing the hot electron injection from the periphery to the center of the beam.

Notice that, for $\alpha(0, r) \neq \text{const}$, the sound speed, Eq. (9), varies radially at the throat. In order to maintain supersonicity and lacking a detailed description of the velocity profile at the throat, we have opted here to keep $M(0, r) = 1.01 = \text{const}$, thus letting $u_{zi}(0, r) \neq \text{const}$ in Eq. (11). The electron response in the simulations shown here is

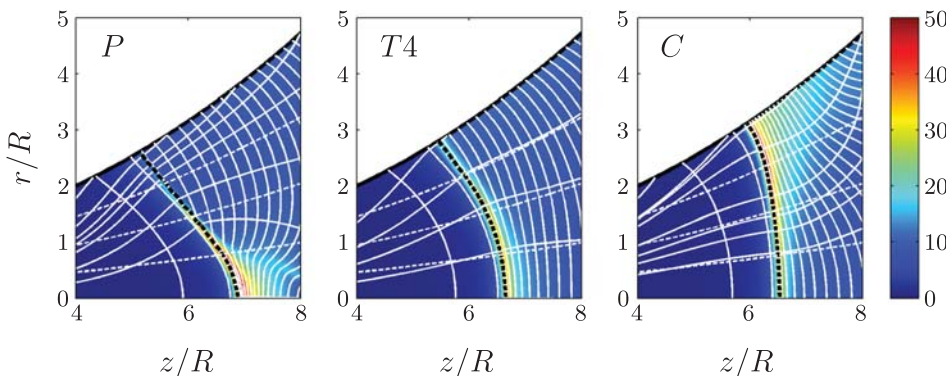


FIG. 6. Detail of the QDL shape of simulations P, T4, and C. The background color shows the intensity of the non-dimensional electric field $\widehat{E} = eER/T_e$. The description of lines is analogous as that of Fig. 1.

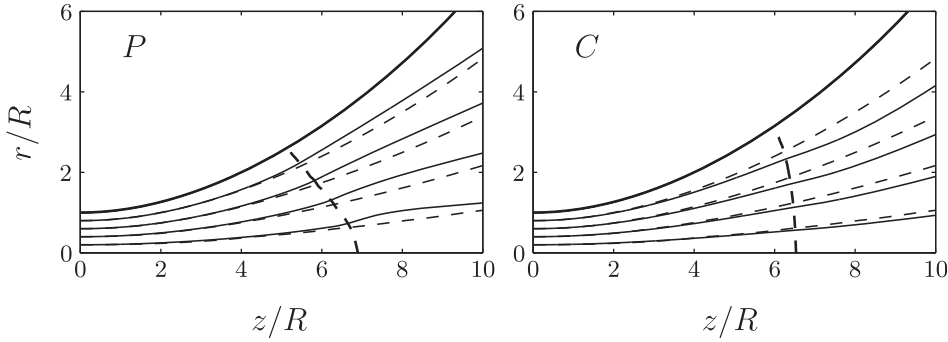


FIG. 7. Effect of the QDL (thick dashed line) on the ion streamtubes (solid) in simulations P and C. The corresponding magnetic lines are plotted for reference (dashed).

the particularization to *each magnetic streamtube* of the electron behavior in the 1D model, i.e., the functions $n_c(\phi, \psi)$, $n_h(\phi, \psi)$, and $c_s(\phi, \psi)$ on each magnetic tube ψ are univocally defined given the hot-electron fraction of that tube at the throat. Notice that now M is fully dependent on (z, r) and not a function of ϕ as before, therefore the QDL does not coincide with any equipotential surface.

A detailed map of the electric potential around the QDL of simulations P, T4, and C is plotted on Fig. 6. On each magnetic tube, higher hot-electron fractions at injection cause the QDL to take place earlier in the expansion, as in the 1D model. Hence, when the injection of hot electrons moves from the periphery towards the center, the curvature of the QDL decreases. Interestingly, the QDL surface is nearly planar in simulation C, and it actually forms a negative \widehat{LB} angle with the local B , illustrated in Fig. 5, revealing the strong influence of the function $\alpha(0, r)$ on the curvature of the layer. It can also be observed that the region of strongest E takes place near the axis for simulation P, while it is located at the periphery in simulation C.

It was already commented that the QDL curvature affects the trajectory of ions, modifying their direction downstream. This effect is clearly more pronounced when $\alpha(0, r) \neq \text{const}$. Figure 7, which displays selected ion streamtubes and their relative position with respect to their reference magnetic streamtubes, shows a remarkable feature of simulations P and C: the more planar QDL of simulation C causes ion streamtubes to deflect inwards around the layer, thus reducing their divergence angle. On the contrary, the strongly curved QDL of simulation P causes ion streamtubes to diverge faster than the magnetic field. These alterations extend into a limited region downstream of the QDL, meaning that its influence is of local character: indeed, after crossing the QDL (and because ions are not sufficiently magnetized downstream), the divergence of ion streamlines

soon decreases and eventually becomes lower than that of the local magnetic field again, resembling that of a 1ET plasma (see, for instance, Fig. 1 of Ref. 42).

The shape and position of the steepening can have a strong influence on the map of ϕ downstream of the QDL, where the extraordinary deflection of the ion flow by the layer needs to be corrected and can lead to $E_{\perp} < 0$ (i.e., $\widehat{EB} < 0$), as illustrated by simulation P in Fig. 6. The possibility of formation of potential barriers and/or shock waves (in an otherwise shock-free flow) as a result of this should be considered. At any rate, it is clear that the structures generated by general 2ET plasmas can result in much more complex electric fields and plasma flows.

V. EFFECT OF THE QDL ON PROPULSIVE PERFORMANCES

In application to magnetic nozzles of space plasma thrusters, it is interesting to discuss the effects of the 2D QDL on the propulsive figures of the plasma beam. The main purpose of a magnetic nozzle stage in a plasma thruster is to increase thrust,²⁴

$$F = \sqrt{2\eta P_a \dot{m}}, \quad (14)$$

where η is the thrust efficiency, P_a the applied power, and \dot{m} the mass flow rate. For a given P_a and \dot{m} , the efficiency η limits the maximum value of F and is a function of the multiple, interconnected phenomena taking place in the thruster, such as plasma ionization, radiation, plasma-wall interaction, and plume expansion and divergence in the magnetic nozzle. The nozzle model presented here does not allow the study of the total thrust efficiency of a given thruster, which requires to match it with the model of the plasma source.⁴³ However, it permits to assess the influence of the plume divergence on η .

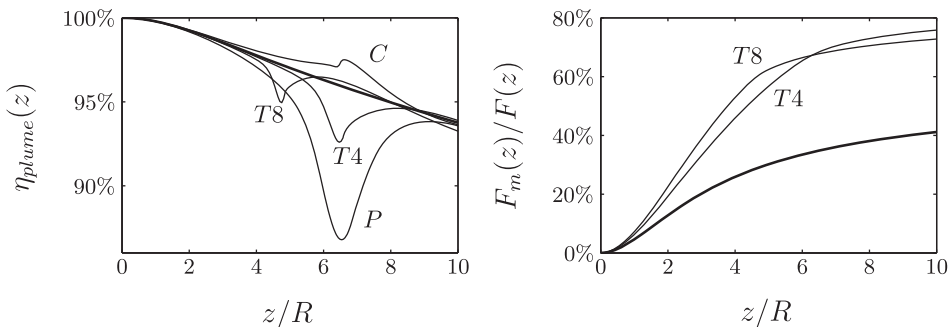


FIG. 8. Plume efficiency $\eta_{\text{plume}}(z)$ (left) and magnetic thrust fraction $F_m(z)/F(z)$ (right) for different simulations. The reference 1ET plasma of simulation T0 has been plotted as a thick line. The graphs of $F_m(z)/F(z)$ for simulations P and C are almost indistinguishable from that of simulation T4, and have not been plotted.

This can be quantified with the plume efficiency function, $\eta_{plume}(z)$, defined in Ref. 29 as the ratio of ion axial-to-total energy fluxes at $z = \text{const}$ sections, i.e.,

$$\eta_{plume}(z) = P_{iz}(z)/P_i(z). \quad (15)$$

The plume efficiency is an intrinsically 2D effect, non recoverable by 1D models. This factor is of utmost importance not only for its contribution to η but also since it can ultimately characterize the plume divergence angle and the plasma detachment losses.⁴⁴ Figure 8 (left) compares the plume efficiency function of the different 2ET plasmas of Table I. The visible non-monotonicity of the curves for 2ET plasmas is due to the fact that $\eta_{plume}(z)$ is being evaluated on $z = \text{const}$ sections, while the QDL is a curved surface. This causes the peripheral part of the QDL to affect the plasma first (i.e., at lower values of z). In the beam periphery, a large radial acceleration is exerted on ions, which explains the local drop of $\eta_{plume}(z)$. When the central part of the QDL is crossed, the strong axial acceleration imparted to the ions in this region raises $\eta_{plume}(z)$ again. Therefore, comparison with 1ET plasmas makes full sense only far downstream of the QDL.

Interestingly, in simulation C, where most of the hot electrons are located about the magnetic nozzle axis and the QDL is more planar, a local increase of $\eta_{plume}(z)$ is observed, which is due to the larger axial acceleration imparted by the QDL in this case. On the other hand, simulation P, with peripheral hot electrons and a more curved QDL, shows the largest local decrease of $\eta_{plume}(z)$. This particular local behavior of simulations C and P can be explained by the deflection of ion streamtubes that was depicted in Fig. 7. All simulations except C show a slightly worse efficiency than T0 after the QDL. In spite of the pronounced local extrema in $\eta_{plume}(z)$ caused by the presence of the QDL, simulations of 2ET plasmas deviate from the reference T0 only in the vicinity of the layer. Downstream of the steepening, most of the plume efficiency of the 1ET plasma is recovered, indicating that the divergence of ion streamlines gradually returns back to that of T0, and further downstream the effect of the QDL on $\eta_{plume}(z)$ becomes marginal. This suggests that the presence of a QDL has little incidence on the final plume efficiency.

In regard to these results, it is important to acknowledge that some of the simplifications of the current model might be responsible of an overly optimistic downstream value of $\eta_{plume}(z)$. In particular, a more realistic description of the electron velocity distribution function could modify the evolution of the hot population downstream of the QDL, possibly reducing the depicted recovery of $\eta_{plume}(z)$.

The main parameter characterizing the usefulness of the magnetic nozzle stage in a plasma thruster is its contribution to the total thrust of the device. In an electromagnetic plasma thruster, there are two contributions to thrust: the *pressure thrust*, F_p , due to the plasma axial pressure on the source walls, and the *magnetic thrust*, F_m , caused by the magnetic axial force that plasma electric currents (mainly in the nozzle stage) induce on the thruster magnetic circuit.²⁹ The pressure thrust can be assimilated to the plasma momentum flow at the nozzle throat ($z = 0$),

$$F_p = 2\pi \int_0^R r dr (nm_i u_{zi}^2 + T_h n_h + T_c n_c), \quad (16)$$

whereas, by virtue of the action-reaction principle, the magnetic thrust function at section $z = \text{const}$, $F_m(z)$, is defined as the integral of the axial magnetic force density exerted on the plasma in the nozzle volume $V(z)$ comprised between the throat, the beam-vacuum edge, and $z = \text{const}$. For $B_\theta = 0$, that force is

$$F_m(z) = - \int_V j_\theta B_r dV. \quad (17)$$

Electrons provide the main contribution to j_θ (Ref. 29). A simple estimate shows that hot electrons have higher azimuthal velocity than cold electrons, but the respective current density, Eq. (8), depends on the density of each species. As such, the contribution of an elemental plasma volume to magnetic thrust depends on the local \mathbf{B} , n_h and n_c .

In order to assess the magnetic thrust, the function $\kappa_{noz}(z) = F_m(z)/F_p$ was computed in Ref. 30 for a 2D, 1ET plasma; the same magnitude was discussed in Ref. 31 for a 1D, 2ET plasma. Defining $F(z) = F_p + F_m(z)$ as the total thrust function along the nozzle, Fig. 8 (right) plots the axial evolution of the *relative* magnetic contribution

$$\frac{F_m(z)}{F(z)} \equiv \frac{\kappa_{noz}(z)}{1 + \kappa_{noz}(z)}, \quad (18)$$

which is found to be a better self-explaining magnitude to understand the propulsive performance of the device, since $F(z)$ is governed by the absorbed power and mass flow rate as expressed by Eq. (14). The curves of Fig. 8 show that the presence of hot electrons can substantially increase the magnetic thrust fraction. Interestingly, the QDL presence and its curvature are marginal for the value of $F_m(z)/F(z)$, which is only dependent on τ and $\bar{\alpha}_0$. Contrary to the behavior of $\eta_{plume}(z)$, no local change of $F_m(z)/F(z)$ is observed across the QDL in Fig. 8. Moreover, simulations T4, P, and C are indistinguishable from each other as they have the same magnetic nozzle and the same value of $\bar{\alpha}_0$. This serves as a “two-dimensional” refutation that the thrust mechanism associated with the presence of a DL is non-existent.

When the upstream hot-electron fraction is small (which is the case of highest practical interest), plasma dynamics upstream from the QDL are dominated by (more abundant) cold electrons, whereas downstream from the QDL, hot electrons dominate the expansion. This means that pressure thrust is settled mainly by the cold electron population, while the magnetic thrust function tends to be dominated by cold and hot electrons upstream and downstream of the QDL, respectively. As $\bar{\alpha}_0$ increases, the QDL moves upstream and the hot electron contributions to F_m and F_p increase. As a result, there is a value of $\bar{\alpha}_0$ that maximizes the downstream value of the fraction F_m/F , as can be inferred from Fig. 8.

An important remark, pointed out by Ahedo³¹ and worth emphasizing here again, is that the increase of the magnetic thrust fraction (in 2ET plasmas with QDLs) cannot be interpreted neither as a net increment of thrust nor as an

enhancement of thruster performance. Equation (14) shows very clearly that $F \propto \sqrt{P_a \dot{m}}$, and the only magnitude that can actually improve the thruster operation is the thrust efficiency η . Here, we have found that η_{plume} (one of the partial efficiencies determining η) is not affected substantially by a 2ET plasma and its associated QDL. On the contrary, η_{plume} depends on the magnetic field intensity and divergence.²⁹

VI. CONCLUSIONS

A 2D model of the expansion of a two-electron-temperature (2ET) plasma in a divergent magnetic field has allowed us to study the formation, position, and 2D shape of a current-free quasi double layer (QDL). The characteristics of these structures have been investigated in terms of (1) the relative fraction of hot electrons, (2) their radial distribution when injected at the nozzle throat, and (3) the geometry and intensity of the applied magnetic field. Since the model developed here is fully quasineutral, the transition from the quasineutral QDL to a non-neutral DL cannot be completed, but it had been previously shown that both structures are the same with just different levels of non-neutrality.

Axial properties of 2ET-QDLs are in accordance with those already analyzed in 1D models. The model yields the curved 2D shape of the QDL, which agrees qualitatively with related experiments on 2ET plasmas. The QDL curvature is found to be mainly the consequence of two features: first, the natural curvature of the electric equipotential lines in a divergent magnetic field, already known for 1ET plasmas; and second, the radial distribution at injection of the high-energy electron population. The curvature of the QDL increases the higher the divergence of the magnetic nozzle, the lower the magnetic strength, and the more peripherally hot electrons are injected. The DL curvature modifies the ambipolar electric field and ion trajectories downstream, which can be made to diverge locally faster or slower than the magnetic field depending on the radial acceleration imparted by the large electric field at the layer.

For propulsive applications, it is confirmed that a 2ET-QDL has a zero effect on thrust. The novel result is that the final plume divergence, far downstream from the QDL, is almost unaffected by its presence and shape. Therefore, no propulsive role of the current-free double layer (CFDL) has been identified yet. To this respect, the only interesting feature we have found (which could merit further consideration) is that the magnetic-to-pressure contribution becomes maximum for a certain (small) fraction of hot electrons.

As stated in the Introduction, the subject of the present study has been exclusively the formation of a CFDL in the 2D expansion of a fully ionized, collisionless, 2ET plasma. This 2D analysis is of interest for the interpretation of the laboratory experiments of Hairapetian and Stenzel and presumably for the operation of a helicon plasma thruster in space. Existing research on the polar wind suggests that the structures developing in auroral plasmas can resemble the 2ET-CFDLs studied here,⁶ although multiple DL structures may form at different altitudes^{45,46} and essential differences such as current across the layer and the effect of the gravitational potential can affect the upward plasma expansion along the polar mag-

netic cusp. On the contrary we cannot assure that the central aspects of our analysis are relevant for understanding the more complex HPD-CFDL, at least until it is clarified whether the presence of two distinguished populations of positive ions is the main instrument for the formation of such DLs.

ACKNOWLEDGMENTS

This work has been sponsored by the Air Force Office of Scientific Research, Air Force Material Command, USAF, under Grant No. FA8655-12-1-2043. The U.S. Government is authorized to reproduce and distribute reprints for Governmental purpose notwithstanding any copyright notation hereon. Supplementary support has been provided by the Spanish R&D National Plan (Project AYA-2010-61699).

¹N. Singh, *Phys. Plasmas* **18**, 122105 (2011).

²G. Hairapetian and R. Stenzel, *Phys. Rev. Lett.* **65**, 175 (1990).

³G. Hairapetian and R. Stenzel, *Phys. Fluids B* **3**, 899 (1991).

⁴B. Bezzerides, D. Forslund, and E. Lindman, *Phys. Fluids* **21**, 2179 (1978).

⁵F. Perkins and Y. Sun, *Phys. Rev. Lett.* **46**, 115 (1981).

⁶A. Barakat and R. Schunk, *J. Geophys. Res.* **89**, 9771 (1984).

⁷E. Ahedo and M. Martínez-Sánchez, *Phys. Rev. Lett.* **103**, 135002 (2009).

⁸N. Singh, *Phys. Rev. Lett.* **106**, 079501 (2011).

⁹C. Charles and R. Boswell, *Appl. Phys. Lett.* **82**, 1356 (2003).

¹⁰C. Charles and R. Boswell, *Phys. Plasmas* **11**, 1706 (2004).

¹¹C. Charles, *Appl. Phys. Lett.* **96**, 051502 (2010).

¹²K. Takahashi, Y. Igarashi, and T. Fujiwara, *Appl. Phys. Lett.* **97**, 041501 (2010).

¹³S. Cohen, X. Sun, N. Ferraro, E. Scime, M. Miah, S. Stange, N. Siefert, and R. Boivin, *IEEE Trans. Plasma Sci.* **34**, 792 (2006).

¹⁴N. Plihon, P. Chabert, and C. Corr, *Phys. Plasmas* **14**, 013506 (2007).

¹⁵E. Scime, I. Biloiu, J. Carr, S. Thakur, M. Galante, A. Hansen, S. Houshmandyar, A. Keese, D. McCarren, S. Sears *et al.*, *Phys. Plasmas* **17**, 055701 (2010).

¹⁶S. K. Saha, S. Raychaudhuri, S. Chowdhury, M. S. Janaki, and A. K. Hui, *Phys. Plasmas* **19**, 092502 (2012).

¹⁷S. Rao and N. Singh, *Phys. Plasmas* **19**, 093507 (2012).

¹⁸P. Zhu and R. Boswell, *Phys. Fluids B* **3**, 869 (1991).

¹⁹A. Degeling, C. Jung, R. Boswell, and A. Ellingboe, *Phys. Plasmas* **3**, 2788 (1996).

²⁰R. Chen and N. Hershkowitz, *Phys. Rev. Lett.* **80**, 4677 (1998).

²¹F. Chen, *Plasma Phys. Controlled Fusion* **33**, 339 (1991).

²²M. Lieberman, C. Charles, and R. Boswell, *J. Phys. D: Appl. Phys.* **39**, 3294 (2006).

²³I. Langmuir, *Phys. Rev.* **33**, 954 (1929).

²⁴E. Ahedo, *Plasma Phys. Controlled Fusion* **53**, 124037 (2011).

²⁵T. Ziemba, J. Carscadden, J. Slough, J. Prager, and R. Winglee, in *41th AIAA/ASME/SAE/ASEE Joint Propulsion Conference & Exhibit*, AIAA 2005-4119 (AIAA, Washington DC, 2005).

²⁶F. Diaz, J. Squire, R. Bengtson, B. Breizman, F. Baity, and M. Carter, in *36th AIAA/ASME/SAE/ASEE Joint Propulsion Conference & Exhibit*, AIAA 2000-3756 (AIAA, Washington DC, 2000).

²⁷G. Krülle, M. Auweter-Kurtz, and A. Sasoh, *J. Propul. Power* **14**, 754 (1998).

²⁸W. Manheimer and R. Fernsler, *IEEE Trans. Plasma Sci.* **29**, 75 (2001).

²⁹E. Ahedo and M. Merino, *Phys. Plasmas* **17**, 073501 (2010).

³⁰E. Ahedo and M. Merino, *Phys. Plasmas* **18**, 053504 (2011).

³¹E. Ahedo, *Phys. Plasmas* **18**, 033510 (2011).

³²M. Raadu, *Phys. Rep.* **178**, 25 (1989).

³³L. Block, *Astrophys. Space Sci.* **55**, 59 (1978).

³⁴N. Hershkowitz, *Space Sci. Rev.* **41**, 351 (1985).

³⁵E. Ahedo and M. Merino, *Phys. Plasmas* **19**, 083501 (2012).

³⁶M. Zucrow and J. Hoffman, *Gas Dynamics* (Wiley, New York, 1976).

³⁷L. Schott, *Phys. Fluids* **30**, 1795 (1987).

³⁸K. Sato and F. Miyawaki, *Phys. Fluids B* **4**, 1247 (1992).

³⁹G. Borg, J. Bright, and I. Kamenski, *Plasma Phys. Controlled Fusion* **40**, 987 (1998).

⁴⁰R. Kinder and M. Kushner, *J. Appl. Phys.* **90**, 3699 (2001).

⁴¹A. Fruchtman, *Phys. Rev. Lett.* **96**, 065002 (2006).

⁴²M. Merino and E. Ahedo, *IEEE Trans. Plasma Sci.* **39**, 2938 (2011).

⁴³J. Navarro, M. Merino, and E. Ahedo, in *48th AIAA/ASME/SAE/ASEE Joint Propulsion Conference & Exhibit*, AIAA-2012-3955 (AIAA, Washington DC, 2012).

⁴⁴M. Merino and E. Ahedo, in *48th AIAA/ASME/SAE/ASEE Joint Propulsion Conference & Exhibit*, AIAA-2012-3843 (AIAA, Washington DC, 2012).

⁴⁵R. Ergun and R. Strangeway, *Geophys. Res. Lett.* **27**, 4053 (2000).

⁴⁶N. Singh and G. Khazanov, *J. Geophys. Res.* **108**, 8007 (2003).

PAGE INTENTIONALLY LEFT BLANK

Helicon thruster plasma modeling: two-dimensional fluid dynamics and propulsive performances

Eduardo Ahedo^{1, a)} and Jaume Navarro-Cavallé¹

ETS Ingenieros Aeronáuticos, Universidad Politécnica de Madrid, Madrid 28040, Spain

An axisymmetric macroscopic model of the magnetized plasma flow inside the helicon thruster chamber is derived, assuming that the power absorbed from the helicon antenna emission is known. Ionization, confinement, subsonic flows, and production efficiency are discussed in terms of design and operation parameters. Analytical solutions and simple scaling laws for ideal plasma conditions are obtained. The chamber model is then matched with a model of the external magnetic nozzle in order to characterize the whole plasma flow and assess thruster performances. Thermal, electric, and magnetic contributions to thrust are evaluated. The energy balance provides the power conversion between ions and electrons in chamber and nozzle, and the power distribution among beam power, ionization losses, and wall losses. Thruster efficiency is assessed and main causes of inefficiency are identified. The thermodynamic behavior of the collisionless electron population in the nozzle is acknowledged to be poorly known and crucial for a complete plasma expansion and good thrust efficiency.

PACS numbers: 52.75.Di, 52.30.Ex, 52.59.Dk

^{a)}Electronic mail: eduardo.ahedo@upm.es; web.fmetsia.upm.es/ep2/

I. INTRODUCTION

The helicon plasma thruster (HPT) is an innovative technology for space propulsion, which, at present, is being researched extensively¹⁻⁷. The device is constituted of a helicon source, where the plasma is generated and heated, and an external divergent magnetic nozzle, where the plasma is accelerated. The physical elements of a HPT are: a cylindrical dielectric chamber; a gas injection system, usually at the back of the chamber; an external antenna wrapped around the chamber emitting rf waves, typically in the range 1-26 MHz, which propagate within the plasma; and a set of magnetic coils (or permanent magnets) that creates a longitudinal magnetic field, typically in the range 10^2 to 10^3 Gauss. In the ‘conventional’ design, the magnetic field is predominantly axial inside the chamber and divergent outside it, and has several roles. First, it makes the plasma column transparent to the propagation of the rf emission as helicon waves. Second, the magnetic field screens the chamber walls, thus reducing greatly plasma losses at them⁸. Third, outside the chamber, the divergent magnetic topology creates a magnetic nozzle that channels the supersonic plasma flow, transforming the plasma internal energy into axially-directed one, in a process very similar to the expansion of a hot gas in a conventional solid nozzle^{9,10}.

The typical operation range of helicon sources is¹¹ $\omega_{lh} \ll \omega \ll \omega_{ce} \ll \omega_{pe}$, with ω_{lh} the lower-hybrid frequency, ω the wave frequency, ω_{ce} the electron cyclotron frequency, and ω_{pe} the plasma frequency. Helicon waves pertain to the branch of whistler waves; in a cold, unbounded plasma, no other waves can propagate in that frequency range¹². Although a unique theory for the absorption of the energy of helicon waves is not fully established yet, the collisional theory, for dense enough plasmas, states that absorption is achieved through the mediation of Trivelpiece-Gould surface waves, which are highly dissipative^{11,13}. The advantage of helicon sources over other rf sources (such as inductively-coupled ones) is that, adjusting conveniently the magnetic intensity ($\omega_{ce} \propto B$), there is not a severe cut-off of plasma density for wave propagation, and values of $10^{18} - 10^{20} \text{m}^{-3}$ are achievable¹⁴.

Other potential advantages of the HPT for space propulsion would be: the lack of electrodes, thus avoiding erosion limitations and promising a long thruster lifetime; the capability of operating with a wide range of propellants^{1,15}; and high throttability, based on the capability of actuating, at constant power, on both the gas flow and the magnetic nozzle¹⁶. However, existing HPT prototypes are still far from achieving propulsive figures

capable of competing with other mature plasma thrusters. For instance, thrust efficiency is below 5% in the few cases where it has been measured directly¹⁷⁻¹⁹. In this context, the understanding of the multiple physical processes taking place in the HPT, the interplay among them, and the assessment of HPT performances are much needed.

A complete model of the HPT must deal with both the plasma-wave interaction and the fluid-dynamics of the plasma discharge. The two processes, although strongly coupled, require well differentiated models. This paper deals exclusively with the fluid-dynamics problem and assumes that the plasma column has absorbed a known amount of rf energy in the form of electron energy. In turn, the analysis of the plasma flow distinguishes between the chamber/internal and the nozzle/external regions. An axisymmetric model for the external region was already derived in Ref. 10 and was applied to discuss the 2D supersonic plasma expansion, the development of electric currents in the plasma, and the magnetic thrust mechanism. Posterior work on the nozzle region has advanced on the plasma/nozzle detachment issue²⁰⁻²² and the formation of double-layer type of structures²³⁻²⁵. The present paper has two main goals: first, to develop an axisymmetric model of plasma fluid-dynamics inside the chamber, and second, to match it to the nozzle model in order to evaluate HPT performances in terms of thrust, useful energy, and thrust efficiency.

The first part of the paper derives the axisymmetric model of the chamber and analyzes plasma generation, heating, wall interaction, and internal flows. The model is based on decoupling partially the radial and axial dynamics through an approximate variable-separation technique, already applied successfully to the plasma discharge in a Hall thruster²⁶; the main coupling parameter between axial and radial dynamics is the local wall-recombination frequency. Fruchtman et al.²⁷ were the first to apply the variable-separation technique to the 2D study of the plasma flow inside the chamber of a HPT. Our chamber model recovers, of course, part of theirs but, at the same time, completes or modifies the following central aspects of theirs: (a) the neutral density is taken constant [in a subsequent paper, Fruchtman²⁸ discussed neutral depletion within a 1D chamber model, still ignoring plasma recombination at the chamber wall], (b) radial plasma dynamics are purely diffusive; (c) ion dynamics are dominated by collisionality; and (d) a closed energy balance within the chamber is attained by assuming an adiabatic electron energy flow at the chamber exit.

Thus, central to our model will be to include the 2D depletion of the injected gas flow, which is governed by the competition between plasma volumetric-production and wall-recombination, the amount of this last one depending mainly on the magnetic screening of the walls. Then, the radial dynamics will show the formation of a quasineutral inertial region between the bulk diffusion region and the lateral Debye sheath, with effects on the lateral deposition of energy. With respect to the ion dynamics and for typical helicon source conditions, ions will be found to be both weakly collisional and weakly magnetized, and their free motion will be governed by the 2D ambipolar electric field. Finally, it will be shown that, in general, the energy balance on the magnetized electron population requires to take into account both the internal and external dynamics.

Apart from deriving the chamber model and computing exact solutions, our study of the chamber region offers two additional contributions. First, asymptotic regimes of the radial and axial dynamics are presented. These are highly valuable, since they provide both the clearest insight of the relevant internal physics and useful scaling laws relating the plasma response to operational and design parameters. Second, a parametric investigation is carried out, aiming at determining the way to maximize plasma production efficiency.

The second part of the paper is devoted to evaluate thruster performances. This requires first to match the 2D chamber model to the 2D magnetic-nozzle model of Ref. 10. Both models have been developed independently and involve assumptions and techniques suitable to the respective plasma conditions. This is going to produce a small mismatching of the internal and external solutions at the vicinity of the mutual interface (i.e. around the chamber exit) with marginal effect on the consistency of results and conclusions.

Thruster performances will be analyzed in terms of both thrust (i.e. plasma momentum) and energy. The different contributions to thrust are evaluated. Partial efficiencies will be defined in order to assess the relevance of the different physical processes (such as ionization, wall losses, plume divergence, etcetera) on the thrust efficiency. The electron energy behavior will be shown to be central for the plasma behavior in the nozzle and the thrust efficiency.

The rest of the paper is organized as follows. Section II presents the 2D chamber model. Section III discusses the plasma response inside the chamber. Section IV matches the chamber and nozzle models and discusses the different contributions to thrust. Section V presents the energy balance and discusses thrust efficiency. Section VI is for conclusions.

II. FORMULATION OF THE CHAMBER MODEL

Figure 1 sketches the HPT, with the chamber and nozzle regions and an example of magnetic topology created by a Maxwell 3-coil arrangement. The magnetic field is near axial inside the chamber (to the left of the third coil), and divergent at the nozzle. The rectangle symbolizes the elongated cylindrical chamber of radius R and length L . Let A, W, and E be the chamber back-wall, lateral, and front-exit, respectively. The magnetic field inside the chamber is approximated as purely axial and constant, $\mathbf{B} = B\mathbf{1}_z$.

A mass flow \dot{m} of neutral gas is injected at the cylinder back-wall (where we set $z_A = -L$) and is ionized by impact of electrons. In steady-state operation, we assume that electrons have been energized by the rf emission, acquiring a steady-state, uniform temperature T_e . The resulting plasma is constituted of singly-charged ion, electrons, and neutrals (subscripts i , e , and n , respectively). Plasma density is, on the one side, high enough for assuming the zero-Debye-length limit and, on the other side, low enough for assuming the zero-beta limit and thus neglect the induced magnetic field²⁹. Thereby, the plasma is quasineutral with $n \equiv n_e = n_i$ except in Debye sheaths around the chamber walls, which constitute surface discontinuities in the quasineutral scale. Thus, the sonic Bohm criterion applies to the perpendicular flow at the edges B and Q of the back and lateral sheath, respectively (Fig. 1). The perpendicular flow is also assumed sonic at the chamber exit section E (where we set $z_E = 0$).

Continuity and momentum equations for each species ($j = i, e, n$) are

$$\nabla \cdot (n_e \mathbf{u}_e) = \nabla \cdot (n_i \mathbf{u}_i) = -\nabla \cdot (n_n \mathbf{u}_n) = n_e n_n R_{ion}, \quad (1)$$

$$\nabla \cdot (m_j n_j \mathbf{u}_j \mathbf{u}_j) = -\nabla p_j + q_j n_j (-\nabla \phi + \mathbf{u}_j \times \mathbf{B}) - \mathbf{S}_j, \quad (2)$$

where: m_j is particle mass and q_j is electric charge (with $q_e = -e$ for electrons); \mathbf{u}_j is macroscopic velocity, n_j is density and $p_j = T_j n_j$ is pressure; ϕ is the ambipolar electric potential, and \mathbf{S}_j groups different collisional processes on each species. These include ionization and elastic electron-neutral, electron-ion, and ion-neutral collisions, with subindexes ion , en , ei , and in , respectively. Collisional rates for these processes, R_k ($k = ion, en, ei, in$), are defined in the Appendix A and plotted in Fig. 2 in terms of T_e .

According to the analyses of Refs. 8, 26, and 27, and for a chamber with $L \gg R$, the following assumptions and conventions are adopted for the model:

1. Axial symmetry: $\partial/\partial\theta = 0$.
2. Neutrals are assumed cold, with $\mathbf{u}_n = u_n \mathbf{1}_z$, and their density and velocity depend only on z . (These simplifications are well justified for a magnetized plasma with small wall recombination.)
3. Ion pressure is much smaller than electron pressure.
4. The plasma current \mathbf{j} satisfies the longitudinal ambipolarity condition $\mathbf{j} - \mathbf{1}_\theta j_\theta = \mathbf{0}$, yielding $u_{ri} = u_{re} \equiv u_r$ and $u_{zi} = u_{ze} \equiv u_z$. (This is rather plausible for an elongated dielectric chamber and the nozzle model considered later.)
5. Plasma density is expressed as

$$n(z, r) = n_z(z)n_r(z, r),$$

with $(2/R^2) \int_0^R r n_r(z, r) dr = 1$ for all z .

6. The electric potential is split as

$$\phi(z, r) = \phi_z(z) + \phi_r(z, r),$$

with $\phi_r(z, 0) = 0$ for all z .

7. $u_{\theta i} \ll u_{\theta e} \equiv u_\theta$, so that magnetic effects of ions are negligible.
8. Longitudinal electron-inertia is negligible, but azimuthal electron-inertia (due to u_θ) is retained.
9. Spatial gradients satisfy the following orderings,

$$\partial n_r / \partial z \ll \partial n_r / \partial r, \quad \partial \phi_r / \partial z \ll \partial \phi_r / \partial r,$$

$$\partial(u_r, u_\theta) / \partial z \ll \partial(u_r, u_\theta) / \partial r, \quad \partial u_z / \partial r \ll \partial u_z / \partial z.$$

These assumptions reduce the 2D model into axial and radial models coupled mainly through the wall recombination function

$$S_w(z) = n_z \nu_w(z),$$

where the frequency $\nu_w(z)$ is an eigenfunction to be determined. Then, the axially-dependent equations are

$$n_z u_z + n_n u_n = g_0, \quad (3)$$

$$\frac{\partial}{\partial z} (n_z u_z) = n_z (n_n R_{ion} - \nu_w), \quad (4)$$

$$u_z \frac{\partial u_z}{\partial z} = c_s^2 \frac{\partial \ln n_z}{\partial z} - n_n (R_{in} + R_{ion}) (u_z - u_n), \quad (5)$$

$$u_n \frac{\partial u_n}{\partial z} = -n_z \left[R_{in} (u_n - u_z) + \frac{\nu_w}{n_n} u_n (1 - \alpha_w) \right], \quad (6)$$

$$e \frac{\partial \phi_z}{\partial z} = T_e \frac{\partial \ln n_z}{\partial z}. \quad (7)$$

Here: $c_s = \sqrt{T_e/m_i}$ is the sound velocity, $g_0 = \dot{m}/(m_i \pi R^2)$ is the (constant) axial flux of heavy species (i.e. ions and neutrals), and $\alpha_w u_n$ is an effective axial velocity of neutrals created from plasma recombination at the lateral wall.

The radially-dependent equations are⁸

$$\frac{1}{r} \frac{\partial}{\partial r} (r n_r u_r) = n_r \nu_w, \quad (8)$$

$$u_r \frac{\partial u_r}{\partial r} = -c_s^2 \frac{\partial \ln n_r}{\partial r} - \frac{eB}{m_i} u_\theta + \frac{m_e}{m_i} \frac{u_\theta^2}{r} - n_n (R_{in} + R_{ion}) u_r, \quad (9)$$

$$u_r \frac{\partial u_\theta}{\partial r} = \frac{eB}{m_e} u_r - [n_n (R_{en} + R_{ion}) + n R_{ei}] u_\theta - \frac{u_\theta u_r}{r}, \quad (10)$$

$$e \frac{\partial \phi_r}{\partial r} = T_e \frac{\partial \ln n_r}{\partial r} + eB u_\theta - m_e \frac{u_\theta^2}{r}. \quad (11)$$

Therefore, the axial model determines the set $(n_z, n_n, u_z, u_n, \phi_z)$, which depends only on z , while the radial model yields, at each z , the set $(n_r, u_r, u_\theta, \phi_r)$. Notice that equations for ϕ_z and ϕ_r are decoupled from the rest.

A. The radial model

The radial model is discussed in detail in Ref. 8. Dimensionless variables are r/R , $n_r/n_r(z, 0)$, $e\phi_r/T_e$, u_r/c_s , and u_θ/c_e , with $c_e = \sqrt{T_e/m_e}$ used for non-dimensionalizing u_θ instead of c_s . Boundary conditions at $r = 0$ are

$$u_r = u_\theta = \ln[n_r/n_r(z, 0)] = \phi_r = 0.$$

The extra condition $u_r = c_s$ at $r = R$ (i.e. the Bohm criterion at the sheath edge) determines the eigenvalue $\nu_w(z)$ in the functional form

$$\frac{\nu_w}{\omega_r} = \hat{\nu}_w \left(\frac{\omega_{lh}}{\omega_r}, \frac{\nu_{ion}}{\omega_r}, \frac{\nu_{en}}{\omega_r}, \frac{\nu_{ei0}}{\omega_r} \right) \quad (12)$$

with $\omega_r = c_s/R$ (the radial-transit frequency), $\omega_{lh} = eB/\sqrt{m_e m_i}$, $\nu_{ei0} = (R_{ei}n)_{r=0}$, $\nu_{en} = R_{en}n_n$, and $\nu_{ion} = R_{ion}n_n$; ion-neutral collisions are negligible in the regimes of interest here.

Reference 8 showed that the main magnetized regime corresponds to

$$\omega_{lh} \gg \nu_{en} + \nu_{ei} + \nu_{ion} + \nu_{in} \geq O(\omega_r).$$

Notice that the magnetized plasma condition $\omega_r/\omega_{lh} \ll 1$ is equivalent to $\ell_e/R \ll 1$, with ℓ_e the electron Larmor radius. In the magnetized regime the radial structure of the plasma column consists of a bulk diffusive region, a thin inertial layer (quasineutral and collisionless), and the thinner Debye sheath. For $\nu_e \equiv \nu_{en} + \nu_{ei} + \nu_{ion} = \text{const}$: the asymptotic universal solution for the bulk region is³⁰

$$\frac{n_r(z, r)}{n_r(z, 0)} = J_0 \left(a_0 \frac{r}{R} \right), \quad \frac{u_r}{c_s} = a_0 \frac{\nu_e \omega_r}{\omega_{lh}^2} \frac{J_1(a_0 r/R)}{J_0(a_0 r/R)}, \quad \frac{u_\theta}{c_e} = \frac{u_r \omega_{lh}}{c_s \nu_e}; \quad (13)$$

the inertial layer covers the range $u_r/c_s \sim \nu_e/\omega_{lh}$ to $u_r/c_s = 1$; and the plasma balance condition, Eq. (12), reduces asymptotically to

$$\nu_w = a_0^2 \frac{\omega_r^2}{\omega_{lh}^2} \nu_e, \quad (14)$$

with $a_0 \simeq 2.405$, the first-zero of the Bessel function of the first kind J_0 .

B. The axial model

After some manipulation, the set of Eqs. (3)-(7) yields

$$(c_s^2 - u_z^2) \frac{\partial u_z}{\partial z} = (u_z - u_n) u_z n_n (R_{in} + R_{ion}) + c_s^2 (n_n R_{ion} - \nu_w), \quad (15)$$

$$(c_s^2 - u_z^2) \frac{\partial n_z}{\partial z} = -n_z [u_z (n_n R_{ion} - \nu_w) - (u_z - u_n) n_n (R_{in} + R_{ion})], \quad (16)$$

$$n_n u_n \frac{\partial u_n}{\partial z} = n_z [u_n \nu_w (\alpha_w - 1) + (u_z - u_n) n_n R_{in}]. \quad (17)$$

Boundary conditions for these equations are imposed at the back-wall sheath edge B and the front exit E:

$$g_0 \text{ known}, \quad u_{nB} = u_{n0}, \quad u_{zB} = -c_s, \quad u_{zE} = c_s.$$

Non-dimensionalization with c_s , g_0 , and L yields that the axial solution depends on the following dimensionless parameters

$$L/L_\star, \quad R_{in,s}/R_{ion}, \quad u_{n0}/c_s, \quad \alpha_w,$$

plus the eigenfunction $\nu_w/(n_n R_{ion})$. Here

$$L_\star = c_s/(R_{ion} n_{n0})$$

is an effective ionization mean-free-path, quotient of the scaled ionization cross section R_{ion}/c_s (which depends only on T_e), and the neutral density $n_{n0} = g_0/u_{n0}$.

For thruster efficient operation, T_e and B are large enough to have

$$\nu_w/(n_n R_{ion}) \ll 1, \quad R_{in,s}/R_{ion} \ll u_{n0}/c_s \ll 1,$$

and (for $\alpha_w = 1$) the axial plasma flow admits the *ideal* (or perfect confinement) solution

$$u_n = u_{n0}, \quad \frac{u_z}{c_s} = \tan \xi, \quad \frac{n}{n_0} = 2\eta_u \cos^2 \xi, \quad \frac{n_n}{n_{n0}} = 1 - \eta_u \sin 2\xi, \quad (18)$$

$$\frac{z + L}{L_\star} = \int_{-\pi/4}^{\xi} \frac{1 - \tan^2 \xi'}{1 - \eta_u \sin 2\xi'} d\xi', \quad (19)$$

where $n_0 = g_0/c_s$ is a plasma reference density, ξ is an auxiliary variable, and $\eta_u = n_E/n_0$ coincides with the propellant utilization. Setting $z = 0$ at $\xi = \pi/4$ in Eq. (19) yields implicitly the relation $\eta_u(L/L_\star)$:

$$\frac{L}{L_\star} = \int_{-\pi/4}^{\pi/4} \frac{1 - \tan^2 \xi}{1 - \eta_u \sin 2\xi} d\xi. \quad (20)$$

Although the functions in Eq.(18) are symmetric with respect to ξ , the function $z(\xi)$ is not symmetric, the point $\xi = 0$ (where $u_{zi} = 0$ and n is maximum) being shifted towards the chamber rear wall.

III. PLASMA RESPONSE INSIDE THE CHAMBER

This section discusses the 2D spatial solution and the resulting performances of the plasma inside the chamber, in terms of the three main operation parameters: the magnetic field B , the gas flow \dot{m} , and the plasma temperature T_e (which will be later related to the absorbed power P_a). Although the discussion can be done in terms of dimensionless

parameters, for sake of clarity we have opted for presenting dimensional results. Thus, we consider a cylindrical chamber with $R = 1\text{cm}$ and $L = 10\text{cm}$, operating nominally with xenon, $B = 600\text{G}$, $\dot{m} = 0.1\text{mg/s}$, and $T_e = 10\text{eV}$. We also take $\alpha_w = 1$ and $u_{n0}/c_s = 0.07$. For these conditions the typical values of dimensionless parameters are $\omega_{lh}/\omega_r = 80$, $\nu_{en}/\omega_r \sim 10$, $\nu_{ei}/\omega_r \sim 3$, $\nu_w/n_n R_{ion} \sim 0.2$, $R_{in,s}/R_{ion} = 0.04$, and $L/L_\star = 3.7$.

A. 2D plasma profiles

Figure 3 plots profiles of main axial magnitudes for two magnetic intensities, 200G and 600G, and compare them with the ideal axial solution of Eqs. (18)-(19). Fig. 4 plots profiles of two radial magnitudes at the chamber rear wall ($z = -L$) and front exit ($z = 0$), for the same magnetic intensities, and compare them with the ideal radial solution of Eq. (13).

Figure 3(a) shows how the injected neutral flow is effectively depleted by ionization. In Fig. 3(b) we observe that the plasma density presents a positive gradient at the back of the chamber, caused by ionization, and then, a negative gradient, caused by ion acceleration. Fig. 3(c) shows the region of backward and forward plasma flow, with $u_{zi} = 0$ marking also the location of the maximum n_e . Observe that the ion back-streaming region occupies only a small part of the chamber; in contrast, the constant- n_n model of Ref. 27 yields symmetric profiles of axial variables around the chamber mid-section, $z = -L/2$. Figure 3(d) plots the effective electron-collision frequency, which decreases by a factor of 8 between the chamber back and front sections, because of the decrease of ν_{en} ($\nu_{en} \propto n_n$). As a consequence, the plasma is more magnetized near the chamber exit, which affects the radial profiles of Fig. 4 and the local wall recombination. In fact, electron collisionality is dominated by collisions with neutrals, near the back wall, and with ions, near the front exit. Figure 3(e) depicts the ratio between wall-recombination and ionization along the chamber, which defines the net plasma production along the chamber. Wall-recombination is moderate for 200G and small for 600G, which explains why the ideal axial solution [dashed line in Figure 3(a)-(c)] is almost indistinguishable from the exact 600G-solution.

The radial profiles plotted in Fig. 4 do not cover the near-axis region $r/R < 0.4$, where gradients of u_r are very small for high magnetization. The agreement of the exact so-

lution with the ideal radial solution is excellent for $B = 600G$ at the back-wall section. Otherwise, at the exit section, the dominance in ν_e of electron-ion collisions, which are proportional to the local n_e , make the radial profile more steepened than in the ideal solution. The profiles of u_r illustrate how a large magnetic confinement prevents developing large perpendicular velocities until the very vicinity of the wall. The same is true for the radial electric field, $-e\phi_r \simeq m_i u_r^2/2$, which is negligible outside the thin inertial layer, of thickness ℓ_e , preceding the Debye sheath.

Figure 5(a) and (b) plot, for 200G, $r - z$ contour maps of plasma density and velocity u_i . The constant-velocity lines are also good approximations for isopotentials. Plasma magnetization, even if moderate as here, tend to concentrate the gradients of the plasma flow around the lateral and rear walls of the chamber. Notice that the radial gradients of n in the bulk region are sustained not by the tiny radial electric field, but by the radial magnetic force generated by the azimuthal electron current. At the chamber exit, the plasma beam is radially-nonuniform and near-sonic.

If magnetic confinement is not large, plasma losses to the lateral wall are not negligible and the fraction of neutrals created from recombination is significant. These are injected back into the plasma with a lower energy than the recombined ions (a process known as accommodation) and not specularly, thus increasing the neutral thermal energy. Within our model framework, this neutral ‘heating’ cannot be reproduced accurately but still we can estimate the sensitivity of the solution to the properties of recombined neutrals by varying the parameter α_w in Eq. (17). Figure 6 compares the solution for three cases: $\alpha_w = 1$, which keeps u_n almost constant; $\alpha_w = 0$, which assumes that neutrals from recombination are injected back with zero energy; and $\alpha_w = 2$, which assumes that new neutrals keep some of the ion axial directed energy before recombination. Although the macroscopic neutral velocity is affected by recombination conditions, the profiles of plasma density (as well as other magnitudes) remain practically unaffected.

B. Chamber performance parameters

The two main parameters characterizing plasma production in the chamber are the *propellant utilization* and the *production efficiency*, defined, respectively, as

$$\eta_u = \frac{\dot{m}_{iE}}{\dot{m}}, \quad \eta_p = \frac{\dot{m}_{iE}}{\dot{m}_{iT}}, \quad (21)$$

where

$$\dot{m}_{iT} = \dot{m}_{iE} + \dot{m}_{iA} + \dot{m}_{iW}$$

is the total ion production rate in the chamber. This production is the sum of the ion mass flows at the chamber exit E, the back wall A, and the lateral wall W:

$$\dot{m}_{iE} = m_i \pi R^2 c_s n_E \quad \dot{m}_{iA} = \dot{m}_{iB} = m_i \pi R^2 c_s n_B, \quad \dot{m}_{iW} = m_i 2\pi R \int_0^L dz (n u_r)_{r=R},$$

respectively.

In the perfect confinement limit, the ideal law $\eta_u(L/L_\star)$, Eq. (20), plotted in Fig. 7(a), is indeed the scaling law for the propellant utilization in terms of L , n_{n0} and T_e . The high propellant utilization regime requires L/L_\star be large; for instance $L/L_\star \geq 2.5$ yields $\eta_u \geq 95\%$. Figure 7(b) plots the influence of a non-perfect confinement on η_u for different plasma temperatures. For each T_e -curve, its knee separates a low-confinement, low-ionization regime from the high-ionization regime. As \dot{m} is increased, the curves of Fig. 7(b) shift towards higher η_u [see Fig. 8 below]. The achievement of high η_u inside the chamber is mandatory for a plasma thruster to be competitive. Outside the chamber, the neutral density decreases and thus ionization drop quickly; in addition, downstream-produced ions acquire lower axial energy than chamber-created ones.

The production efficiency η_p measures the fraction of the produced plasma being ejected from the chamber and thus contributing efficiently to thrust. In the perfect confinement case and for a purely axial magnetic field, it would be $\dot{m}_W = 0$ and $\dot{m}_B = \dot{m}_E$, and the production efficiency would reach a meagre maximum of only 50%. Figure 7(c) plots the influence of T_e and B on η_p . The qualitative behaviour is similar to the case of η_u , with the curve knee separating the two regimes, and η_p tending to the limit $\simeq 50\%$ at high confinement. The production efficiency increases weakly with T_e (due to a decrease of electron-ion collisionality).

Figure 8(a) and (b) plot parametric curves $\eta_u(B, \dot{m}) = \text{const}$ and $\eta_p(B, \dot{m}) = \text{const}$ for two values of T_e . They allow us to determine optimal values of B and \dot{m} and to assess

the sensitivity of plasma production to these parameters. Notice that a high η_u requires minimum values of B and \dot{m} . If, additionally, we want to keep η_p close to its maximum of 50%, the optimal values of B and \dot{m} are near the knee of the curve $\eta_u(B, \dot{m}) = \text{const}$, which is also the region less sensitive to changes on the operational parameters. As T_e increases, the optimal values of B and \dot{m} decrease. Notice that for $B = \text{const}$ and \dot{m} increasing, η_u increases but η_p decreases.

Screening of the lateral wall by the axial magnetic field has been shown to make losses there negligible. At the same time, the lack of magnetic screening at the rear wall penalizes strongly η_p and thus thruster performances. The penalty is due to the plasma flow to the rear-wall being similar to the front-exit one and requiring re-ionization. This large loss would be avoided by screening the back wall too. Magnetic screening of both the rear and lateral chamber walls is feasible by appropriate design of the magnetic circuit (via either coils or permanent magnets) but redounds in a 2D magnetic topology, which again cannot be treated accurately within our model framework. Nonetheless, a quantitative assessment can be made for the limit of *large local* screening of the rear wall, by just assuming that the plasma backflow to that wall is negligible. This implies to impose the boundary condition $u_z(-L) = 0$ instead of $u_z(-L) = -c_s$. Figure 9(a) shows that the maximum density is at the back wall, indicating that the forward-flow region $u_z > 0$ occupies the whole chamber. Since for a non-screened back wall, the back-streaming region was already short, the global changes on the 2D plasma response are small, but, as Fig. 9(b) confirms, screening of the rear-wall typically doubles the production efficiency, which can now approach 100%.

IV. THRUST

A. Matching chamber and nozzle models

The 2D chamber model can be matched now to the 2D divergent nozzle model of Ahedo and Merino³¹. This model assumes a collisionless, non-subsonic plasma, which fits well with the plasma exiting the chamber if, as desired, $\eta_u \approx 1$ and the plasma is hot (say $T_e > 10\text{eV}$). Still there is a mismatching between the two models, caused by the plasma flow not fulfilling a regular sonic transition at section E: at present, the chamber model

ends with a singular sonic flow, and the nozzle model starts with a slightly supersonic flow (typically with a Mach number ≈ 1.01). An additional mismatching, caused by the limit $\ell_e/R = 0$ assumed in the nozzle model, is that the thin inertial layer next to the chamber lateral wall is neglected in the nozzle, which, in our computations, means a 2-3% loss in mass flow. In total, we estimate that the two mismatchings yield an error below 5%. The shape of the wall-less magnetic nozzle, $r = R_V(z)$ with $R_V(0) = R$, sketched in Fig. 1, corresponds to the plasma/vacuum edge V. Two-dimensional profiles of the supersonic plasma expansion are discussed in Ref. 10.

At present, the nozzle model cannot be extended into the far-downstream region because two important issues, the plasma/nozzle detachment and the vanishing of the electric field, are not solved fully yet^{20,22}. Thus, in order to close the problem in a reasonable way, an isolated (metallic) plate, represented by P in Fig. 1, will mark here the end of the nozzle region. The plate is located at a distance L_n from the chamber exit and collects the plasma beam (without reinjecting it). Surface D in Fig. 1 is the edge of the Debye sheath developing in front the plate. Observe that the plate is not merely an artefact, it could model a material surface for processing³², a plasma momentum flux sensor for indirect thrust measurement^{33,34}, or the downstream wall of the vacuum chamber.

Both B_0 and \dot{m} have an important role on chamber performances, as we have shown before, but they have a minor role on the plasma expansion in the nozzle. Therefore, in this and the next section, B_0 and \dot{m} are fixed to their nominal values of 600G and 0.1mg/s, and the discussion of thruster performances is focused on the the influence of T_e and the nozzle length L_n .

B. Thrust contributions

Adding for the three species, the momentum flux equation of the whole plasma is

$$\nabla \cdot \bar{\bar{M}} = e(n_e - n_i)\nabla\phi - en_e\mathbf{u}_e \times \mathbf{B}, \quad (22)$$

where

$$\bar{\bar{M}} = \sum_{j=i,e,n}(m_j n_j \mathbf{u}_j \mathbf{u}_j + p_j \bar{\bar{I}})$$

is the plasma momentum flux tensor. The axial momentum flow across section $z = \text{const}$ is

$$F_z(z) = 2\pi \int_0^{R_V(z)} dr r M_{zz}(z, r) \quad (23)$$

with $R_V(z) = R$ inside the chamber.

Physically, the thrust F is the net backwards force exerted by the whole plasma on the thruster. This (axial) force is the sum of three different contributions, namely,

$$F = F_{pres} - F_{elec} + F_{mag}. \quad (24)$$

Here:

$$F_{pres} = F_{zA} - D_W, \quad (25)$$

is the axial dynamic pressure of the plasma at the chamber walls, with $F_{zA} = F_z(-L)$ and $D_W = \pi R^2 m_i \int_{-L}^0 dz n_z \nu_w (u_{zi} - \alpha_w u_n)$;

$$F_{elec} = \pi \epsilon_0 \int_0^R dr r \left(\frac{d\phi}{dz} \right)_A^2 \quad (26)$$

is the axial electric force between the positive electric charge in the sheath AB and the negative electric charge at the back wall (ϵ_0 is the vacuum dielectric permittivity); and

$$F_{mag} = 2\pi \int_0^{L_n} dz \int_0^{R_V(z)} dr r (-j_\theta) B_r \quad (27)$$

is the axial magnetic force of the azimuthal plasma current on the thruster magnetic circuit, here expressed as the reaction force of the applied magnetic field on the plasma currents, j_θ .

For our simple geometric configuration

$$F_{cham} = F_{pres} - F_{elec}$$

is the chamber (or internal) thrust²⁸, while the magnetic thrust, F_{mag} , is exclusively external thrust. Particularizing $F_z(z)$ at sections A, B, E, and D yields the relations between the plasma momentum flow and the different contributions to thrust:

$$\begin{aligned} F_{zB} &= F_{zA} - F_{elec}, \\ F_{zE} &= F_{zB} - D_W = F_{cham}, \\ F_{zD} &= F_{zE} + F_{mag} = F. \end{aligned} \quad (28)$$

The chamber thrust depends on the plasma temperature, $F_{cham}(T_e)$. For $B = 600G$, when lateral wall screening is large, the plasma ‘drag’ on the lateral wall is negligible: $D_w/F_{cham} \simeq 0.01$. On the contrary, the negative contribution of the electric force is significant: taking $F_{pres} \simeq F_{zA}$ and the well-known Debye sheath solution for a floating wall, one has

$$\frac{F_{elec}}{F_{pres}} \simeq 1 - \frac{F_{zB}}{F_{zA}} \simeq 1 - \frac{2}{\sqrt{1 + \ln(m_i/(2\pi m_e))}} \simeq 0.38,$$

the last numerical value being for argon. Notice that if wall secondary-electron emission is important, F_{elec} decreases but F_{cham} does not change.

The magnetic thrust depends on both T_e and L_n , but the ratio

$$\kappa_F = F_{mag}/F_{cham},$$

shown in Fig. 10(a) –and called κ_{noz} in Ref. 20–, is nearly-independent of T_e (except for the weak dependence of ion magnetization on T_e), monotonic with L_n , and tending asymptotically to about 1. Therefore, we can write

$$F(T_e, L_n) \simeq F_{cham}(T_e) [1 + \kappa_F(L_n)]. \quad (29)$$

As an illustration, Fig. 11(a) plots the thrust of our simulated thruster versus the nozzle length and the plasma temperature. Recent experimental measurements on a HPT¹⁷ yield values of κ_F about 0.4-0.7 which agrees well with the results of Fig. 10(a).

It is worth to observe that the net force exerted by the plasma beam on the downstream plate P, F_{plate} , is the dynamic pressure on the plate *minus* the electric force due to positive electric charge in the adjacent Debye sheath,

$$F_{elec,P} = \pi\epsilon_0 \int_0^{R_V(L_n)} dr r (d\phi/dz)_P^2.$$

Thus one has

$$F_{plate} = F_{zP} + F_{elec,P} = F_{zD} = F. \quad (30)$$

This equivalence between the thrust on the thruster and the plasma force on a downstream plate has been validated experimentally, the average discrepancy being a 2%³⁴. Notice that the equivalence is valid as long as (i) the plate presence does not modify substantially the upstream plasma beam, and (ii) there is no thrust contribution of the beam downstream of the plate location. This last condition requires to know well the plasma behavior far-downstream, which is still an open problem.

The monotonic behavior of $\kappa_F(L_n)$ means that, for given T_e , the total thrust and the plasma momentum flow increase with the length of the nozzle region, Fig. 11(a). The question to be solved in the next Section is whether that increment of plasma momentum flow with L_n comes from an enhancement of the thrust efficiency or an increment on the power P_a to be deposited into the plasma.

V. THRUST EFFICIENCY

A. Energy balance

The energy equation determines the plasma temperature T_e in terms of the plasma absorbed power P_a , which is the dominant contribution to the energy balance of the discharge. Instead, Fruchtman et al.²⁷ claim that the power (i.e. energy) balance determines the plasma density, n , an assertion that we find incorrect: n is indeed determined mainly by the mass flow \dot{m} , as the dimensionless solution for n/n_0 , with $n_0 = \dot{m}/(m_i\pi R^2 c_s)$, of Sec. III shows clearly. Also, the setting of T_e in the present externally-heated discharge is totally different to the one taking place in a near-quiescent, self-sustaining glow discharge³⁵, where the mass balance between volumetric ionization and wall recombination, yields T_e as a function of $n_n R$ and the magnetic strength; in fact that function is Eq. (12) for the case $\nu_w \equiv n_n R_{ion}$.

The assumption of electron isothermality has the advantage that a *global* energy balance relates easily P_a to the rest of discharge parameters. The discussion of the energy balance will be restricted here to the relation among P_a , T_e and L_n , for given values of B , \dot{m} , R , and L .

The energy equation for the plasma, grouping contributions from all species can be expressed as

$$\nabla \cdot \dot{\mathbf{P}} = \mathbf{j} \cdot \mathbf{E} + \dot{P}_a - \dot{P}_{ion}. \quad (31)$$

Here:

$$\dot{\mathbf{P}}(z, r) = \frac{n_n}{2} m_i u_n^2 \mathbf{u}_n + \frac{n}{2} [m_i u_i^2 \mathbf{u}_i + (m_e u_{\theta e}^2 + 5T_e) \mathbf{u}_e] + \mathbf{q}_e \quad (32)$$

is the plasma power density, with \mathbf{q}_e the electron heat flux; \dot{P}_a is the absorbed power density; and

$$\dot{P}_{ion} = E'_{ion} n n_n R_{ion} \equiv \nabla \cdot (E'_{ion} n \mathbf{u}_i)$$

groups energy losses due to ionization and excitation, with $E'_{ion}(T_e)$ an effective ionization energy defined in the Appendix. In the nozzle, the contribution of neutrals to $\dot{\mathbf{P}}$, Eq. (32), is negligible and the contribution of the electron azimuthal energy $m_e u_{\theta e}^2/2$ must be kept small for the nozzle model being consistent^{10,21}; in the simulations to follow it will be kept below 10%.

Making use of $\nabla \cdot \mathbf{j} = 0$, the work of the electric field satisfies $\mathbf{j} \cdot \mathbf{E} = -\nabla \cdot (\phi \mathbf{j})$ and the energy equation takes the conservation form

$$\nabla \cdot \left[\dot{\mathbf{P}} + E'_{ion} n \mathbf{u}_i + \phi \mathbf{j} \right] = \dot{P}_a. \quad (33)$$

Integrating this equation over the whole plasma domain, limited by chamber walls A and W, the nozzle/vacuum edge V, and the downstream plate P, the energy conservation balance can be expressed as

$$P_{ion} + P_{wall} + P_{beam} = P_a. \quad (34)$$

On the right-hand side, the contributions of ionization (plus radiation), wall heating, and downstream beam are

$$\begin{aligned} P_{ion} &= E'_{ion} \dot{m}_{iT} / m_i, \\ P_{wall} &= P_W + P_A, \\ P_{beam} &= P_P, \end{aligned} \quad (35)$$

respectively. Here

$$\begin{aligned} P_W &= P_Q = 2\pi R \int_{-L}^0 dz \mathbf{1}_z \cdot \dot{\mathbf{P}}(z, R), \\ P_A &= P_B = -2\pi \int_0^R dr r \mathbf{1}_z \cdot \dot{\mathbf{P}}(z_B, r), \\ P_P &= P_D = P_E = 2\pi \int_0^{R_V(z_D)} dr r \mathbf{1}_z \cdot \dot{\mathbf{P}}(z_D, r), \end{aligned} \quad (36)$$

represent radial and axial energy flows at different surfaces. The equalities $P_A = P_B$, $P_Q = P_W$, and $P_D = P_P$ express that there is no energy spent by the current-free plasma in sheaths AB, QW, and DP, just an energy transfer from electrons to ions. Then, the equality $P_E = P_D = P_{beam}$ also means that there are no energy sources in the nozzle.

The chamber model determines $P_{ion}(T_e)$ and $P_{wall}(T_e)$. Then, the nozzle model yields

$$P_{beam} = P_i(z) + P_e(z) = \text{const}, \quad (37)$$

with

$$\begin{aligned} P_i(z) &= \pi \int_0^{R_V(z)} dr r n m_i u_i^2 u_{zi}, \\ P_e(z) &\simeq \pi \int_0^{R_V(z)} dr r (5T_e + 2q_{ze}); \end{aligned} \quad (38)$$

$m_e u_\theta^2 \ll 2T_e$ was assumed. Equation (37) expresses the transfer of electron ‘internal’ energy to ion ‘kinetic’ energy along the nozzle.

The nozzle model determines $P_i(z)$, with $P_i(0)$ corresponding to the sonic ion flow at section E. In fact and as for κ_F , the ratio

$$\kappa_P = P_i(z)/P_i(0) - 1$$

is almost independent of T_e (constant), and the parametric dependence of the ion power can be expressed as

$$P_{iD}(T_e, L_n) \simeq P_{iE}(T_e)[1 + \kappa_P(L_n)]. \quad (39)$$

Figure 10(b) plots $\kappa_P(L_n)$, which is approximately proportional to the square of the local r -averaged Mach number in the nozzle; thus $\kappa_P = 10$ corresponds to a Mach number of ≈ 3 .

The electron energy flow is the sum of enthalpy and heat flows. For $T_e = \text{const}$, the enthalpy flow, $(5/2)T_e \dot{m}_{iE}/m_i$, is constant along the nozzle, and the non-zero electron heat flux, q_{ze} , can be determined directly only at the plate sheath edge D. The fluid-to-kinetic correspondence for energy fluxes (of a near-Maxwellian population) at the edge of a collisionless sheath yields³⁶

$$\frac{5}{2}T_e n u_{ze} + q_{ze} = \left(2 + \frac{1}{2} \ln \frac{m_i}{2\pi m_e}\right) T_e n u_{ze}, \quad (40)$$

and integrating on section D

$$P_{eD}(T_e) = \left(2 + \frac{1}{2} \ln \frac{m_i}{2\pi m_e}\right) T_e \frac{\dot{m}_{iE}}{m_i}. \quad (41)$$

Substituting Eqs. (39) and (41) in Eq. (37), the parametric dependence of the beam power becomes

$$P_{beam}(T_e, L_n) = P_{eD}(T_e) + P_{iE}(T_e)[1 + \kappa_P(L_n)]. \quad (42)$$

Since $P_{iE} \simeq T_e \dot{m}_{iE}/(2m_i)$, one has

$$P_{iE}(T_e)/P_{eD}(T_e) \simeq \left(4 + \ln \frac{m_i}{2\pi m_e}\right)^{-1},$$

so, at the chamber exit, only a small fraction (about one-fifteenth for argon) of the plasma energy is deposited on the (sonic) ion flow.

Returning to the energy balance, Eq. (34), the absorbed power P_a required to create and expand a plasma of temperature T_e along a nozzle of length L_n satisfies the functional relation

$$P_a = P_{ion}(T_e) + P_{wall}(T_e) + P_{beam}(T_e, L_n) \quad (43)$$

(for B and \dot{m} given). Figure 11 (b) plots $P_a(L_n)$ for different plasma temperatures. For T_e given, one has

$$P_a(L_n) - P_a(0) = P_{iD}(L_n) - P_{iE} = P_{eD}(0) - P_{eD}(L_n).$$

Therefore, for given T_e , the increase of absorbed power with L_n is supplied to the beam at the chamber exit as an increase of the electron heat flow. On the contrary, if the absorbed power is kept constant, and the plate location is moved, it is evident from Fig. 11(b) that, as L_n increases, the plasma temperature (determined globally) decreases. The isothermal electron model and its consequences are further discussed below.

B. Partial efficiencies

Thrust efficiency is defined as

$$\eta = F^2/2\dot{m}P_a. \quad (44)$$

Figure 11(c) shows that thrust efficiency is enhanced when either T_e or L_n are increased; both cases imply an increase of the absorbed power. For our present thruster and plasma model, thrust efficiency remains below 30%. In order to understand this relatively modest performance figure, we evaluate next how the different phenomena taking place on the plasma affect the thrust efficiency.

Thrust efficiency is based on magnitudes external to the plasma discharge, which facilitates its computation. Alternatively, plasma beam properties are used by Sutton³⁷ in the definition of the thruster internal efficiency,

$$\eta_{int} = P_{ziD}/P_a, \quad (45)$$

with

$$P_{ziD} = \pi \int_0^{R_V(L_n)} dr r n m_i u_{zi}^3(L_n, r)$$

the flow of ion axial kinetic energy at final section D. The two efficiencies coincide only if the beam expansion is complete. The internal efficiency can be factorized as

$$\eta_{int} = \eta_{cham}\eta_{con}\eta_{div}, \quad (46)$$

with

$$\begin{aligned} \eta_{cham} &= P_{beam}/P_a \equiv 1 - \epsilon_{ion} - \epsilon_{wall}, \\ \eta_{con} &= P_{iD}/P_{beam}, \\ \eta_{div} &= P_{ziD}/P_{iD}, \end{aligned} \quad (47)$$

partial efficiencies related to chamber processes, internal-to-kinetic energy conversion in the nozzle, and the beam or plume divergence, respectively; $\epsilon_{ion} = P_{ion}/P_a$ and $\epsilon_{wall} = P_{wall}/P_a$, are the relative losses due to ionization and wall heating.

Figure 12(a) shows for a long nozzle ($L_n/R = 30$) the dependence on T_e of ϵ_{ion} , ϵ_{wall} , η_{int} , and η ; the two other efficiencies are independent of T_e , being $\eta_{con} \simeq 0.44$ and $\eta_{div} \simeq 0.95$. The back wall contributes the most to ϵ_{wall} and its increase with T_e is due to $P_{wall} \propto T_e^{3/2}$. The decrease of ϵ_{ion} when T_e increases is due to the transition to the high-ionization region and the decrease of excitation collisions. The positive difference between η and η_{int} for large T_e is due to the electron contribution to thrust not having a correspondence on η_{int} ; the negative difference at low T_e is due to the poor propellant utilization. Figure 12(b) plots the same partial efficiencies versus the absorbed power instead of T_e . The difference between both groups of curves is summarized in the fact that increments of P_a are spent in ionizing more gas, at low power, and in heating the plasma, at high power.

Figure 12 yields that the maximum thrust efficiency of our modeled thruster is below 30%. We are now in conditions to identify the main causes reducing efficiency (excepting, of course, those related to plasma-wave interaction). First, it is clear that the thruster must operate in the high ionization regime. For instance, for $L_n/R = 30$ and $P_a = 150\text{W}$, ionization-plus-radiation losses amount only to a 10% of the efficiency loss, according to Fig. 12(b). The same Figure states that a 30% of the efficiency loss is due to energy losses at the chamber back-wall. Therefore, screening adequately that wall (without affecting much the rest of the chamber) would yield $\eta_{cham} \sim 80\%$ instead of 60%. The rest of efficiency losses takes place in the nozzle. First, the beam-divergence efficiency is excellent ($\eta_{div} \simeq 95\%$), but this can be due to the limited extension of our nozzle region.

Further studies on the plasma detachment region are needed to confirm the behavior of η_{div} . Second, the efficiency loss caused by the conversion of electron-to-ion energy is poor, $\eta_{con} \simeq 44\%$. This result is very dependent on the electron equation of state we have assumed, so a discussion on this subject is very pertinent.

C. On the electron equation of state

An isothermal electron population has been assumed here for both chamber and nozzle models. Isothermality was used in previous 1D magnetic-nozzle models⁹ and the (isothermal) Boltzmann relation is very often invoked in plasma plume models³⁸. Except for the small drift flows into the chamber walls and the downstream plume, electrons constitute a population well confined both electrostatically and magnetically. This promotes that, in a stationary situation, electrons are not far from thermodynamic equilibrium thus supporting isothermality.

Fruchtman et al.²⁷, who study only the chamber region of a HPT, assume isothermality inside the chamber, but impose an adiabatic condition (i.e. zero heat flow) at the chamber exit. This would be consistent with an adiabatic expansion of the plasma beam along the magnetic nozzle, similar to the one taking place for a hot dense gas in a solid nozzle³⁷. However, the plasma beam of a HPT is tenuous and high-collisionality cannot be claimed to support local thermodynamic equilibrium and isentropic expansion.

The choice isothermal versus adiabatic has important consequences on the downstream plasma expansion, the energy balance, and the thruster internal efficiency. For an isothermal, collisionless magnetic nozzle, we have found that: the ambipolar electric potential decreases without bound (as L_n increases); the electron enthalpy flow is constant along the nozzle, while the electron heat flow at the chamber exit increases as L_n increases (in order to balance the total gain of ion kinetic energy in the nozzle); and the electron-to-ion energy conversion efficiency is poor.

On the contrary, from the similarity with hot-gas physics, in the adiabatic expansion of a collisional plasma, one would have that: the ambipolar electric field tends to zero downstream; the electron heat flow at the chamber exit and within the nozzle is zero; the gain in ion energy is balanced by the decrease of the electron enthalpy; and the energy conversion efficiency is high. A welcome consequence of adiabaticity is that the beam power

is known independently of the expansion in the nozzle^{27,39}: $P_{beam}(T_e) \simeq 3T_e \dot{m}_{iE}/m_i$. Figure 9 of Ref. 39 shows graphically the relation $P_a(T_e)$ in the adiabatic limit.

Although the non-local character of the electron energy transport in our isothermal model is more suitable for a near-collisionless population, we acknowledge that both limit cases, isothermal and adiabatic, are crude models for the equation of state of a collisionless electron population. Indeed, there is some experimental evidence of plasma cooling in magnetized and unmagnetized plumes^{38,40}. Also, non-local collisionless cooling of electrons has been studied theoretically with a quasi-1D time-dependent model by Arefiev and Breizman⁴¹. Cooling would be caused by the partial depletion of a Maxwellian distribution function along a divergent magnetic nozzle with a traveling rarefaction wave acting as downstream ‘reflection boundary’. Martínez-Sánchez and Ahedo⁴², analyzed the partially equivalent problem of a steady-state quasi-1D ion flow in a convergent magnetic geometry, and indeed obtained spatially-varying *parallel* and *perpendicular* temperatures and *non-zero* heat flows. These two works show the way for analyzing non-local collisionless cooling of electrons and the corresponding equation of state in a 2D stationary divergent flow.

VI. CONCLUSIONS

A 2D fluid model of the plasma flow inside the magnetized chamber of a helicon thruster has been developed, with assumptions based on expected ranges of plasma density and temperature. Ionization, confinement, and 2D plasma flow have been discussed in terms of design and operational parameters, i.e. chamber dimensions, injected gas flow, magnetic field strength, and plasma temperature, the last one a function of the plasma absorbed power. Analytical solutions for an ideal, near-collisionless plasma have been derived, and provide simple scaling laws for the plasma parametric response. Optimal values of design and operational parameters that maximize propellant utilization and production efficiency have been investigated.

The chamber model has then been matched with an existing nozzle model. The whole model provides a complete picture of the fluiddynamic processes of the plasma discharge in a helicon thruster (heating, generation, confinement, and acceleration) and the capability of assessing thruster performances, such as thrust, power balance, and thruster efficiencies,

assuming isothermal electrons. In particular, the analysis of the momentum and energy equations of the whole plasma has determined (i) the thermal, electric, and magnetic contributions to thrust, (ii) the power conversion between ions and electrons in chamber and nozzle, and (iii) the power distribution among beam power, ionization losses, and wall losses.

Thrust and internal efficiencies have been evaluated, obtaining maximum values below 30% for the cases simulated here. The main causes of inefficiency are two: the deficient magnetic screening of the chamber walls (mainly the rear wall for a near axial magnetic field) and the incomplete plasma expansion in the nozzle (at least for isothermal electrons).

Indeed, that expansion depends on the thermodynamics of collisionless electrons in the nozzle divergent geometry, which is bad known and thus constitutes the most uncertain aspect when determining thruster performances. Isothermal and polytropic equations of state are shown to yield rather different plasma responses. For an isothermal flow, we were forced to place a downstream collecting plate in order to close the energy balance, and the plasma temperature depends on both the absorbed power and the nozzle region length. Far downstream plasma response is also affected by plasma/nozzle detachment.

A complete model of the plasma discharge in a helicon thruster will match the present fluiddynamic model with a 2D model of the wave-plasma interaction and energy transfer. It is known from simple wave-plasma models that antenna-plasma coupling is more efficient within particular ranges of plasma density and magnetic strength and can be more critical for helicon thruster operation than the thrust efficiency analyzed here. The wave-plasma interaction model should also assess whether (or under which conditions) suprathermal electrons are created. This can be instrumental in the formation of double-layer class structures in the supersonic plasma flow.

Finally, in search of tractability, several simplifications have been adopted in the fluid model, such as the 1D magnetic topology in the chamber, the absence of double-charged ions (which are not insignificant in the expected range of T_e), and the approximate separation between radial and axial dynamics. These limitations should not alter the main trends of the plasma response here but reduce the accuracy of the results. Their overcoming requires presumably to opt for particle-in-cell or hybrid schemes, instead of fluid ones, as it has been already the case with other plasma thrusters^{43,44}.

ACKNOWLEDGMENTS

The authors thank Mario Merino for providing plasma simulations of the magnetic nozzle stage. Partial versions of this work were presented in two Conference papers^{39,45}. The research has been sponsored by Spain's R&D National Plan (Project AYA-2010-61699) and FPU scholarship program. Additional support has been provided by the Air Force Office of Scientific Research, Air Force Material Command, USAF, under grant number FA8655-12-1-2043. The U.S Government is authorized to reproduce and distribute reprints for Governmental purpose notwithstanding any copyright notation thereon.

Appendix A: Collision rates

The expressions proposed below for the different collision rates are reasonable approximations for the purposes of this work. The rates for ionization, electron-neutral collisions, electron-ion collisions, and ion-neutral collisions are, respectively,

$$R_{ion}(T_e) = c_e \sqrt{\frac{8}{\pi}} \sigma_{ion} \left(1 + \frac{T_e E_{ion}}{(T_e + E_{ion})^2} \right) \exp\left(-\frac{E_{ion}}{T_e}\right), \quad (\text{A1})$$

$$R_{en}(T_e) = \sqrt{\frac{8T_e}{\pi m_e}} \sigma_{en}, \quad (\text{A2})$$

$$R_{ei}(T_e, n_e) = \left(\frac{T_e}{1 \text{ eV}}\right)^{-3/2} \frac{\ln \Lambda(T_e, n_e)}{10} \cdot 9.2 \cdot 10^{-13} \text{ m}^3 \text{ s}^{-1}, \quad (\text{A3})$$

with E_{ion} the first ionization energy. For ion-neutral collisions and $c_{in} = |\mathbf{u}_i - \mathbf{u}_n|$, we have

$$R_{in}(c_{in}) = c_{in} (k_2 - k_1 \log_{10} c_{in})^2, \quad (\text{A4})$$

which can be expressed as,

$$R_{in}(c_{in}) = R_{in,s}(T_e) \hat{c}_{in} (1 - a_1 \log_{10} \hat{c}_{in})^2, \quad (\text{A5})$$

with $\hat{c}_{in} = c_{in}/c_s$, $c_s = \sqrt{T_e/m_i}$, $R_{in,s} = R_{in}(c_s)$, and $a_1 = k_1(k_2 - k_1 \log_{10} c_s)^{-1}$. The constants involved in the above expressions are gas-dependent. For argon, we will take $E_{ion} = 15.76 \text{ eV}$, $\sigma_{ion} = 2.8 \cdot 10^{-20} \text{ m}^2$, $\sigma_{en} = 15 \cdot 10^{-20} \text{ m}^2$, $k_2 = 10.5 \cdot 10^{-10} \text{ m}$, and $k_1 = 1.67 \cdot 10^{-10} \text{ m}$.

For $T_e = \text{const}$ and a given gas, R_{ion} , R_{en} , and $R_{in,s}$ are constant; R_{ei} is a constant too if an average value is used for $\ln \Lambda(n_e, T_e)$. Observe that the non-linear expression used

for R_{in} correspond to the high-pressure case of Fruchtman et al.²⁷, but, even for this case, ion-neutral collisions will be found negligible in the desired operation range.

Excitation collisions are taken into account through the effective ionization energy $E'_{ion}(T_e) = E_{ion}\alpha_{ion}(T_e)$ and α_{ion} the ionization cost factor. From Dugan⁴⁶, a fitting formula for argon is

$$\alpha_{ion}(T_e) \approx 1.4 + 0.4 \exp(0.7 E_{ion}/T_e). \quad (\text{A6})$$

REFERENCES

REFERENCES

- ¹T. Ziemba, J. Carscadden, J. Slough, J. Prager, and R. Winglee, in *41th Joint Propulsion Conference & Exhibit*, AIAA 2005-4119 (2005).
- ²M. West, C. Charles, and R. Boswell, *Journal of Propulsion and Power* **24**, 134 (2008).
- ³O. Batishchev, *IEEE Transaction on Plasma Science* **37**, 1563 (2009).
- ⁴D. Pavarin et al, in *31th International Electric Propulsion Conference*, IEPC 2009-205 (2009).
- ⁵E. Ahedo, *Plasma Dynamics in a Helicon Thruster*, in *EUCASS Advances in Aerospace Sciences, Vol. IV: Progress in Propulsion Physics*, (L. DeLuca, C. Bonnal, O. Haidn, and S. Frolov, Eds., Torus Press, ISBN 978-2-7598-0876-2, 2013) pp. 337–354.
- ⁶K. Shamrai et al, in *42th Joint Propulsion Conference & Exhibit*, AIAA 2006-4845 (2006).
- ⁷D. Palmer et al, in *44th Joint Propulsion Conference & Exhibit*, AIAA-2008-4925 (2008).
- ⁸E. Ahedo, *Physics of Plasmas* **16**, 113503 (2009).
- ⁹S. Andersen, V. Jensen, P. Nielsen, and N. D’Angelo, *Phys. Fluids* **12**, 557 (1969).
- ¹⁰E. Ahedo and M. Merino, *Physics of Plasmas* **17**, 073501 (2010).
- ¹¹F. Chen, *Plasma Physics and Controlled Fusion* **33**, 339 (1991).
- ¹²R. Boswell, *Plasma Physics and Controlled Fusion* **26**, 1147 (1984).
- ¹³K. Shamrai and V. Taranov, *Plasma Physics and Controlled Fusion* **36**, 1719 (1994).
- ¹⁴M. Lieberman and A. Lichtenberg, *Principles of plasma discharges and materials processing* (Wiley-Blackwell, 2005).
- ¹⁵G. Parissenti et al, in *Proceedings of Space Propulsion 2010*, SP2010-1841086 (2010).
- ¹⁶E. Ahedo, *Plasma Physics and Controlled Fusion* **53**, 124037 (2011).
- ¹⁷K. Takahashi, T. Lafleur, C. Charles, P. Alexander, and R. Boswell, *Physical Review Letters* **107**, 235001 (2011).
- ¹⁸L. Williams, in *47th AIAA/ASME/SAE/ASEE Joint Propulsion Conference & Exhibit*, AIAA 2011-5893 (2011).
- ¹⁹S. Pottinger, V. Lappas, C. Charles, and R. Boswell, *Journal of Physics D: Applied Physics* **44**, 235201 (2011).

- ²⁰E. Ahedo and M. Merino, *Physics of Plasmas* **18**, 053504 (2011).
- ²¹M. Merino and E. Ahedo, *Physics of Plasmas* **19**, 083501 (2012).
- ²²M. Merino and E. Ahedo, in *48th AIAA/ASME/SAE/ASEE Joint Propulsion Conference & Exhibit*, AIAA-2012-3843 (2012).
- ²³E. Ahedo and M. Martínez-Sánchez, *Physical Review Letters* **103**, 135002 (2009).
- ²⁴E. Ahedo, *Physics of Plasmas* **18**, 033510 (2011).
- ²⁵M. Merino and E. Ahedo, *Physics of Plasmas* **20**, 023502 (2013).
- ²⁶E. Ahedo, J. Gallardo, and M. Martínez-Sánchez, *Physics of Plasmas* **10**, 3397 (2003).
- ²⁷A. Fruchtman, G. Makrinich, and J. Ashkenazy, *Plasma Sources Science and Technology* **14**, 152 (2005).
- ²⁸A. Fruchtman, *IEEE Transactions on Plasma Science* **36**, 403 (2008).
- ²⁹E. Ahedo, *Physics of Plasmas* **18**, 103506 (2011).
- ³⁰L. Tonks, *Physical Review* **56**, 360 (1939).
- ³¹M. Merino and E. Ahedo, in *Proceedings of Space Propulsion 2010*, SP2010-1841391 (2010).
- ³²K. Schoenberg, R. Gerwin, R. Moses, J. Scheuer, and H. Wagner, *Physics of Plasmas* **5**, 2090 (1998).
- ³³D. Chavers and F. Chang-Díaz, *Review of Scientific Instruments* **73**, 3500 (2002).
- ³⁴B. Longmier, B. Reid, A. Gallimore, F. Chang-Díaz, J. Squire, T. Glover, G. Chavers, and E. Bering III, *Journal of Propulsion and Power* **25**, 746 (2009).
- ³⁵R. Franklin, *Plasma phenomena in gas discharges* (Clarendon Press, Oxford, 1976).
- ³⁶E. Ahedo and D. Escobar, *Physics of Plasmas* **15**, 033504 (2008).
- ³⁷G. Sutton and O. Biblarz, *Rocket propulsion elements* (Wiley, 2010).
- ³⁸I. D. Boyd, *Journal of Spacecraft and Rockets* **38**, 381 (2001).
- ³⁹E. Ahedo, in *31th International Electric Propulsion Conference*, IEPC 2009-193 (2009).
- ⁴⁰K. Dannenmayer et al, in *48th AIAA/ASME/SAE/ASEE Joint Propulsion Conference & Exhibit*, AIAA-2012-4117 (2012).
- ⁴¹A. Arefiev and B. Breizman, *Physics of Plasmas* **15**, 042109 (2008).
- ⁴²M. Martínez-Sánchez and E. Ahedo, *Physics of Plasmas* **18**, 033509 (2011).
- ⁴³F. Parra, E. Ahedo, M. Fife, and M. Martínez-Sánchez, *Journal of Applied Physics* **100**, 023304 (2006).
- ⁴⁴F. Taccogna, S. Longo, M. Capitelli, and R. Schneider, *Contributions to Plasma Physics*

47, 635 (2007).

⁴⁵J. Navarro et al, in *48th AIAA/ASME/SAE/ASEE Joint Propulsion Conference & Exhibit*, AIAA-2012-3840 (2012).

⁴⁶J. Dugan and R. Sovie, Tech. Rep. NASA TN D-4150 (1967).

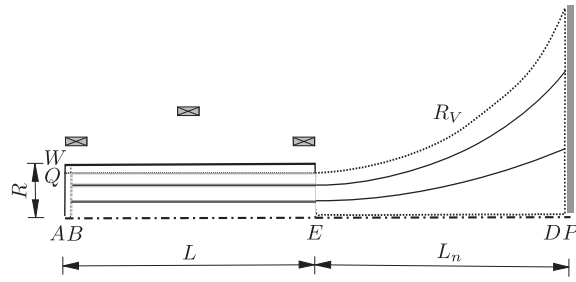


Figure 1. Sketch of the model (not done to scale).

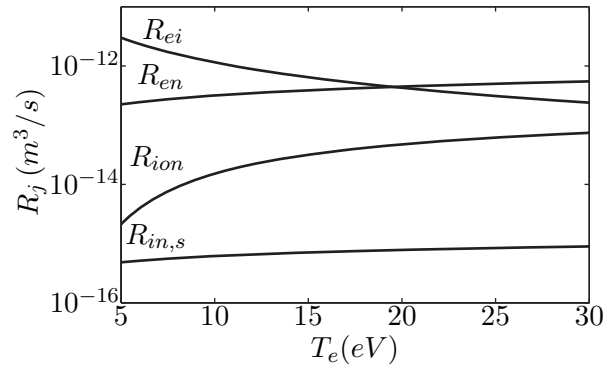


Figure 2. Ionization and collision rates, $R_j(m^3/s)$, for $j = ei, en, ion$ and (in, s) .

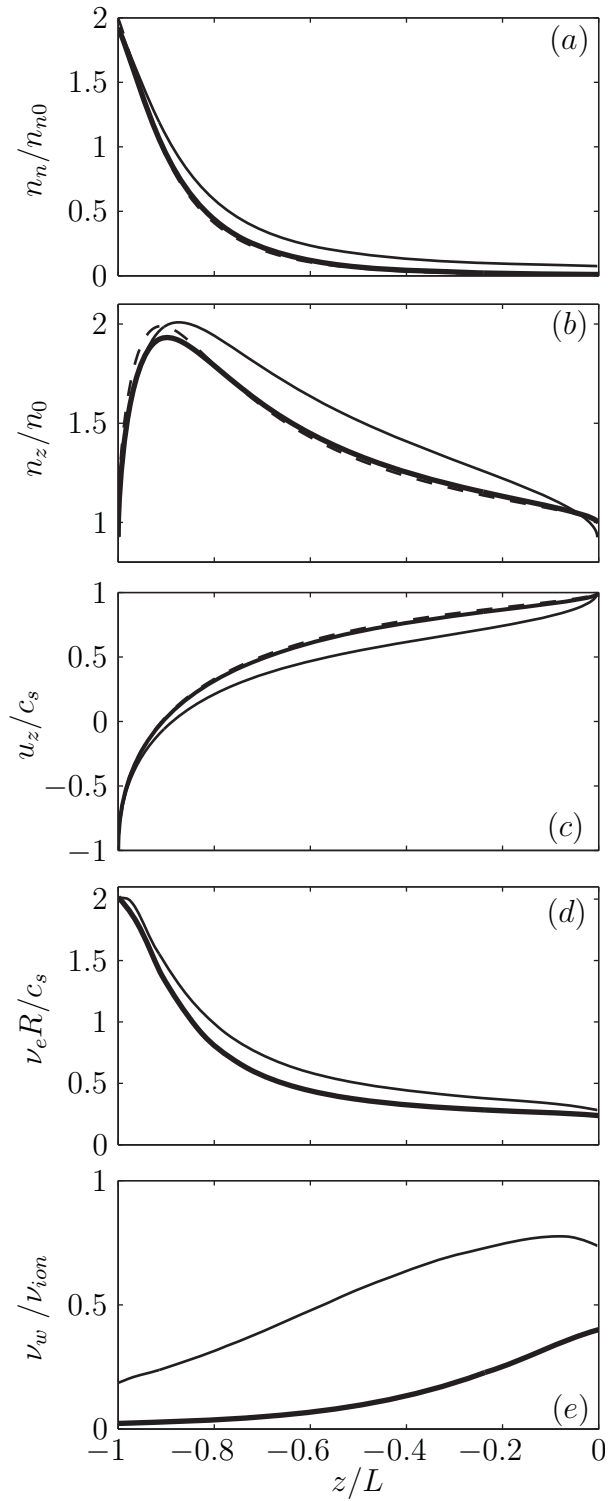


Figure 3. Dimensionless axial profiles inside the chamber of (a) neutral density, (b) plasma density, (c) plasma velocity, (d) radially-averaged electron collision frequency, (e) plasma recombination-to ionization ratio. Solid lines are for $B_0 = 600\text{G}$ (thick) and 200G (thin), and dashed lines are for the ideal axial solution. Normalization constants are defined in the main text.

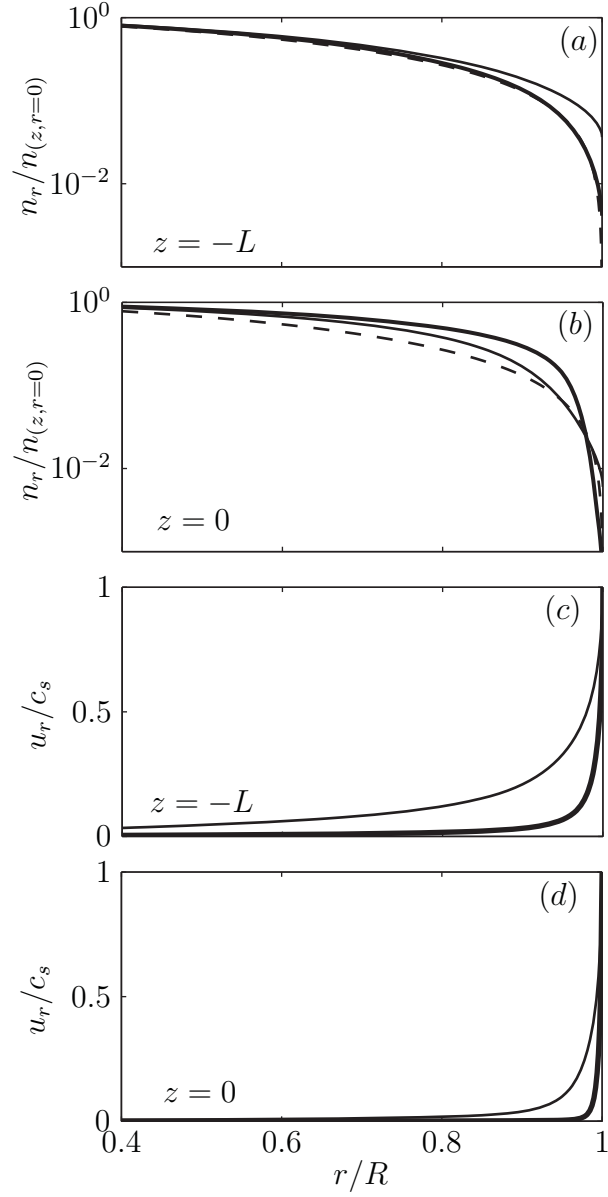


Figure 4. Dimensionless radial profiles inside the chamber of (a,b) plasma density and (c,d) radial velocity u_r/c_s , at (a,c) the rear wall, $z = -L$, and (b,d) the exit section, $z = 0$. Solid lines are for $B_0 = 600\text{G}$ (thick) and 200G (thin), and dashed lines are for the ideal radial solution. Normalization constants are defined in the main text.

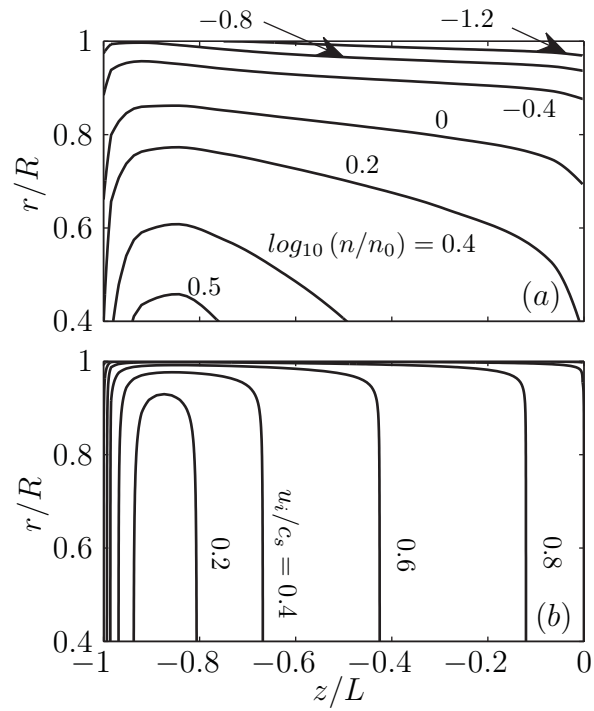


Figure 5. Two-dimensional maps inside the chamber of plasma (a) density and (b) velocity, for $B_0 = 200\text{G}$.

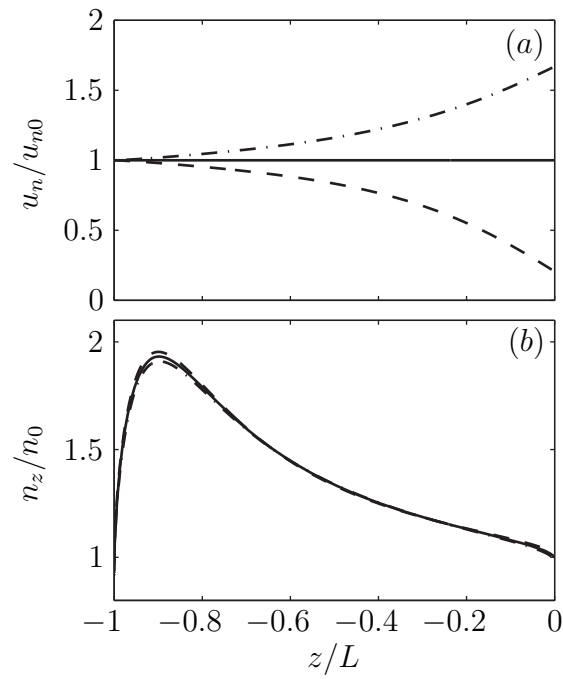


Figure 6. Axial profiles inside the chamber of neutral (a) velocity and (b) density, for different values of the re-emission velocity parameter: $\alpha_w = 1$ (solid), 0 (dashed), and 2 (dot-and-dash).

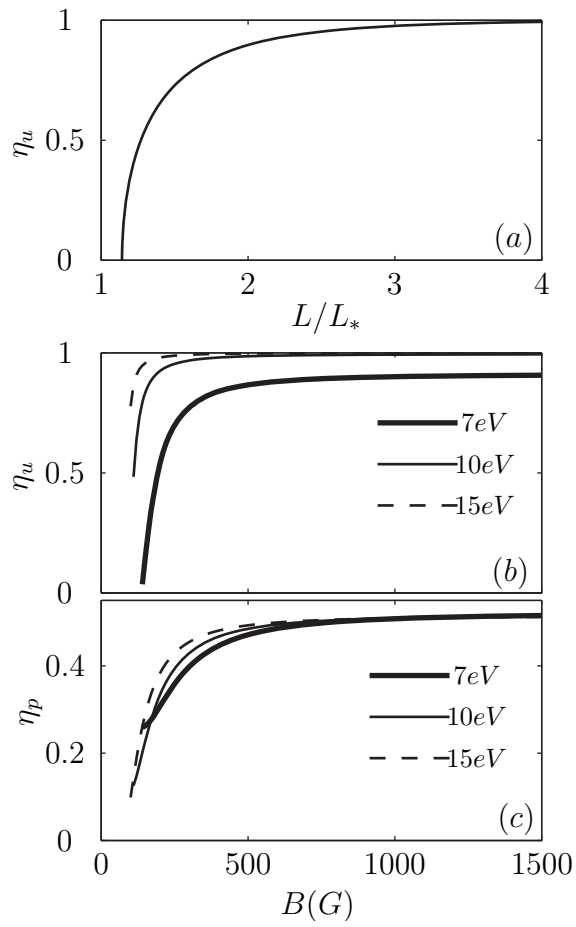


Figure 7. Parametric investigation of chamber performances. (a) Ideal scaling law for propellant utilization. (b) Propellant utilization and (c) production efficiency, in terms of B and T_e , for $\dot{m} = 0.1\text{mg/s}$.

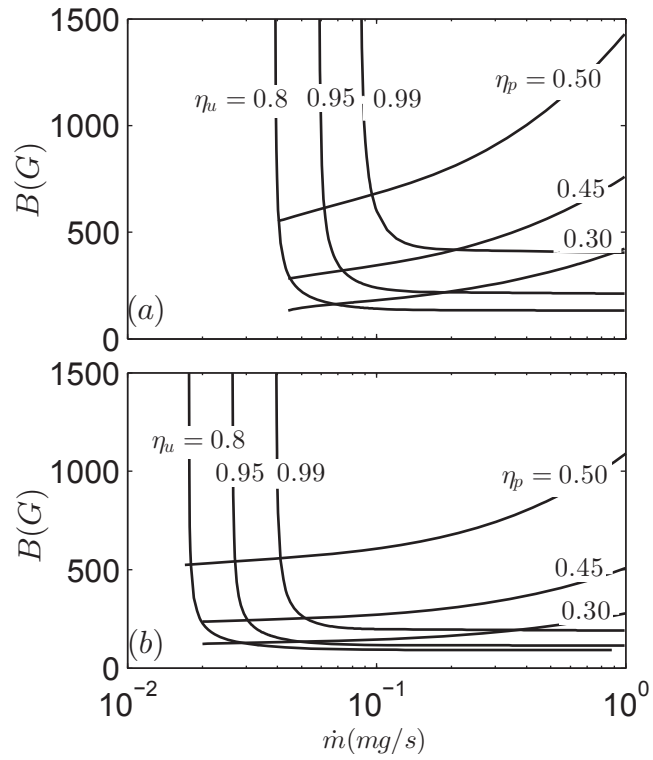


Figure 8. Constant-level contours of propellant utilization and production efficiency in the parametric plane $\dot{m} - B$ for $T_e = 10\text{eV}$ (a) and 20eV (b).

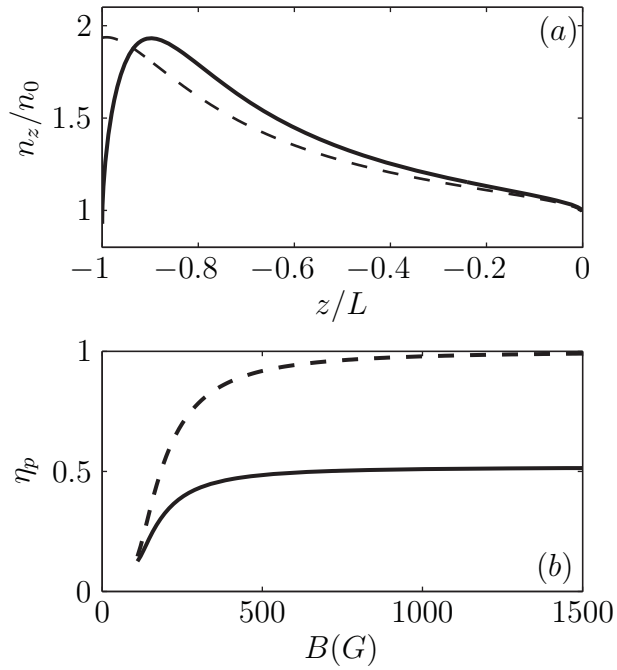


Figure 9. Effects of magnetic screening of the back-wall: (a) Axial profile of plasma density and (b) production efficiency versus axial magnetic field. Solid and dashed lines are for $u_{zB}/c_s = -1$ and 0, respectively, modeling zero and total magnetic screening.

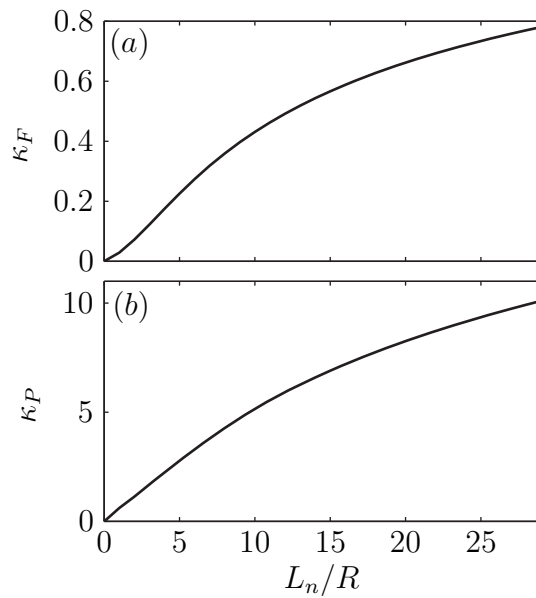


Figure 10. (a) Thrust gain and (b) ion-power gain, versus nozzle length.

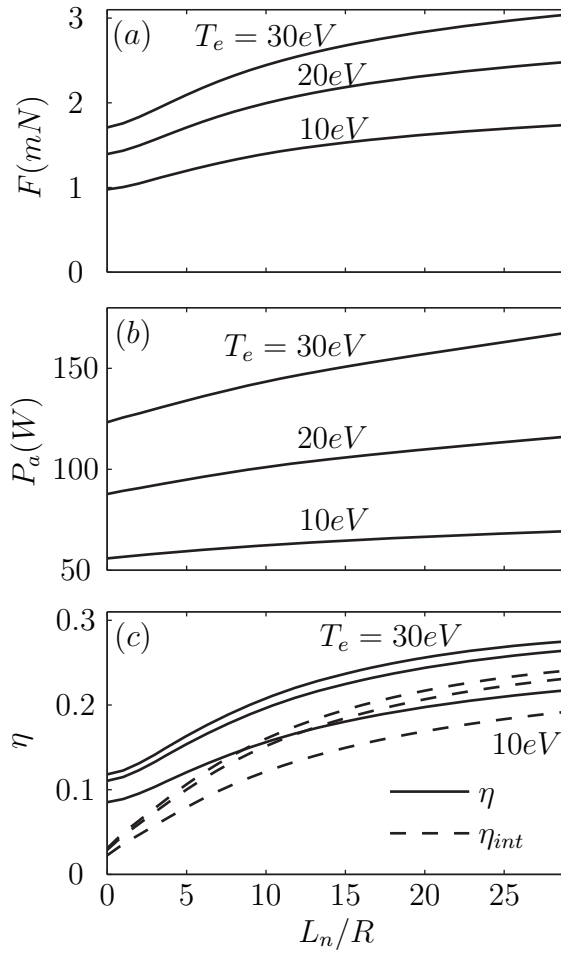


Figure 11. Influence of nozzle length and plasma temperature on (a) thrust, (b) required absorbed power, (c, solid) thrust efficiency, and (c, dashed) internal efficiency. In all figures, curves are for $T_e = 10eV$, $20eV$, and $30eV$; in (c) both η and η_{int} increase with T_e . Results are for $B = 600G$ and $\dot{m} = 0.1mg/s$.

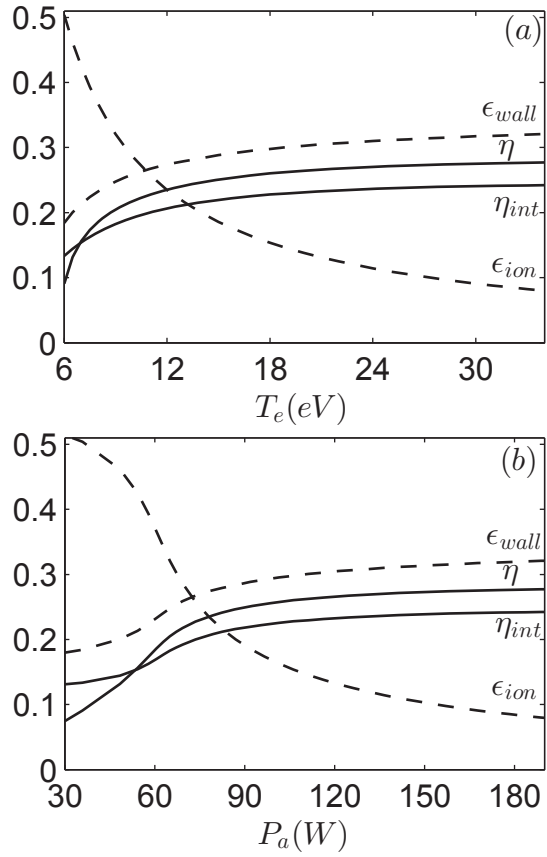


Figure 12. Dependence of (solid lines) thrust and internal efficiencies and (dashed lines) ionization and wall losses with (a) T_e and (b) P_a , for $L_n = 30\text{cm}$, $B = 600\text{G}$, and $\dot{m} = 0.1\text{mg/s}$.

PAGE INTENTIONALLY LEFT BLANK

Theory of Plasma Detachment in a Propulsive Magnetic Nozzle

Mario Merino and Eduardo Ahedo

ETS Ingenieros Aeronáuticos, Universidad Politécnica de Madrid, Madrid 28040, Spain

An axisymmetric model of the divergent propulsive magnetic nozzle demonstrates that demagnetization of mass-carrying ions is the key mechanism enabling inwards detachment of the supersonically-expanded plasma jet, even in the asymptotic limit of fully-magnetized electrons. In contrast, incipient electron demagnetization is detrimental for inwards beam detachment, and magnetic strength must thus be tuned to optimize both beam channeling and acceleration in the near region and detachment in the far region. It is shown that only a marginal fraction of the beam flows back, and that the divergence angle of the 95%-mass flow tube measures the effectiveness of detachment and permits comparisons with plumes of other plasma thrusters.

PACS numbers: 52.75.Di, 52.30.Ex, 52.59.Dk

Magnetically-channeled plasmas are fundamental in many applications, ranging from material treatment to fusion and space propulsion. In particular, several plasma thruster concepts[1–6] employ, as their acceleration stage, a longitudinal magnetic field to create a divergent magnetic nozzle (MN), which transforms the internal energy of the plasma into axially-directed kinetic energy, thus producing a highly supersonic plasma beam[7]. While the expansion of a plasma in a MN vaguely resembles that in a solid, de Laval nozzle[8], the central role of long-range forces in MNs sets them apart from their solid counterparts. First, a MN has the key advantage of operating in a contactless manner, thereby avoiding severe plasma losses and wall durability problems. Second, the expansion is far from quasi-one-dimensional[9], and depends strongly on the form and/or species in which the internal plasma energy is stored, which can be different in each particular device[10]. Lastly, there are significant differences in the processes of *thrust production* and *plasma detachment from the nozzle*.

The mission of any propulsive nozzle is to increment the delivered thrust. In a solid nozzle, the physical mechanism that enables this is the pressure exerted on the nozzle divergent walls. In a wall-less MN, as we showed theoretically[9] and Takahashi et al. later confirmed experimentally[5], thrust is of magnetic character. The magnetized plasma develops diamagnetic azimuthal currents on electrons that oppose those running in the thruster coils, thus creating two repelling magnetic forces: one yields positive thrust on the thruster, while the second one accelerates the plasma[11]. The MN contribution to the total thrust of the device is expected to be about 50% for a plasma jet emitted sonically by the source[9], and even a larger fraction if the plasma contains two disparate electron populations[12, 13].

There is ample consensus that the main uncertainty about the applicability of MNs in space propulsion is the ability of the plasma to detach from the closed magnetic lines[14]: once accelerated, it is imperative that the plasma beam releases itself from the magnetic field downstream and continues to expand freely into vacuum. Were

this not the case, the returning plasma would cancel the produced thrust and impinge on the delicate spacecraft surfaces.

Two important aspects to take into account when dealing with the detachment of a plasma jet are, first, that ions carry almost totally the plasma mass flow; and second, that a small backflow is unavoidable in any plasma plume expanding into vacuum. Therefore, the detachment problem must determine (*i*) which mechanism allows ion streamtubes to detach inwards from the magnetic lines and avoid flowing back; (*ii*) which fraction of the beam mass flow is backflowing; and (*iii*) how the efficiency of a MN in generating a high-energy, low-divergence beam is measured.

Prevailing detachment theories developed specifically for plasma thrusters with MN have focused on *electron detachment*, on the assumption that quasineutrality and current ambipolarity make ion and electron streamtubes coincide in a current-free plasma. In a first scenario, resistivity[15] or electron-inertia[16] would produce diffusive detachment of electron streamtubes. In a second scenario, the plasma-induced magnetic field would stretch the MN downstream[17]. Unfortunately, these three mechanisms do not lead to *inwards* electron detachment in a propulsive MN[11, 18]: electron diffusion detaches electron tubes *outwards* from the magnetic lines, and the magnetic field induced by diamagnetic plasma currents opposes the applied one, thus increasing the divergence of the resulting MN.

The goal of this Letter is to demonstrate that *ion inwards detachment* caused by ion demagnetization is the key mechanism for the detachment of a plasma jet in a propulsive MN, and that it takes place even in the fully-magnetized-electrons asymptotic limit. Additionally, it is shown that the divergence angle of the ion streamtube carrying, say, 95% of the ion/plasma mass flow is a direct measure of plasma detachment and allows a direct comparison of MN-based plumes with those of more conventional devices, such as ion or Hall-effect thrusters. Finally, the influence of plasma rarefaction and finite electron magnetization on the jet detachment is commented.

Vacuum-chamber measurements of the near-region of MNs of different thrusters are confirming ion detachment as a real and robust phenomenon[5, 19–22]. However, measuring plasma expansion and detachment far downstream is more challenging due to chamber size constraints. Theoretically, we already identified ion detachment as a relevant 2D beam feature[9, 11], but again, the study covered only the MN near region, limited downstream by the MN turning point. Here, a new intrinsic integration algorithm allows to overcome the MN turning point limitation and to look into the MN far region, both downstream and laterally.

The steady macroscopic, two-fluid model[9] describes the z - r expansion of a quasineutral, collisionless and current-free plasma column of radius R injected sonically at the MN throat (located at $z = 0$). We assume the upstream internal energy is deposited mainly on electrons, and a magnetic field strength such that ions are partially-magnetized but massless electrons are fully-magnetized. Then, electron and magnetic streamtubes coincide everywhere and the magnetic tube with initial radius $r = R$, constitutes the plasma-vacuum edge. After manipulation of electron and ion equations, the 2D evolution of ion density and (longitudinal) velocity are found to be described by a closed set of three hyperbolic differential equations, which are integrated along characteristic lines in the intrinsic coordinates.

Ion magnetization is characterized by the local ion gyrofrequency parameter $\hat{\Omega}_i(z, r) = eRB(z, r)/\sqrt{T_e m_i}$. The particular coil layout of the thruster defines the shape of the MN, that is $B(z, r)/B_0$, with subindex 0 referring to the origin, $(z, r) = (0, 0)$, while acting on the coil currents modifies the MN strength B_0 and thus $\hat{\Omega}_{i0}$. This is the main dimensionless parameter in the present discussion. Since both the MN shape and the plasma density profile at the throat, $n(0, r)/n_0$, are not essential for the detachment mechanism, the magnetic field of Fig. 1, and the density profile of Fig. 2(a) in Ref. 9, will be used here. The curves of constant $B/B_0 \equiv \hat{\Omega}_i/\hat{\Omega}_{i0}$ in Fig. 1 show the demagnetization rate in the divergent MN. Since envisaged MN-based thrusters relying on electron internal energy and medium-to-heavy propellants have $\hat{\Omega}_{i0} < \mathcal{O}(10)$, ions are typically unmagnetized everywhere (i.e., $\hat{\Omega}_i \ll 1$), except perhaps near the throat, where it can be $\hat{\Omega}_i > 1$ locally.

Figure 1(a) and (b) depict, for two magnetic strengths amply covering the foreseen application range, the integrated ion flux from the axis (0%) to the plasma-vacuum boundary (100%), and the ion streamtubes containing 50%, 95%, and 100% of the ion flux. Except for the 100%-tube, where quasineutrality ensures that ion and electron streamtubes coincide, the progressive detachment of ion tubes from their corresponding magnetic tubes is evident. The separation it is clearly linked to ion demagnetization, with lower values of $\hat{\Omega}_{i0}$ leading to more pronounced tube separation in the far-region. As in more

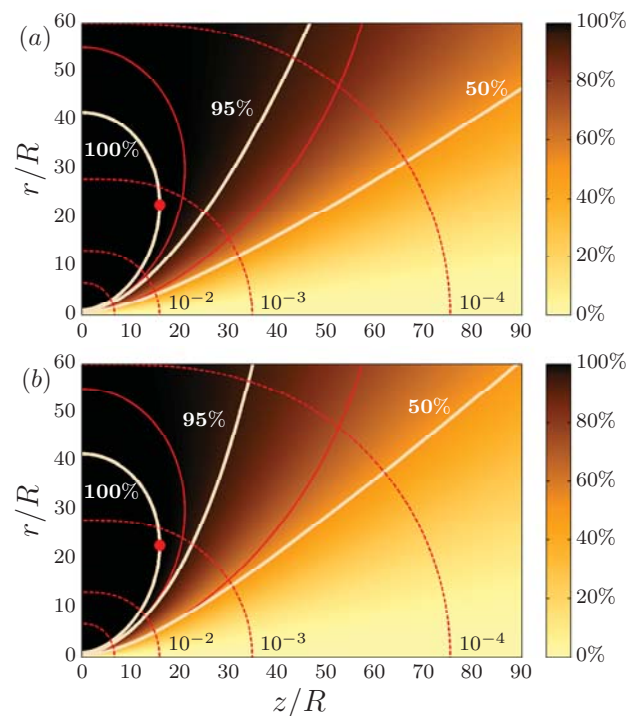


FIG. 1. (Color online) Ion inwards detachment for two magnetic strengths: (a) $\hat{\Omega}_{i0} = 1$ and (b) $\hat{\Omega}_{i0} = 200$. Thick solid lines are streamtubes containing 50%, 95%, and 100% of the plasma mass flow. The thin solid lines show the initially-corresponding magnetic streamtubes. The integrated mass flow from the axis to the lateral boundary is depicted in the 2D map. Dashed lines show the order of magnitude of B/B_0 . The field is generated by a single current loop of radius $3.5R$ located at $z = 0$. The dot marks the MN ‘turning point’.

conventional thrusters, the 95%-flow tube can be used to define the ‘practical’ boundary of the plasma beam and to assess the plume divergence. We observe that this tube becomes more straight downstream, while only a very marginal fraction of the ion flow (less than 1% in present simulations) is deflected backwards around the turning point.

To better quantify the effect of ion initial magnetization, Fig. 2 plots the spatial evolution of the divergence angle of the 95%-mass flow streamtube, α_{div} , for the two cases of Fig. 1 and for the total ion-magnetization case, $\hat{\Omega}_i = \infty$, in which ion detachment would be null everywhere. Clearly, the larger $\hat{\Omega}_{i0}$ is, the later ion detachment starts to be apparent, and the larger the plume divergence. Nevertheless, the most striking result are the modest differences between the ‘near unmagnetized’ case ($\hat{\Omega}_{i0} = 1$) and the ‘high magnetization’ case ($\hat{\Omega}_{i0} = 200$), which, in spite of the large $\hat{\Omega}_{i0}$, is still far away from the $\hat{\Omega}_{i0} = \infty$ limit. This indicates that ion detachment is a robust mechanism even for very large initial magnetization of ions. Finally, notice that the plume divergence

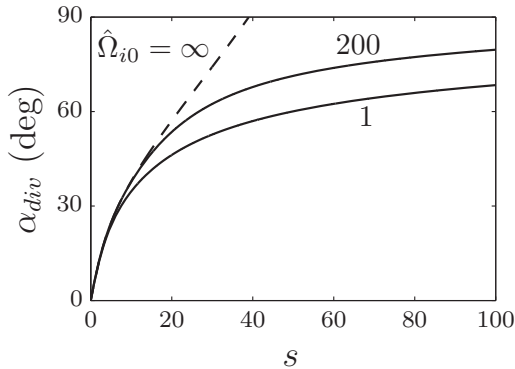


FIG. 2. Evolution of the divergence angle of the 95%-mass flow tube along its arc-length s in the meridional plane, for different $\hat{\Omega}_{i0}$. The dashed line shows the divergence of the 95% magnetic tube, which coincides with the ion full-magnetization limit, $\hat{\Omega}_{i0} = \infty$.

efficiency and the thrust gain[9, 18], parameters not plotted here, can be used to quantify the MN performance in more detail than α_{div} .

We now turn to analyze the physics behind the 2D acceleration and detachment of the plasma jet. In general, each plasma species expands under the action of the ambipolar electric force, its own pressure gradient, and the magnetic force due to its own currents. The consequence is that *massless, confined* electrons and *inertia-driven* ions behave very differently. For electrons, momentum equations assert (in addition to electron tubes coinciding everywhere with magnetic ones) that (i) in each magnetic tube, the electric potential $\phi(z, r)$ and plasma density n are related by a tube-dependent Boltzmann relation, and, (ii) in the direction *perpendicular* to the magnetic tubes, the expanding pressure force component f_p is balanced by the confining electric and magnetic force components, f_e and f_m , that is $f_p = f_e + f_m$. Figure 3(a) plots the relative strength of these perpendicular forces. At the source exit, one has $f_m \approx f_p \gg f_e$ for hot magnetized electrons. Downstream, however, the electric force gradually takes over the confinement task, and the magnetic force becomes secondary, except at the plasma-vacuum edge, where $f_m \approx f_p \gg f_e$ remains large.

On the other hand, the change of momentum of (quasi-cold) ions is caused by the same ambipolar electric field and a magnetic force, proportional to the local ion magnetization and tube separation. For $\hat{\Omega}_{i0}$ small, the ion magnetic force is negligible in the whole MN, and the electric force completely dominates axial ion acceleration and radially-outward deflection of ion tubes. For $\hat{\Omega}_{i0}$ large, a *paramagnetic azimuthal* ion velocity, $u_{\theta i}$, develops, which generates a \mathbf{B} -perpendicular, outward force in the near-region with two negative effects on the ion flow: axial deceleration and increment of ion divergence.

Our results state, and experimental evidence seems to agree, that the combined electric and magnetic deflec-

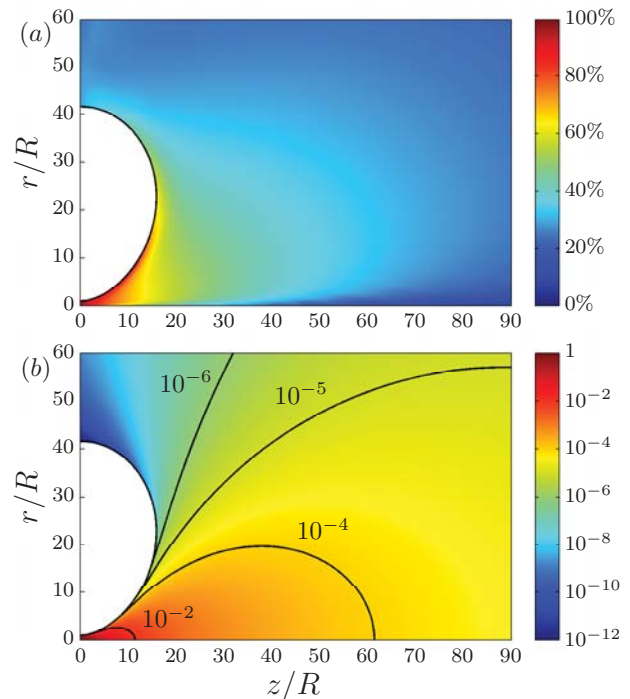


FIG. 3. (Color online) Maps for the $\hat{\Omega}_{i0} = 1$ case of (a) perpendicular magnetic-to-pressure force ratio on electrons, f_m/f_p , and (b) normalized plasma density, n/n_0 .

tion of ion tubes are insufficient to match them with electron/magnetic tubes. In other words, the *ambipolar condition* $\mathbf{j} = \mathbf{0}$, with \mathbf{j} the electric current density, cannot be satisfied everywhere in a 2D, divergent, globally-current-free jet even if $\nabla \cdot \mathbf{j} = 0$ is satisfied naturally and $\mathbf{j} = \mathbf{0}$ is imposed at a certain jet cross-section[18]. Indeed, the ambipolar electric field self-adjusts in order to preserve quasineutrality, but allows ion and electron tubes to separate inside the plasma volume. Furthermore, the more supersonic the ion beam becomes, the less its divergence is affected by electric and magnetic forces, and the more it approaches a free-expansion regime, as the decreasing growth rate of α_{div} in Fig. 2 confirms.

The above *ideal* model, based on the assumptions of quasineutrality and fully-magnetized electrons, demonstrates that plasma inwards detachment is caused essentially by ion demagnetization. The relaxation of these ideal conditions modifies the electric field and consequently alters ion detachment. First, Fig. 3(b) shows that plasma rarefaction is huge downstream and particularly sideways. Since space-charge effects grow as $\propto n^{-1}$, quasineutrality eventually fails near the plasma edge and far downstream. Fortunately, space-charge sets an upper-bound to the electric field, and thus to the deflecting force on ion tubes, which is expected to facilitate ion detachment, specially in the periphery.

Second, for finite electron magnetization, resistivity,

electron-inertia, and the plasma-induced magnetic field were shown to deteriorate electron confinement, leading to outward electron detachment[11, 18], which adversely increases the effective MN divergence. The desirability of full electron magnetization on one hand (to minimize these three phenomena and ensure proper channeling and acceleration of the plasma beam), and low ion magnetization on the other (to foster downstream detachment and achieve low beam divergence), set two conflicting requirements to the magnetic strength of the MN. Once the physics are understood, each thruster should optimize both the strength and shape of the MN to maximize thrust efficiency. Note that the use of heavy, singly-ionized ions alleviates the requirement conflict.

Additionally, while the ideal model is simple and consistent enough to demonstrate the crucial role of ion demagnetization on detachment, it presents some limitations that become important as the jet expands further downstream. First, the presence of a tenuous background plasma (*i*) smooths the hard plasma-vacuum edge assumed here, and (*ii*) when the beam and background densities become comparable, it will affect/limit the development of the electric field. Second, ion-electron separation generates longitudinal electric currents in the globally-current-free jet, which must close both upstream (i.e., inside the source) and downstream (possibly through residual resistivity, geometric vanishing, and interaction with the background plasma). Third, the transition from a magnetized to an unmagnetized electron model needs to be addressed consistently. The downstream vanishing of the magnetic force (Fig. 3(a)) seems promising in this regard.

Fourth, and most important, the assumption of electron isothermality, while not central for the detachment process, leads to a nonphysical, infinite (logarithmically-slow) drop of the electric potential downstream. Limited laboratory and in-space evidence (with unmagnetized collisionless plumes) suggests that the electric potential vanishes proportionally to $n^{\gamma-1}$ with $\gamma \sim 1.1 - 1.2$. Unfortunately, no established theory exists for the expansion of a collisionless electron population. Theoretical approaches, based on the kinetic theory, suggest a collisionless cooling of electrons based on adiabatic invariants and effective potential barriers[23, 24].

Finally, the fundamental differences with the MN theory of Takahashi *et al.* [5] seem pertinent to be noted here. Their 2D-claimed model neglects ion radial-inertia, when it is indeed a dominant-order term in the radial momentum equation of inertia-driven ions. This leads to a non-physical behavior, where $u_{\theta i}$ corresponds to the $E \times B$ drift of a zero-inertia species and creates a *diamagnetic* force on ions that stretches axially the ion streamtubes. Furthermore, by postulating that the effective beam cross-section is $\pi R^2 B(z, 0)/B_0$ and imposing a self-similar density profile, their model is actually quasi-1D, and avoids the central issue of plasma expansion beyond

the MN turning point.

This work has been sponsored by the Air Force Office of Scientific Research, Air Force Material Command, USAF (grant FA8655-12-1-2043) and Spain R & D National Plan (Project AYA-2010-61699).

-
- [1] G. Krülle, M. Auweter-Kurtz, and A. Sasoh, *J. Propulsion and Power* **14**, 754 (1998).
 - [2] A. Arefiev and B. Breizman, *Phys. Plasmas* **11**, 2942 (2004).
 - [3] R. Winglee, T. Ziemba, L. Giersch, J. Prager, J. Carscadden, and B. Roberson, *Phys. Plasmas* **14**, 063501 (2007).
 - [4] O. Batishchev, *IEEE Trans. on Plasma Sci.* **37**, 1563 (2009).
 - [5] K. Takahashi, T. Lafleur, C. Charles, P. Alexander, and R. Boswell, *Phys. Rev. Lett.* **107**, 235001 (2011).
 - [6] E. Ahedo, *Plasma Phys. and Controlled Fusion*(2011).
 - [7] S. Andersen, V. Jensen, P. Nielsen, and N. D'Angelo, *Phys. Fluids* **12**, 557 (1969).
 - [8] G. Sutton and O. Biblarz, *Rocket propulsion elements* (Wiley, 2010).
 - [9] E. Ahedo and M. Merino, *Phys. Plasmas* **17**, 073501 (2010).
 - [10] A. Sasoh, *Phys. Plasmas* **1**, 464 (1994).
 - [11] E. Ahedo and M. Merino, *Phys. Plasmas* **18**, 053504 (2011).
 - [12] E. Ahedo and M. Martínez-Sánchez, *Phys. Rev. Lett.* **103**, 135002 (2009).
 - [13] M. Merino and E. Ahedo, *Phys. Plasmas* **20**, 023502 (2013).
 - [14] R. Gerwin, G. Marklin, A. Sgro, and A. Glasser, *Tech. Rep. AFSOR AL-TR-89-092* (Los Alamos National Laboratory, 1990).
 - [15] R. Moses, R. Gerwin, and K. Schoenberg, in *Proceedings 9th Symp. on Space Nuclear Power Systems*, (1992) pp. 1293–1303.
 - [16] E. Hooper, *J. Propulsion and Power* **9**, 757 (1993).
 - [17] A. Arefiev and B. Breizman, *Phys. Plasmas* **12**, 043504 (2005).
 - [18] E. Ahedo and M. Merino, *Phys. Plasmas* **19**, 083501 (2012).
 - [19] W. Cox, C. Charles, R. Boswell, and R. Hawkins, *App. Phys. Lett.* **93**, 071505 (2008).
 - [20] C. Deline, R. Bengtson, B. Breizman *et al*, *Phys. Plasmas* **16**, 033502 (2009).
 - [21] K. Terasaka, S. Yoshimura, K. Ogiwara, M. Aramaki, and M. Tanaka, *Phys. Plasmas* **17**, 072106 (2010).
 - [22] J. P. Squire, C. S. Olsen, F. R. Chang-Díaz *et al*, in *32nd Int. Electric Propulsion Conf.* (2011).
 - [23] D. Dorozhkina and V. Semenov, *Phys. Rev. Lett.* **81**, 2691 (1998).
 - [24] A. Arefiev and B. Breizman, *Phys. Plasmas* **15**, 042109 (2008).

Two-Fluid and PIC-Fluid Code Comparison of the Plasma Plume in a Magnetic Nozzle

J. Navarro* and M. Merino† and E. Ahedo‡

Universidad Politécnica de Madrid, Madrid 28040 Spain

The HPMN hybrid (PIC/fluid) code is characterized and validated against the DIMAGNO two-fluid, collisionless code of the plasma flow in a magnetic nozzle. A globally current-free, fully-ionized plasma generated by a helicon source is injected at the magnetic nozzle throat of each code and simulated. Comparison of the plasma properties of each solution highlights the differences and similarities between both codes. Results on main plasma magnitudes agree well, supporting the validity and accuracy of HPMN and suggesting points of further improvement.

I. Introduction

Magnetic nozzles (MN) are envisaged as a promising acceleration system for advanced plasma thrusters. By using an axisymmetric, divergent applied magnetic field, the hot plasma of these engines can be efficiently channeled and expanded into vacuum to produce thrust in an equivalent way to a solid de Laval nozzle. The central advantages of MN over their solid counterparts are the strong reduction of plasma losses and wall damage thanks to magnetic confinement, and the possibility to control thrust and specific impulse in flight by modifying the geometry and intensity of the applied field, which allows to adapt to different mission profiles. Examples of electric thrusters using of MN are: the Helicon thruster,¹⁻⁴ the applied-field MPD thruster^{5,6} and the VASIMIR.⁷ Once accelerated, the plasma needs to free itself from the imposed magnetic field to form a directed axial beam, a phenomenon known as detachment.

A good understanding of plasma physics in the MN is central for the development of a successful and efficient thruster that can compete with the current array of highly optimized electric propulsion systems, or extend the current performance envelope. In this regard, numerical simulations are of paramount importance to attain this understanding and complement experiments, since they can provide the necessary insight in the mechanisms for plasma acceleration and detachment.

In the last years, we have studied the physics of the MN with DIMAGNO,⁸⁻¹⁰ a two fluid, two dimensional code of a totally ionized, quasineutral, collisionless plasma. DIMAGNO code reproduces the fundamental physics of the MN, including fluxes of ions and electrons, electric potential, electric currents and induced magnetic fields. It achieves high computational speed and accuracy thanks to the Method of Characteristics (MoC) used in the integration of the supersonic flow. This code has permitted the analysis of the acceleration mechanisms in the nozzle, the radial rarefaction of the expansion, the generation and transmission of thrust, and the parametric investigation of propulsive performances.⁸ Additionally, an initial study of the detachment problem in a hot plasma has been carried out, where DIMAGNO showed that plasma induced magnetic field, resistivity, and azimuthal electron inertia cause radially-outwards detachment.⁹

In spite of its success and adequacy for the study of the fundamental physics of a MN, the approach followed in DIMAGNO is constrained by the assumption of a collisionless plasma and the inherent characteristics of a fluid model, precluding the analysis of interesting phenomena such as resistive diffusion in the plume. To overcome this and other limitations, a 2D hybrid particle/fluid, quasineutral code called HPMN after ‘hybrid particle magnetic nozzle’ has been developed at EP2.¹¹ This code nourishes on the large experience and confidence acquired on the well-tested HPHall2 code used in our group,¹² originally conceived for

*PhD student, Equipo de Propulsión Espacial y Plasmas (EP2), web.fnetsia.upm.es/ep2, student AIAA member (jaume.navarro@upm.es).

†PhD student, EP2, student AIAA member (mario.merino@upm.es).

‡Professor, EP2, senior AIAA member (eduardo.ahedo@upm.es).

the simulation of Hall effect thrusters. In HPMN, heavy species are simulated with the particle-in-cell (PIC) methodology, while fully-magnetized electrons are modeled as a magnetized fluid. Collisions are treated with Monte Carlo (MC) methods. This hybrid approach means a convenient trade-off between complexity and detail, and allows to recover physical aspects unattainable with a fully fluid model, such as the ion energy distribution function (EDF). However, some accuracy and the “cleanness” which characterize fluid models such as DIMAGNO are unavoidably sacrificed. One the advantages of the HPMN code is that it takes into account electron collision effects, and allows exploring the gentle diffusive transition between the dense jet and the near-vacuum region, whereas DIMAGNO necessarily employs a sharp plasma-vacuum edge.

The goal of this paper is, first of all, to carry out the validation of the HPMN code. Validation of this newer code needs to be performed based on previous knowledge of MNs. To this end, identical plasma flows are simulated with DIMAGNO and HPMN, and we compare and cross-validate the results. The calculated plasma profile at the exit of a helicon source will be employed in both simulations. Comparisons are made in terms of plasma density distribution, ion current density flows, induced azimuthal currents, and thrust gain. From this analysis, we reach conclusions about the suitability of each code to simulate the different physics present in a MN. Our second objective is the investigation and characterization of the new physical phenomena present in HPMN that were unavailable in DIMAGNO. Our focus here is on the diffusion due to collisions.

The paper is organized as follows. First, a short summary of the fluid model of DIMAGNO and the hybrid model of HPMN is provided in sections II and III, respectively. Then, in section IV, the upstream plasma provided by a helicon source is characterized. This knowledge provides the initial flow conditions for the simulations of DIMAGNO and HPMN. The comparison of results and the main discussion is carried out in section V. Finally, conclusions and planned future developments are gathered in section VI.

II. Fluid model (DIMAGNO)

Summarily, the fluid model of DIMAGNO describes the axisymmetric, steady-state flow of a totally-ionized, quasineutral, collisionless, supersonic plasma in the divergent magnetic field \mathbf{B} . Electrons are modeled as a hot, isotropic species of constant temperature T_e , while ions are modeled as a cold one with mass m_i . A detailed account of the derivation of the model, its nomenclature, and the integration strategy, can be found in previous publications,^{8,9} including a discussion of the main results. The ion and electron equations are presented here in abridged form for convenience:

$$\nabla \cdot (n\mathbf{u}_i) = 0, \quad (1)$$

$$m_i (\mathbf{u}_i \cdot \nabla) \mathbf{u}_i = e (-\nabla\phi + \mathbf{u}_i \times \mathbf{B}), \quad (2)$$

$$0 = -T_e \nabla \ln n - e (-\nabla\phi + \mathbf{u}_e \times \mathbf{B}). \quad (3)$$

The main characteristics of the model stem from the hypotheses of: (1) negligible collisions, i.e. that the Hall parameter $\chi_H = eB/m_e\nu_e \gg 1$; and (2) completely magnetized electrons and negligible electron inertia, i.e. electron Larmor radius $\ell_e = \sqrt{m_e T_e}/(eB) \ll R$, with R the macroscopic length of the plasma. Electron streamtubes are therefore assumed to coincide with magnetic streamtubes. Ions, however, are only partially magnetized, and separate inwards from the electron streamtubes depending on their magnetization degree, giving rise to longitudinal currents⁸ and facilitating detachment.¹³ The validity of these assumptions is justified inasmuch as an efficient MN requires that at least the electrons are magnetized, so that the plasma will describe the geometry of the magnetic field, and that the flow collisionality is low to achieve good magnetic confinement. The resultant model is dependent on the geometry and intensity of the magnetic field (the latter measured by the non-dimensional ion gyrofrequency, $\hat{\Omega}_{i0} = eBR/\sqrt{m_i T_e}$, which is the key parameter that controls ion magnetization), and the initial conditions at the nozzle throat.

For a given magnetic field \mathbf{B} , Eqs. (1)–(3) are hyperbolic if ions are supersonic, and they can be integrated with the method of characteristics (MoC). This leads to a highly accurate and computationally inexpensive integration scheme.¹⁴ As a consequence, DIMAGNO is regarded as a valuable tool for validation of more complex codes such as HPMN.

As pointed out in the introduction, DIMAGNO reproduces the fundamental MN physics of plasma expansion and acceleration, electric currents, thrust generation, etc., and has been used to study the main aspects of the operation of these devices. Certain advanced physics can also be analyzed by extending this model. For instance, the plasma-induced magnetic field, which can play an important role in detachment, can be taken into account with a simple iteration procedure.¹⁵ The influence of collisions was recently studied

with a perturbation analysis.^{9,16} The dominant electron inertia effects (finite Larmor radius effects) can be easily incorporated into the model.^{17,18} Support for multiple-temperature electron distributions has been added, allowing the study of the formation of quasi-double-layers in the flow.¹⁹ Latest developments include the capability to simulate the flow beyond the magnetic turning point to analyze the far-field plume.¹³

III. Hybrid PIC/fluid model (HPMN)

The core of the hybrid model used here inherits from the well-known HPHall2 hybrid code,¹² an improved version of HPHall,²⁰ which was designed to describe the plasma physics in a Hall thruster. The fundamentals and intricacies of the new HPMN code were presented in Ref. 11.

Heavy species (neutrals and ions) are treated as macroparticles in a conventional PIC subcode. The spatial grid is axisymmetric and structured. Collisions that involve ions and neutrals can be accounted for using Monte-Carlo methods. Main properties of the quasineutral plasma provided by the PIC subcode are the plasma density and ion currents.

HPMN models electrons as a magnetized fluid. Main differences compared with DIMAGNO are (1) the inclusion of collisions in the momentum equation and (2) the possibility of taking into account ionization processes. Thus, Eqs. (1) and (3) of previous section are extended here to include these terms,

$$\nabla \cdot (n\mathbf{u}_i) = \nabla \cdot (n\mathbf{u}_e) = \dot{n}_e \quad (\Rightarrow \nabla \cdot \mathbf{j} = 0), \quad (4)$$

$$0 = -T_e \nabla \ln n - e(-\nabla\phi + \mathbf{u}_e \times \mathbf{B}) + m_e \nu_e \mathbf{u}_e. \quad (5)$$

The fluid model of electrons is based on projecting Eqs. (4) and (5) onto the magnetic reference frame, $\mathbf{1}_{\parallel}, \{\mathbf{1}_{\perp}, \mathbf{1}_{\theta}\}$, where, $\mathbf{1}_{\parallel} = \mathbf{B}/B$, and $\mathbf{1}_{\perp} = \mathbf{1}_{\theta} \times \mathbf{1}_{\parallel}$ is the normal unit vector to the magnetic field. The result of splitting Eq. (5) along each of these directions is, respectively,

$$e\phi(r, z) = -H_e(\psi) + T_e(\psi) \ln n(r, z), \quad (6)$$

$$u_{\theta e} = -\chi_H u_{\perp e}, \quad (7)$$

$$u_{\perp e} = -\frac{r\chi_H}{1 + \chi_H^2} \frac{\partial H_e}{\partial \psi}, \quad (8)$$

where only azimuthal resistivity has been kept due to its zero-order character on the definition of $u_{\perp e}$, ψ is the magnetic streamfunction, and the rest of symbols are conventional

Equation (6) constitutes the Boltzmann relation in the parallel direction, in which $-H_e/e$ is the thermalized potential, known from flow conditions at the MN throat. Equations (7) and (8) describe, respectively, the azimuthal and perpendicular behaviour of the electron flow. Notice that the last one becomes $u_{\perp e} = 0$ in the collisionless limit $\chi_H \rightarrow \infty$, recovering the corresponding expression of DIMAGNO. Eq. (8) may be regarded as the Ohm's law in the perpendicular direction.

Local current ambipolarity (LCA) is not fulfilled everywhere within the plasma domain, even for a globally current-free plume.⁸ This idea stands out from Eq. (4) when it is projected along $\mathbf{1}_{\perp}$ and integrated on each magnetic tube:

$$\frac{\partial I_{\perp}(\psi)}{\partial \psi} = \frac{2\pi j_z}{B \cos \alpha} \Big|_{throat} - \frac{2\pi j_z}{B \cos \alpha} \Big|_{end}, \quad (9)$$

where $I_{\perp}(\psi) = I_{\perp i} + I_{\perp e}$ is the net current across the magnetic surface given by $\psi = \text{const}$, between the throat ($z = 0$) and downstream end sections ($z = z_{end}$), in the direction of $\mathbf{1}_{\perp}$. Ion current $I_{\perp i}$ is provided by the PIC sub-code, whereas electron $I_{\perp e}$ stems from Eq. (8) and the local density n (resulting from PIC calculations). Both of them ($j = i, e$) can be expressed as

$$I_{\perp j} = q_j \int_{\psi} n u_{\perp j} d\sigma, \quad (10)$$

with $d\sigma$ a differential area element of the magnetic surface.

Electrons are treated as an isothermal species in this model. We emphasize that a non-isothermal model $T_e(\psi)$ could be easily considered once a closure for the heat flux is provided for the energy equation. In order to facilitate the comparison of the results with DIMAGNO, ionization mechanisms are also switched off.

IV. Upstream Plasma characterization

The focus of this work is on the MN flow of plasmas generated using a helicon plasma source. In this section the fluid model of helicon source described in Ref. 21 is used to obtain the radial equilibrium and plasma fluxes at the throat. This boundary condition serves then as the starting point of integration for the two codes described above.

Within the dielectric tube, radial plasma pressure is balanced by (1) the force created by the external axial magnetic field and plasma azimuthal currents, and (2) the radial ambipolar electric field. The same electric field pulls ions towards the wall of the source. The higher the magnetic field, the stronger the magnetic confinement compared to the electric one, and the smaller the plasma losses to the wall.

The plasma is accelerated along the source up to the ion sonic velocity, $c_s = \sqrt{T_e/m_i}$, reached at the exit section, where the MN throat is located.

The matching between source and MN requires some additional comments. In the case of DIMAGNO, the profile requires some adaptation as follows: first, due to the requirement of hyperbolicity of the equations, the initial Mach number is chosen $M_0 = 1.01$, slightly higher than 1. This introduces a small error ($< 5\%$) in continuity, momentum and energy conservation equations. (2) DIMAGNO's collisionless plasma flow must be parallel to \mathbf{B} at the plasma edge. This is dealt with by cutting off a small fraction of the plasma flow near the edge, where the largest radial velocity is located. Since density is low in this region, the amount of plasma which is disregarded in the nozzle simulation of DIMAGNO is negligible. The small radial velocity within the retained plasma is also neglected.

In the matching with the HPMN model, on the other hand, we need to express the plasma flux using a kinetic formulation, because ions are modeled by a PIC code. These particles are injected through the MN throat along the \mathbf{B} direction according to a distribution function of particles velocity. This function must retain plasma properties at the source exit section (i.e. density n and plasma flux $n\mathbf{u}$).

IV.A. MN throat conditions

The chosen source parameters are listed next: ion mass $6.6 \cdot 10^{-26}$ kg (Ar), mass flow $\dot{m} = 0.1$ mg/s, tube radius $R = 0.01$ m and length $L = 0.1$ m, plasma temperature $T_e = 10$ eV, and magnetic field intensity $B_0 = 200$ G (assumed constant along the dielectric tube).

For these values, the non-dimensional ion gyrofrequency is $\hat{\Omega}_{i0} = ReB/\sqrt{(m_i T_e)} \simeq 0.1$. The useful power, in accordance with enumerated parameters, is in the power range 50–100 W, so this study refers to the analysis of a mini-helicon plasma thruster (e.g. Ref. 4).

Figure 1a shows the radial structure of the plasma density. Plasma radial velocity is depicted in 1b. Taking into account that $-e\phi \sim 1/2m_i u_{ri}^2$, the radial electric field can be neglected, except at the vicinity of the plasma edge (inertial layer, which precedes the Debye sheath. Ref. 22).

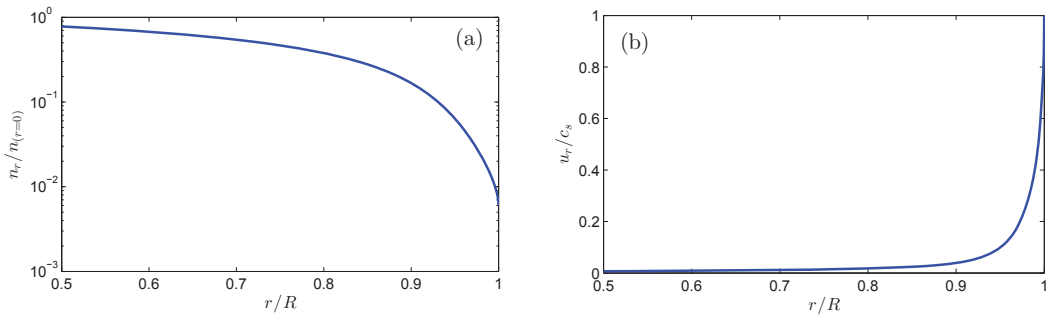


Figure 1. (a) Plasma density at the MN throat $n(r)/n_{r=0}$. (b) Plasma radial velocity u_{ri}/c_s .

Simulations of the source indicate that propellant utilization η_u , which relates ion flow at the source exit to the total mass flow, is over 92%. Consequently, the flux through MN throat is practically fully-ionized, and residual neutral density is low enough to neglect plasma ionization within the plasma plume. Increasing the magnetic field up to 600 G, η_u goes up to $\simeq 99\%$.

V. Comparison of results

Figure 2 presents 2D maps of the plasma density in the MN plume for both codes. HPMN reproduces the same behaviour of DIMAGNO, and the agreement in this regard is high. Numeric results obtained using the hybrid model also fit with the full fluid code response. Spatial gradients of the plasma density in HPMN are coherent with DIMAGNO. The large radial rarefaction is reproduced by both hybrid and fluid codes. Obviously, DIMAGNO is still more accurate because of its MoC approach.

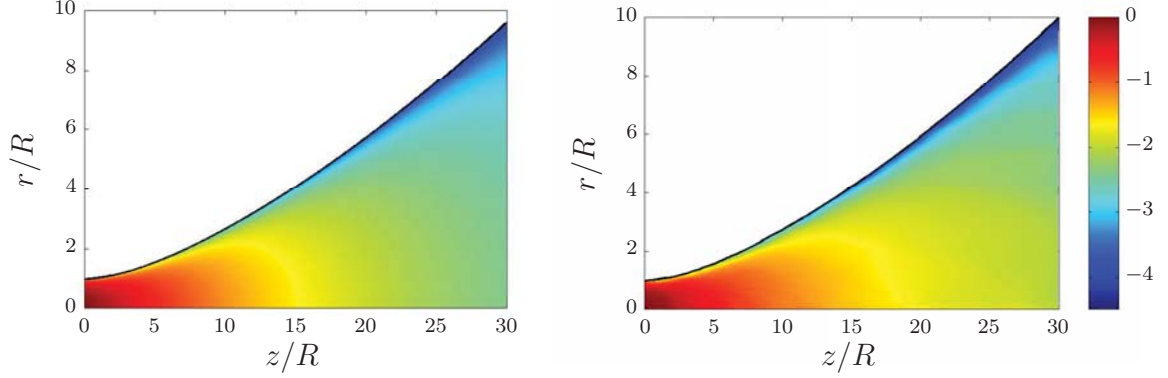


Figure 2. Plasma density $\log_{10} n_e$ (part/m^3) DIMAGNO (left) and HPMN (right).

The correlation between plasma density maps allows to know beforehand that electric potential, Figure 3, should exhibit similar results. According to Eq. (6), electric potential ϕ is equivalent to the thermalized potential, which is constant along each magnetic surface, plus a correction comparable to the plasma temperature and $\ln n$. The thermalized potential is the same in both models because it only depends on MN throat conditions. Consequently, electric potential from HPMN agrees with DIMAGNO results. However, a slight mismatch on the results is appreciable. These local deviations appear as a consequence of PIC fluctuations in properties and interpolation errors. Consequently, equipotential surfaces obtained with the hybrid model are not as smoothly defined as in DIMAGNO.

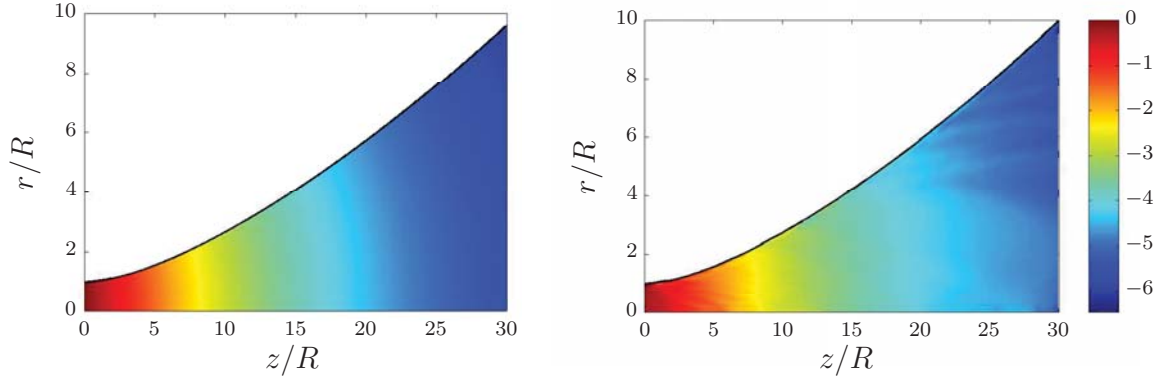


Figure 3. Electric potential $\phi(V)$ DIMAGNO (left) and HPMN (Right).

This is further manifested by the potential drop along the axis line, relative to the potential at the MN throat, is about $5.5T_e$ at $z = 0.3$ m as shown in Figure 4. The tendency in both models is almost the same from the MN throat until $z = 0.1$ m. However, the loss of correlation from $z = 0.1$ m and downstream along the plasma plume cannot be neglected. The numerical behaviour of HPMN downstream, where MN area is by far larger than that measured at the throat section, requires some comments.

First, in spite of injecting a huge number of macroparticles per cell (N) at the MN throat, it is not possible to avoid the low N we find at the far plume. This reduction is due to the strong rarefaction that takes place in the plume, plus the lack of ionization processes that would increase N .

Second, the reduction of N induces the statistical failure of the weighting algorithms as shown in Figure

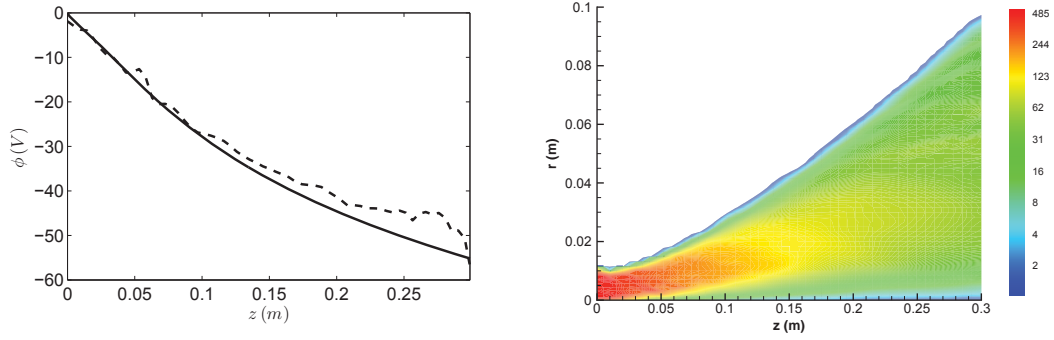


Figure 4. Left: Electric potential along axis, DIMAGNO (solid line) and HPMN (dashed line). Right: Number the particles per cell, N , according HPMN simulation.

5 (right), which plots the ion Mach number distribution within the plasma plume $M_i(z, r) = \sqrt{u_{zi}^2 + u_{ri}^2}/c_s$. The natural response to the monotonically drop of the electric potential ϕ (Figure 3) should be a continuous acceleration of charged particles, as depicted in DIMAGNO results, Figure 5 (left). In fact, all ions in the PIC simulation are (independently) accelerated along z positive direction. But the macroscopic flow velocity \mathbf{u} obtained from weighting across particles does not retain this behaviour because it is influenced by the low N , the particle velocity dispersion, and the numerical density background, n_{bg} .

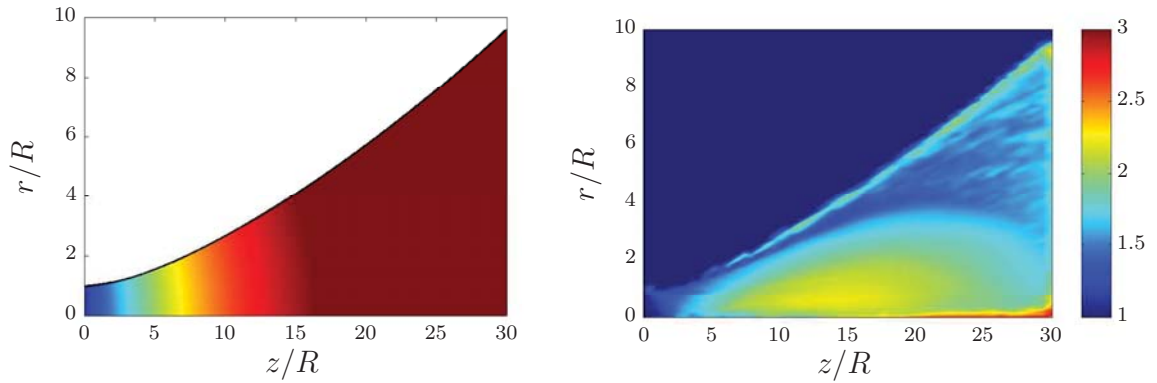


Figure 5. Ion Mach number M_i , DIMAGNO (left), and HPMN (right).

This background is necessary to avoid PIC model inconsistencies. Nonetheless, here is still overly large and produces an undesirable effect. In this research, the treatment of n_{bg} has been improved compared with the model in Ref.¹¹ Now, n_{bg} is reduced progressively to a more appropriate value according to the average value of N .

This upgrade is not enough to correct or improve the weighting algorithm results that try to reproduce the second or higher-order moments of the ion distribution function, i.e., particle flux $n\mathbf{u}$, momentum flux and successive moments. The first-order moment of the ion distribution function, necessary to deal with the ion density (i.e. the plasma density), is not affected by the particle velocity dispersion, and has been improved thanks to the new model.

Plasma density governs the effective electron collision frequency, $\nu_e = \nu_{ei} = n_e R_{ei}$, which drives the electron perpendicular dynamics inside the plasma plume. R_{ei} is the rate of *electron-ion* collisions which depends on the plasma temperature and the Coulomb logarithm. In fact, the diffusive electron transport in the plasma plume is controlled by the Hall parameter χ_H , which is illustrated in Figure 6 (left). Perpendicular currents, Eq. (10), are depicted in Figure 6 (right). All currents are zero at the axis of symmetry. I_e increases radially due to collisions, which permit electrons to move outward (see Eq. (8)), but near the plasma edge it decreases again due to the significant growth of χ_H . Magnetic field intensity increases there, and collisions decrease at the same rate as the density drop.

Results from HPMN support the collisionless limit of DIMAGNO as a good approximation for large values of χ_H . Both models present a similar response of $u_{\theta e}$ (Figure 7) as expected, since collisions do not

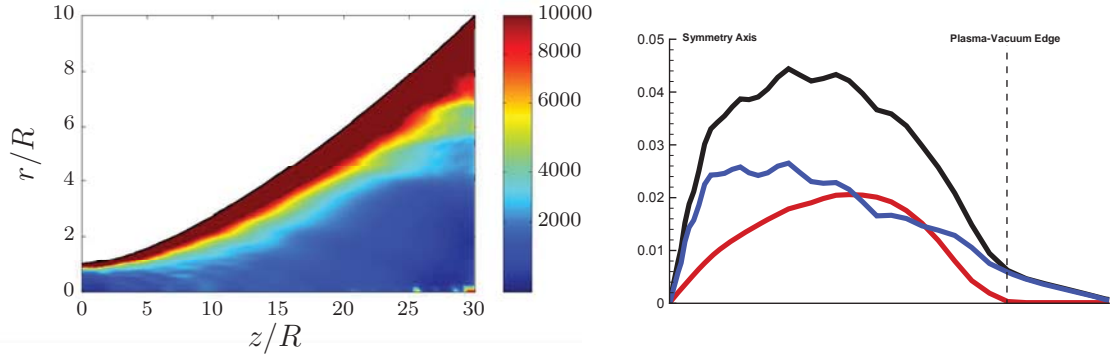


Figure 6. Left: Hall parameter χ_H in the HPMN simulation. Right: Inward-pointing perpendicular electric currents (Amperes) through magnetic surfaces between axis line and plasma edge surface, both limits are indicated by vertical dashed-lines (HPMN). Total current I_{\perp} in black, ion current I_i in blue, electron current I_e in red. The ion current at the Helicon source exit section, using the values presented in section IV.A, is 0.23A.

affect $u_{\theta e}$ up to first order. This property varies according to Eq. (7), which in the DIMAGNO limit only depends on the thermalized potential and the MN divergence.

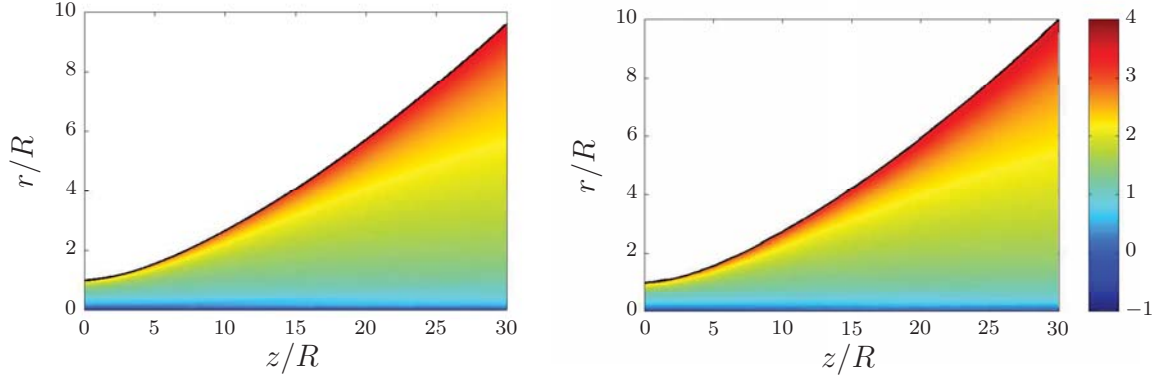


Figure 7. Electrons azimuthal velocity $\log_{10}(u_{\theta e})$. DIMAGNO (left), and HPMN (right).

Improvements on HPMN, such as n_{bg} progressive reduction, have allowed a fine closure of I_e at the vicinity of the plasma edge, Eq. (10), which was one of the difficulties encountered in the previous version. Near the plasma edge, large gradients of some plasma properties cannot be captured by the PIC mesh, producing high electric fields that disturb the behaviour of the PIC subcode. To deal with this problem a finer PIC submesh will be required in future work, to assess the gentle plasma-vacuum edge, increasing by far, the computational effort. The coarse grid of the PIC subcode near this region and its interaction with the magnetic frame (electron subcode), using interpolation algorithms, also explain the unexpected closures and mismatch of the perpendicular currents.

The global error committed at the MN (HPMN model) can be estimated in terms of the charge conservation law, Eq. (4). This error is lower than 5% for electrons. For ions it is lower than 10% and can be neglected if ion charge balance is carried out on the full domain. This higher error is attributable to the interpolation error between the PIC mesh and the magnetic grid at the plasma edge.

Finally, it is interesting to compare the thrust gain due to the MN. Dimensionless thrust of both models is depicted in Figure 8, using the ion momentum plus plasma pressure at the source exit, F_0 , as the reference value. The monotonic HPMN thrust increase correlates very well with the thrust gain obtained by DIMAGNO. The last one includes the contribution of ion momentum flux and plasma pressure, while the thrust computed by HPMN only takes into account the ion momentum flux that flows through each $z = \text{const}$ surface. Despite this difference, HPMN thrust gain is higher than DIMAGNO's. Note that a lower thrust would be expected in the HPMN results because it neglects the plasma pressure contribution. Probably, this variation is due to the fluid-kinetic conversion of the ion flow injected at the MN throat, which might introduce a slight error on plasma momentum conservation law.

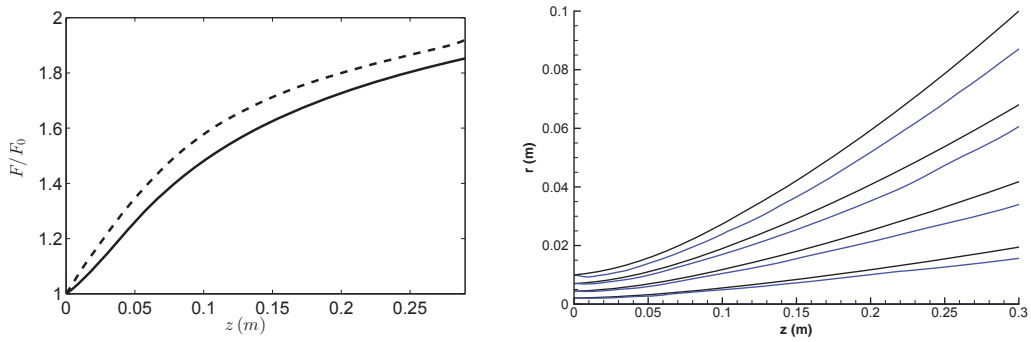


Figure 8. Left: MN dimensionless thrust gain F/F_0 as a function of the MN length z . F_0 is the ion momentum plus the plasma pressure at the source exit section (MN throat). Right: Ion detachment, black solid lines depicts the magnetic stream surfaces, and blue lines show ions streamlines.

Ion detachment is depicted in Figure 8 (right). Ion streamlines, obtained in accordance with the ion current density, clearly detach inwards from the magnetic surfaces. Overall, this result agrees with DIMAGNO, Refs.^{8,13} This behaviour also explains the increasing ion current through magnetic surfaces $I_i > 0$ (Figure 6 right). Near the vacuum edge, where density is lower, ion streamlines should move closer to magnetic surfaces to fulfil the quasineutral-plasma hypothesis.

VI. Conclusion

A comparison between DIMAGNO and HPMN codes, which describe the plasma flow in a magnetic nozzle, has been carried out in terms of main plasma properties, with the aim to validate the later and correlate results.

The cleanness and high resolution of DIMAGNO, inherent to the fluid model and method of characteristics, is unattainable with the hybrid code. Despite this disadvantage, some HPMN results, such as plasma density, electric potential or electron azimuthal velocity, agree very well with fluid model results. Even the thrust gain computed by HPMN correlates closely with DIMAGNO.

The central advantage of HPMN is that it introduces collisions in the nozzle flow, and thus allows to study phenomena not available in DIMAGNO.

Regarding perpendicular diffusion and according to the case simulated here (parameters of Sec. IV), HPMN measures a low electron conductivity across magnetic surfaces. This result supports again the DIMAGNO hypothesis of collisionless plasma.

This work also points out some limitations of HPMN to be overcome in the future. First, the failure of weighting algorithms if the number of particles-per-cell drops as a consequence of the diverging geometry. Second, the response of the PIC subcode is slightly perturbed near the plasma-vacuum edge due to the coarse mesh of the PIC subcode. In this regard, the grid should be refined in order to improve overall accuracy.

Acknowledgments

This work has been sponsored by the Air Force Office of Scientific Research, Air Force Material Command, USAF, under grant number FA8655-12-1-2043. The U.S Government is authorized to reproduce and distribute reprints for Governmental purpose notwithstanding any copyright notation hereon. Additional support comes from the Spanish Government (Project AYA-2010-61699).

References

- ¹Ziamba, T., Carscadden, J., Slough, J., Prager, J., and Winglee, R., "High Power Helicon Thruster," *41th AIAA/ASME/SAE/ASEE Joint Propulsion Conference & Exhibit*, AIAA 2005-4119, 2005.
- ²Batishchev, O., "Minihelicon Plasma Thruster," *IEEE Transaction on Plasma Science*, Vol. 37, 2009, pp. 1563–1571.
- ³Charles, C., Boswell, R., and Lieberman, M., "Xenon ion beam characterization in a helicon double layer thruster," *Applied Physics Letters*, Vol. 89, 2006, pp. 261503.
- ⁴Pavarin, D., Ferri, F., Manente, M., Curreli, D., Guclu, Y., Melazzi, D., Rondini, D., Suman, S., Carlsson, J., Bramanti,

C., Ahedo, E., Lancellotti, V., Katsonis, K., and Markelov, G., "Design of 50W Helicon Plasma Thruster," *31th International Electric Propulsion Conference*, IEPC 2009-205, 2009.

⁵Krülle, G., Auweter-Kurtz, M., and Sasoh, A., "Technology and application aspects of applied field magnetoplasmadynamic propulsion," *J. Propulsion and Power*, Vol. 14, 1998, pp. 754–763.

⁶Tikhonov, V., Semenikhin, S., Brophy, J., and Polk, J., "Performance of 130kw mpd thruster with an external magnetic field and Li as a propellant," *Proceedings of the 25th International Electric Propulsion Conference*, 1997, pp. 728–733.

⁷Diaz, F., Squire, J., Bengtson, R., Breizman, B., Baity, F., and Carter, M., "The Physics and Engineering of the VASIMR Engine," *36th AIAA/ASME/SAE/ASEE Joint Propulsion Conference & Exhibit*, AIAA 2000-3756, 2000.

⁸Ahedo, E. and Merino, M., "Two-dimensional supersonic plasma acceleration in a magnetic nozzle," *Physics of Plasmas*, Vol. 17, 2010, pp. 073501.

⁹Ahedo, E. and Merino, M., "On plasma detachment in propulsive magnetic nozzles," *Physics of Plasmas*, Vol. 18, 2011, pp. 053504.

¹⁰Merino, M. and Ahedo, E., "Simulation of plasma flows in divergent magnetic nozzles," *IEEE Transactions on Plasma Science*, Vol. 39, No. 11, 2011, pp. 2938–2939.

¹¹Navarro, J. and Ahedo, E., "Hybrid model simulation of a plasma plume in a magnetic nozzle," *32th International Electric Propulsion Conference, Wiesbaden, Germany*, IEPC 2011-048, 2011.

¹²Parra, F., Ahedo, E., Fife, M., and Martínez-Sánchez, M., "A two-dimensional hybrid model of the Hall thruster discharge," *Journal of Applied Physics*, Vol. 100, 2006, pp. 023304.

¹³Merino, M. and Ahedo, E., "Magnetic Nozzle Far-Field Simulation," *48th AIAA/ASME/SAE/ASEE Joint Propulsion Conference & Exhibit*, No. AIAA-2012-3843, AIAA, Washington DC, 2012.

¹⁴Zucrow, M. and Hoffman, J., *Gas dynamics*, Wiley, New York, 1976.

¹⁵Merino, M. and Ahedo, E., "Plasma detachment mechanisms in a magnetic nozzle," *47th AIAA/ASME/SAE/ASEE Joint Propulsion Conference & Exhibit*, No. AIAA-2011-5999, AIAA, Washington DC, 2011.

¹⁶Ahedo, E. and Merino, M., "Preliminary assessment of detachment in a plasma thruster magnetic nozzle," *46th AIAA/ASME/SAE/ASEE Joint Propulsion Conference & Exhibit*, No. AIAA 2010-6613, AIAA, Washington DC, 2010.

¹⁷Ahedo, E. and Merino, M., "On electron inertia and current ambipolarity in magnetic nozzles models," *32th International Electric Propulsion Conference, Wiesbaden, Germany*, edited by F. Electric Rocket Propulsion Society, IEPC 2011-050, 2011.

¹⁸Ahedo, E. and Merino, M., "Two-dimensional plasma expansion in a magnetic nozzle: separation due to electron inertia," *Physics of Plasmas*, Vol. 19, 2012, pp. 083501.

¹⁹Merino, M., "2D plasma flow in a magnetic nozzle with a bi-modal Electron Energy Distribution Function," *50th AIAA Aerospace Sciences Meeting*, No. AIAA 2012-0139, AIAA, Washington DC, 2011.

²⁰Fife, J., *Hybrid-PIC Modeling and Electrostatic Probe Survey of Hall Thrusters*, Ph.D. thesis, 1998.

²¹Navarro, J., Merino, M., and Ahedo, E., "A fluiddynamic performance model of a helicon thruster," *48th AIAA/ASME/SAE/ASEE Joint Propulsion Conference & Exhibit*, No. AIAA-2012-3955, AIAA, Washington DC, 2012.

²²Ahedo, E., "Parametric analysis of a magnetized cylindrical plasma," *Physics of Plasmas*, Vol. 16, 2009, pp. 113503.

PAGE INTENTIONALLY LEFT BLANK

Magnetic Nozzle Far-Field Simulation

M. Merino* and E. Ahedo†

Universidad Politécnica de Madrid, Madrid 28040 Spain

An analysis of the far-field plasma plume generated by a magnetic nozzle is presented, covering (1) the residual forces on the plasma in the downstream region, (2) the ion self-detachment from the magnetic field and free-plume formation, and (3) a preliminary investigation of secondary physical mechanisms that affect the plasma jet. This study is based on an extended version of our DIMAGNO code that allows simulation beyond the magnetic nozzle turning point. Results for different magnetization degrees show that ions naturally detach from the magnetic field and that the bulk of the plasma does not turn back along the magnetic field, supporting the viability of these devices for plasma propulsion.

I. Introduction

A magnetic nozzle (MN), consisting of an applied convergent-divergent axisymmetric magnetic field, constitutes the main acceleration stage of several advanced plasma propulsion concepts. Illustrative examples are the Helicon thruster,¹⁻⁴ the applied-field MPD thruster^{5,6} and the Variable Specific Impulse Magnetoplasma rocket (VASIMIR).⁷ The purpose of the MN is to harness and control the expansion of the hot plasma in order to deliver a high-velocity, efficient plasma beam, while keeping plasma-wall contact to a minimum. The plasma acceleration through the nozzle results in a magnetic reaction force on the magnetic circuit of the device, producing thrust.⁸ An additional possible advantage of MNs is their ability to tailor thrust and specific impulse in-flight to different mission requirements by changing the geometry and intensity of the applied field.

The plasma in a MN can be roughly divided into two zones: in the acceleration region (or near-field), the supersonic plasma expansion is dominated by the interplay between pressure and magnetic forces. The largest fraction of thrust is generated here. In the detachment region (or far-field), most of the internal energy of the plasma has been already converted into directed kinetic energy, and its evolution is subject to the residual pressure, magnetic and electric fields. At this point, the plasma needs to detach itself from the imposed magnetic field to form a free plume. Failure to do so would result in a substantial amount of plasma turning around along the magnetic lines and coming back to the spacecraft, ruining efficiency, attacking sensitive surfaces, and polluting the environment of the payload.

Modeling and simulation of the different processes in these two regions is fundamental for a good understanding of the physics behind the MN, and an essential step towards the design and optimization of a real device. We have recently studied the acceleration region of the MN with the aid of our DIMAGNO code, a two-fluid, two-dimensional code of the partially magnetized, collisionless plasma flow.⁸ The influence of ion magnetization and field geometry, the acceleration mechanisms, the formation of longitudinal electric currents and the propulsive performances were investigated. Subsequently, a critical review of detachment theories based on plasma-induced magnetic field, plasma resistivity, and electron inertia was undertaken.⁹⁻¹²

At this stage, characterization of the far-region becomes necessary for a proper assessment of the detachment processes in the MN. This article presents a preliminary study of the MN far-field, limited to a low- β , quasineutral, collisionless plasma. To this end, DIMAGNO has been extended to allow the simulation beyond the turning-point of the outermost magnetic streamtube containing plasma, i.e. the MN edge, hence facilitating the study of the plasma far into the downstream region. The paper is structured as follows. Section II briefly highlights the main characteristics of the updated DIMAGNO model. Sections

*PhD student, Equipo de Propulsión Espacial y Plasmas (EP2, web.fnetsia.upm.es/ep2), student AIAA member (mario.merino@upm.es).

†Professor, EP2, senior AIAA member (eduardo.ahedo@upm.es).

III to V pursue the three-fold objectives of this paper: first, we analyze the characteristics and balance of the residual forces in the far-field (section III). Second, we assess the detachment and performances of the produced plasma plume (section IV). Third, we quantify the relevance of secondary effects not included in the model using a perturbation approach (section V), which will provide a valuable indication of the validity of the current model and the necessary extensions for a detailed analysis. Finally, conclusions and concepts requiring further work are gathered in section VI.

II. DIMAGNO model and extension of the code

DIMAGNO's two-fluid model describes the steady-state flow of a fully ionized plasma in a MN. A brief overview of its main aspects is given below. For a detailed description of the model, its equations and the integration procedure, the reader is directed to our previous articles.^{8,9,13} The notation followed in this paper is the same as the one therein.

The general equation of motion for a simply-charged species j in a magnetic field B is

$$m_j n_j (\mathbf{u}_j \cdot \nabla) \mathbf{u}_j = -\nabla \cdot \mathcal{P} + q_j n_j (-\nabla \phi + \mathbf{u}_j \times \mathbf{B}) + \mathbf{R}_j, \quad (1)$$

where \mathcal{P} is the pressure tensor, and $\mathbf{R}_j = \pm m_e \nu_{ei} (\mathbf{u}_i - \mathbf{u}_e)$ the corresponding resistive term for each species (minus sign for ions, plus for electrons). Under the hypotheses of (1) quasineutral ($n_i = n_e \equiv n$), collisionless plasma, (2) fully-magnetized, isothermal electrons of negligible inertia, and (3) cold ions, the longitudinal and azimuthal ion equations of motion can be written as

$$m_i \left(\frac{\tilde{u}_i^2}{\rho_i} \mathbf{1}_{\perp i} + \frac{1}{2} \frac{\partial \tilde{u}_i^2}{\partial \mathbf{1}_{\parallel i}} \mathbf{1}_{\parallel i} \right) = -e \nabla \phi + e u_{\theta i} B \mathbf{1}_{\perp}, \quad (2)$$

$$m_i r u_{\theta i} + e \psi = D_i (\psi_i), \quad (3)$$

whereas the longitudinal electron equation is:

$$0 = -T_e \nabla \ln n + e \nabla \phi - e u_{\theta e} B \mathbf{1}_{\perp}. \quad (4)$$

Note that a collisionless, electron-magnetized flow is a requisite for proper magnetic confinement and thus for an efficiently designed MN thruster. In these expressions, ρ_i and \tilde{u}_i are the meridional curvature radius and velocity of ions, ψ is the magnetic streamfunction, and D_i is a property of the ion streamtube, known from the initial flow conditions. Here, $\mathbf{1}_{\parallel i}$, $\mathbf{1}_{\perp i}$ and $\mathbf{1}_{\parallel}$, $\mathbf{1}_{\perp}$ are meridional unit vectors parallel and perpendicular to ion and magnetic streamtubes, respectively. Full electron magnetization implies $\mathbf{u}_e = \tilde{u}_e \mathbf{1}_{\parallel} + u_{\theta e} \mathbf{1}_{\theta}$, and requires dropping the azimuthal electron equation (which can be used to calculate $u_{\perp e}$ as a correction^{9,12}). A consequence of this is electron isorotation,⁸ i.e., $u_{\theta e}/r = u_{\theta e}(\psi)$.

Equations (2)–(4) plus the relevant continuity equations (not shown here) constitute a hyperbolic set for the supersonic plasma flow that is integrated from an initial section using the method of characteristics (MoC).^{8,14} This approach endows DIMAGNO with high accuracy and speed. The magnetic field is calculated analytically for any distribution of current loops. For moderate plasma- β cases, the plasma-induced magnetic field \mathbf{B}_p (which would make the system elliptic) can also be taken into account with a simple iterative process,¹¹ by taking $\mathbf{B} = \mathbf{B}_a + \mathbf{B}_p$, with \mathbf{B}_a the externally-applied field.

DIMAGNO's algorithm has been rewritten to perform the integration in the intrinsic coordinates of the ion trajectories, instead of propagating the characteristic lines in the cylindrical coordinates with z as the parameter. This improvement permits to integrate around and beyond the turning point of the MN, which was previously infeasible when characteristic lines became vertical. Additionally, this upgrade has proven to enhance integration speed and accuracy, which is measured as the error in conservation of total ion momentum and energy.

The resulting model depends on the magnetic field intensity and geometry, and the plasma conditions at the magnetic throat ($z = 0$ and $0 \leq r \leq R$). For the sake of simplicity, the field generated by a simple current loop of radius $R_L = 3.5R$, located at $z = 0$, will conform the MN here. The resulting MN has a mild divergence as depicted in Figure 1, and a turning point located at $(z/R, r/R) \simeq (16, 23)$. The current analysis focuses on MN flows with a simple initial density profile (the one expected to result from a helicon source¹⁵), low plasma- β (i.e., negligible plasma-induced magnetic field), negligible initial ion rotation, and

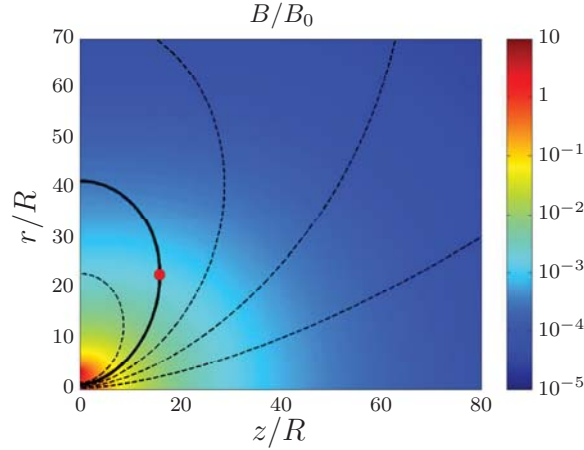


Figure 1. Normalized magnetic field B/B_0 (logarithmic scale) for the single current loop of radius $R_L = 3.5R$. The plasma is injected sonically at the nozzle throat ($z = 0, r \leq R$). Selected magnetic lines have been plotted. The thicker line denotes the last plasma streamline in the model. The turning point of the MN has been denoted with a red dot.

different degrees of ion magnetization. The flow is then completely defined given the plasma properties at the throat:

$$\begin{aligned} \tilde{\mathbf{u}}_i(r) &= \tilde{\mathbf{u}}_e(r) = M_0 c_s, & \phi(r) &= u_{\theta i}(r) = 0, \\ n(r) &= n_0 J_0(ar/R), & u_{\theta e} &= -[T_e/(eB)] \partial \ln n / \partial r \end{aligned} \quad (5)$$

where we will choose $M_0 = 1.01$ to ensure hyperbolicity in the whole divergent domain, and $a = 0.99a_0$ (where $a_0 = 2.405$ is the first zero of the Bessel function of the first kind J_0). Non-dimensional variables are obtained by normalizing with e, m_i, T_e, n_0 and R , and are denoted with a hat (e.g. $\hat{u}_i = \sqrt{m_i/T_e} u_i$). The intensity of the magnetic field is characterized by the non-dimensional ion gyrofrequency at the origin, $\hat{\Omega}_{i0} = eB(0,0)R/\sqrt{m_i T_e}$. A low magnetization case (simulation 1, with $\hat{\Omega}_{i0} = 0.1$) and a high magnetization case (simulation 2, with $\hat{\Omega}_{i0} = 100$) will be used in the discussions of the following sections. The low ion magnetization case yields in practice the unmagnetized-ion solution. These two simulations cover most of the spectrum of envisaged applications (see tables 1 and 2).

m_i , Kg	10^{-27} – 10^{-25} (H–Xe)
B_0 , G	200–10000
T_e , eV	5–50
n_0 , m^{-3}	10^{16} – 10^{20}
R , m	0.01–0.1

Table 1. Typical range of main MN parameters, encompassing the wide spectrum of expected propulsion applications. As an example, the helicon thruster of Ref. 2, operating on Argon or Nitrogen, has $B_0 = 1000$ G, $T_e = 20$ eV, $n_0 = 7 \cdot 10^{18} \text{ m}^{-3}$, and $R = 0.01$ m.

$\hat{\Omega}_{i0}$	0.04–500
$\hat{\beta}_0$	10^{-8} –0.1
$\hat{\chi}_0$	10 – 10^9
$\hat{\ell}_{e0}$	$6 \cdot 10^{-5}$ –0.08
$\hat{\lambda}_{D0}$	10^{-5} – 10^{-2}

Table 2. Minimal and maximal values of the non-dimensional plasma parameters at the magnetic throat, based on the expected ranges of operation of table 1: ion gyrofrequency $\hat{\Omega}_{i0} = eB_0 R / \sqrt{m_i T_e}$; plasma beta $\hat{\beta}_0 = \mu_0 n_0 T_e / B_0^2$; Hall parameter $\hat{\chi}_{H0} = \Omega_{e0} / \nu_{ei0}$; electron Larmor radius $\hat{\ell}_{e0} = \sqrt{m_e T_e} / (e B_0 R)$; and Debye length $\hat{\lambda}_{D0} = \sqrt{\epsilon_0 T_e} / (n_0 e^2) / R$. The large ratio of the parameter m_i/m_e is 1837 for Hydrogen and 239327 for Xenon.

III. Far-field force balance

The far-field plasma expansion is presented in Figure 2, where it is seen that density decreases by several orders of magnitude after the plasma passes the turning point (marked in red in Figure 1). Interestingly, the largest decrease takes place in the peripheral plasma. Both simulations yield very similar results, suggesting that magnetization has little influence in the considered range.

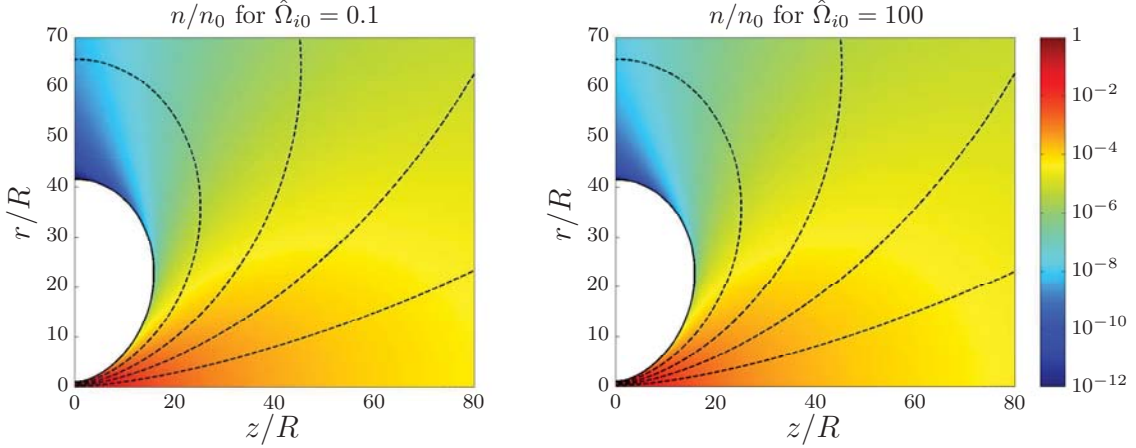


Figure 2. Normalized plasma density n/n_0 (logarithmic scale) in the far-field plume and beyond the turning point of the magnetic field. Magnetic tubes have been indicated in dashed lines. Left: low magnetization; right: high magnetization. Density in the periphery of the plasma is higher in the high-magnetization case.

The forces on the electron fluid control the expansion of the plasma in the MN. According to Eq. (4), a delicate equilibrium forms between the pressure ($-\nabla p_e$), electric ($en\nabla\phi$) and magnetic ($-enu_{\theta e}B\mathbf{1}_{\perp}$) forces. All three rapidly decrease as the plasma moves into the far region, as can be anticipated by the evolution of density in Figure 2. In spite of this, it is found that the magnitude of these forces per unit particle roughly remains in the same order of magnitude through the far plume, decreasing only at a very low rate. Figure 3 displays the perpendicular pressure gradient per electron, $(\partial p_e/\partial\mathbf{1}_{\perp})/\hat{n}$, providing a sense of the magnitude of all other forces-per-particle as well. Throughout the expansion, perpendicular pressure always acts in the outward direction, i.e., $\partial p_e/\partial\mathbf{1}_{\perp} > 0$, and hence electric and magnetic confinement keeps the plasma away from the thruster (even after the turning point). In the parallel direction, however, pressure is only counteracted by the electrostatic forces. The resulting ambipolar electric field, which couples ion and electron motion, simultaneously accelerates ions. Dashed lines in these plots denote the curves where $\partial p_e/\partial z = 0$ and $\partial p_e/\partial r = 0$. They help identify the regions of the plasma where the plasma pressure acts in the $z > 0, r > 0$ direction (region under curve (a)), in the $z < 0, r > 0$ direction (region between both curves), and in the $z < 0, r < 0$ direction (to the left of curve (b)). Visibly, magnetization degree has only a small influence on them in the range under study.

The competition between electric and magnetic forces to confine the perpendicular pressure defines the character of the expansion. Figure 4 presents the perpendicular magnetic-to-pressure force ratio for the low and high magnetization cases. While initially only \mathbf{B} confines the plasma, perpendicular electric fields gradually develop and these gain importance until they eventually dominate the magnetic force. The larger magnetization in simulation 2 results in a larger region of dominance of magnetic forces that extends well into the downstream region. This is a consequence of ions requiring less $E_{\perp i}$ field to expand according to the geometry of the MN, as the perpendicular magnetic force on ions increases the higher $\hat{\Omega}_{i0}$ is (see section IV below). Nevertheless, in all cases electric confinement progressively gains in importance in the far-field. This natural evolution of the force ratio illustrates the smooth transition from a magnetized plasma to a free plume, where the external magnetic interaction must ultimately become negligible.

Regarding the collective behavior of ions and electrons, the model shows that the residual longitudinal magnetic force on the plasma (which is the only external force in the MN), albeit small, is still beneficial. This force continues to confine the plasma locally in the far-field, pushing it away from the thruster even beyond the turning point and hence contributing (minimally) to thrust. Assuming $B_r > 0$ in $(z, r) > 0$

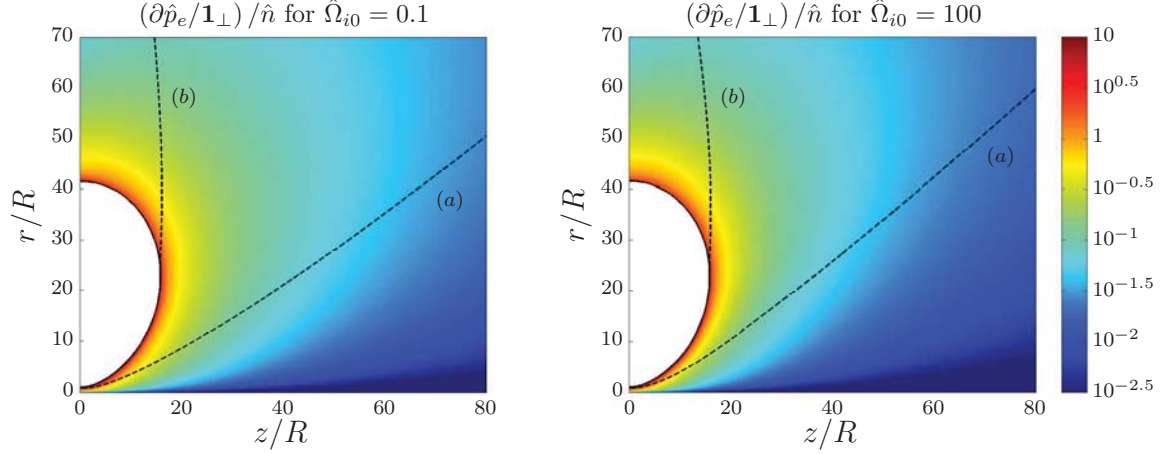


Figure 3. Non-dimensional pressure force per unit particle in the perpendicular direction, $(\partial p_e / \partial \mathbf{1}_\perp) / \hat{n}$ (logarithmic scale). The lines of $\partial p_e / \partial z = 0$ (a) and $\partial p_e / \partial r = 0$ (b) are also shown in the figure. Left: low magnetization; right: high magnetization.

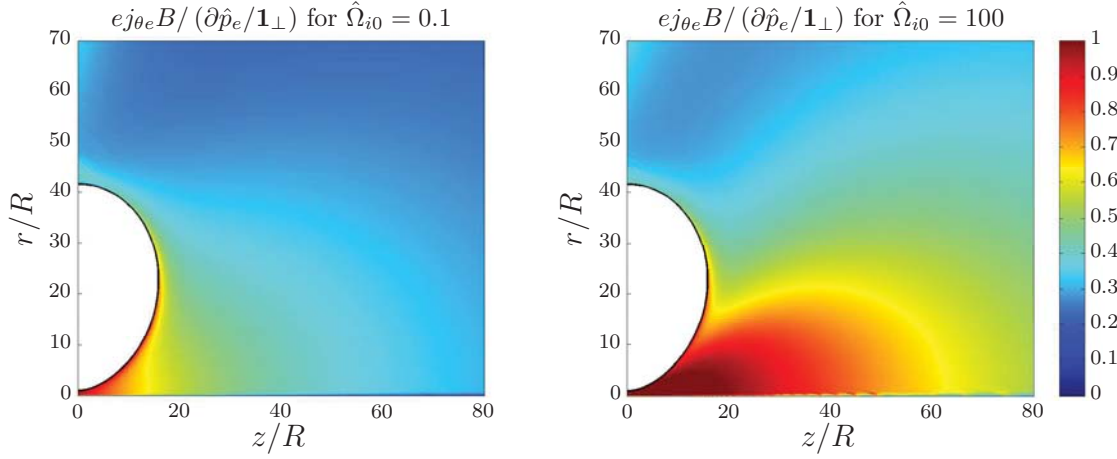


Figure 4. Magnetic-to-pressure force ratio on electrons in the far-field, $e j_{\theta e} B / (\partial p_e / \partial \mathbf{1}_\perp)$. Electric and magnetic perpendicular forces sum up to confine the perpendicular pressure. Left: low magnetization; right: high magnetization.

without loss of generality, the condition for local positive thrust is $u_{\theta i} - u_{\theta e} < 0$, or analogously,

$$\frac{D_i(\psi_i) - e\psi}{m_i r} < r w_{\theta e}(\psi). \quad (6)$$

This is fulfilled in a cylindrical hot plasma in equilibrium (as those expected at the MN throat in propulsive applications), independently of the initial rotation of ions, since the combined magnetic force on ions and electrons needs to confine the existing pressure. Expression (6) helps find regions of the MN, if any, where the magnetic force can reverse, i.e., act to expand and decelerate the plasma. Interestingly, this inversion does not take place in the studied hot plasmas in the region of analysis, not even in the simulation with $\hat{\Omega}_{i0} = 100$ (representative of a practical high-limit case with high $u_{\theta i}$ and low $u_{\theta e}$). In conclusion, the residual magnetic field in the plume should not be regarded as detrimental, for its absence would result in less confinement, and consequently, a more divergent plume. Therefore, the lack of magnetic detachment, in the sense of liberating the plasma from the external magnetic field, constitutes a problem *only* when/where $u_{\theta i} - u_{\theta e} > 0$.

IV. Ion self-detachment and nozzle performance

The motion of ions responds to the geometry of the applied field and the magnetized electron dynamics, as it adapts to fulfill quasineutrality in the plasma domain. When the (small) centrifugal term in $u_{\theta i}^2$ is

neglected, Eq. (2) indicates that longitudinal ion trajectory curvature radius ρ_i results from a combination of electric ($eE_{\perp i}$) and magnetic ($eu_{\theta i}B_{\parallel i}$) forces on the ions. A perpendicular electric field develops when ion magnetization is insufficient by itself to deflect the ion trajectories as commanded by the MN. Clearly, the high-magnetization case requires much lower perpendicular fields in order to accomplish the ion expansion (see Figure 4). From Eq. (2), we find that

$$\rho_i \simeq m_i \tilde{u}_i^2 (eE_{\perp i} + eu_{\theta i}B_{\parallel i})^{-1}, \quad (7)$$

which highlights the rapid growth of ρ_i in the far-field as u_i increases (see Figure 5), and both the electric and magnetic fields decrease. This expression predicts an eventual transition to almost conical ion streamtubes, which gradually separate from their initial magnetic tubes. This trend is observed in Figure 5, which shows the ion and magnetic streamlines, and ion velocity in the background. It is clear that most of the ion flow *does not turn around with the field*.

Additionally, the perpendicular electric field required for the deflection is associated to a large perpendicular rarefaction, as was seen in Figure 2. This behavior is beneficial, as the bulk of the plasma remains in the core of the plume and hence radial losses are kept small. Only a tiny fraction of the peripheral ions are required to expand beyond the turning point in order to fulfill quasineutrality in this region. This separation of ions from the field can be termed *ion self-detachment*, and facilitates the formation of a free plume.

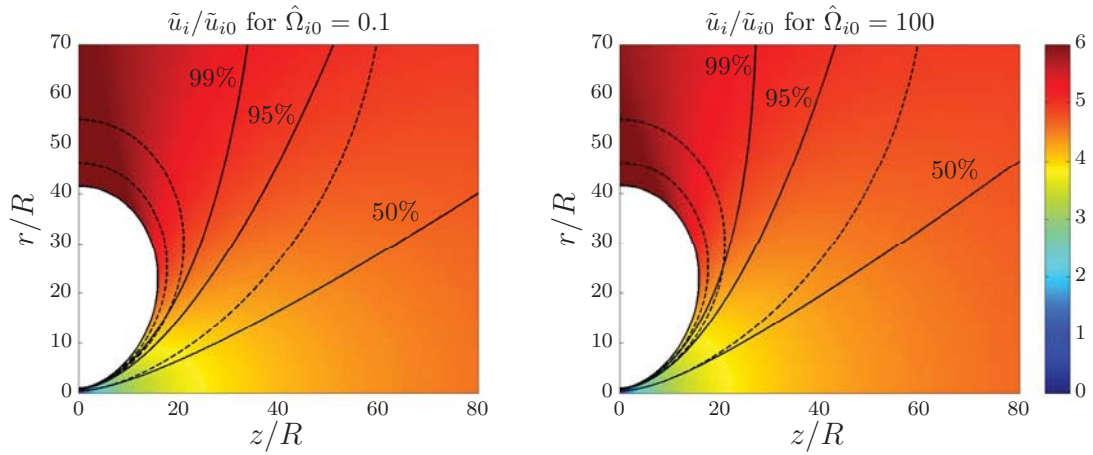


Figure 5. Ion (solid) and magnetic (dashed) streamtubes for both simulations. Each pair of lines initially coincide at the nozzle throat. The tubes of 99% mass flow and initially-coincident magnetic tubes are shown as thicker lines. Normalized ion velocity u_i/u_{i0} (coincident with Mach number M in this isothermal plasmas) is plotted on the background. Left: low magnetization; right: high magnetization.

Magnetization is a key parameter to the final angle of ion trajectories and to the amount of coming-back plasma, as observed in Figure 5. Ions remain attached to the field roughly until $\hat{\Omega}_i \sim 1$. However, the fast decrease of Ω_i ($\Omega_i/\Omega_{i0} = B/B_0$, which is plotted on Figure 1) means that, even for the high magnetization simulation with $\hat{\Omega}_{i0} = 100$, this occurs already before $z/R \simeq 20$. Hence, a much higher $\hat{\Omega}_{i0}$ is needed to keep ions magnetized beyond the turning point ($\hat{\Omega}_{i0} > 10^3$). This explains the slow increase of ion attachment with initial magnetization, and incidentally, also the small differences of n and other variables between each simulation.

It must be noted that the loss of a small fraction of the jet due to back-flowing is not unique to MNs. This phenomenon is common and inherent to any jet propulsion system in vacuum, since a fan-expansion forms at the exit of the thruster to fill the surrounding space and a insignificant amount of propellant expands backwards.¹⁴ The particularity of MNs is that they lack the well-defined “end” that their solid counterparts have, making it difficult to assign them a clear value of the thrust gain and other performance figures, while in solid nozzles these can be evaluated at the exit section. These losses are acceptable when they constitute a negligible fraction of the plume flux. In consequence, a sensible approach to study the propulsive performances of a MN flow is to focus on the bulk of the plume (e.g., the ion tube containing 99% of the ion flux) and neglecting the plasma outside of it. Figure 6 presents thrust and plume efficiency of the plasma contained within the 99% ion mass flow tube, resp. $F_{99\%}$ and $\eta_{plume,99\%}$. These are defined

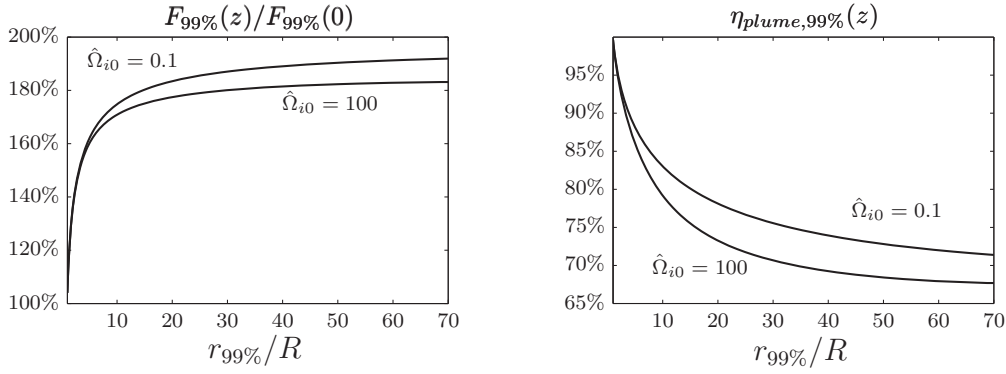


Figure 6. Evolution of thrust and plume efficiency of the plasma contained in the 99% mass flux tube for the low and high magnetization cases. The lines are plotted against $r_{99\%}$, radius of this tube.

as integrals on $z = \text{const}$ sections from the axis to $r = r_{99\%}(z)$, the radius of the 99%-flux tube,

$$F_{99\%}(z) = 2\pi \int_0^{r_{99\%}(z)} nr (m_i u_{zi}^2 + T_e) dr, \quad \eta_{plume,99\%}(z) = \frac{\int_0^{r_{99\%}(z)} nr (m_i u_{zi}^3) dr}{\int_0^{r_{99\%}(z)} nr (m_i u_i^2 u_{zi}) dr}, \quad (8)$$

and can be calculated at any z (as long as the 99% mass flux line does not turn around). These plots indicate that a higher $\hat{\Omega}_{i0}$ leads to worse MN performances, in agreement with Ref. 8, and also suggest that the rate of variation of these values progressively decreases downstream, where both thrust and efficiency become almost constant (apparently approaching free plume values).

V. Other far-field phenomena and model validity

Apart from the dominant forces described in section III, a number of additional physical effects are present in the plasma, but have been neglected in the model. Although these effects are negligibly small in the near-field of an efficient MN, their role may gain importance or even dominate the expansion in the far-field as the ordering of terms changes in the plasma equations. A careful look is required in order to assess the range of validity of the model, find out which hypotheses are likely to break first, and improve our understanding of how plasma evolves in the plume.

This section aims to explore the significance of the following phenomena in the downstream region: (1) the plasma-induced magnetic field, (2) ion-electron collisions, (3) electron finite Larmor radius (FLR) effects and (4) non-neutral effects. The approach followed here is to analyze the magnitude of these effects as a perturbation to the solution of the ideal model of section II. The forces of all these effects are essentially plasma internal interactions, and as such they can alter the plasma flow but do not directly participate in thrust generation. The interaction between plasma azimuthal currents and the applied field is still the only externally applied force and the only source of thrust in the MN.⁸ In addition to the enumerated effects, others such as the presence of ambient particles or background fields could also affect the plume, but these will not be discussed here.

The plasma-induced magnetic field \mathbf{B}_p created by the azimuthal currents was studied in Ref. 11 in the near-field of a medium- β plasma. There, it is shown that the relevant parameter for the quantification of B_p/B_a is the local beta $\beta = \mu_0 n/B^2$, which has been plotted in Figure 7 for simulation 1 based on the solution of the ideal model. Notice that the ratio β/β_0 behaves alike in both simulations due to the similar distribution of density n in the far-field. This figure indicates that induced field effects progressively and monotonically become more important in the far-field in the bulk of the plasma, since n decreases slower than B^2 there. This means that, eventually, a region of $\beta = 1$ will occur downstream, and \mathbf{B}_p will dominate in the plume thereafter. The induced magnetic field affects mainly the core of the plasma (denser), while leaving the peripheral plasma near the MN edge essentially unaffected. The tendency of B_p (diamagnetic character with respect to B_a) is to expel the field out of the plasma domain. Our preliminary analysis of B_p (Ref. 11) showed that this increases the divergence rate of the nozzle, and can give rise to magnetic separatrices and field-reversed configurations in the plume. A detailed study of these possibilities will be object of future work.

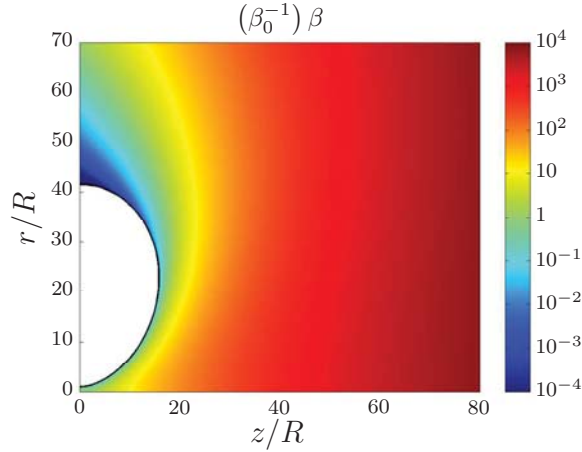


Figure 7. Relative plasma beta β in the MN (logarithmic scale; based on the unperturbed solution), for the $\hat{\Omega}_{i0} = 0.1$ simulation. The normalization with respect to β_0 allows to remove the dependency on the initial conditions. This figure is essentially the same in the $\hat{\Omega}_{i0} = 100$ case, as density behaves similarly in both (see Figure 2). The expected range of values of β_0 can be found in table 2.

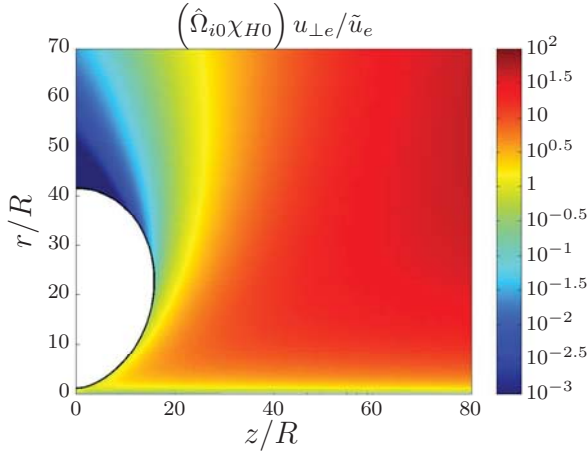


Figure 8. Relative cross-field electron diffusion velocity due to collisions, $u_{\perp e}/u_{\parallel e}$ (as a perturbation to the ideal solution), for the $\hat{\Omega}_{i0} = 0.1$ simulation. The normalization with $\hat{\Omega}_{i0}\chi_{H0}$ helps this figure describe both simulation cases, as χ_H/χ_{H0} (and, consequently, the value plotted here) behaves very similarly in both. χ_{H0} expected range can be found in table 2.

Collisions can facilitate the outwards diffusion of electrons across the B field.^{9,10} An adequately high Hall parameter $\chi_H = \Omega_e/\nu_{ei}$, with $\nu_{ei} \propto n/T_e^{3/2}$, ensures negligible plasma resistivity effects, since the cross-field velocity is $u_{\perp e} = u_{\theta e}/\chi_H$ (see Eq. (6) of Ref. 9). The Hall parameter χ_H remains almost constant in the core of the plume and increases several orders of magnitude in the rarefied, peripheral plasma. Note that, due to its dependency on $u_{\theta e}$, the cross-field diffusion $u_{\perp e}$ further decreases for higher $\hat{\Omega}_{i0}$, because the azimuthal velocity satisfies $\hat{u}_{\theta e} \propto 1/\hat{\Omega}_{i0}$. In first approximation, $u_{\perp e}$ can be calculated as a perturbation to the zeroth-order solution. The ratio $u_{\perp e}/\tilde{u}_e$ —which measures the local electron- magnetic field separation—is shown in Figure 8. This ratio increases slowly downstream for intermediate radial positions in the plasma, suggesting that electron trajectories can ultimately separate outwards from the magnetic field in the far plume, as $u_{\perp e}$ becomes more important due to collisions. Consequently, this means that resistivity can eventually break the weak residual magnetic confinement in the far plume.

Electron FLR effects (or electron inertia) can also affect the electron trajectories, separating them from the magnetic field. At least one of the multiple FLR effects detaches electrons outwards of the magnetic field,^{9,10,12} thus increasing the effective nozzle divergence rate in a similar fashion to collisions. A small ratio of electron Larmor radius ($\ell_e = \sqrt{T_e m_e}/(eB)$) to electron meridional curvature radius, ℓ_e/ρ_e , indicates proper electron magnetization and inconsequential electron FRL effects.¹² This ratio is displayed in Figure 9, where it can be seen that the largest increase takes place in the periphery of the plume, and well beyond the

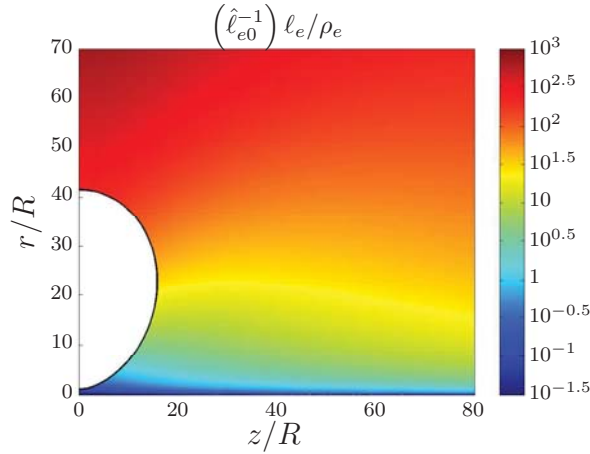


Figure 9. Larmor-to-curvature ratio for electrons, ℓ_e/ρ_e (logarithmic scale). The plot has been normalized with $\hat{\ell}_{e0}$ to remove the dependency on initial plasma conditions and field intensity, making this graph equally valid for both simulation cases. Based on the full electron magnetization solution, $\rho_e \equiv \rho_B$, where $\rho_B = (\mathbf{B}/B \cdot \nabla) (\mathbf{B}/B)$ is the magnetic curvature radius. Table 2 contains the expected range of values of $\hat{\ell}_{e0}$.

MN turning point. Consequently, initially well-magnetized electrons (i.e., $\hat{\ell}_{e0} \ll 10^{-2}$) remain so in most of the far plume, as electron FLR effects grow very slowly in the downstream direction.

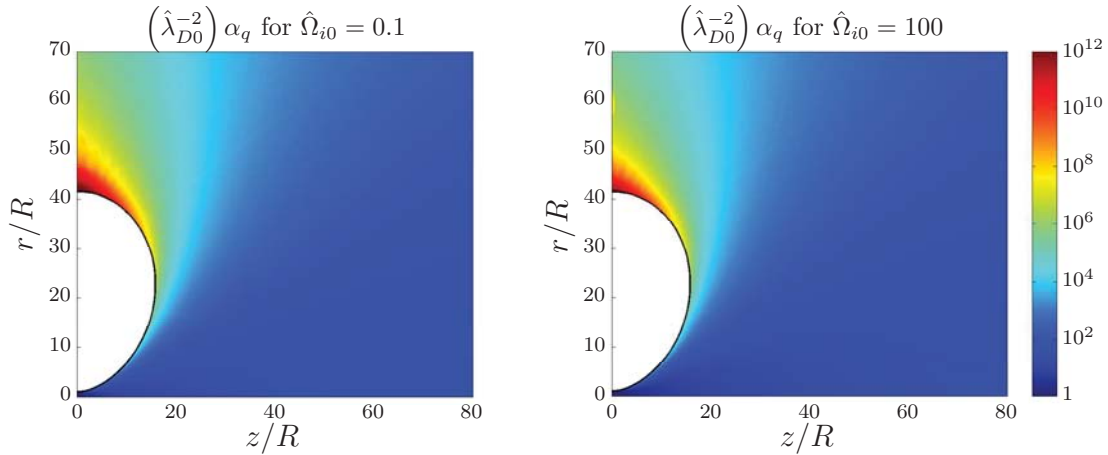


Figure 10. Relative charge density α_q . The factor λ_{D0}^{-2} removes the dependence on initial conditions. Left: low magnetization; right: high magnetization. Table 2 contains the expected range of values of $\hat{\lambda}_{D0}$.

Lastly, the strong rarefaction that takes place in the plume—and specially near the plasma edge—can give rise to non-neutral phenomena, breaking the hypothesis of quasineutrality. Quasineutrality was established to substitute the Poisson equation,

$$\varepsilon_0 \nabla^2 \phi = e (n_e - n_i), \quad (9)$$

with $n_i = n_e \equiv n$. The adequacy of this assumption can be checked quantitatively by analyzing the relative charge density $\alpha_q = (n_i - n_e)/n_e$ that results from introducing the potential ϕ of the quasineutral solution into Eq. (9),

$$\alpha_q = -\hat{\lambda}_{D0}^2 \frac{\hat{\nabla}^2 \hat{\phi}}{\hat{n}}, \quad (10)$$

where λ_{D0} is the Debye length of the plasma at the origin. The relative space-charge in the MN is displayed in Figure 10. Clearly, it is negligible in most of the domain for the expected application values of λ_{D0} (see Table 2). However, the large increment near the border of the plasma jet after the turning point suggests that non-neutral effects can be important in this region and that the quasineutrality hypothesis does not hold except for the coldest, densest plasmas (smaller λ_{D0}). Magnetization seems to play a little role on this in the considered range. Non-neutral effects in the periphery of the plasma plume will certainly modify the

quasineutral solution, as they set a bound to the increase of the perpendicular electric field, which is the responsible of pushing sideways the ion flow. Therefore, they are expected to further enhance ion detachment from the magnetic field. A detailed study is needed to clarify the consequences of the non-neutral region.

As a final comment to this section, electron cooling (not contemplated in the current model due to the lack of information on the evolution of the electron energy distribution function, and at any rate expected to be small—see for instance Ref. 16) would contribute to reduce the plasma beta β , slightly increase the collision frequency ν_{ei} , and reduce electron Larmor radius ℓ_e . Additionally, the discussed mechanisms can interact with each other. For instance, the induced magnetic field \mathbf{B}_p tends to counteract the applied magnetic field \mathbf{B}_a , thus resulting in a lower effective magnetic field, a lower Hall parameter χ_H , and hence a more important role of collisions.

VI. Conclusions and future work

An analysis of the far-field plasma plume of a magnetic nozzle has been carried out, covering the expected application range of ion magnetization. The balance of residual forces, the gradual detachment of ions, and nozzle performances, have been studied thanks to an improved version of our DIMAGNO code.

Pressure, magnetic and electric forces per particle are all comparable in the far region. Magnetization strength has a large influence on the extent of the region where magnetic forces dominate confinement. As the free-plume forms, the confining electric force gradually gains importance. A criterion was presented to assess whether the applied magnetic field is locally beneficial or detrimental for acceleration and confinement in the plume. This condition was always met in the region under study for all magnetization degrees considered.

Ion and magnetic streamtubes closely coincide until $\tilde{\Omega}_i \sim 1$ roughly, after what ion tubes separate and become almost conical as \tilde{u}_i grows. This result highlights that “plasma detachment” does not constitute an issue in the operation of a magnetic nozzle, as the bulk of the plasma naturally separates and forms a free plume. Indeed, only a negligible amount of plasma ($< 1\%$) turns around along the magnetic lines in the studied cases.

Additionally, a preliminary investigation of secondary physical mechanisms in the far plume has been performed using a perturbation approach. The region of validity of each model hypothesis has been discussed based on the throat value of certain parameters. The rapid increase in plasma beta β suggests that induced magnetic field will likely be the first effect to modify the solution in the expected operation regimes. The demagnetization that ensues can enhance other secondary effects such as collisions and electron inertia. Also, we have argued that quasineutrality may not be met at the plasma edge beyond the nozzle turning point.

A more detailed study of these effects must follow to ascertain these results, to better understand their role in the plume formation, and to preclude any negative interaction among them. Other phenomena that have to be carefully examined as well are the influence of ambient plasma and background fields, and the evolution of the electron energy distribution function. Our group is currently developing a hybrid PIC/fluid code named HPMN for the advanced simulation of collisional magnetic nozzle flows,¹⁷ which is proving to be a valuable tool to investigate these aspects.

In summary, all results support the applicability of magnetic nozzles to space propulsion as an efficient mechanism for plasma acceleration and collimated plume formation thanks to the self-detachment of ions. Furthermore, the magnetic field should be kept to a minimum while complying with all other requirements for proper operation, in order to reduce the free-plume divergence angle and to improve overall performance.

Acknowledgments

This work has been sponsored by the Air Force Office of Scientific Research, Air Force Material Command, USAF, under grant number FA8655-12-1-2043. The U.S Government is authorized to reproduce and distribute reprints for Governmental purpose notwithstanding any copyright notation hereon. Additional support for this research was provided by the Gobierno de España (Project AYA-2010-61699).

References

¹Ziembra, T., Carscadden, J., Slough, J., Prager, J., and Winglee, R., “High Power Helicon Thruster,” *41th AIAA/ASME/SAE/ASEE Joint Propulsion Conference & Exhibit*, AIAA 2005-4119, 2005.

²Batishchev, O., “Minihelicon Plasma Thruster,” *IEEE Transaction on Plasma Science*, Vol. 37, 2009, pp. 1563–1571.

- ³Charles, C., Boswell, R., and Lieberman, M., "Xenon ion beam characterization in a helicon double layer thruster," *Applied Physics Letters*, Vol. 89, 2006, pp. 261503.
- ⁴Pavarin, D., Ferri, F., Manente, M., Curreli, D., Guclu, Y., Melazzi, D., Rondini, D., Suman, S., Carlsson, J., Bramanti, C., Ahedo, E., Lancellotti, V., Katsonis, K., and Markelov, G., "Design of 50W Helicon Plasma Thruster," *31th International Electric Propulsion Conference*, IEPC 2009-205, 2009.
- ⁵Krülle, G., Auweter-Kurtz, M., and Sasoh, A., "Technology and application aspects of applied field magnetoplasmadynamic propulsion," *J. Propulsion and Power*, Vol. 14, 1998, pp. 754–763.
- ⁶Tikhonov, V., Semenikhin, S., Brophy, J., and Polk, J., "Performance of 130kw mpd thruster with an external magnetic field and Li as a propellant," *Proceedings of the 25 th International Electric Propulsion Conference*, 1997, pp. 728–733.
- ⁷Diaz, F., Squire, J., Bengtson, R., Breizman, B., Baity, F., and Carter, M., "The Physics and Engineering of the VASIMR Engine," *36th AIAA/ASME/SAE/ASEE Joint Propulsion Conference & Exhibit*, AIAA 2000-3756, 2000.
- ⁸Ahedo, E. and Merino, M., "Two-dimensional supersonic plasma acceleration in a magnetic nozzle," *Physics of Plasmas*, Vol. 17, 2010, pp. 073501.
- ⁹Ahedo, E. and Merino, M., "On plasma detachment in propulsive magnetic nozzles," *Physics of Plasmas*, Vol. 18, 2011, pp. 053504.
- ¹⁰Ahedo, E. and Merino, M., "Preliminary assessment of detachment in a plasma thruster magnetic nozzle," *46th AIAA/ASME/SAE/ASEE Joint Propulsion Conference & Exhibit*, No. AIAA 2010-6613, AIAA, Washington DC, 2010.
- ¹¹Merino, M. and Ahedo, E., "Plasma detachment mechanisms in a magnetic nozzle," *47th AIAA/ASME/SAE/ASEE Joint Propulsion Conference & Exhibit*, No. AIAA-2011-5999, AIAA, Washington DC, 2011.
- ¹²Ahedo, E. and Merino, M., "Two-dimensional plasma expansion in a magnetic nozzle: separation due to electron inertia," *Physics of Plasmas*, Vol. 19, 2012, pp. 083501.
- ¹³Merino, M. and Ahedo, E., "Simulation of plasma flows in divergent magnetic nozzles," *IEEE Transactions on Plasma Science*, Vol. 39, No. 11, 2011, pp. 2938–2939.
- ¹⁴Zucrow, M. and Hoffman, J., *Gas dynamics*, Wiley, New York, 1976.
- ¹⁵Ahedo, E., "Parametric analysis of a magnetized cylindrical plasma," *Physics of Plasmas*, Vol. 16, 2009, pp. 113503.
- ¹⁶Inutake, M., Ando, A., Hattori, K., Tobar, H., and Yagai, T., "Characteristics of a Supersonic Plasma Flow in a Magnetic Nozzle," *J. Plasma Fusion Res.*, Vol. 78, 2002, pp. 1352–1360.
- ¹⁷Navarro, J., Merino, M., and Ahedo, E., "Two-Fluid and PIC-Fluid Code Comparison of the Plasma Plume in a Magnetic Nozzle," *48th AIAA/ASME/SAE/ASEE Joint Propulsion Conference & Exhibit*, No. AIAA-2012-3840, AIAA, Washington DC, 2012.

PAGE INTENTIONALLY LEFT BLANK

A fluiddynamic performance model of a helicon thruster

J. Navarro*, M. Merino† and E. Ahedo‡

Universidad Politécnica de Madrid, 28040 Madrid, Spain

A helicon thruster consists of a cylindrical helicon source, where the plasma is generated and heated, and a magnetic nozzle, where the plasma beam is accelerated supersonically. Two dimensional models of the plasma flow inside the source and in the external magnetic nozzle are derived, for a known amount of absorbed power from rf waves. 2D plasma structure and response inside the source are described, comprising the processes of neutral depletion, losses to chamber walls, and backward and forward flows. Conditions for high propellant utilization and high current efficiency are determined. The matching with the magnetic nozzle model yields the overall characterization of helicon thruster performances in terms of power, thrust and efficiency.

I. Introduction

Research in the helicon plasma thruster (HPT) carried out during last years suggests this kind of thruster as a candidate to gain a share in space propulsion. Different prototypes have been tested [1–4]. Opportunities in this challenge remain largely on the thrust efficiency figure. Recent studies [5,6] have measured the thrust of a low magnetic field HPT, obtaining a thrust efficiency below 5%. However, other authors [2,3] claim that good thrust efficiency can be achieved. The possibility of operating with different propellants and the lack of electrodes are other valuable assets of the HPT. Otherwise, the complexity of the physics involved, plasma-wave interaction coupled with the flow dynamics of the magnetized plasma, has forced, so far, to analyze separately each physical process within the HPT.

Summarily, a helicon thruster, Fig. 1, can be divided into two parts: (i) the helicon source where plasma is produced (purple coloured) and (ii) the magnetic nozzle (MN) in which plasma is guided and accelerated (blue coloured). In the sketch and in the simulations presented later, a Maxwell coil set is used to generate the magnetic field in the source and in the MN. This kind of coils arrangement produces an almost constant ($\nabla|\mathbf{B}| \sim 0$) axial magnetic field along the dielectric tube (light green), that diverges smoothly downstream, forming the MN.

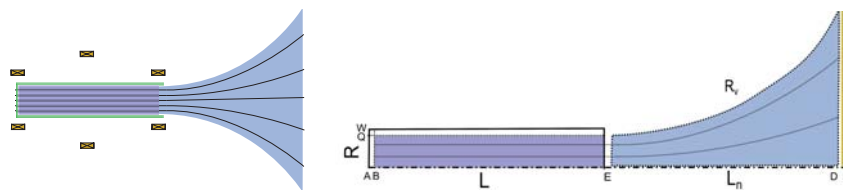


Figure 1. Helicon thruster sketch (left) and splitting into source and nozzle (right), labelling each part or main dimensions.

Inside the source, the plasma is quasineutral except at Debye sheaths, AB and QW, attached to the rear and lateral walls, respectively. At the source exit section E the plasma is assumed to flow sonically. Source and whole thruster efficiencies depend on the ionization degree reached inside the source. Along the

*PhD Student, jaume.navarro@upm.es, Full Adress: ETSI Aeronáuticos, Plaza Cardenal Cisneros, 28040 Madrid, Spain, Student AIAA Member.

†PhD Student, mario.merino@upm.es.

‡Professor, eduardo.ahedo@upm.es, Senior AIAA Member.

MN, from E until collecting plate P, the plasma beam is accelerated supersonically. As discussed later, the helicon thruster power balance, under the isothermal plasma hypothesis, requires to consider the whole cloud of confined electrons. For this reason and lacking a plasma detachment model, the conductive plate P has been included to close downstream the problem; a Debye sheath DP develops at the plate.

It is suitable to split the helicon thruster plasma physics in two mechanisms: (i) the plasma-wave interaction and (ii) the plasma flow dynamics. Regarding the first mechanism, an external antenna (not sketched in Fig. 1) is wrapped around the dielectric tube. This antenna emits RF waves which propagate within the plasma as helicon waves [7]. Thanks to plasma-wave interaction mechanisms, electromagnetic power is absorbed by the plasma [8–10]. The plasma-wave interaction process is not considered here: we will just assume that the plasma absorbs a power P_a from the rf emission. This work is devoted exclusively to study the plasma flow dynamics.

The previous description of HPT parts, points out the possibility of dividing the HPT fluid model into 'source' and 'magnetic nozzle' models. Furthermore, plasma properties in each sub-domain are different, allowing to assume different hypotheses. First, a 2D axisymmetric model of the source is derived following a variable-separation procedure in the radial and the axial direction. This technique was applied successfully by Ahedo et al. [11] in a Hall thruster. Fruchtman et al. [12,13] where the first to apply it to a helicon source. Later, Ahedo [14] introduced several improvements and modifications in that model, such as: a 2D model of neutral depletion, a more consistent model of radial dynamics, an analytic solution of axial dynamics, and parametric studies of source performances.

Fruchtman et al. [12] proposed cleverly that the relation between the constant plasma temperature T_e and the absorbed power could be obtained from a global energy balance. However, they consider only the plasma source region for that balance. Here, we will show this to be inconsistent: the whole plasma region (i.e. source plus MN) needs to be considered for that balance. To achieve this purpose, the MN model of Ref. [15] is here matched with the source at section E. As commented before, plasma properties in the MN admit to modify partially some hypotheses. The MN model assumes the supersonic expansion of a collisionless, fully-ionized plasma. A slight mismatching between source and MN models might introduce a discontinuity in plasma properties at E. Nevertheless, if propellant utilization is high enough, the mismatching is small and overall performances in terms of thrust efficiency and power contributions are obtained.

The rest of the paper is organized as follows. Section II derives the helicon source fluid model. Then, sections III and IV provide, respectively, the plasma structure within the source and its performances. The matching between the source and the MN is presented in section V, in which overall thrust and power balances are carried out. Finally, main conclusions are summarized in section VI.

II. Helicon source plasma model

This model is basically the one derived in Ref. [14] so only a summary is presented here. An axisymmetric plasma is immersed in an axial magnetic field $\mathbf{B} = B\mathbf{1}_z$. The zero-Debye limit is invoked because plasma density is assumed high enough. Consequently, quasineutral plasma $n_e = n_i$ is assumed except in Debye sheaths. At the same time, plasma density is also low enough to assume the zero-beta limit, neglecting any induced magnetic field. Electrostatic sheaths, AB and WQ, are attached to the dielectric walls. Bohm criterion must be satisfied at sheath edges, B and Q. At the rear wall A, neutral gas \dot{m} is injected and ionized due to collisions along the dielectric tube of length L and radius $R \ll L$.

Continuity and momentum equations, which describe the fluid-dynamic macroscopic behaviour of the plasma, are written down for the three species: ions (i), neutrals (n) and electrons (e),

$$\nabla \cdot (n_e \mathbf{u}_e) = \nabla \cdot (n_i \mathbf{u}_i) = -\nabla \cdot (n_n \mathbf{u}_n) = n_e n_n R_{ion}, \quad (1)$$

$$\nabla \cdot (m_j n_j \mathbf{u}_j) = -\nabla T_j n_j - q_j n \nabla \phi + q_j n_j \mathbf{u}_j \times \mathbf{B} - \mathbf{S}_j. \quad (2)$$

Here: n is the density; \mathbf{u} is the velocity; m the mass of the particle; T the temperature of each specie; q is the electric charge; ϕ is the ambipolar electric potential; \mathbf{S}_j includes momentum-transfer collisions, such as ionization (hereafter ion subscript) and elastic electron-ion (ei), ion-neutral (in), and electron-neutral (en) collisions; R_l ($l = ion, ei, in, en$) is the collisional rate of the different processes, and expressions are given in Appendix of Ref. [14].

Reference [14] explained the variable-separation method. The following hypotheses and conventions are made: electrons are isothermal; ion and neutral pressure are neglected; $\mathbf{u}_n = u_n \mathbf{1}_z$ and $n_n(r, z) = n_n(z)$;

there is local current ambipolarity, $\mathbf{j} - j_\theta \mathbf{1}_\theta = \mathbf{0}$; plasma density is decoupled as $n(z, r) = n_z(z)n_r(z, r)$, with $\int_0^R r n_r(z, r) dr = R^2/2$; the electric potential is decoupled as $\phi(z, r) = \phi_z(z) + \phi_r(z, r)$; and radial gradients are much higher than axial gradients. These assumptions lead to define axial and radial models coupled only through the wall-recombination function $S_w(z) \equiv n_z \nu_w(z)$, where $\nu_w(z)$ is the effective frequency of plasma recombination at the wall. As explained later, it is also the eigenvalue of the radial model. Next subsections present axial and radial models, listing equations that drive the behavior of the plasma.

A. Axial equations

The set of equations that control the axial behaviour along the dielectric tube becomes:

$$n_z u_z + n_n u_n = g_0, \quad (3)$$

$$(c_s^2 - u_z^2) \frac{\partial u_z}{\partial z} = (u_z - u_n) u_z n_n (R_{in} + R_{ion}) + c_s^2 (n_n R_{ion} - \nu_w), \quad (4)$$

$$(c_s^2 - u_z^2) \frac{\partial n_z}{\partial z} = -n_z [u_z (n_n R_{ion} - \nu_w) - (u_z - u_n) n_n (R_{in} + R_{ion})], \quad (5)$$

$$n_n u_n \frac{\partial u_n}{\partial z} = n_z [u_n \nu_w (\alpha_w - 1) + (u_z - u_n) n_n R_{in}]. \quad (6)$$

Here: g_0 the mass flux, $c_s = \sqrt{T_e/m_i}$ the sonic velocity, α_w is an adjustable parameter that retains the momentum loss/gain due to recombination at the lateral wall. The set of equations is solved for n_z , u_z , n_n and u_n with the following boundary conditions,

$$u_{zB} = -c_s, \quad u_{zE} = c_s, \quad u_{nB} = u_{n0}, \quad g_0 \text{ known}; \quad (7)$$

u_{n0} is the neutral velocity at section B. The above equations yield that the main dimensionless parameters that controlling the axial behavior of the plasma are

$$L_* = c_s u_{n0} / R_{ion} g_0, \quad R_{in} / R_{ion}, \quad u_{n0} / c_s, \quad \alpha_w. \quad (8)$$

The recombination parameter $\nu_w / n_n R_{ion}$ also controls the axial plasma response but it is determined by the radial model.

An analytical solution of the axial is found invoking the asymptotic limits of high magnetic confinement, $\nu_w / n_n R_{ion} \ll 1$, and low ion collisionality, $R_{in} / R_{ion} < u_{n0} / c_s \ll 1$. That solution is

$$u_n = u_{n0}, \quad \frac{u_z}{c_s} = \tan \xi, \quad \frac{c_s}{g_0} n_z = 2\eta_u \cos^2 \xi, \quad \frac{u_{n0}}{g_0} n_n = 1 - \eta_u \sin 2\xi, \quad (9)$$

$$\frac{z}{L_*} = \int_{-\pi/4}^{\xi} \frac{1 - \tan^2 \xi'}{1 - \eta_u \sin 2\xi'} d\xi', \quad (10)$$

with $\eta_u = \dot{m}_{iE} / \dot{m}$ the propellant utilization, and ξ an auxiliary parameter in the interval $\xi \in (-\pi/4, \pi/4)$.

B. Radial equations

The radial model was extensively discussed in Ref. [16]. Main equations are

$$\frac{1}{r} \frac{\partial}{\partial r} (r n_r u_r) = n_r \nu_w, \quad (11)$$

$$u_r \frac{\partial u_r}{\partial r} = -c_s^2 \frac{\partial \ln n_r}{\partial r} - \frac{eB}{m_i} u_\theta + \frac{m_e}{m_i} \frac{u_\theta^2}{r} - n_n (R_{in} + R_{ion}) u_r, \quad (12)$$

$$u_r \frac{\partial u_\theta}{\partial r} = \frac{eB}{m_e} u_r - [n_n (R_{en} + R_{ion}) + n R_{ei}] u_\theta - \frac{u_\theta u_r}{r}, \quad (13)$$

$$e \frac{\partial \phi_r}{\partial r} = T_e \frac{\partial \ln n_r}{\partial r} + eB u_\theta - m_e \frac{u_\theta^2}{r}. \quad (14)$$

Here, ν_w is the eigenvalue that assures the correct plasma flow balance. Equations are solved for n_r , u_r , $u_\theta \equiv u_{\theta e}$, and ϕ_r with the following homogeneous boundary conditions at the axis of symmetry,

$$u_r = u_\theta = \phi_r = \ln(n_r/n_r(z, r=0)) = 0. \quad (15)$$

Radial integration is carried out, in different cross-sections (i.e. different z), from the axis until the transition to the Debye-sheath Q. There, u_r must fulfill the Bohm criterion setting properly ν_w . The radial structure of the plasma is divided in three regions from the axis to the lateral wall. The bulk diffusive quasineutral region, a thin inertial layer where finite Larmor-radius effects cannot be neglected and the Debye sheath.

An analytic solution of the main, bulk region also exists. Here, the asymptotic limit is the high-magnetized regime $\omega_{lh} \gg \nu_e$. Moreover, the effective frequency of electron collisions $\nu_e = nR_{ei} + n_n R_{en} + n_n R_{ion}$ must be assumed radially constant $\nu_e = \text{const.}$ Whereas in the complete model, ν_e varies radially due to $\nu_{ei} = n_r(z, r)R_{ei}$. This limit yields,

$$\frac{n_r(z, r)}{n_r(z, 0)} = J_0\left(a_0 \frac{r}{R}\right), \quad \frac{u_r}{c_s} = a_0 \frac{\nu_e \omega_r}{\omega_{lh}^2} \frac{J_1(a_0 r/R)}{J_0(a_0 r/R)}, \quad \frac{u_\theta}{c_s} = \frac{u_r}{c_s} \frac{\omega_{lh}}{\nu_e}, \quad (16)$$

being $a_0 \simeq 2.405$ the first zero of Bessel function J_0 , $c_e = \sqrt{T_e/m_e}$ the thermal electron velocity, and $\omega_r = c_s/R$ the radial transient frequency.

III. Plasma structure inside the source

This section shows main results of the 2D source model derived above. Axial, radial and 2D plasma structures are detailed. First of all, geometric and operational parameters are listed. The first group includes the tube length $L = 10\text{cm}$ and its radius $R = 1\text{cm}$. On the other hand, operational parameters are the mass flow $\dot{m} = 0.1\text{mg/s}$, the plasma temperature $T_e = 10\text{eV}$, the neutral velocity $u_{n0} = 350\text{m/s}$ and the magnetic field B . Two cases are studied: case 1 with $B = 200\text{G}$ and case 2 with $B = 600\text{G}$. In both cases, all other parameters are maintained constant. $\alpha_w = 1$ is assumed here.

A. Axial response

Neutral depletion, Fig. 2(a), is governed by plasma ionization, $\nu_{ion} \propto n_n R_{ion}(T_e)$, and wall recombination ν_w . Higher temperatures and magnetic fields, and longer tubes improve the propellant utilization η_u . Plasma density, Fig. 2(b), presents a peak near $u_z \sim 0$ as indicated in Fig. 2(c). The positive gradient of the plasma density close to B is due to ionization; the negative gradient in the forward flow region is related to the plasma acceleration. Case 2 solution is almost indistinguishable from the analytical one (dashed line) because plasma parameters agree with asymptotic limit hypotheses. Otherwise, case 1 is more influenced by the role of wall losses in the plasma axial dynamics, Fig. 3(a), resulting in a worse correlation with the ideal-analytical solution.

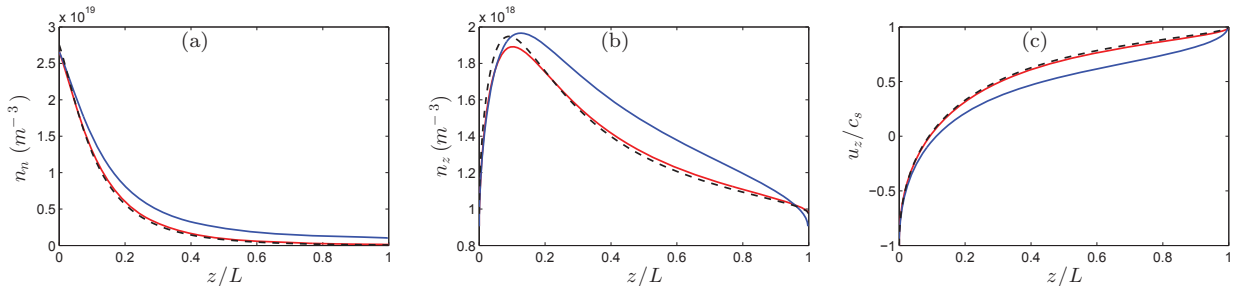


Figure 2. Blue solid line refers to the Case 1 (200G), red line refers to Case 2 (600G). The dashed line depicts asymptotic solution. This color-linestyle code is maintained in all other figures presented in this section. Fig. 2(a) depicts neutral depletion n_n (m^{-3}). Fig. 2(b) plots the plasma density axial profile n_z (m^{-3}). Plasma velocity response u_z/c_s is showed in Fig. 2(c).

Effective electron collisions ν_e , Fig. 3(b), which steer the plasma radial dynamics, decrease along the chamber, thus increasing radial magnetic confinement. Note that $\nu_e \sim \nu_{en}(z)$ near B and $\nu_e \sim \nu_{ei}(z, r)$ near

E. In other words, ν_e is dominated by electron-neutral collisions near B, where neutral density is still high, and this allows to assume that collisions are radially constant. On the other side, close to E, electron-ion collisions dominate. Consequently, the hypothesis of radially constant collisions cannot be assumed.

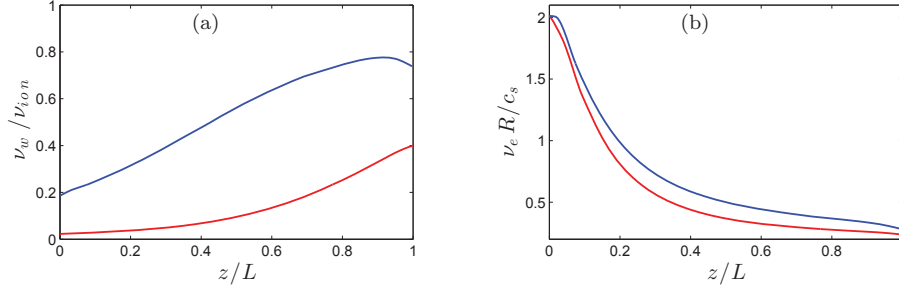


Figure 3. The role of wall losses is estimated in Fig. 3(a) in comparison with ionization rate ν_w/ν_{ion} . Fig. 3(b) depicts the axial variation of the dimensionless electron collisions frequency $\nu_e R/c_s$, necessary to estimate the radial magnetic confinement.

B. Radial response

Fig. 4(a) depicts plasma density profiles at the rear section B. There, case 2 is in agreement with the asymptotic solution proposed by Ref. [16], because both $\omega_{lh} = eB/\sqrt{m_e m_i} \gg \nu_e$ (highly-magnetized plasma) and $\nu_e(z, r) \sim \nu_{en}(z)$ (radially-constant collisions). Case 1 does not fulfil the analytical solution because $\omega_{lh} \sim \nu_e$. Fig. 4(b) refers to section E, where $\nu_e(r) \sim \nu_{ei}(r) \propto n_r$ makes these profiles more steepened. Profiles of $u_r(r)$ in Fig. 5(a) illustrate the high magnetic confinement of the plasma. Taking into account that $-e\phi \sim m_i u_r^2/2$, last results point out that radial electric field is only important in a thin inertial layer preceding the Debye sheath. $u_\theta(r)$ develops thanks to collisions, Fig. 5(b). The azimuthal plasma current provides the magnetic force that sustains the large radial density drop as in a θ -pinch.

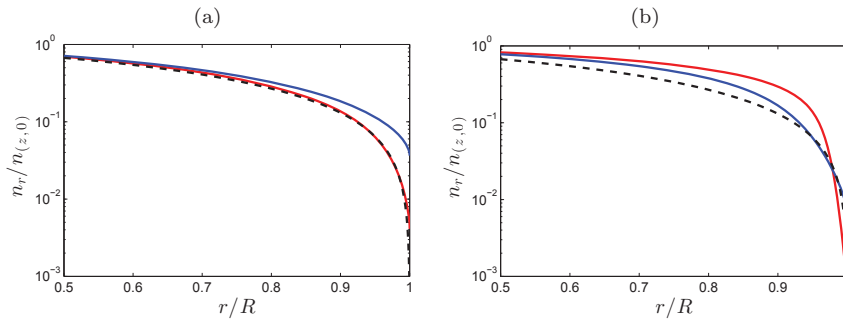


Figure 4. Fig. 4(a) depicts the plasma density radial profile in a cross section located at the rear part of the tube, close to B. The same property is shown in a section close to E, Fig. 4(b). Profiles are dimensionless, using as a reference value the density at the axis line ($z, r = 0$)

C. 2D density distribution in the helicon source

A 2D map of the plasma density is presented in Fig. 6. It is the natural response of the 200G case. Large gradients of the plasma density appear close to all walls. Radial gradients increase with magnetic confinement, in fact with the effective Hall parameter ω_{lh}/ν_e . Axial gradients close to A/B are due to electrostatic confinement and drive the backstreaming flow, which has been depicted in Fig. 2(c).

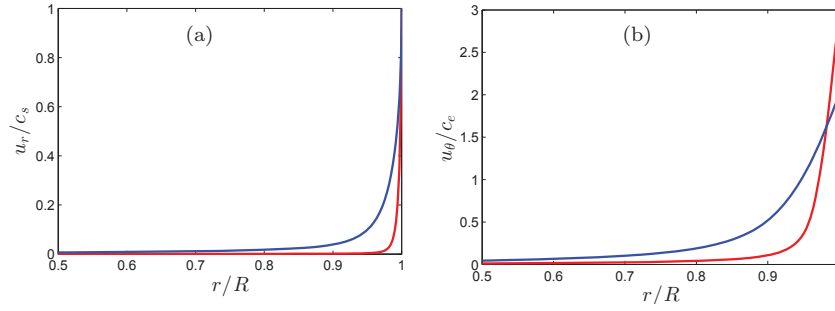


Figure 5. Fig. 5(a) plots the radial velocity u_r/c_s . Fig. 5(b) shows the radial profile of the electron azimuthal velocity.

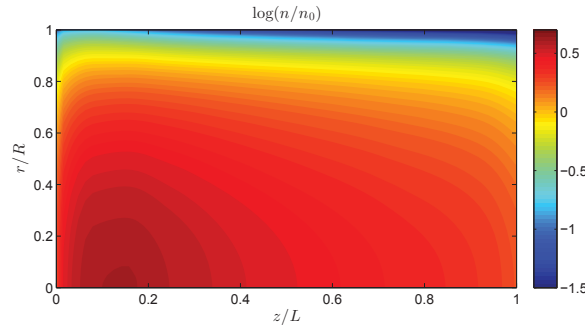


Figure 6. 2D plasma density distribution

IV. Source Performances

Assessment of the helicon source efficiencies is carried out in terms of the propellant utilization η_u and the production efficiency η_p ,

$$\eta_u = \frac{\dot{m}_{iE}}{\dot{m}}, \quad (17)$$

$$\eta_p = \frac{\dot{m}_{iE}}{\dot{m}_{iA} + \dot{m}_{iW} + \dot{m}_{iE}}. \quad (18)$$

Propellant utilization measures the amount of ionized gas ejected through the exit section E relative to the injected mass flow. On the other hand, production efficiency compares the ionized gas flowing through E relative to the total amount of ionized gas produced inside the source.

Eq. (10), derived in the axial analytical model, states that η_u increases with T_e , L and \dot{m} . High efficiencies $\eta_u > 0.95$ require $L_* > 2.5$ as shown in Fig. 7(a). Figure 7(b) plots $\eta_u - B$ curves for different electron temperatures. The knee of each η_u curve separates low-utilization regimes (low-magnetized plasmas) from the high-utilization regimes. Note also, even for very high magnetic field intensities, high-utilization regimes are limited by the plasma temperature, noticeable in the case $T_e = 7 \text{ eV}$, in which ionization is compensated by wall losses, limiting the maximum η_u available. Fig. 7(c) indicates that the flow to the rear wall should be reduced because it represents almost 50% of η_p losses. If a perfect magnetic screening is assumed at the rear wall, η_p may reach values over 90% within the typical range of magnetic field intensities 500 – 1000G.

V. Matching with the magnetic nozzle

The source model matches the 2D MN model of Ahedo and Merino [15], which provides the supersonic plasma expansion. Currents developed at the plasma plume are closed at P, where $\phi_P = \text{const}$. This

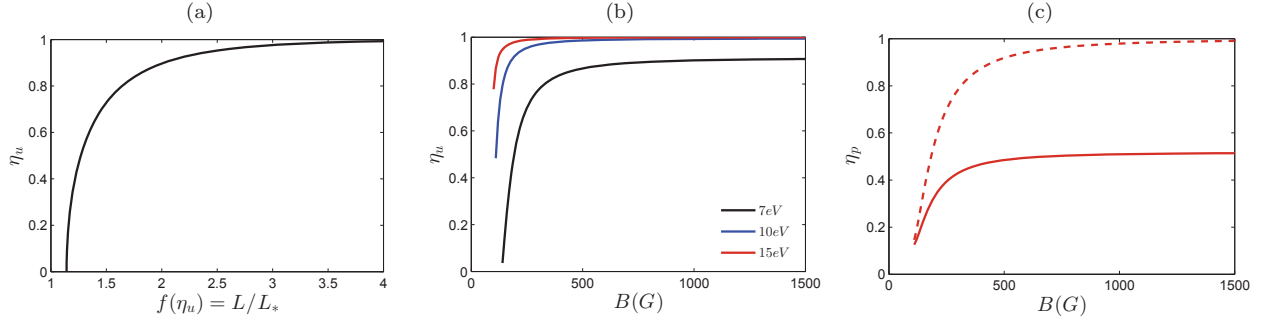


Figure 7. Fig. 7(a) plots the law of Eq. (10). Propellant utilization as a function of the magnetic field is depicted in Fig. 7(b) for different values of the electron temperature. Fig. 7(c) shows the differences on the production efficiency if the backstreaming flow is neglected (dashed line) thanks to an hypothetical screening system (This example uses the Case 2, 600G, as the reference case, solid line).

potential is solved from a fluid-kinetic formulation at the sheath transition D. MN model hypotheses have been commented partially in Sec. I. Other essential hypotheses are listed next. This fluid model of the plasma expansion assumes: (i) fully-magnetized electrons whereas ions are partially-magnetized; (ii) the plasma is current free; (iii) current ambipolarity is not sustained within the plume. (iv) the flow at E must be parallel to the magnetic field streamlines; and (v) the ion Mach number slightly supersonic, in order to fulfill the requirements of the hyperbolic MN model.

Taking into account all hypothesis enumerated above, only the bulk region $r/R \leq 0.98$ of the plasma flowing through E is considered. It supposes a small mismatching in the continuity, momentum and energy laws. The error committed is smaller than 5%. The plasma density distribution along the complete device is depicted in Fig. 8. It shows how density varies much less inside the source than in the plume, where it may drop up to 4 orders of magnitude, presenting a high *radial rarefaction*.

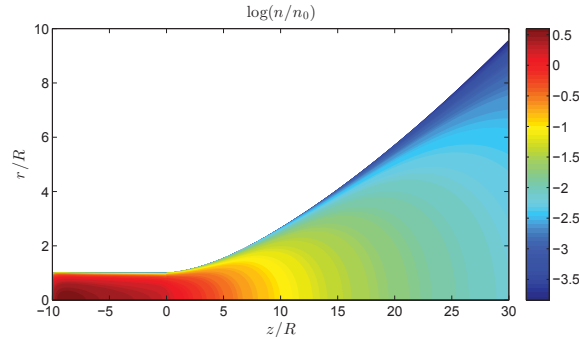


Figure 8. 2D map of the plasma density in the whole thruster $\log(n/n_0)$. Case 1 - 200G. Plasma density reference defined as $n_0 = g_0/c_s$.

After obtaining MN results it is possible to evaluate both the power balance and the total thrust, as well as partial contributions to this thrust. Next subsections presents these balances.

A. Energy balance

Energy balance in the whole thruster determines the relation between the absorbed power P_a , the constant temperature of the electron cloud, and the length L_n of the MN region. Obtaining an implicit law $P_a = P_a(T_e, L_n)$ as Fig. 9(a) illustrates. The most general form of the energy equation, grouping all contributions of all species becomes

$$\nabla \cdot \dot{\mathbf{P}} = \mathbf{j} \cdot \mathbf{E} + \dot{P}_a - \dot{P}_{ion}, \quad (19)$$

where

$$\dot{\mathbf{P}}(z, r) = \frac{n_n}{2} m_i u_n^2 \mathbf{u}_n + \frac{n}{2} [m_i u_i^2 \mathbf{u}_i + (m_e u_{\theta e}^2 + 5T_e) \mathbf{u}_e] + \mathbf{q}_e, \quad (20)$$

\mathbf{q}_e is the heat flux, $\mathbf{j} \cdot \mathbf{E}$ is the electric field work, \dot{P}_a the absorbed power density, and \dot{P}_{ion} is the the power density for ionization and excitation processes, defined as

$$\dot{P}_{ion} = E'_{ion} n n_n R_{ion} \equiv \nabla \cdot (E'_{ion} n \mathbf{u}_i), \quad (21)$$

with E'_{ion} the effective ionization energy (see Appendix of Ref. [14]).

Equation (19) can be easily integrate over the whole domain, yielding

$$P_{ion} + P_{wall} + P_P = P_a. \quad (22)$$

where P_a is the absorbed power from the wave, P_{ion} groups ionization and excitation energy losses, $P_{wall} = P_A + P_W$ groups losses at tube rear wall A and lateral wall W, and P_P is the plasma power impacting at plate P. The three magnitudes on the left-hand side on Eq. (22) depend on T_e ; additionally, P_P depends on the length L_n of the MN region.

If $T_e = \text{const}$, P_a increases as MN length is extended, because P_P rises monotonically in this MN isothermal model. Reciprocally, T_e decreases for longer MN and $P_a = \text{const}$. At $L_n = 0$ (i.e. the plate is at the exit of the source), the difference between P_a , case 1, from that obtained in case 2, responds to the lower production efficiency of the source, penalized by wall losses and ionization of the recombined flux, $P_{wall} + P_{ion} \simeq 0.7P_a$, see Fig. 9(b). Case 2 is shown as an efficient case, $P_P \simeq 0.40P_a$. Ionization cost is similar in both cases $P_{ion}/P_a \sim 0.3$. The absorbed power obtained in these results belongs to the range 50 – 100W. It is in accordance with experimental devices that use similar operational and geometric parameters, such as the one in Ref. [17].

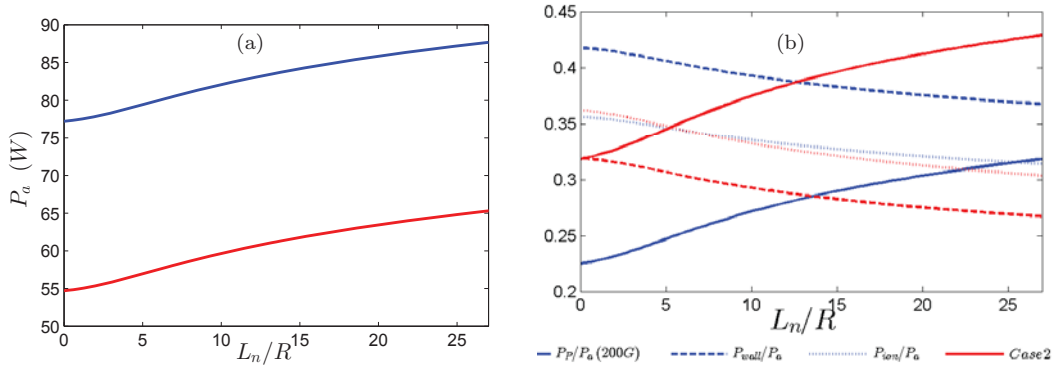


Figure 9. Fig. 9(a) plots the obtained power absorption law $P_a = P_a(L_n, T_e = 10eV)$. Fig. 9(b) shows the ratios P_P/P_a , P_{wall}/P_a and P_{ion}/P_a .

B. Thrust balance

Finally, regarding the thrust balance, this research focuses the effort on breaking down all contributions to the total thrust F ,

$$F = F_{pres} + F_{elec} + F_{mag}. \quad (23)$$

As Eq. 23 indicates, three contributions can be taken into account. First, F_{pres} includes the thrust due to the pressure on the helicon source walls, mainly at the rear section A. Moreover, a small negative contribution is due to the loss of momentum at the lateral wall as a consequence of plasma-wall recombination. The second term, F_{elec} is the electric force between the negative electric charge at surface A and the positive electric charge at sheath AB. The third contribution, F_{mag} , comes from the thrust gain due to the MN, as a result of the interaction between azimuthal plasma currents and the magnetic circuit (i.e. applied divergent magnetic field).

Naturally, the thrust contributions are related to the axial momentum flow of the plasma at different sections $z = \text{constant}$, defined as

$$F_z(z) = 2\pi \int_0^{R_V(z)} dr r M_{zz}(z, r) \quad (24)$$

where $\mathbf{M} = \sum_{k=i,e,n} m_k n_k \mathbf{u}_k \mathbf{u}_k + p_e \mathbf{I}$ is the plasma momentum flux tensor. From this definition, it is possible to relate each contribution in Eq. (23) with the axial momentum flow evaluated at sections E and D,

$$F_{zE} = F_{pres} + F_{elec}, \quad (25)$$

$$F_{zD} = F. \quad (26)$$

Therefore, $F_{mag} = F_{zD} - F_{zE}$. Finally, with the computed thrust $F = F(L_n, T_e)$ and the absorbed power, the thrust efficiency η is defined as follows,

$$\eta = \frac{F^2}{2\dot{m}P_a}. \quad (27)$$

Figure 10 plots $\eta = \eta(L_n, T_e = 10eV)$. In the highly-magnetized case (600G) thrust efficiency is over 20% if $L_n/R \geq 14$.

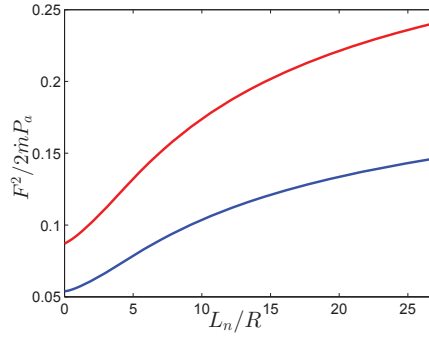


Figure 10. Source + MN thrust efficiency η

VI. Conclusions

A 2D fluid model of the helicon source has been derived and matched to a similar model of the magnetic nozzle. Attention has been given to the 2D neutral depletion and the plasma confinement from rear and lateral walls of the source. Source performances are given in terms of the propellant utilization and production efficiency. Ranges of design and operational parameters for optimal performances are identified. Analytic solutions compare well with numerical solutions within appropriate parametric ranges.

The matching of the source model with a divergent MN model has allowed the first complete characterization of the plasma discharge in a helicon plasma thruster. Additionally, it has allowed to solve a previous inconsistency in relating the plasma temperature with the absorbed power, which turns out to involve the plasma expansion in the MN. The different contributions to the thrust and the energy balance have been analyzed. Encouraging values of the thrust efficiency are obtained.

Further work should try to couple this plasma flow model with a 2D model of the plasma-wave interaction, in order to ascertain the validity of the assumptions made in the flow model here or how they should be modified. For instance, a non-Maxwellian distribution function of electrons could modify the results. Also, a downstream plasma detachment model would allow us to avoid the downstream plate included here.

Acknowledgments

This work has been supported by the Spanish Government (Project AYA-2010-61699) and the Air Force Office of Scientific Research, Air Force Material Command, USAF (grant FA8655-12-1-2043). The U.S Government is authorized to reproduce and distribute reprints for Governmental purpose notwithstanding any copyright notation thereon.

References

- ¹Pavarin, D., Manente, M., Guçlua, Y., Curreli, D., Bettanini, C., Zaccariotto, M., Walker, M., Palmer, D., Carlsson, J., Bramanti, C., et al., "Feasibility Study of Medium-Power Helicon Thruster," *44th AIAA/ASME/SAE/ASEE Joint Propulsion Conference & Exhibit*, 2008.
- ²Ziemba, T., Carscadden, J., Slough, J., Prager, J., and Winglee, R., "High Power Helicon Thruster," *41th Joint Propulsion Conference, Tucson, AR*, edited by A. I. of Aeronautics and W. Astronautics, AIAA 2005-4119, 2005.
- ³Batishchev, O., "Minihelicon Plasma Thruster," *IEEE Transaction on Plasma Science*, Vol. 37, 2009, pp. 1563–1571.
- ⁴Lafleur, T., Charles, C., and Boswell, R., "Characterization of a helicon plasma source in low diverging magnetic fields," *Journal of Physics D: Applied Physics*, Vol. 44, 2011, pp. 055202.
- ⁵Takahashi, K., Lafleur, T., Charles, C., Alexander, P., Boswell, R., Perren, M., Laine, R., Pottinger, S., Lappas, V., Harle, T., et al., "Direct thrust measurement of a permanent magnet helicon double layer thruster," *Applied Physics Letters*, Vol. 98, 2011, pp. 141503.
- ⁶Ling, J., West, M., Lafleur, T., Charles, C., and Boswell, R., "Thrust measurements in a low-magnetic field high-density mode in the helicon double layer thruster," *Journal of Physics D: Applied Physics*, Vol. 43, 2010, pp. 305203.
- ⁷Boswell, R., "Very efficient plasma generation by whistler waves near the lower hybrid frequency," *Plasma Physics and Controlled Fusion*, Vol. 26, 1984, pp. 1147–1162.
- ⁸Chen, F., "Plasma ionization by helicon waves," *Plasma Physics and Controlled Fusion*, Vol. 33, 1991, pp. 339.
- ⁹Shamrai, K. and Taranov, V., "Resonance wave discharge and collisional energy absorption in helicon plasma source," *Plasma Physics and Controlled Fusion*, Vol. 36, 1994, pp. 1719–1735.
- ¹⁰Lieberman, M. and Lichtenberg, A., *Principles of plasma discharges and materials processing*, Wiley-Blackwell, 2005.
- ¹¹Ahedo, E., Gallardo, J., and Martínez-Sánchez, M., "Effects of the radial-plasma wall interaction on the axial Hall thruster discharge," *Physics of Plasmas*, Vol. 10, No. 8, 2003, pp. 3397–3409.
- ¹²Fruchtman, A., Makrinich, G., and Ashkenazy, J., "Two-dimensional equilibrium of a low temperature magnetized plasma," *Plasma Sources Science and Technology*, Vol. 14, 2005, pp. 152–167.
- ¹³Fruchtman, A., "Neutral depletion in a collisionless plasma," *Plasma Science, IEEE Transactions on*, Vol. 36, No. 2, 2008, pp. 403–413.
- ¹⁴Ahedo, E., "Cylindrical model of a helicon-generated plasma," *31th International Electric Propulsion Conference, Ann Arbor, Michigan, USA*, edited by F. Electric Rocket Propulsion Society, IEPC 2009-193, 2009.
- ¹⁵Ahedo, E. and Merino, M., "Two-dimensional supersonic plasma acceleration in a magnetic nozzle," *Physics of Plasmas*, Vol. 17, 2010, pp. 073501.
- ¹⁶Ahedo, E., "Parametric analysis of a magnetized cylindrical plasma," *Physics of Plasmas*, Vol. 16, 2009, pp. 113503.
- ¹⁷Pavarin, D., Ferri, F., Manente, M., Curreli, D., Guclu, Y., Melazzi, D., Rondini, D., Suman, S., Carlsson, J., Bramanti, C., Ahedo, E., Lancellotti, V., Katsonis, K., and Markelov, G., "Design of 50W Helicon Plasma Thruster," *31th International Electric Propulsion Conference, Ann Arbor, Michigan, USA*, edited by F. Electric Rocket Propulsion Society, IEPC 2009-205, 2009.

Advanced simulation of magnetic nozzles for plasma thrusters

Mario Merino, Eduardo Ahedo

Plasmas & Space Propulsion Team
 Universidad Politécnica de Madrid, Spain

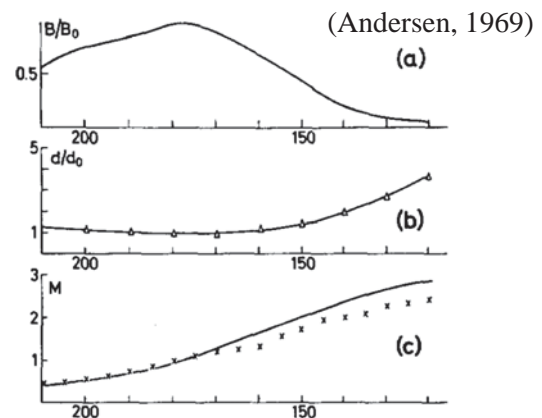
www.fmetsia.upm.es/ep2



SP 2012, Bordeaux, May 7-10

Magnetic nozzles in plasma thrusters

- A magnetic nozzle is an **applied, divergent magnetic field** that channels and accelerates a plasma beam
- It is being proposed as the **acceleration stage** of several plasma thrusters



AF-MPDT

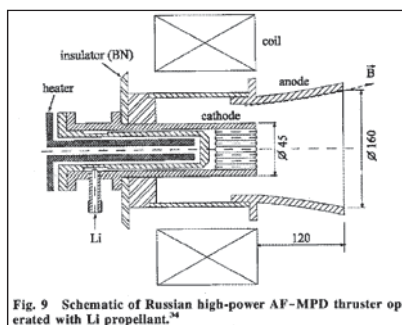


Fig. 9 Schematic of Russian high-power AF-MPDT thruster operated with Li propellant.³⁴

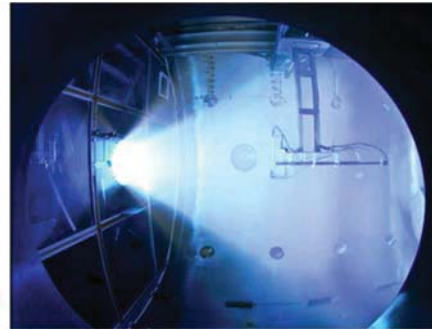
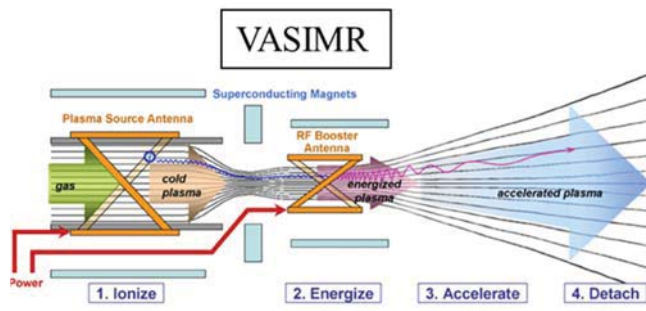
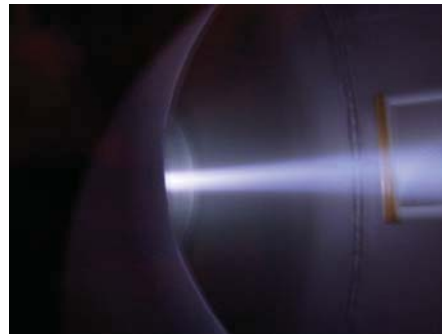


MAILiLFA



Magnetic nozzles in plasma thrusters

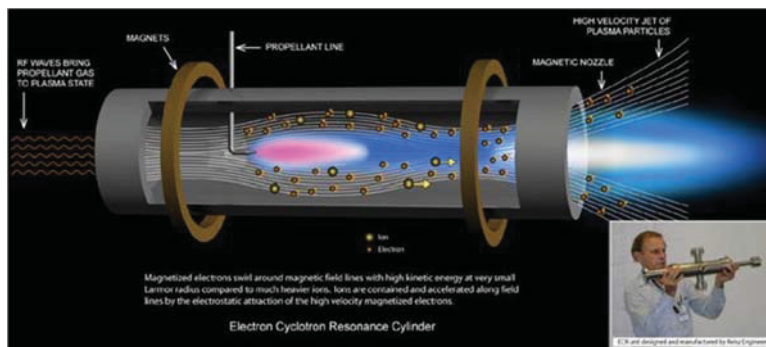
Helicon thruster



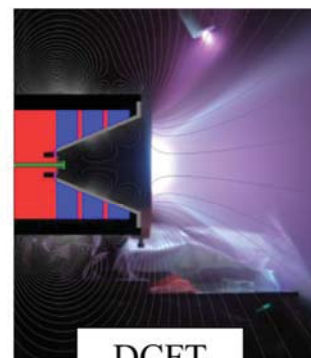
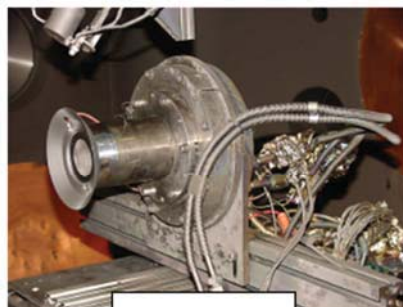
Advanced simulation of magnetic nozzles for plasma thrusters

Magnetic nozzles in plasma thrusters

ECR thruster



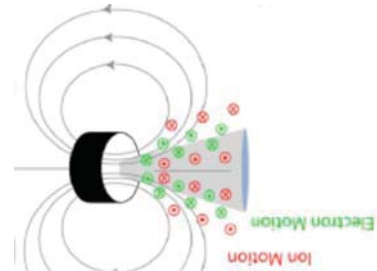
Hall thruster with magnetic cusps



Advanced simulation of magnetic nozzles for plasma thrusters
Distribution A: Approved for public release; distribution is unlimited.

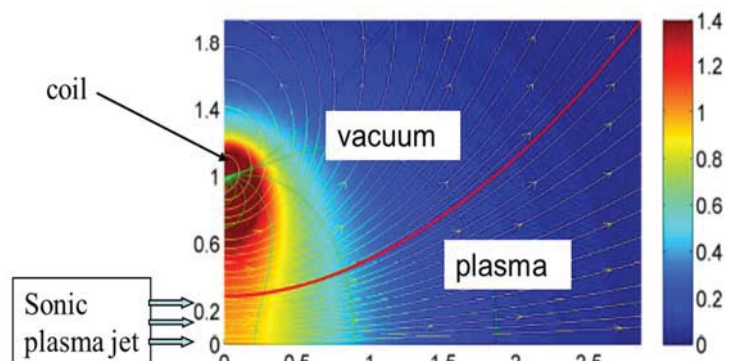
What is a magnetic nozzle ?

- From hot gas expansion in solid (de Laval) nozzles, we know:
 - There is **energy conversion** of 'internal' into 'axial kinetic'
 - supersonic gas in divergent nozzle
 - There is a **thrust gain** from the gas pressure on the divergent walls
- We expect both phenomena to occur in a **magnetic nozzle (MN)**
- Nonetheless:
 - Plasma expansion is **more complex** than gas expansion
 - Plasma expansion is **strongly 2D**
 - Different sources of internal energy in plasma → **different MNs**
 - MN has **no walls**:
 - No energy losses, **no heat loads !!**
 - Thrust gain mechanism is **totally different**
 - Eventually plasma **must detach** from turning-back magnetic lines



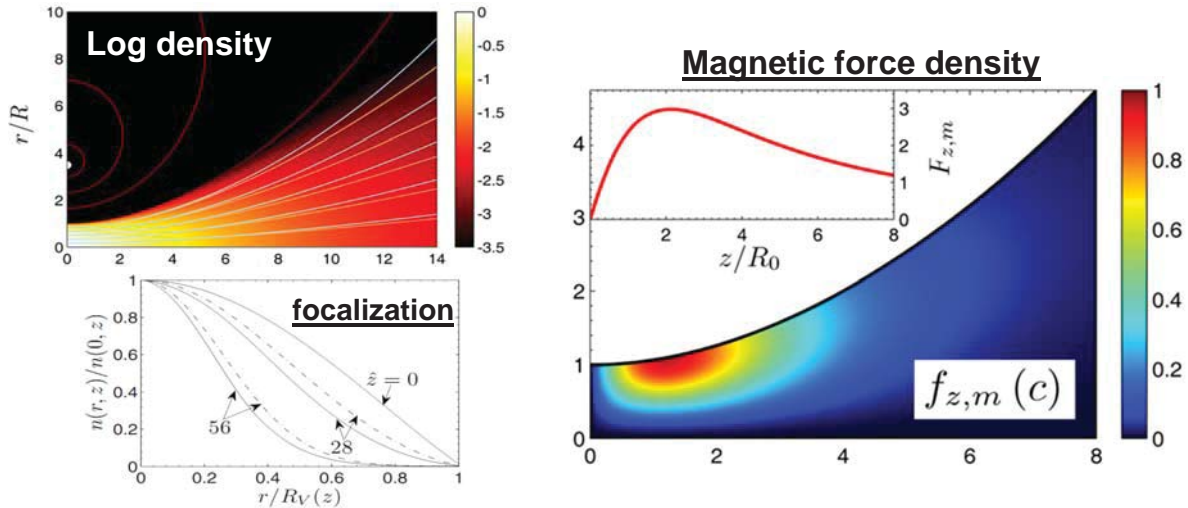
DIMAGNO: A 2D plasma/nozzle code

- UPM code, first version in 2010: Phys. Plasmas, vol 17, 073501,
- **Supersonic plasma expansion** in 2D divergent magnetic nozzle
- **Multi-fluid** model
- Source emits at the MN throat a **sonic, fully-ionized, current-free, hot plasma** (relevant to propulsion in vacuum)
- **Partially-magnetized, cold ions** (consistent with thruster designs)
- **Fully magnetized, hot electrons** (i.e. energy stored in electrons)
- To be removed later:
 - $m_e/m_i \sim 10^{-4}$ → **electron inertia neglected**
 - Pressure-ratio $\equiv \beta \ll 1$ → **induced field effects neglected**



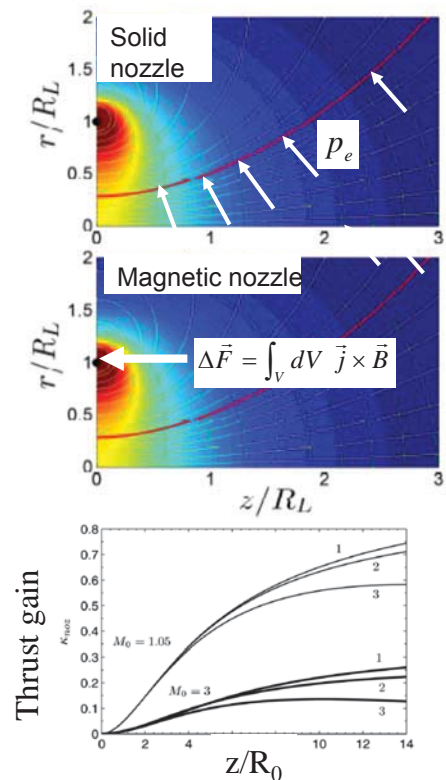
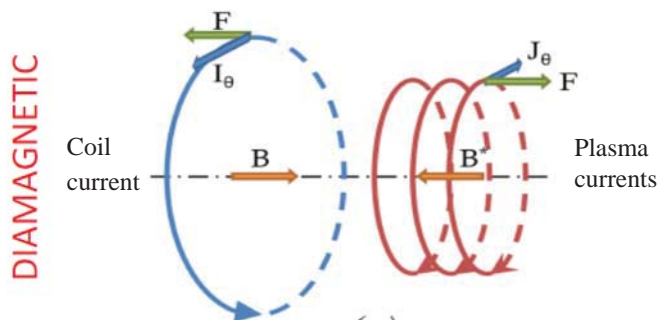
2D plasma expansion

- Quasineutrality + Partially-magnetized ions $\rightarrow \mathbf{E}_{\text{perp}}$ develops \rightarrow non-uniform 2D plasma \rightarrow **Relative focalization** of density profile
- θ -pinch balance on electrons: **pressure force = magnetic force + electric force**
No Boltzmann relation along $\mathbf{1}_{\text{perp}}$!!!
- Magnetic force confines electrons $\rightarrow j_{\theta e}$ is **diamagnetic**



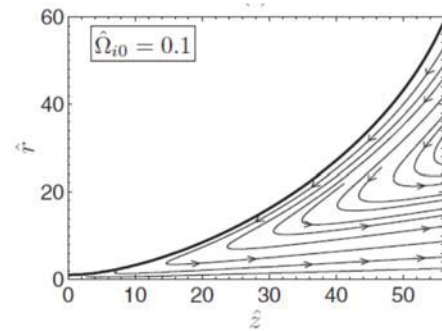
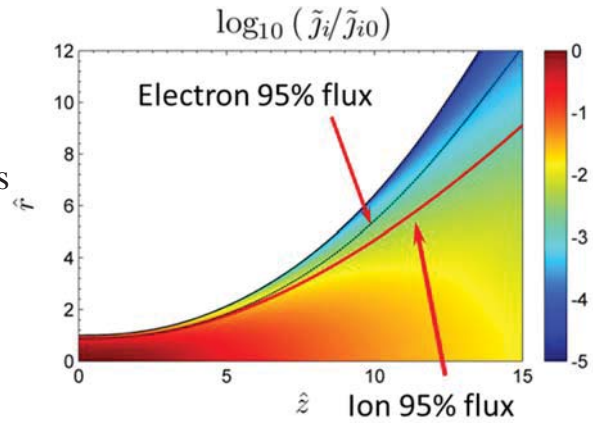
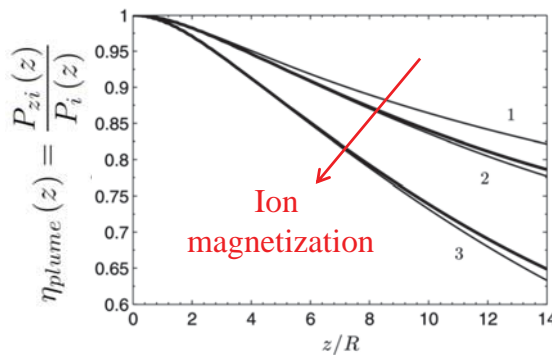
Magnetic thrust gain

- Thrust gain in a divergent
 - solid nozzle comes from **pressure** on the walls
 - magnetic nozzle is the reaction force to the (volumetric) **magnetic force** on the plasma
- For positive plasma acceleration & thrust gain $\rightarrow j_{\theta}$ from plasma must be diamagnetic (running opposite to coil current)
- Maximum thrust gain (~100%) for:
 - 1) sonic flow at throat, 2) weakly-magnetized ions



Ion detachment & plume efficiency

- These are genuine **2D effects**
- Electron streamtubes = magnetic streamtubes \neq ion streamtubes
 - **Ion detachment** from B-lines
 - **No current ambipolarity** ($j_{e,meridian} \neq j_{i,meridian}$)
 - Small paramagnetic $j_{\theta i}$
- Plume efficiency is the nozzle penalty

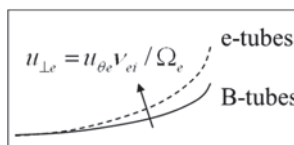


Electron detachment: resistivity

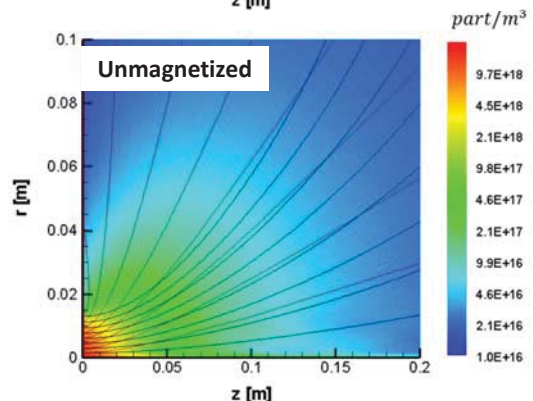
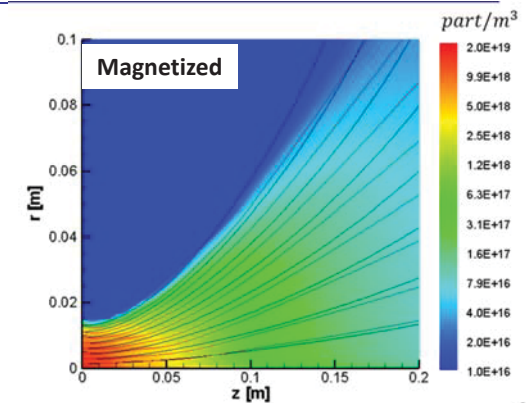
- Mechanisms of electron detachment ($\beta \ll 1$)
 - a) electron inertia
 - b) resistivity

$$e u_{\perp e} B = (m_e/r) \tilde{u}_e \cdot \nabla(r u_{\theta e}) + m_e \nu_{ei} u_{\theta e}$$

- Small resistivity studied through perturbation of DIMAGNO collisionless solution → Plasma beam **detaches outwards** \propto **inverse Hall parameter**

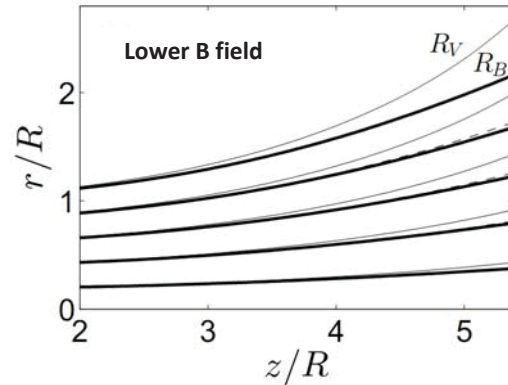
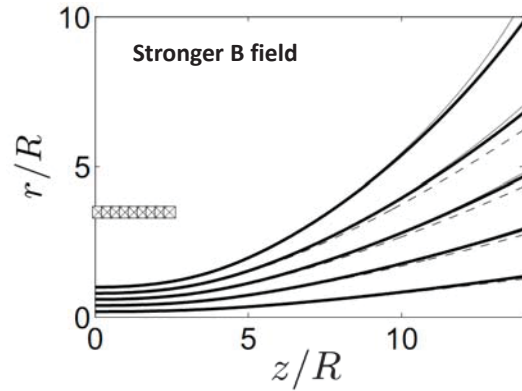


- **New hybrid (fluid/PIC) code** will allow to fully analyze resistivity & demagnetization



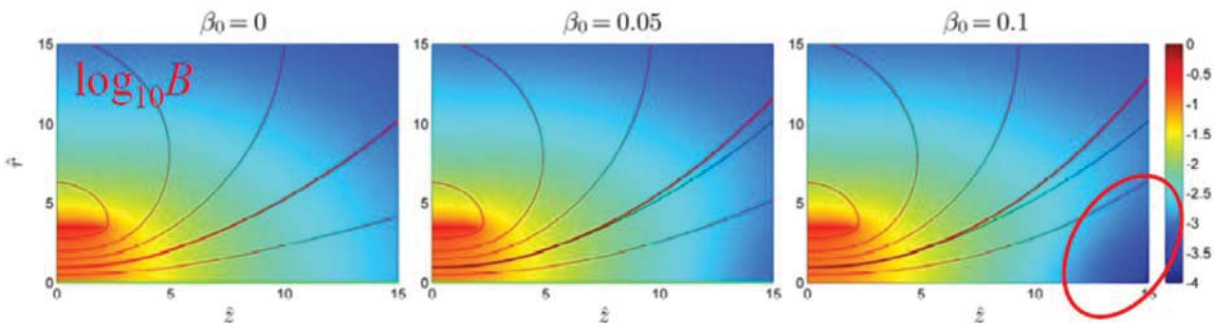
Electron detachment: inertia

- DIMAGNO has been extended to include **nonlinear e-inertia** effects
- Generalized **conservation laws for electron**: azimuthal momentum, total energy, and azimuthal isorotation
- Electron **detachment is always outwards** for a magnetized plasma beam (in equilibrium upstream)
- **Hooper's class** of nonzero inertia models, **based on local current ambipolarity** and claiming inwards electron detachment, is **non-physical**:
 - it does not satisfy that the electron azimuthal velocity is the $[\mathbf{E} + (\text{grad } p)/en] \times \mathbf{B}$ drift

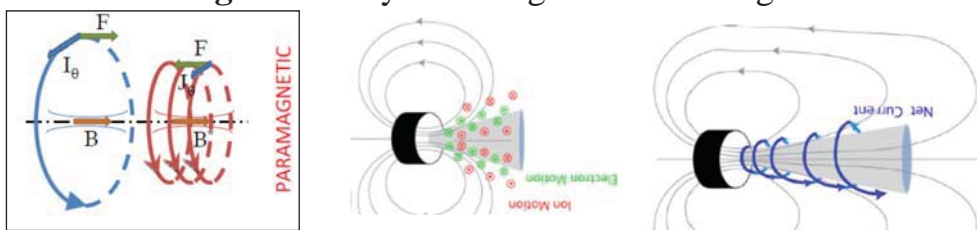


Induced field effects

- **Diamagnetic** plasma current \rightarrow induces B-field that tends to cancel applied B-field \rightarrow Nozzle shape is modified and becomes **more divergent**
 - \rightarrow Bad: **Outwards electron detachment** from original nozzle
 - \rightarrow Good: **Electron demagnetization is enhanced**

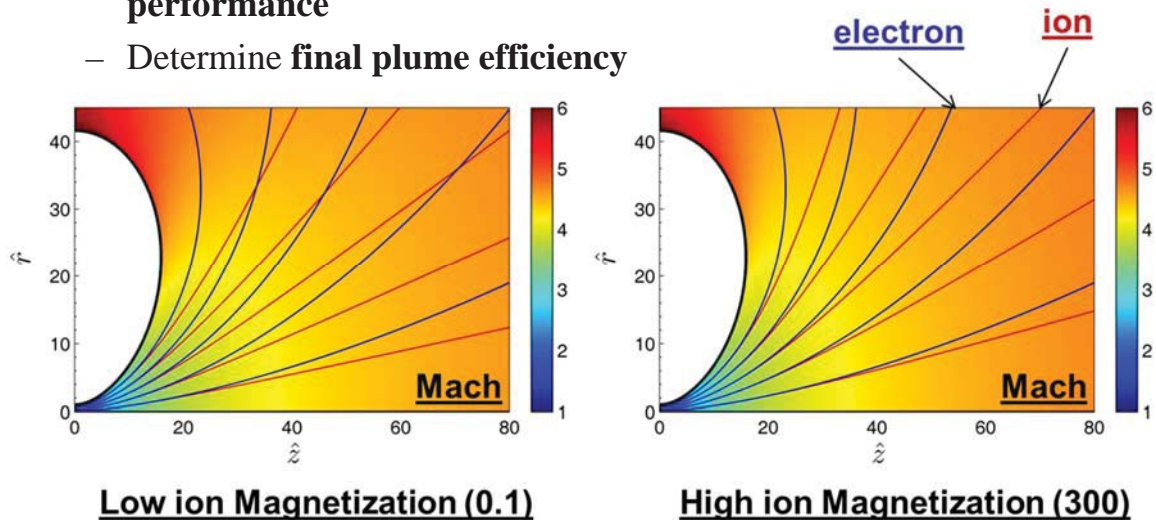


- This scenario **disagrees** totally with magnetic-stretching one of Arefiev&B.



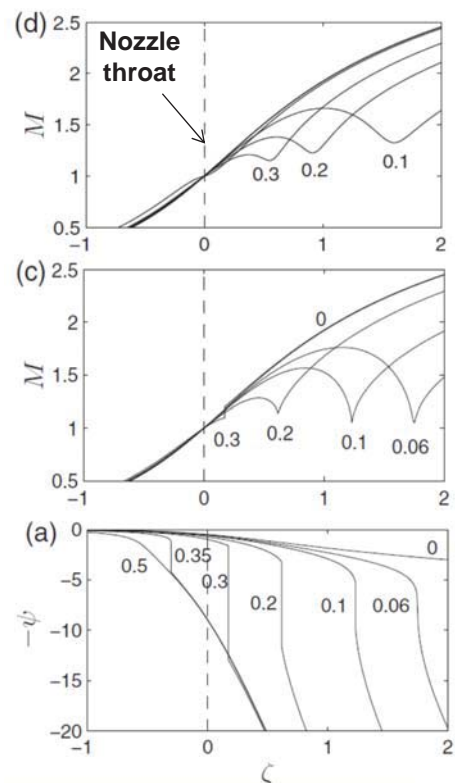
Downstream of the turning point

- Most recent achievement: computation of plasma expansion **beyond MN turning point**, in order to
 - Characterize **far downstream behavior**
 - Confirm that **ion detachment** is key feature for **good MN performance**
 - Determine **final plume efficiency**



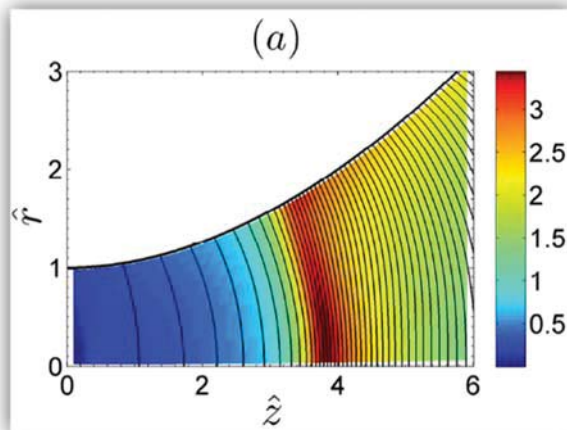
Two-electron temperature (TET) plasma

- Existing debate on the presence of **current-free double layers (CF-DLs)** and their application as a new propulsion concept (HDLT)
- Ahedo&Martínez ('09, '11):
 - **1D model of CF-DL** in a collisionless, TET, magnetically-expanded plasma
 - a) why a CF-DL is formed? It is a consequence of the varying sound speed leading to multiple sonic points (**'anomalous thermodynamics'**)
 - b) Thrust gain associated to a CFDL? **None**
- Still: * which is the 2D shape of a CFDL and its effect on η_{plume} ?
 - * CFDL useful for plasma diagnosis



TET plasma & 2D CFDL

- DIMAGNO is being extended to determine the **2D shape of TET quasi-CFDLs** and its effect on thrust gain and plume efficiency



ϕ -isolines and electric field map for $\tau = 9, \alpha_S = 0.2$

- TET activity is part of a project attempting to implement in DIMAGNO **different thermodynamic models**, covering most MN types: warm ions, swirl energy (AF-MPD), adiabatic electrons (including collisionless cooling), anisotropic T_e (ECR thrusters), and anisotropic T_i (VASIMR)



Conclusions

- An **innovative 2D code for propulsive magnetic nozzles** has been fully developed at UPM . The code stands out:
 - the 2D character of the supersonic plasma expansion,
 - the weak-magnetization and detachment of ions (non MHD plasma)
 - the role of azimuthal plasma currents in confinement and thrust
 - the lack of current ambipolarity
 - the amount of magnetic thrust gain
 - The plume or nozzle efficiency
- **Extensions of the code** are demonstrating
 - Electron outwards detachment caused by either e-inertia or resistivity
 - Enhanced nozzle divergence and plasma demagnetization caused by induced field effects, when $\beta=O(1)$.
 - Double layer formation in TET plasmas
- **New thermodynamic models** are been considered in order to cover different magnetic nozzle types



*Thank you for
your attention*

More info in www.fmetsia.upm.es/ep2

Support from : FP7 grant 218862; MECC project AYA2010-16699;
US-AFOSR grant FA8655-12-1-2043



Advanced simulation of magnetic nozzles for plasma thrusters

17

PAGE INTENTIONALLY LEFT BLANK



POLITÉCNICA

Plasma Structure Inside and Outside a Helicon Thruster

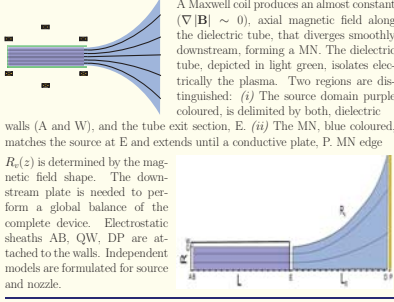
J. Navarro, M. Merino and E. Ahedo

Plasmas and Space Propulsion Team, Universidad Politécnica de Madrid



A helicon thruster consists of a cylindrical helicon source, where the plasma is generated and heated, and a magnetic nozzle, where the plasma beam is accelerated supersonically. Two dimensional models of the plasma flow inside the source and in the external magnetic nozzle (MN) are derived, for a known amount of absorbed power from rf waves. 2D plasma structure and response inside the source are described, comprising the processes of neutral depletion, losses to chamber walls, and backward and forward flows. Conditions for high propellant utilization and high current efficiency are determined. The matching with the MN model allows to obtain an overall characterization of helicon thruster performances in terms of power, thrust and efficiency.

Helicon Thruster Sketch



Plasma dynamics inside the source is driven by continuity and plasma momentum equations:

$$\nabla \cdot (n_j \mathbf{u}_j) = \nabla \cdot (n_j \mathbf{u}_j) = -\nabla \cdot (n_j \mathbf{u}_j) = n_e n_p R_{ion}$$

n_j for densities, \mathbf{u}_j for velocities, T_j for temperatures, m_j and q_j species mass and charge, ϕ the electric potential, R for ionization/collision rates, S includes momentum sources/sinks terms. Subscript $j = \text{ion, electron, neutral}$.

- Hypotheses:**
 - Quasineutral plasma $n_e = n_i$ delimited by B and Q.
 - Zero-beta limit \rightarrow negligible induced magnetic field.
 - Isothermal plasma with $T_e \gg T_i, T_n$.
 - Axial symmetry $\partial/\partial\theta = 0$.
 - Cold neutrals, $\mathbf{u}_n = u_n \mathbf{1}_z$ and $n_n(z, r) = n_n(z)$.
 - Current ambipolarity $\mathbf{j} - j_{\parallel} \mathbf{1}_z = 0$.
 - Decoupled density, $n(z, r) = n_e(z) n_i(z, r)$, with $\int_0^R n_i(z, r) dr = R^2/2$.
 - Decoupled electric potential, $\phi(z, r) = \phi_e(z) + \phi_i(z, r)$.
 - Ion pressure negligible compared with electron pressure.
 - $u_{\theta} \ll u_{\phi} \equiv u_{\theta}$
 - Spatial gradients satisfy: $\partial\chi/\partial z \ll \partial\chi/\partial r$ for $\chi = n_e, \phi_e, u_r, u_z, u_{\theta}$.

These hypotheses reduce the 2D problem into radial and axial models coupled through the wall recombination function, $S_w(z) \equiv n_e \nu_w(z)$.

Axial equations

After manipulating main equations, using properly all hypotheses, the set of equations that control the axial behaviour of the plasma along the dielectric tube becomes:

$$c_s^2 - u_z^2 \frac{\partial u_z}{\partial z} = (u_z - u_n) u_z n_n (R_{in} + R_{ion}) + c_s^2 (n_n R_{ion} - \nu_w)$$

g_0 the mass flux, $c_s = \sqrt{T_e/m_i}$ the sonic velocity, α_w is an adjustable parameter that retains the momentum loss/gain due to recombination at the lateral wall.

Boundary conditions: $u_z|_B = -c_s$, $u_z|_E = c_s$, $u_{\theta}|_B = u_{\theta}|_E = g_0$ known. The plasma axial response depends on four dimensionless parameters:

$$L_e = c_s u_{\theta 0} / R_{ion} g_0, \quad R_{in} / R_{ion}, \quad u_{\theta 0} / c_s, \quad \alpha_w$$

(ν_w is obtained self-consistently solving the radial model)

Analytical solution is found invoking asymptotic limits, high-confinement $\nu_w / n_n R_{ion} \ll 1$ and $R_{in} / R_{ion} < u_{\theta 0} / c_s \ll 1$.

$$u_n = u_{\theta 0}, \quad \frac{u_z}{c_s} = \tan \xi, \quad \frac{c_s}{g_0} n_z = 2 \eta_w \cos^2 \xi, \quad \frac{u_{\theta 0}}{g_0} n_{\theta} = 1 - \eta_w \sin 2\xi$$

$$\frac{z}{L_e} = \int_{-\xi/4}^{\xi} \frac{1 - \tan^2 \xi'}{1 - \eta_w \sin 2\xi'} d\xi', \quad \eta_w$$

Radial Equations

The radial model was treated in Ref. [3], main equations are listed next. ν_w is the eigenvalue that assures the correct plasma flow balance.

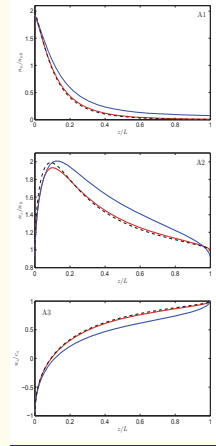
$$\frac{1}{r} \frac{\partial}{\partial r} (r n_r u_r) = n_r \nu_w$$

Matching with the MN Model

The source model matches the 2D MN model of Ahedo and Merino Ref. [4]. It provides the supersonic plasma expansion. Currents developed at the plasma plume are closed at P, where $\phi_P = \text{const}$. This potential is solved mixing kinetic formulation at the sheath transition D.

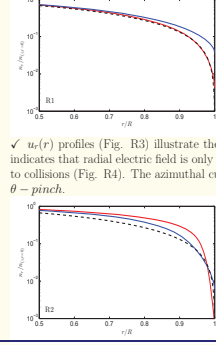
- MN Hypotheses:**
 - Isothermal, quasi-neutral plasma expansion.
 - Collisionless.
 - Fully-magnetized electrons and partially-magnetized ions.
 - Current free plasma.
 - No current ambipolarity.

Axial Response



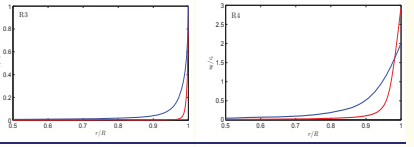
- Case 1 (200G)** **Case 2 (600G)** **Analytical solution, dashed line.**
- All other parameters: $T_e = 10 \text{ eV}$, $\dot{m} = 0.1 \text{ mg/s}$, $\alpha_w = 1.0$, $u_{\theta 0} = 350 \text{ m/s}$ remain constant. **Neutral depletion** (Fig. A1) is governed by plasma ionization, $\nu_{ion} \propto n_n R_{ion}(T_e)$, and wall recombination (ν_w). Higher temperatures and magnetic fields, and longer tubes improve the propellant utilization η_p .
- Plasma density (Fig. A2) presents a peak near $u_z \sim 0$ (Fig. A3). The positive gradient of this magnitude close to B is due to ionization. $\partial n_e / \partial z < 0$ in the forward flow region is related to the plasma acceleration.
- Case 2 solution is almost indistinguishable from the analytical one because plasma parameters agree with asymptotic limit hypotheses. Otherwise, case 1 shows the role of the wall losses ν_w on the plasma axial dynamics (Fig. A4), resulting a clear correlation with the ideal-analytical solution.
- Effective electron collisions (Fig. A5), governing radial dynamics, decrease along the chamber, thus increasing radial magnetic confinement. Note also that $\nu_e \sim \nu_{en}(z)$ near B and $\nu_e \sim \nu_{en}(z, r)$ near E.

Radial Response



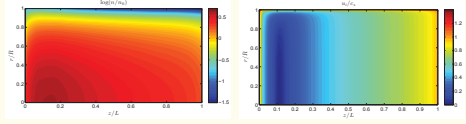
- Fig. R1 depicts plasma density profiles at the rear section B. There, case 2 is in agreement with the asymptotic solution proposed by Ref. [3], because both $\omega_{ce} = eB/\sqrt{m_e m_i} \gg \nu_e$ (high-magnetized plasma) and $u_e(z, r) \sim v_{en}(z)$ (radially-constant collisions). Case 1 does not fulfill the analytical solution because $\omega_{ce} \sim \nu_e$. Fig. R2 refers to section E, where $u_e(r) \sim v_{en}(r) \propto n_e$, makes these profiles more steepened.
- Analytical solution:** $n_e(z, r) = n_e(z, 0) J_0(a_0 r / R)$ where a_0 is the first 0 of Bessel function, J_0 .

$u_r(r)$ profiles (Fig. R3) illustrate the high magnetic confinement. Taking into account that $-e\phi \sim m_e u_{\theta}^2/2$, last result indicates that radial electric field is only important in a thin inertial layer preceding the Debye sheath. $u_{\theta}(r)$ develops thanks to collisions (Fig. R4). The azimuthal current provides the magnetic force that sustains the large radial density drop as in a θ -pinch.

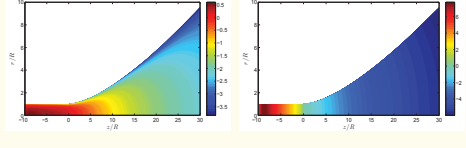


2D Maps

Source details: Case 1 results are presented below for the plasma density and velocity. Large gradients of these magnitudes appear close to all walls. Radial gradients increase with magnetic confinement, in fact with the Hall parameter ω_{ce}/ν_e . Axial gradients close to A/B are due to electrostatic confinement and drive the backstreaming flow.

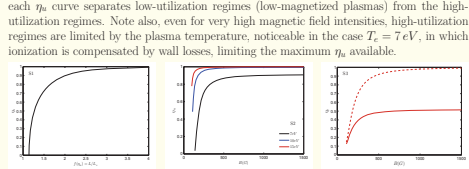


Helicon Thruster maps: The plasma density distribution along the complete device is depicted here. $\log(n_e/n_0)$, being $n_0 = g_0/c_s$. It manifests how density varies much less inside the source than in the plume, where it may drop up to 4 orders of magnitude, presenting a **high radial rarefaction**. Electric potential gradients inside the source are purely axial, because plasma is radially confined by the magnetic field. Equipotential lines become curved as advancing along the MN.



Helicon Source Performances

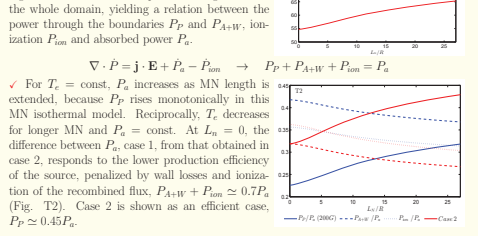
- Propellant utilization:** $\eta_p = \frac{\dot{m}_p}{\dot{m}}$ **Production efficiency:** $\eta_p = \frac{\dot{m}_p}{\dot{m}_i + \dot{m}_n + \dot{m}_e}$
- Analytical law for $L_e/L_0 = f(\eta_p)$ states that η_p increases with T_e , L and \dot{m} , requiring $L_e > 2.5$ to obtain a high propellant utilization, $\eta_p > 0.95$ (Fig. S1).
- $\eta_p - B$ curves are plotted for different electron temperatures (Fig. S2). The knee of each η_p curve separates low-utilization regimes (low-magnetized plasmas) from the high-utilization regimes. Note also, even for very high magnetic field intensities, high-utilization regimes are limited by the plasma temperature, noticeable in the case $T_e = 7 \text{ eV}$, in which ionization is compensated by wall losses, limiting the maximum η_p available.



- The flow to the rear wall should be reduced because represents almost 50% of η_p losses (Solid red line in Fig. S3). If a perfect magnetic screening is assumed at the rear wall, η_p may reach values over 90% for the typical range of magnetic field intensities 500 - 1000G (dashed red line).
 - Curves of constant efficiencies, η_p and η_p , are depicted on the parametric plane $B - \dot{m}$ (Fig. S4). These are useful to:
 - Optimize the helicon source efficiencies.
 - Obtain a clear map of the region where the sensitivity to parametric deviations is smaller, here, the knee of η_p curves.
- It may be predicted that operating the source close to this zone is a good choice in terms of parameter sensitivities and efficiency.

Helicon Thruster Performances

- Global energy balance** determines the relation between the absorbed power, the **constant plasma temperature**, and the length L_e of the nozzle region (Fig. T1). The energy equation grouping all contributions of all species is integrated over the whole domain, yielding a relation between the power through the boundaries P_P and P_{A+W} , ionization P_{ion} and absorbed power P_e .



- For $T_e = \text{const}$, P_e increases as MN length is extended, because P_P rises monotonically in this MN isothermal model. Reciprocally, T_e decreases for longer MN and $P_e = \text{const}$. At $L_e = 0$, the difference between P_e , case 1, from that obtained in case 2, responds to the lower production efficiency of the source, penalized by wall losses and ionization of the recombined flux, $P_{A+W} + P_{ion} \approx 0.7 P_e$ (Fig. T2). Case 2 is shown as an efficient case, $P_P \approx 0.45 P_e$.
- Thrust efficiency**, $F^2/2\dot{m}P_e$, is evaluated taking into account all contributions to the thrust F : $F = F_{grc} + F_{dec} + F_{mag}$
- Terms on the RHS retain the contribution of pressure on walls F_{grc} , electrostatic sheath at the back wall F_{dec} , and MN contribution F_{mag} . Thrust is related to plasma axial momentum flow, F_z , at sections E and D. $F_{z,E} = F_{grc} + F_{dec}$ and $F_{z,D} = F_z$. Case 2 thrust efficiency is over 20% if $L_e/R \geq 14$ (Fig. T3).

Conclusions

- A 2D model (Source + MN) of the helicon plasma thruster has been derived.
- Optimum regimes for source-related efficiencies have been determined.
- Analytical models are recovered at the high-magnetized regime.
- First model assessing global Helicon Thruster performances, including thrust efficiency and power losses.
- Plasma temperature depends on nozzle length.
- This fluiddynamic model should be coupled to plasma-wall interaction model.
- Main uncertainties are: power absorption, electron distribution function, radiation losses, downstream plasma detachment

References

[1] Ahedo, E., Gallardo, J. M., & Martínez-Sánchez, M. (2003). Effects of the radial-plasma wall interaction on the axial Hall thruster discharge. *Physics of Plasmas*, 10(8), 3397-3409.

[2] Ahedo, E. (2009). Cylindrical model of a helicon-generated plasma. *31th International Electric Propulsion Conference*, Ann Arbor, Michigan, USA. IEP-2009-193.

[3] Ahedo, E. (2009). Parametric analysis of a magnetized cylindrical plasma. *Physics of Plasmas*, 16, 113503.

[4] Ahedo, E., & Merino, M. (2010). Two-dimensional supersonic plasma acceleration in a magnetic nozzle. *Physics of Plasmas*, 17, 073501.

[5] Batschelet, O. V. (2009). Minilab Helicon Thruster. *IEEE Transaction on Plasma Science*, 37, 1563-1571.

[6] Fruchtman, A., Makrinich, G., & Ashkury, J. (2005). Two-dimensional equilibrium of a low temperature magnetized plasma. *Plasma Sources Science and Technology*, 14, 152-167.

[7] Ladner, T., Charles, C., & Boswell, R. W. (2011). Characterization of a helicon plasma source in low diverging magnetic fields. *Journal of Physics D: Applied Physics*, 44, 055202.

[8] Pavarini, et al. (2009). Design of 50W Helicon Plasma Thruster. *31th International Electric Propulsion Conference*, Ann Arbor, Michigan, USA. IEP-2009-205.

[9] Shugh, J., Winglee, R., & Zienba, T. (2006). Performance enhancement and modeling of the high power helicon plasma thruster. In W. D. C. American Institute of Aeronautics and Astronautics (Ed.), *43th Joint Propulsion Conference*, Sacramento, CA. AIAA 2006-5257.

Acknowledgments

- Support comes from the Spanish Government (Project AYA-2010-61699) and the Air Force Office of Scientific Research, Air Force Material Command, USAF (grant FA8655-12-1-2043).

39th IEEE International Conference on Plasma Science (2P-185) Edinburgh, 8-12 July 2012
E.T.S.I. Aeronáutica, Pza. Cardinal Cisneros 3, 28040 Madrid, Spain
http://www.iee.es/area/iaa/2012
mailing address: eahedo@upm.es, javier.navarro@upm.es

PAGE INTENTIONALLY LEFT BLANK

Advanced Plasma Propulsion with Magnetic Nozzles: Plasma detachment

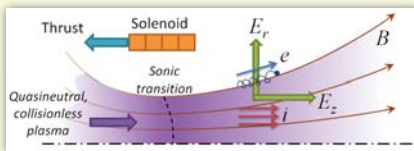
Mario Merino and Eduardo Ahedo
Universidad Politécnica de Madrid

Three existing detachment theories are shown to be inadequate for magnetic nozzles. Our 2D code DIMAGNO is extended to allow iterative calculation of the induced magnetic field, include electron inertia effects, and to integrate beyond the turning point of the plasma tube. Two novel detachment modes are proposed and simulated within our ideal plasma: Plasma self-demagnetization due to the induced magnetic field, and ion self-separation, which leads to the formation of quasi-conic plume with highly-rarefied peripheral plasma. Results support the applicability of magnetic nozzles for propulsion applications.

Magnetic Nozzles for Plasma Propulsion

A magnetic nozzle is an axisymmetric, divergent magnetic field that harnesses and controls the expansion of a supersonic plasma jet.

1. The field is sufficient to magnetize electrons, which are attached to the field and describe its geometry.
2. Ions (heavier) are not magnetized (or only partially).
3. Electrons pull ions via ambipolar electric field.
4. Pressure is confined by the magnetic force acting on plasma electric currents
5. Ions are expanded radially and accelerated axially, producing thrust



Advantages over solid nozzles:

- Wall-plasma contact is avoided
- Modifying field geometry and intensity can allow to control thrust and I_{sp}
- Applicable to a wide range of thrusters (helicon, AF-MPD, VASIMR...) and powers (50 W to MW)

Failure of existing detachment theories

Theories claim convergent detachment based on plasma resistivity (Hooper et al. [7]), electron inertia (Moses et al. [8]), and on the plasma currents stretching the magnetic field to infinity (Arefiev et al. [9]).

A perturbation analysis [2] of our ideal solution shows that:

- Electron inertia (its dominant terms, [4]) and resistivity both cause outward diffusion of the plasma → divergent detachment (instead of convergent):

$$\frac{e\mathbf{u}_e \cdot \mathbf{B}}{\text{Outward diffusion } (> 0)} = \frac{(m_e/r)\mathbf{u}_e \cdot \nabla(r\mathbf{u}_{\theta e})}{\text{Inertia } (> 0)} + \frac{m_e \nu_{ei} \mathbf{u}_{\theta e}}{\text{Resistivity } (> 0)}$$

- Plasma-induced magnetic field does not stretch the field, but opens it instead (increased divergence).

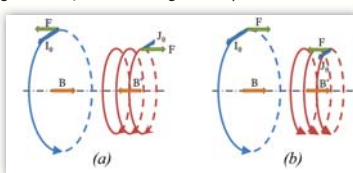
$$\nabla \times \mathbf{B}_p = \mu_0 (\mathbf{j}_i - \mathbf{j}_e) = \mu_0 e n (\mathbf{u}_i - \mathbf{u}_e)$$

→ Diamagnetic induced field

→ The three theories are inadequate for propulsive magnetic nozzles

The central reason lays in the omitted diamagnetic electron currents that are natural in the hot plasma, which confine and accelerate the plasma magnetically, producing and conveying thrust back to the thruster.

The diamagnetic character (i.e., repulsion) is essential for thrust generation, but is missing in cold-plasma models.



Acceleration and increased divergence

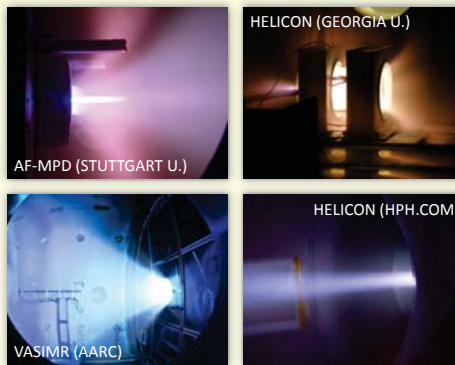
Deceleration and stretching

The need for plasma detachment

Electrons tend to remain tied to the closed magnetic lines. If ions were to follow,

- Thrust would be cancelled,
- Efficiency would be ruined,
- The energetic coming-back plasma could affect satellite

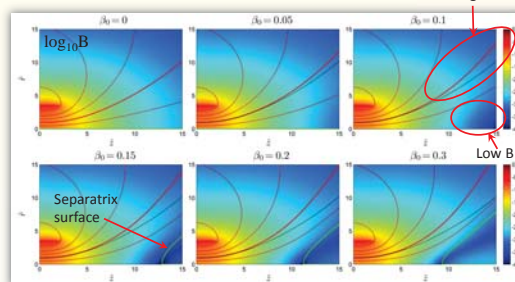
Plasma detachment is a requirement for space propulsion: the plasma must get rid of the field and form a free plume once accelerated



Detachment via self-demagnetization

The diamagnetic induced field does not stretch the field, but it causes the following:

- (1) Increased nozzle divergence, which is more pronounced for higher $\beta_0 = \mu_0 \rho_e \omega / B^2$.
- (2) Formation of a low-B region about the axis.



The low-B region causes the demagnetization of the core of the plasma beam (plasma is demagnetized when electron Larmor radius $\ell_e \sim L$; typical helicon thrusters need $\ell_e / \ell_{e0} \sim 10^2 - 10^3$). Demagnetization means that plasma becomes effectively uninfluenced by the applied magnetic field (i.e., the plasma in the core is detached).

The magnetic field can even cancel out as the induced field competes with the applied one, forming a magnetic separatrix. This surface divides nozzle into "internal" and "external" regions.

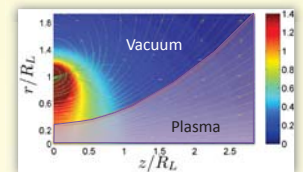
The downstream evolution of the external region must be dictated by residual pressure and fields, to form a "plasma plume"

The rarefied peripheral plasma is not yet demagnetized. The applied magnetic field continues to repel the peripheral plasma away from the thruster, so its effect is still beneficial.

The DIMAGNO 2D model and code

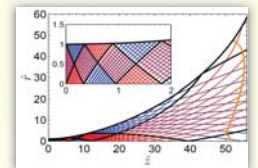
DIMAGNO is our in-house developed code for 2D magnetic nozzle plasma flow simulation.

DIMAGNO describes the supersonic expansion of a fully-ionized, hot plasma (i.e. near collisionless) in the magnetic field generated by a set of solenoids and/or current loops. It is a multifluid, quasineutral code. Main assumptions: fully magnetized electrons and partially magnetized ions.



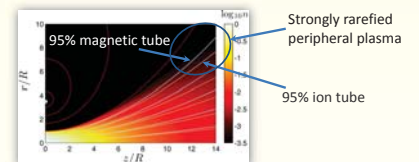
The code is extended here to allow the iterative calculation of the plasma-induced field (for up to mild plasma pressures, $\beta=0(1)$), to allow the integration of the flow beyond the turning point of the field, and to include the dominant electron inertia terms.

The Method of Characteristics is used to integrate ion flow → Fast and accurate code. Electron equations are algebraic.



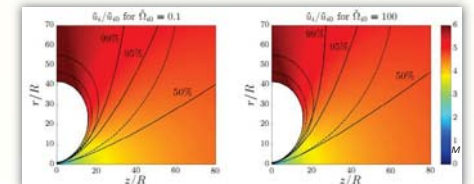
Detachment via ion self-separation

While light electrons are fully magnetized; massive ions are not ($m_i/m_e \sim 10^4$). The ambipolar \mathbf{E}_\perp field needed to expand ions radially to maintain quasineutrality implies a large density gradient, causing a strong 2D rarefaction of beam.

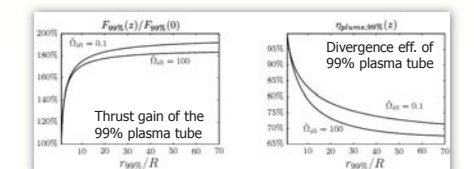


As ion velocity increases, \mathbf{E}_\perp is not sufficient to deflect ion trajectories, and they begin to separate inwards from the magnetic field. Stronger magnetization defers separation.

Far downstream, ion self-separation leads to the gradual formation of an almost-conical plume. Ion magnetization plays only a small role (in the studied range).



Most of the plasma beam does not turn back (< 1% of flow), supporting that detachment will not be a major issue for propulsive applications.



[1] Two-dimensional supersonic plasma acceleration in a magnetic nozzle, E. Ahedo and M. Merino, Phys. Plasmas 17, 073501 (2010)
 [2] On plasma detachment in propulsive magnetic nozzles, E. Ahedo and M. Merino, Phys. Plasmas 18, 053504 (2011)
 [3] Simulation of Plasma Flows in Divergent Magnetic Nozzles, E. Ahedo, IEEE Trans. Plasma Sci. 39, v. 11, 2938 (2011)
 [4] Two-dimensional plasma expansion in a magnetic nozzle: separation due to electron inertia, E. Ahedo and M. Merino, Phys. Plasmas 19, 083501 (2012)

[5] Plasma detachment mechanisms in a magnetic nozzle, M. Merino and E. Ahedo, AIAA-2011-5999
 [6] Magnetic Nozzle Far-Field Simulation, M. Merino and E. Ahedo, AIAA-2012-3943
 [7] E.B. Hooper, J. Prop. and Power 9, 757 (1993)
 [8] R.W. Moses et al., AIP Conference Proceedings 246, 1293 (1992)
 [9] A.V. Arefiev and B.N. Breizman, Phys. Plasmas 12, 043504 (2005)

Acknowledgments

This work has been sponsored by the Air Force Office of Scientific Research, USAF (Grant No. FA8655-12-1-2043). The authors would like to thank the Air Force Office of Scientific Research for providing the facilities and support for this research was provided by the Gobierno de España (Project AYA-2010-61699). Thank you to providers of thruster pictures.

Contact

mario.merino@upm.es
 eduardo.ahedo@upm.es
 http://web.fimetsia.upm.es/ep2



Distribution A: Approved for public release; distribution is unlimited.

PAGE INTENTIONALLY LEFT BLANK